Robotic Fabrication of Shear Timber Connections

Exploring the Structural Behavior of Robotically Fabricated Mechanical and Adhesive Shear Connections in Timber Structures

Bindels, Thom H.W.

Award date:
2024

EINDHOVEN UNIVERSITY OF TECHNOLOGY

Department of the Built Environment
Unit Structural Engineering and Design

Robotic Fabrication of Shear Timber Connections

Exploring the Structural Behavior of Robotically Fabricated Mechanical and Adhesive Shear Connections in Timber Structures

Master's Thesis

T.H.W. (Thom) Bindels

June 10, 2024

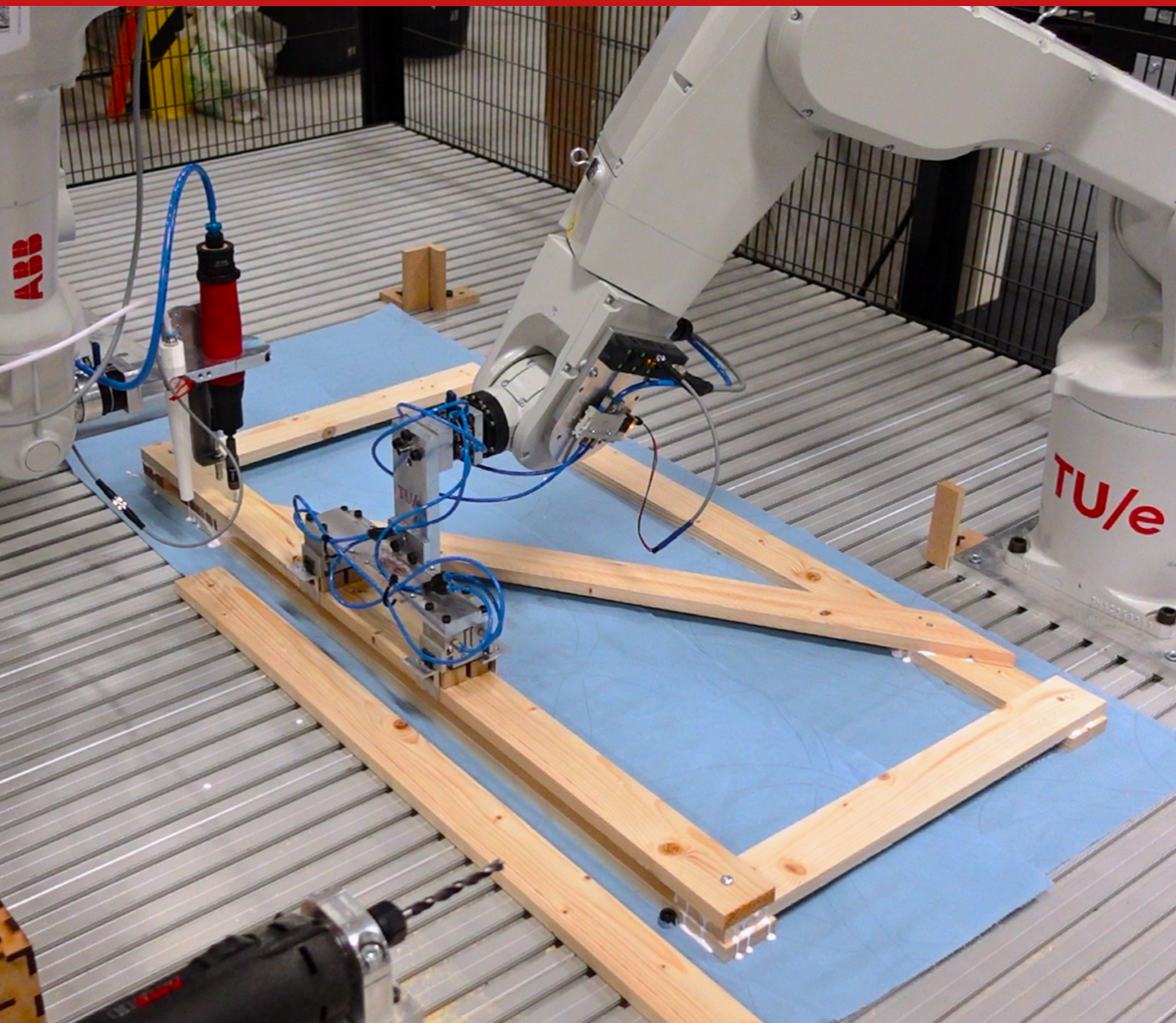

General

Title	Robotic Fabrication of Shear Timber Connections
Subtitle	Exploring the Structural Behavior of Robotically Fabricated Mechanical and Adhesive Shear Connections in Timber Structures
Document	Master's Thesis
Date	June 10, 2024

Student

Author	T.H.W. (Thom) Bindels
Student ID	0944588
Email (student)	t.h.w.bindels@student.tue.nl
Email (personal)	thom.bindels@gmail.com
University	Eindhoven University of Technology
Faculty	Built Environment
Master program	Architecture, Building and Planning
Master track	Structural Engineering and Design

Graduation committee

Committee chair	dr.ir. S.P.G. (Faas) Moonen | Associate Professor ISD
Committee member	ir. A.P.H.W. (Arjan) Habraken | Assistant Professor ISD
Committee member	M.T. (Matthew) Ferguson, EngD | External

Abstract

Keywords: *robotic fabrication, automation, fastener, adhesive, connection, timber, digital design, computational design*

The construction industry faces significant challenges across multiple aspects, including, but not limited to, productivity, costs, demand, and sustainability. To address these challenges, the industry must innovate rapidly to adapt to current demands. One approach to achieving this is by increasing digitization and automation within the industry. While sectors such as manufacturing adopted automated workflows long ago, the construction industry still lags behind. Recent developments indicate gradual progress, such as the growing use of prefabricated elements, which offer numerous advantages over traditional construction methods. This research delves into the prefabrication possibilities within the construction industry, specifically focusing on the robotic fabrication of structural elements. It concentrates on the robotic fabrication of timber trusses using either mechanical fasteners or adhesives, both of which are highly suitable for integration into a robotic workflow. By doing so, this thesis contributes to the advancement of knowledge on robotic applications in the construction industry.

Contents

List of Tables

List of Figures

List of Symbols

Adherend

ρ_{k}	5 percentile material density
ρ_{mean}	Mean material density
$E_{\mathrm{m,0,k}}$	5 percentile modulus of elasticity parallel to grain
$E_{\mathrm{m,0,mean}}$	Mean modulus of elasticity in bending parallel to grain
$E_{\mathrm{m,90,mean}}$	Mean modulus of elasticity in bending perpendicular to grain
$f_{\mathrm{c,0,k}}$	Compressive strength parallel to the grain
$f_{\mathrm{c,90,k}}$	Compressive strength perpendicular to the grain
$f_{\mathrm{m,k}}$	Bending strength
$f_{\mathrm{t,0,k}}$	Tensile strength parallel to the grain
$f_{\mathrm{t,90,k}}$	Tensile strength perpendicular to the grain
$f_{\mathrm{v,k}}$	Shear strength
G_{mean}	Mean shear modulus of elasticity
l	Member length
t	Member thickness
w	Member width

Loading and geometry

α	Load angle
l_{joint}	Joint member overlap

Mechanical fastener

d_1	Nominal diameter
d_2	Thread diameter
$f_{\mathrm{ax,k}}$	Withdrawal resistance parameter
$f_{\mathrm{y,k}}$	Characteristic yield strength
$M_{\mathrm{y,k}}$	Characteristic yield moment
$t_{\mathrm{tens,k}}$	Characteristic tensile strength

Adhesive

ν_{a}	Poisson's ratio
E_{a}	Modulus of elasticity
l_{a}	Bond length
t_{a}	Thickness

Robotic system

ρ_{a}	Dispensed adhesive per area
ρ_{req}	Required adhesive per area according supplier
N	Peristaltic pump flow rate
Q	System flow rate
s	Adhesive spread
v	Robot speed

1 Introduction

1.1 Scope

The architecture, engineering, and construction (AEC) industry faces many challenges. Some of these challenges are:

- Demand for (affordable) housing is increasing rapidly, especially in the Netherlands (Maskuriy et al., 2019).
- Increased material and labor costs result in significantly higher construction costs for new developments (Dixit, 2020).
- An aging workforce and increasing housing demand leads to a higher productivity demand (Hasan et al., 2018).

To tackle these challenges as an industry, the way of building must adapt. Ideally, new building methodologies should decrease construction timelines and expenses without compromising quality. Progress in computational design, fabrication methods, and robotics enables a whole range of opportunities for this within the building industry. Yet, while these technologies have been applied in other industries, the construction sector lags behind in their adoption.

Robotic fabrication of building elements for the construction industry has many promising advantages that can help with the challenges the AEC industry is facing, of which some are:

- **Increased productivity:** in theory, robotic processes only stop due to faulty equipment. The process is not dependent on human endurance and working times, and can run continuously.
- **Decreased on-site building speed:** by fabricating (parts of) buildings off-site, building times on-site reduce. In well-developed robotic processes, assembly times on-site (which are more challenging conditions) are a fraction of on-site construction.
- **Quality control:** robots have higher accuracy than humans, and can perform at a constant quality level. This increases the product quality and reduces construction mistakes.
- **Improved worker safety:** construction work takes its toll on construction workers, which is evident from the younger pension age (Järvholm et al., 2014). By replacing labor intensive tasks by robot workflows, worker safety increases.
- **Worker shortage:** worker shortages increase building times and slow down developments. By developing robotic processes that can take over these tasks, the worker shortage can be relieved.
- **Mass customization:** while increasing productivity, customization is not necessarily decreased. Technological advancements in digital design allow for a large variety in design options, which will be advanced rapidly by the recent developments in AI learning models.

1.2 Relevance

Many of the problems in the AEC industry can be linked to two main themes: productivity and sustainability. Productivity is particularly critical as demand continues to increase while the industry's productivity fails to keep pace. Robotic processes offer a significant improvement by enabling continuous, off-site fabrication of building parts. These processes are not affected by weather conditions or the availability of skilled labor. Moreover, on-site assembly of these prefabricated elements requires fewer laborers and is much quicker.

Robotic fabrication also has the potential to reduce environmental impact by using materials more efficiently and minimizing waste. When digital design processes are aimed at robotic fabrication, waste can be further reduced through smart assembly and patterning algorithms. Additionally, processes can easily adapt to new building materials, including biobased options.

Timber is a particularly suitable material for sustainable use, provided it is sourced properly. Timber is well-suited for robotic processes, as it does not require drying or layering like 3D printing materials, nor does it involve complex and energy-intensive processes like 3D steel printing. The primary drawback is that robotic fabrication with timber tends to be subtractive, necessitating careful design and detailing to minimize waste.

1.3 State-of-the-Art

Research on robotic applications within the built environment is rapidly evolving and there is a wide range of research that touches upon this topic. In structural applications that use timber as a building material, several notable research projects stand out. One prominent example is the DFAB HOUSE, shown in Figure 1.1a, which is a collaboration of multiple ETH Zurich chairs and faculties as well as industrial partners (Graser et al., 2020). The DFAB HOUSE is designed, planned, and (mostly) fabricated using digital processes. One of the processes utilized, is the assembly of the spatial modules, of which one is shown in Figure 1.1b (Thoma et al., 2019). This robotic process is both digitally planned and executed using multiple robotic techniques. It ensures the precise placement of structural members and incorporates additional tools for fastening and assembly. These tools include sawing, in-place milling, and a tracking system, all integrated into the robotic workflow.

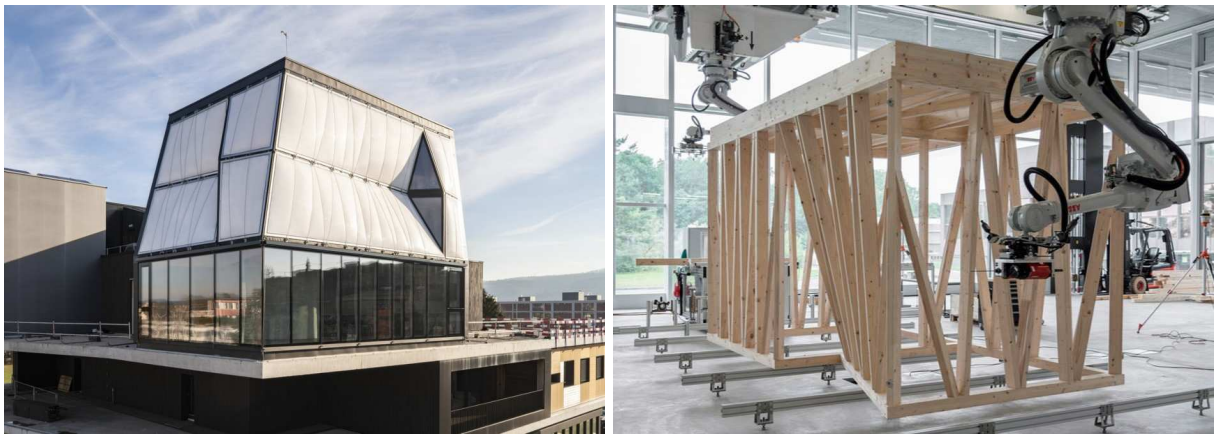

(a) DFAB HOUSE (b) Spatial structure

Figure 1.1: Finished DFAB house and spatial structure (Graser et al., 2020).

Another notable example that utilizes adhesive is the BUGA Wood Pavilion by the University of Stuttgart (Wagner et al., 2020). This project requires a complex digital design and assembly sequence to ensure all the cassettes fit together properly. The fabrication of these cassettes involves multiple tasks, including picking and placing the elements, adhesive dispensing, nail fastening, and milling. Since adhesive connections are subject to strict building code regulations, the adhesive dispensing process had to undergo thorough testing with numerous parameter studies.

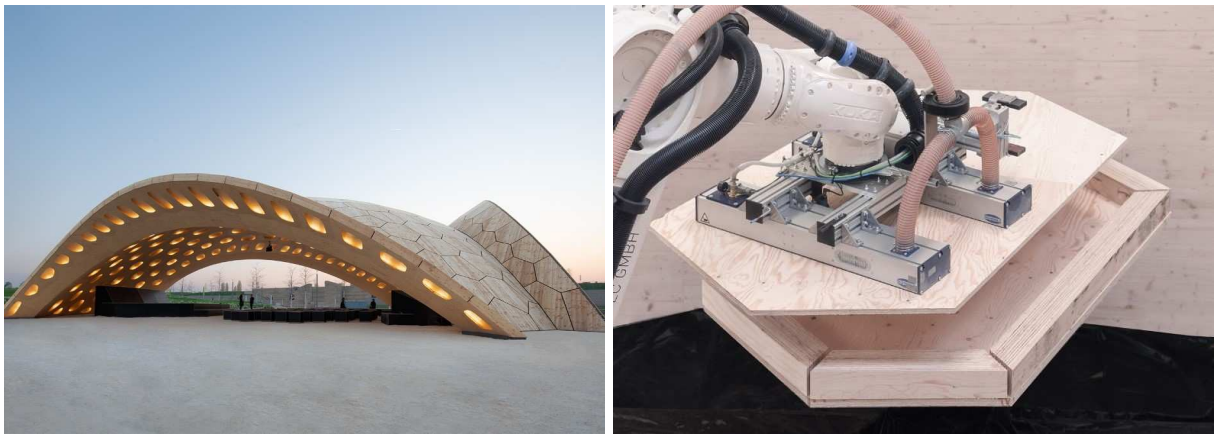

(a) BUGA Wood Pavilion (b) Fabrication

Figure 1.2: Finished BUGA Wood Pavilion and the fabrication process of the timber cassettes (Wagner et al., 2020).

Last, another project of ETH Zurich is referenced: The roof structure of the university's digital fabrication lab, where the DFAB spatial structures mentioned earlier are fabricated. These trusses are parametrically designed and robotically fabricated in collaboration with industry partners (Gramazio Kohler Research, 2016). The trusses have multiple lap joints fastened using mechanical fasteners. Placement algorithms for the fasteners were crucial to avoid collisions while ensuring sufficient strength.

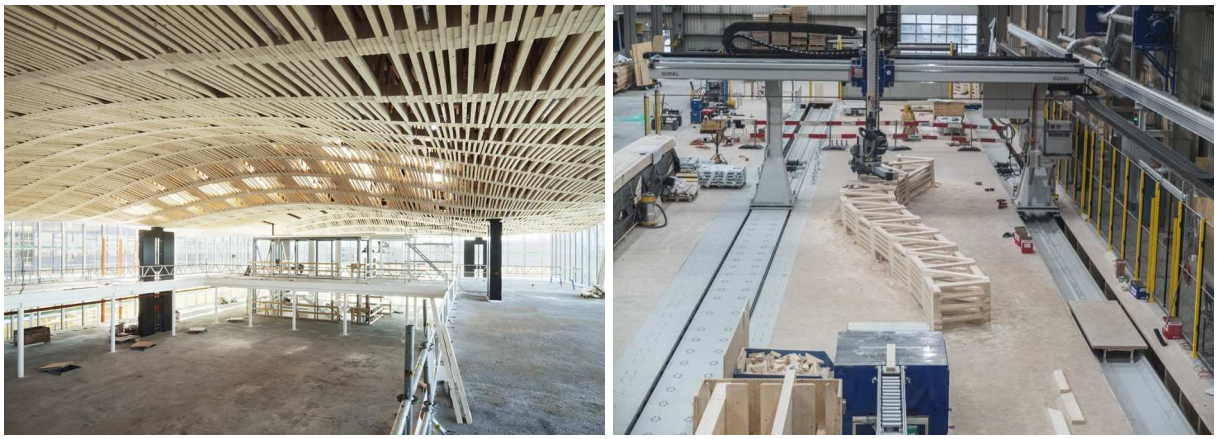

(a) Arch_Tec_Lab roof (b) Fabrication

Figure 1.3: Arch_Tec_Lab timber roof trusses (Gramazio Kohler Research, 2016).

1.4 Objectives

This research aims to develop a robotic fabrication process that is capable of fabricating timber trusses either glued or mechanically fastened. By doing so, it provides a process that can fabricate structural members suitable for load-bearing applications in an automatic process. It builds upon previous research, of which examples are shown in Section 1.3, by combining the various robotic processes, joining methods, and structural elements it adds to existing literature. To achieve this, the following research question must be answered:

> **"How Can Adhesive And Mechanical Shear Timber Connections Be Fabricated Robotically While Ensuring Their Structural Integrity?"**

To answer this research question, the following sub-questions must be answered:

- How can adhesive or mechanical shear joints be optimized during the design phase?
- What are the different parameters of an adhesive dispensing system, and how are these controlled to ensure reliable dispensing of the adhesive?
- Which subsystems are required to ensure proper curing of the adhesive joint?
- How can an individual adhesive dispensing system be integrated in a robotic workflow?
- What strength and reliability can be achieved in an adhesive timber joint fabricated by a robotic process?

To answer the set research objectives, the following steps are taken. First, a design toolbox using Grasshopper is developed. This toolbox quickly assesses and analyzes mechanical joints in a truss configuration, allowing the study of different parameters' effects on strength. Additionally, the toolbox serves as a general tool for designers to experiment with or optimize specific design scenarios. Next, a robotic setup is developed in the structural engineering lab to fabricate such a truss physically. This setup includes various existing tools, adapted tools, and newly developed tools that must be integrated to function as a cohesive system. The robotically fabricated elements are then tested in shear to evaluate any differences between the proposed robotic process and traditional fabrication methods. All these results are gathered to: First, assess whether the proposed robotic setup can fabricate equally strong connections as traditional methods. Second, assess different design options and their various parameters, and how they affect the structural performance.

This thesis starts by providing important background information on mechanical and adhesive shear connections in Chapters 2 and 3 respectively. These sections cover general information about the available connections, stress and/or strength calculations, and design considerations. Next, in Chapter 4 the used approaches are elaborated. These are split into three sections. First, the design toolbox to generate and optimize mechanical shear connections in trusses is presented in Section 4.1. Second, the physical robotic setup used for fabrication and its subsystems and their parameters are presented in Section 4.2. Last, the experimental setup and corresponding FEM models used to evaluate the robotically fabricated samples is elaborated in Section 4.3. Next, the results gathered using these methods are presented in Sections 5.1 to 5.3. The findings are discussed in Chapter 6, after which recommendations for further research are given in Chapter 7. Last, the thesis concludes in Chapter 8.

2 Mechanical Shear Connections

Mechanical shear connections in timber structures transfer forces through fasteners that are placed at an angle to the load path. The fasteners will be loaded in shear or as a combination with axial forces. This is realized using various dowel-type fasteners. These can be designed as ductile connections, by utilizing yielding of the fasteners. Resulting in the advantage that it avoids brittle failure modes of timber, if designed properly.

In design codes such as the EN 1995-1-1, the approach often starts with the determination of the strength of a single fastener (CEN, 2014). This is dependent on two main aspects: On the one hand, the resistance of the timber, called the embedment strength, which will be discussed in Section 2.2.1. On the other hand, the resistance of the fastener, which requires the fastener yield moment, which will be discussed in Section 2.2.2. With these properties known, the shear resistance of the fastener can be calculated. For this, the European yield model (EYM) developed by Johansen is utilized, which is presented in Section 2.2.3. Once the shear resistance of a single fastener is known, it can be utilized to determine the shear resistance of the entire connection. For this, an effective number of fasteners n_{ef} equal to or lower than the total number of fasteners is used. This includes the effects caused by the group effect, presented in Section 2.3.4.

2.1 Dowel-Type Fasteners

Dowel-type fasteners can be divided in a few groups, of which the most commonly used ones are shown in Figure 2.1: nails, screws, staples, dowels, and bolts. In EN 14592 the requirements are specified for these types, such as geometry and dimensions (CEN, 2022).

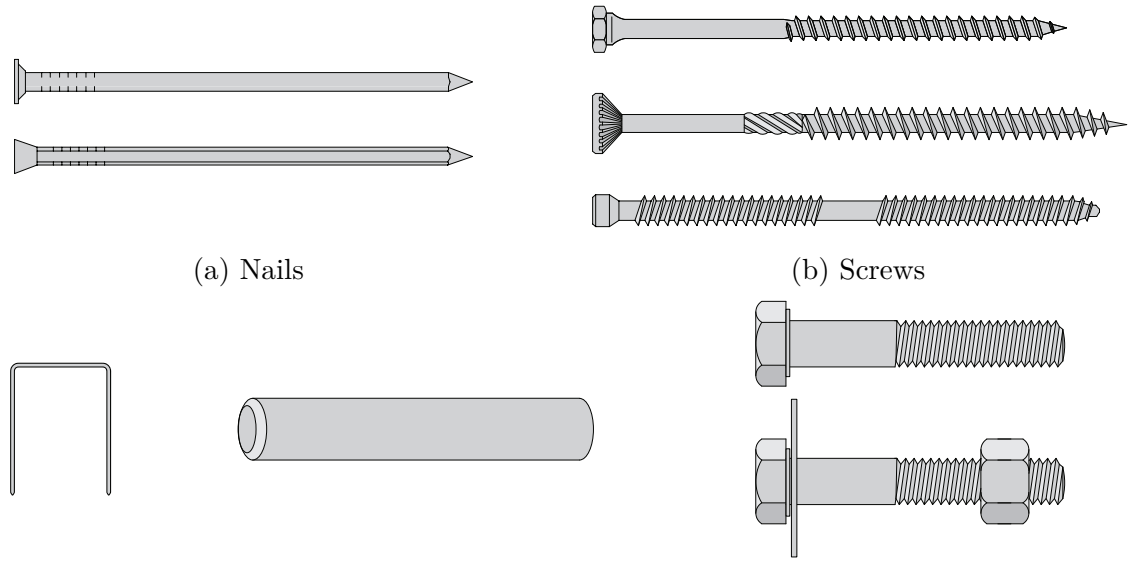

(a) Nails (b) Screws

(c) Staple (d) Dowel (e) Bolts

Figure 2.1: Common dowel-type fasteners (Kliger et al., 2022).

Nails have a maximum diameter of 8 mm. EN 1995-1-1 makes a distinction between smooth and other nails. Smooth nails have an entirely smooth shank, whereas other nails can have some kind of profile.

Screws have a maximum diameter of 24 mm. They have a (partly) threaded shank, which can be turned down from the original shank, or by rolling or forging the wire rod outwards. In the former case the outer thread diameter is equal to the shank diameter, in the latter case the inner thread diameter is equal to the shank diameter. Due to their threaded geometry, screws are suitable for axially loaded connections.

Staples are two-legged fasteners. They can be rectangular or have a curved segment. The diameter of the legs is related to the global dimensions of the staple.

Dowels have a constant prismatic shape with a minimum diameter of 6 mm and a maximum of 30 mm. The shank can be circular or fluted, where in case of a fluted shank the inner diameter may not be less than 95% of the outer diameter. In contrast to nails and screws, dowels do not have a head.

Bolts have a minimum diameter of 6 mm and a maximum of 30 mm. They have a (partly) threaded shank to accommodate nuts. The head of the bolt is often hexagonal, but other geometries are available. In contrast to screws, bolts require pre-drilling of the hole.

Another type of mechanical shear connection can be realized by plates. Two common plates are nail plates and punched metal plates. These variations are shown in Figure 2.2. The nail plates have pre-drilled holes so that minimum distances are ensured and act as a template for certain fastener patterns. The nail plates are fastened using either nails or screws. Punched metal plates have folded parts, which directly act as the nails. They are often assembled off-site, for example in roof trusses.

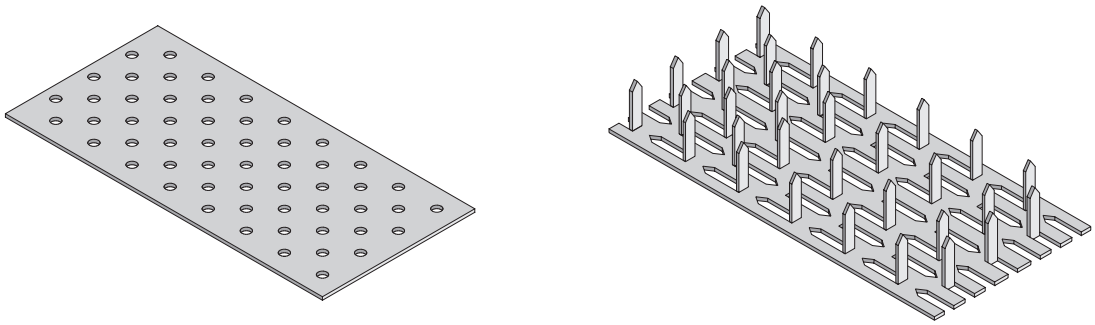

(a) Nail plate (b) Punched metal plate

Figure 2.2: Plate fasteners (Kliger et al., 2022).

2.2 Single Fastener Shear Strength

2.2.1 Timber Embedment Strength

2.2.1.1 Embedment Stress

The embedment strength is a property that describes the resistance of a piece of timber against compression caused by a dowel-type fastener loaded in shear. It is not an inherent material

property of the timber, as it also depends on the fastener diameter. The test procedure to determine the embedment strength is described in EN 383 (CEN, 2007). The test, as shown in Figure 2.3, is performed using a stocky dowel, where the embedment strength is

$$f_{\mathrm{h,k}} = \frac{F_{\max}}{A} = \frac{F_{\max}}{d\,t} \tag{2.1}$$

where $F_{\max}$ is the maximum load reached
A is the projected dowel area

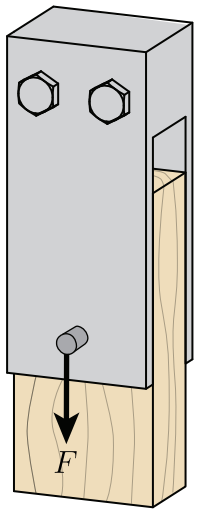

Figure 2.3: Test procedure to determine embedment strength $f_{\mathrm{h,0,k}}$ according to EN 383.

EN 1995-1-1 provides empirical relationships to determine the embedment strength of softwood parallel to the grain. For nail diameters up to 8 mm and screws smaller than 6 mm it can be calculated using

$$f_{\mathrm{h,0,k}} = 0.082\,\rho_{\mathrm{k}}\,d^{-0.3} \quad [\mathrm{N/mm^2}] \quad \text{without predrilled holes} \tag{2.2}$$

$$f_{\mathrm{h,0,k}} = 0.082\,(1 - 0.01\,d)\,\rho_{\mathrm{k}} \quad [\mathrm{N/mm^2}] \quad \text{with predrilled holes} \tag{2.3}$$

where ρ_{k} is the timber characteristic density [kg/m^3]
d is the fastener diameter [mm]

For nails larger than 8 mm, screws larger than 6 mm, bolts, and dowels the following relationship must be used

$$f_{\mathrm{h,0,k}} = 0.082\,(1 - 0.01\,d)\,\rho_{\mathrm{k}} \quad [\mathrm{N/mm^2}] \tag{2.4}$$

In general, Equation (2.2) must be used for fasteners that are not predrilled, such as nails. In other cases, Equation (2.4) must be used. This can be explained by the fact that, when a hole is not predrilled, the fibers are locally not parallel to the grain anymore. As a result, the shear load of the dowel is not transferred as compression parallel to the grain, but as a combination of compression parallel and perpendicular to the grain. This behavior is shown in Figure 2.4.

(a) Predrilled (b) Not predrilled

Figure 2.4: Fiber orientation around a fastener.

From these relationships it can be seen that the embedment strength increases for increasing timber density and decreases with increasing fastener diameter. The former is evident, as a denser material can resist higher loads. However, the expressions provided by EN 1995-1-1 are not fully agreed upon. Sandhaas et al., 2013 showed that the EN 1995-1-1 method overestimates the embedment strength of lower densities and underestimates the strength of higher densities. They proposed an embedment strength of

$$f_{\mathrm{h,0,m}} = 0.082\,\rho_{\mathrm{m}} \quad [\mathrm{N/mm^2}] \tag{2.5}$$

where $f_{\mathrm{h,0,m}}$ is the mean embedment strength parallel to the grain [$\mathrm{N/mm^2}$]
ρ_{m} is the timber mean density [$\mathrm{kg/m^3}$]

Hübner et al., 2008 showed that the EN 1995-1-1 equations are not accurate, based on their own test results as well as database results. They propose to calculate the embedment strength using the following adjusted equation, to give higher more accurate embedment strength for high-density woods

$$f_{\mathrm{h},\alpha,\mathrm{k}} = \frac{0.015\,\rho_{\mathrm{k}}^{1.3}\,d^{-0.2}}{(0.62 + 0.035\,d)\sin^2(\alpha) + \cos^2(\alpha)} \quad [\mathrm{N/mm^2}] \tag{2.6}$$

where $f_{\mathrm{h},\alpha,\mathrm{k}}$ is the embedment strength at an angle to the grain [$\mathrm{N/mm^2}$]
ρ_{k} is the timber characteristic density [$\mathrm{kg/m^3}$]
d is the fastener diameter [mm]
α is the angle of the load to the grain

Equations (2.2) and (2.4) provided by EN 1995-1-1 are compared in Figure 2.5. It is clear that there is a significant difference in embedment strength in case of predrilling. In the worst case, it can lead to a 42% reduction in embedment strength for fasteners with a diameter of 8 mm.

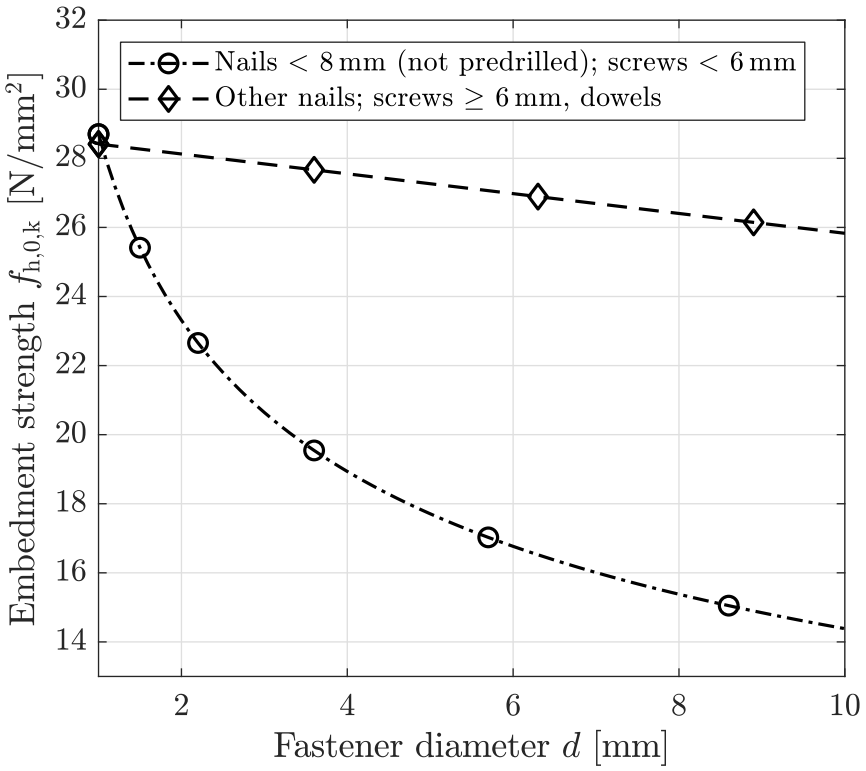

Figure 2.5: Embedment strength $f_{\mathrm{h,0,k}}$ of C24 wood ($\rho_{\mathrm{k}} = 350\,\mathrm{kg/m^3}$) using EN 1995-1-1.

2.2.1.2 Timber Loaded Perpendicular to the Grain

The embedment strength as presented in Section 2.2.1.1 is for timber loaded parallel to the grain. In case the timber is loaded under an angle to the grain, the embedment stress decreases as the timber is increasingly loaded in compression perpendicular to the grain. The embedment strength at an angle to the grain can be calculated by

$$f_{\mathrm{h},\alpha,\mathrm{k}} = \frac{f_{\mathrm{h,0,k}}}{k_{90}\,\sin^2(\alpha) + \cos^2(\alpha)} \quad [\mathrm{N/mm^2}] \tag{2.7}$$

where
- $f_{\mathrm{h},\alpha,\mathrm{k}}$ is the embedment strength at an angle to the grain [N/mm^2]
- $f_{\mathrm{h,0,k}}$ is the embedment strength parallel to the grain [N/mm^2]
- k_{90} is the ratio parallel-perpendicular embedment strength [-]
- α is the angle of the load to the grain

EN 1995-1-1 gives expressions to determine the k_{90} ratio by

$$k_{90} = 1.35 + 0.015\,d \qquad \text{for softwoods} \tag{2.8}$$

$$k_{90} = 0.95 + 0.015\,d \qquad \text{for hardwoods} \tag{2.9}$$

The ratio between the parallel embedment strength and the embedment strength under an angle to the grain is shown in Figure 2.6 for a fastener with a diameter of 9 mm. It can be seen that the embedment strength quickly decreases, once the load is perpendicular to the grain ($\alpha = 90°$) only 67% of the parallel embedment strength remains.

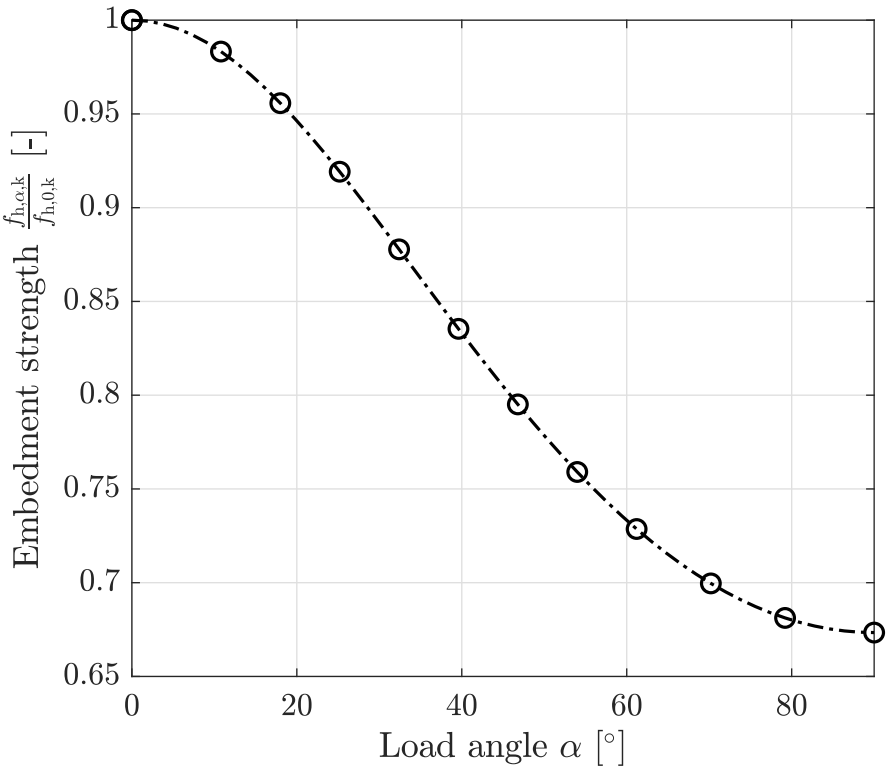

Figure 2.6: Embedment strength at an angle to the grain ($d = 9\,\text{mm}$).

The embedment stresses around a fastener are not constant, which are shown in Figure 2.7. In calculations, a simplified stress distribution is used, directly relating the applied load to the stresses by

$$F = \sigma_\text{h}\, t\, d \tag{2.10}$$

where σ_h is the embedment stress

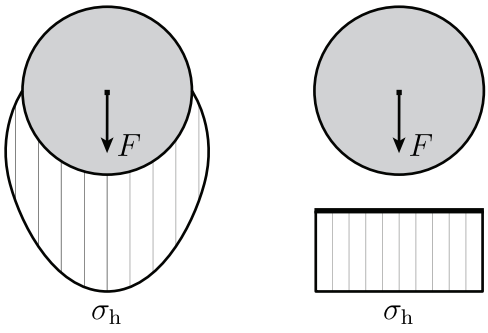

Figure 2.7: Real embedment stresses (left) and simplified stress distribution (right).

2.2.2 Fastener Yield Moment

The fastener yield moment can be derived analytically by assuming yielding of the entire cross section, as schematized in Figure 2.8. The centers of gravity of the semicircles with respect to

the centerline are located at a distance of

$$z_{\mathrm{s}} = \frac{4\,r}{3\,\pi} \tag{2.11}$$

The couple of the two resultant forces gives the fastener yielding moment by

$$M_{\mathrm{y}} = 2\,(f_{\mathrm{y}}\,z_{\mathrm{s}}\,A_{\mathrm{s}}) \tag{2.12}$$

$$= 2\left(f_{\mathrm{y}}\,\frac{4\,r}{3\,\pi}\,\frac{\pi\,r^2}{2}\right) \tag{2.13}$$

$$= \frac{1}{6}\,f_{\mathrm{y}}\,d^3 \tag{2.14}$$

where z_{s} is the semicircle center of gravity

A_{s} is the semicircle area

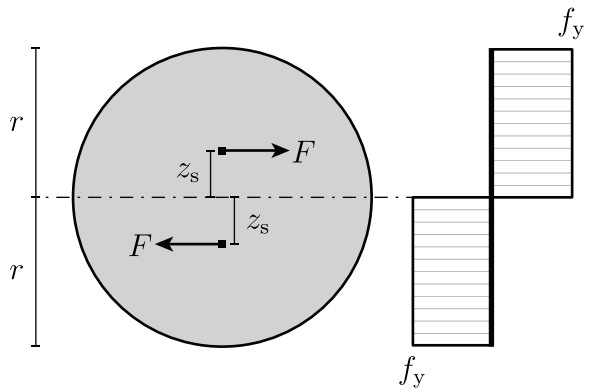

Figure 2.8: Fastener yielding of the entire cross section for a circular fastener.

The fastener yield moment can be derived experimentally, of which a procedure is prescribed in the EN 409 standard (CEN, 2009). This procedure is a four-point bending test, where it is assumed that the yield moment occurs at a rotation angle of 45° or earlier. The test is schematized in Figure 2.9, EN 409 prescribes the load F_i and distances l_i to be used.

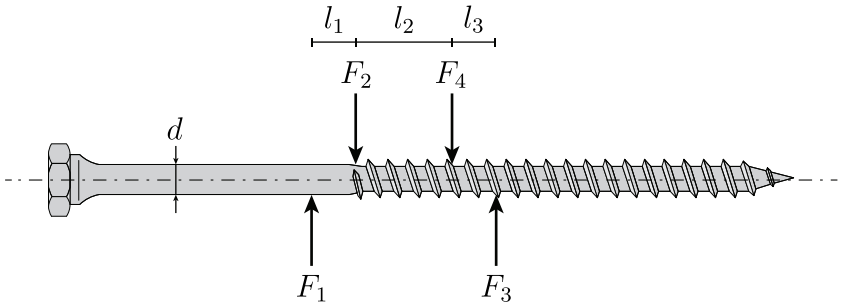

Figure 2.9: Test procedure to determine fastener yield moment $M_{\mathrm{y,k}}$ according to EN 409.

EN 1995-1-1 gives empirical expressions to determine the characteristic yield moment of fasteners. For dowel-types, except square nails and staples, it can be calculated using

$$M_{\mathrm{y,k}} = \frac{3}{10}\,f_{\mathrm{u,k}}\,d^{2.6} \tag{2.15}$$

where $f_{\mathrm{u,k}}$ is the characteristic tensile strength

This method differs in a few ways from the result obtained in Equation (2.14). First, the constant is lower. Second, the characteristic tensile strength is used instead of the yield strength. The yield strength is about 0.6 to 0.8 times smaller than the ultimate tensile strength for common steel grades (S235, S275, S355, S450). Last, the power of the diameter is lower.

The analytical and EN 1995-1-1 method are compared in Figure 2.10 for S235 steel. From the results it is clear that the two methods are in agreement for smaller fastener diameters up to about 15 mm. For lager diameters the EN 1995-1-1 approach is more conservative, resulting in lower fastener yield moments.

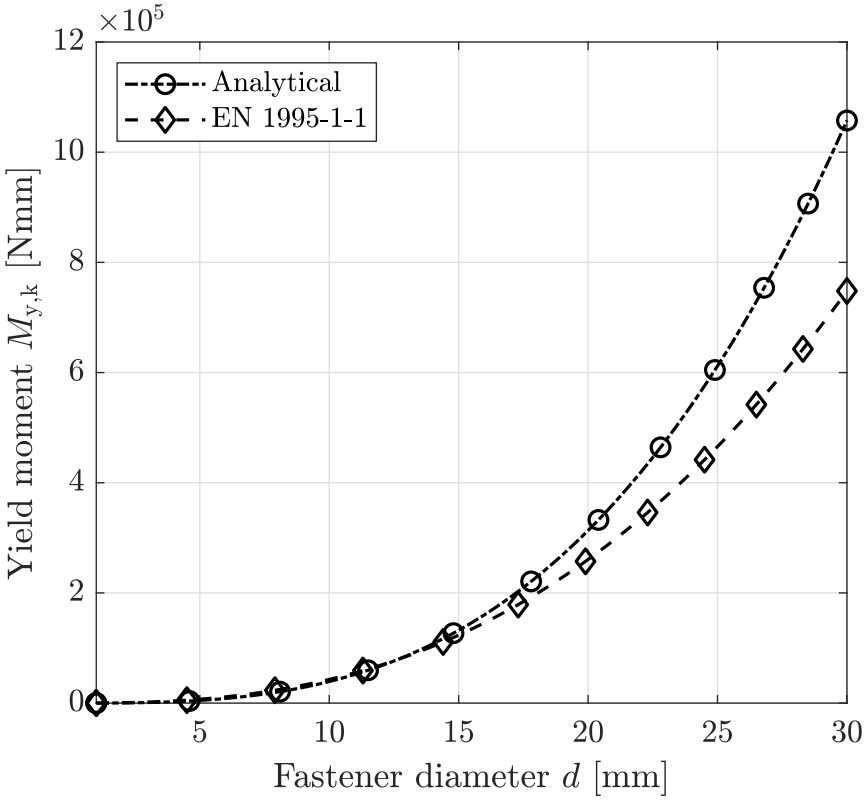

Figure 2.10: S235 dowel yield moment $M_{y,k}$ using the analytical and EN 1995-1-1 method.

The lower yield moment for larger diameters can be explained by the assumed bending angle of 45° for the formation of a full plastic hinge. To explain this, tests performed on connections following EN 26891 are investigated (CEN, 1991). In these tests, the connection is assumed to fail at a lateral displacement of $\delta = 15$ mm. However, a large number of tests performed by Jorissen and Blaß, 1998 showed that the bending angle of 45° was rarely achieved, visualized in Figure 2.11. Therefore, the analytical yield moment overestimates the strength of the connection. Consequently, H. Blaß et al., 2000 proposed a different expression to calculate the yield moment, which equals Equation (2.15) currently used in EN 1995-1-1. It is important to calculate with the (lower) yield moment that only assumes partial plasticity of the fastener. Otherwise, the design equations used in later sections overestimate the shear resistance of a joint due to an overestimation of the yield moment of the fasteners.

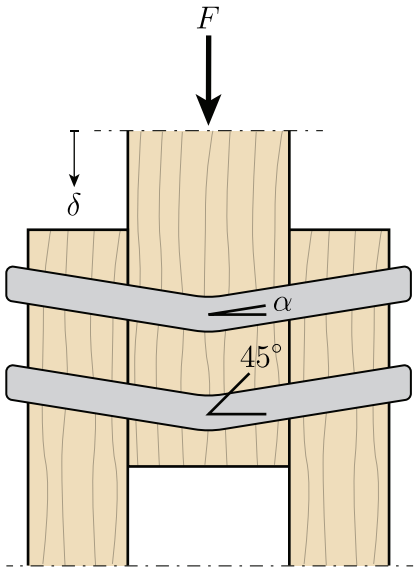

Figure 2.11: Failure of a dowel-type connection, where the fastener angle is significantly less than 45°. Failure is reached when $\delta = 15\,\text{mm}$.

Manufacturers of fasteners must meet the requirements specified in EN 14592 for their products. EN 14592 refers to the test procedure described in EN 409 to determine the yield moment. Rothoblaas is a manufacturer producing a wide variety of mechanical fasteners, which all meet these requirements. One of these fasteners is the KOS hexagonal head bolt, as shown in Figure 2.12. The technical data sheet is given in Appendix E.1. Using the fastener properties, the yield moment is calculated using the analytical and EN 1995-1-1 method. This is compared to the specified yield moments by Rothoblaas, the results are shown in Figure 2.13.

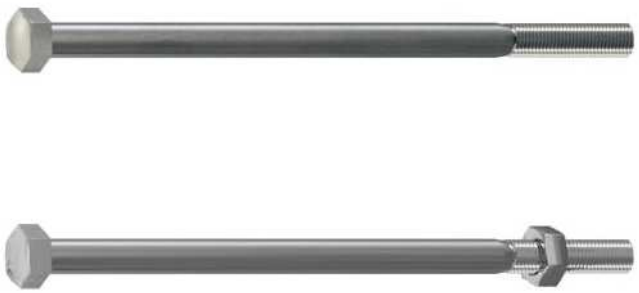

Figure 2.12: Rothoblaas KOS grade 8.8 hexagonal head bolt with a smooth shank.

It is clear that the yield moment determined by Rothoblaas is almost identical to that of the EN 1995-1-1 approach. This is in line with expectations, as EN 409 prescribes rotation angles for bolts. For these specific bolts, those rotation angles are limited to 12° or lower. Therefore, the yield moments extracted from the tests take into account that only partial plasticity is achieved. This explains the small deviation from the EN 1995-1-1 approach.

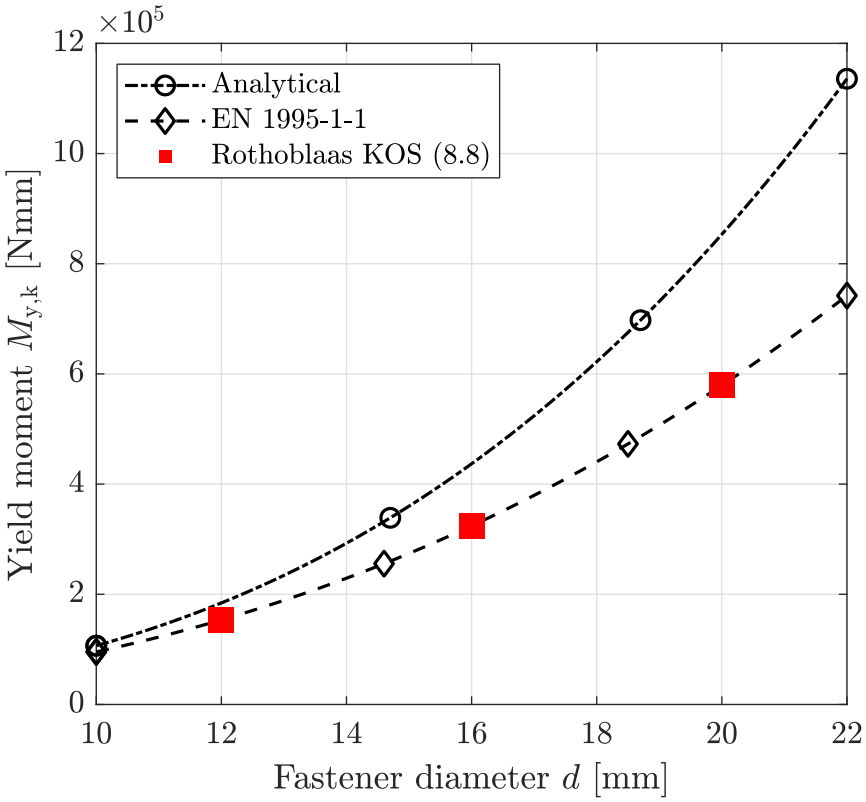

Figure 2.13: Rothoblaas grade 8.8 KOS fastener yield moment $M_{y,k}$. Manufacturer product information compared to the analytical and EN 1995-1-1 method.

The Rothoblaas carbon steel ($f_{y,k} = 1000\,\mathrm{N/mm^2}$) VGS fastener is compared to the analytical and EN 1995-1-1 method. The technical data sheets, given in Appendix E.2, give the characteristic tensile strength as an absolute force, so it must be recalculated to a characteristic tensile stress to be able to apply the EN 1995-1-1 approach. To do this, the characteristic tensile strength is divided by the diameter of the screw. Important to note, the area of the screw is calculated using the inner thread diameter d_2, as the threads are assumed to not contribute to the yield moment (especially considering the lower bending angles for fastener yielding, where not the entire cross section is yielding). This is different for other screws, for example partly threaded screws that have a shank. The geometry is shown in Figure 2.14 and corresponding material properties are shown in Table 2.1. It can be seen that the recalculated tensile strength is roughly equal to the yield strength. Therefore, it is assumed that the tensile strength is equal to the yield strength.

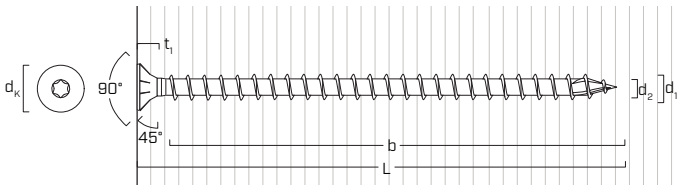

Figure 2.14: Rothoblaas VGS fastener geometry (Appendix E.2).

Table 2.1: Rothoblaas carbon steel VGS properties.

Property	Unit	Nominal diameter d_1 [mm]			
		9	11	13	15
Effective diameter $d_{\text{ef}} = d_2$	[mm]	5.9	6.6	8	9.1
Yield strength $f_{\text{y,k}}$	[N/mm^2]	1000	1000	1000	1000
Characteristic tensile strength $f_{\text{tens,k}}$	[kN]	11	20	32	45
Characteristic tensile strength $f_{\text{u,k}}$	[N/mm^2]	929	1111	1054	999

The VGS fastener yield moments given by Rothoblaas are plotted together with the analytical and EN 1995-1-1 approach in Figure 2.15. It can be seen that the manufacturer data once again closely matches the EN 1995-1-1 approach (by using a recalculated tensile strength in N/mm^2 using the effective (inner thread) diameter). Therefore, in upcoming sections the fastener yield moment will be taken as the one specified by the manufacturer.

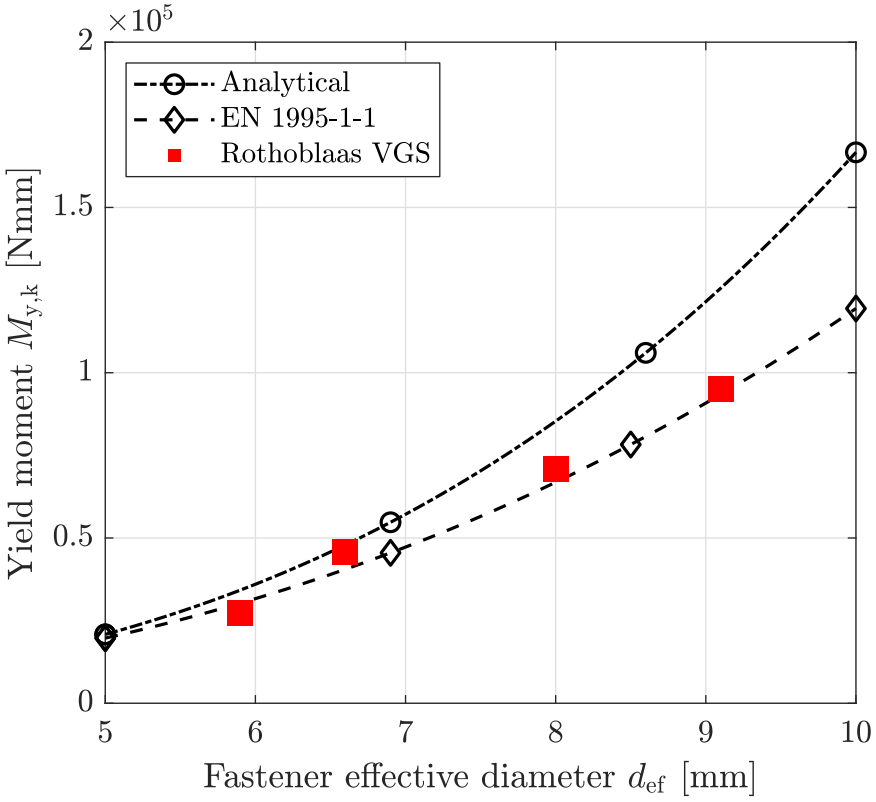

Figure 2.15: Rothoblaas carbon steel VGS fastener yield moment $M_{\text{y,k}}$. Manufacturer product information compared to the analytical and EN 1995-1-1 method.

2.2.3 European Yield Model

Dowel-type joints in timber structures loaded in shear can fail in multiple ways. This is first presented by Johansen, 1949, which describes three distinct failure modes I to III. These failure modes are based on the number of plastic hinges developing in the fastener:

I No plastic hinges develop, only embedment of the timber.

II One plastic hinges develops.

III Two plastic hinges develop.

Important to recognize is that these failure modes have a different level of safety. Embedment of the timber is considered a brittle failure mode, whereas failure of the dowel with two plastic hinges is considered a plastic mode. In the design of the connections it is important to consider the desired ductility.

The basis of the design rules given by EN 1995-1-1 is based on this theory. There are some small adjustments, that will be discussed in Section 2.2.3.4. Within this theory, failure depends on the two important parameters discussed before: Timber embedment strength and fastener yield moment. In case the timber members are of a different species or one of the members is loaded at an angle to the grain, the embedment strengths are related by

$$\beta = \frac{f_{\mathrm{h,2,k}}}{f_{\mathrm{h,1,k}}} \tag{2.16}$$

As a convention, for single lap joints the subscript "1" refers to the thinnest member, whereas "2" refers to the thicker member. In case of double lap joints, "1" refers to the outer members whereas "2" refers to the inner member. For double lap joints it is assumed that the outer members are of equal thickness. This model is also referred to as the European yield model (EYM). The failure modes in EN 1995-1-1 are shown in Figure 2.16. In the upcoming sections the equations for single lap joints are dervied, the procedure to derive the ones for double lap joints is similar.

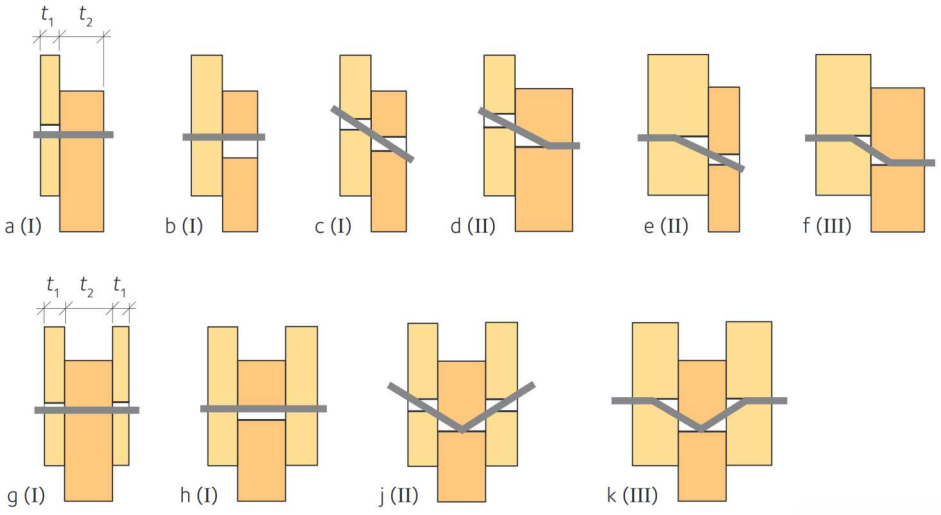

Figure 2.16: EYM failure modes included in EN 1995-1-1 (Kliger et al., 2022).

2.2.3.1 Failure Mode I (Brittle Failure)

Failure mode I contains all the failure modes where timber embedment is governing. Two cases can occur, as shown in Figure 2.17: Embedment of the timber member with the lowest embedment strength (Figure 2.17a), or rotation of the dowel by embedding in both timber members (Figure 2.17b). Dowel rotation can only occur for single lap joints, due to symmetry it will not occur in double lap joints.

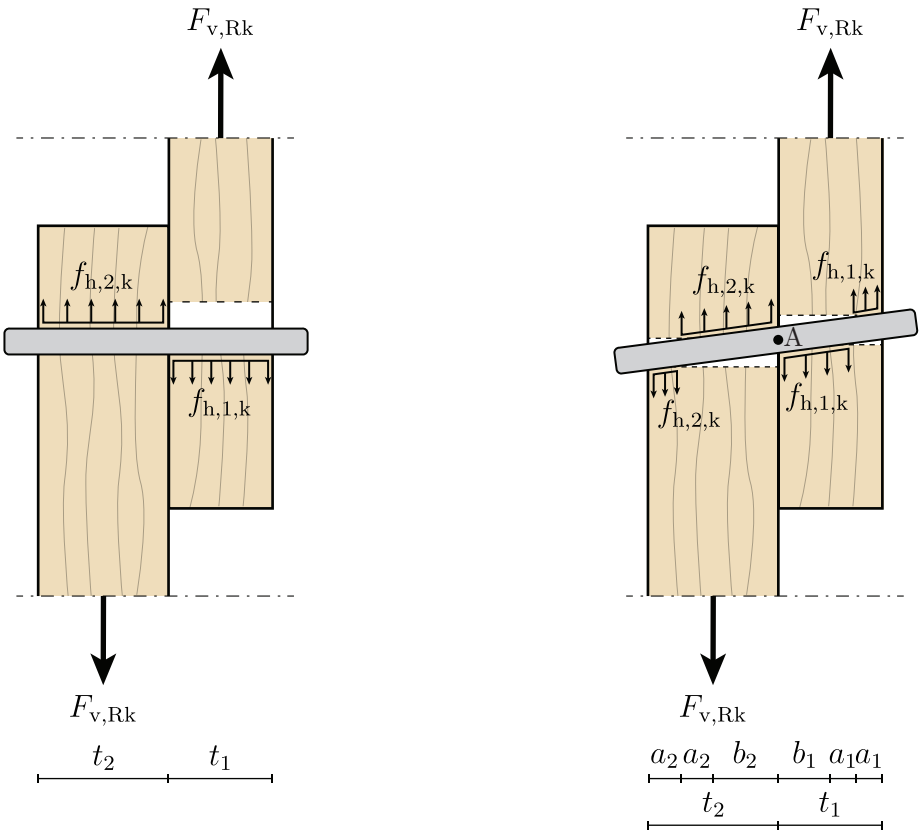

(a) Embedment (b) Dowel rotation

Figure 2.17: Structural scheme failure mechanism I.

The shear resistance of timber embedment failure can be calculated using

$$F_{v,Rk} = \min\left(f_{h,1,k}\, t_1\, d,\, f_{h,2,k}\, t_2\, d\right) \tag{2.17}$$

In Figure 2.17a equal embedment strengths are assumed while member t_1 is thinner, thereby member t_1 fails.

For dowel rotation as shown in Figure 2.17b, shear equilibrium is defined as

$$\sum V = 0: \qquad f_{h,2,k}\left(a_2 - a_2 + b_2\right) + f_{h,1,k}\left(b_1 + a_1 - a_1\right) = 0 \tag{2.18}$$

$$f_{h,1,k}\, b_1 = f_{h,2,k}\, b_2 \tag{2.19}$$

Substitution of Equation (2.16) gives

$$b_1 = \beta\, b_2 \tag{2.20}$$

Moment equilibrium to the left of A gives

$$M_{A,left} = h_{h,2,k}\, d\left(\frac{b_2^2}{2} + a_2\left(b_2 + \frac{a_2}{2}\right) - a_2\left(b_2 + \frac{3\,a_2}{2}\right)\right) \tag{2.21}$$

$$M_{A,left} = h_{h,2,k}\, d\left(\frac{b_2^2}{2} - a_2^2\right) \tag{2.22}$$

Similarly, moment equilibrium to the right of A can be written as (and substitution of Equation (2.16))

$$M_{\mathrm{A,right}} = \beta\, h_{\mathrm{h,2,k}}\, d \left(a_1^2 - \frac{b_1^2}{2} \right) \tag{2.23}$$

Next, the following geometric relations hold

$$a_1 = \frac{t_1 - b_1}{2} \tag{2.24}$$

$$a_2 = \frac{t_2 - b_2}{2} \tag{2.25}$$

Substituting Equations (2.20), (2.24) and (2.25) after equaling Equations (2.22) and (2.23) gives the following quadratic equation

$$b_1^2 \left(\frac{1+\beta}{\beta} \right) + 2\, b_1\, (t_1 + t_2) - \left(t_1^2 + \beta\, t_2^2 \right) = 0 \tag{2.26}$$

The embedment strength can be defined as

$$F_{\mathrm{v,Rk}} = f_{\mathrm{h,1,k}}\, b_1\, d = f_{\mathrm{h,2,k}}\, b_2\, d = f_{\mathrm{h,1,k}}\, \beta\, b_2\, d \tag{2.27}$$

Solving Equation (2.26) for b_1 and substitution in Equation (2.27) gives

$$F_{\mathrm{v,Rk}} = \frac{f_{\mathrm{h,1,k}}\, t_1\, d}{1+\beta} \left(\sqrt{\beta + 2\,\beta^2 \left(1 + \frac{t_2}{t_1} + \left(\frac{t_2}{t_1} \right)^2 \right) + \beta^3 \left(\frac{t_2}{t_1} \right)^2} - \beta \left(1 + \frac{t_2}{t_1} \right) \right) \tag{2.28}$$

In case the embedment strength and thickness of both members is equal ($\beta = 1$), the solution simplifies to

$$F_{\mathrm{v,Rk}} = f_{\mathrm{h,1,k}}\, t\, d \left(\sqrt{2} - 1 \right) \tag{2.29}$$

Comparing Equations (2.28) and (2.29) shows that in case the members are of equal thickness and embedment strength, dowel rotation is the governing failure mode.

2.2.3.2 Failure Mode II (Intermediate Failure)

Failure mode II is the mode where one plastic hinge forms in the steel fastener, it is visualized in Figure 2.18.

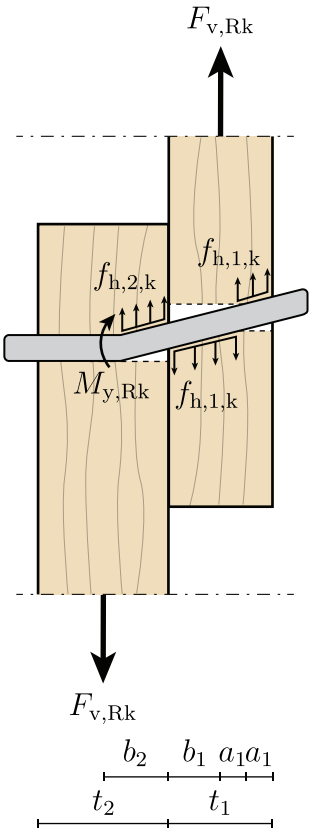

Figure 2.18: Structural scheme failure mechanism II.

Shear equilibrium of the fastener forces gives

$$\sum V = 0: \qquad f_{h,2,k}\, b_2 + f_{h,1,k}\,(\text{-}b_1 - a_1 + a_1) = 0 \tag{2.30}$$

$$f_{h,1,k}\, b_1 = f_{h,2,k}\, b_2 \tag{2.31}$$

Substitution of Equation (2.16) gives

$$b_1 = \beta\, b_2 \tag{2.32}$$

Moment equilibrium about the yielding fastener gives

$$M_{y,Rk} + f_{h,1,k}\ (b_1 + a_1) = f_{h,2,k}\, b_2 + f_{h,1,k}\, a_1 \tag{2.33}$$

Substitution of Equations (2.16), (2.24) and (2.32) in Equation (2.33) gives

$$b_1^2 + t_1\, \frac{2\beta}{2+\beta}\, b_1 - \frac{\beta\, t_1^2}{2+\beta} - \frac{4\,\beta}{2+\beta}\, \frac{M_{y,Rk}}{f_{h,1,k}\, d} = 0 \tag{2.34}$$

Solving for b_1 gives

$$b_1 = \frac{t_1}{2+\beta} \left(\sqrt{2\,\beta(1+\beta) + \frac{4\,\beta(2+\beta)\, M_{y,Rk}}{f_{h,1,k}\, d\, t_1^2}} - \beta \right) \tag{2.35}$$

The embedment strength can be defined as

$$F_{\mathrm{v,Rk}} = f_{\mathrm{h,1,k}}\, b_1\, d = f_{\mathrm{h,2,k}}\, b_2\, d = f_{\mathrm{h,1,k}}\, \beta\, b_2\, d \tag{2.36}$$

Substitution of Equation (2.35) in Equation (2.36) gives

$$F_{\mathrm{v,Rk}} = \frac{f_{\mathrm{h,1,k}}\, t_1\, d}{2+\beta}\left(\sqrt{2\,\beta\,(1+\beta) + \frac{4\,\beta\,(2+\beta)\,M_{\mathrm{y,Rk}}}{f_{\mathrm{h,1,k}}\, d\, t_1^2}} - \beta\right) \tag{2.37}$$

2.2.3.3 Failure Mode III (Ductile Failure)

Failure mode III is the mode where two plastic hinges form in the steel fastener, it is visualized in Figure 2.19.

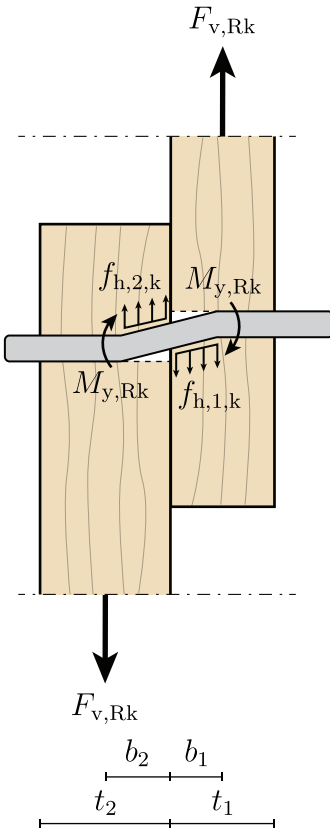

Figure 2.19: Structural scheme failure mechanism III.

Shear equilibrium of the fastener gives

$$\sum V = 0: \qquad f_{\mathrm{h,1,k}}\, b_1 = f_{\mathrm{h,2,k}}\, b_2 \tag{2.38}$$

Substitution of Equation (2.16) gives

$$b_1 = \beta\, b_2 \tag{2.39}$$

Moment equilibrium about a yielding fastener gives

$$M_{\mathrm{y,Rk}} + M_{\mathrm{y,Rk}} + f_{\mathrm{h,1,k}}\, b_1\left(b_2 + \frac{b_1}{2}\right) = f_{\mathrm{h,2,k}}\, b_2\, \frac{b_2}{2} \tag{2.40}$$

Substitution of Equations (2.16) and (2.39) in Equation (2.40)

$$b_1 = \sqrt{\frac{2\,M_{\mathrm{y,Rk}}}{f_{\mathrm{h,1,k}}\,d}}\sqrt{\frac{2\,\beta}{1+\beta}} \tag{2.41}$$

The embedment strength can be defined as

$$F_{\mathrm{v,Rk}} = f_{\mathrm{h,1,k}}\,b_1\,d = f_{\mathrm{h,2,k}}\,b_2\,d = f_{\mathrm{h,1,k}}\,\beta\,b_2\,d \tag{2.42}$$

Substitution of Equation (2.41) in Equation (2.42) gives

$$F_{\mathrm{v,Rk}} = \sqrt{\frac{2\,\beta}{1+\beta}}\sqrt{2\,M_{\mathrm{y,Rk}}\,f_{\mathrm{h,1,k}}\,d} \tag{2.43}$$

2.2.3.4 EN 1995-1-1 Implementation

In EN 1995-1-1, the shear resistances of the connections shown in Figure 2.16 realized using dowel-type fasteners are calculated by the equations shown in Figures 2.20 and 2.21.

$F_{\mathrm{v,Rk}} = f_{\mathrm{h,1,k}} t_1 d$	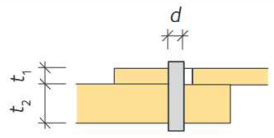
$F_{\mathrm{v,Rk}} = f_{\mathrm{h,2,k}} t_2 d$	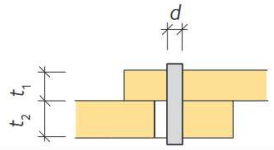
$F_{\mathrm{v,Rk}} = \frac{f_{\mathrm{h,1,k}} t_1 d}{1+\beta}\left(\sqrt{\beta + 2\beta^2\left(1+\frac{t_2}{t_1}+\left(\frac{t_2}{t_1}\right)^2\right)+\beta^3\left(\frac{t_2}{t_1}\right)^2} - \beta\left(1+\frac{t_2}{t_1}\right)\right) + \frac{F_{\mathrm{ax,Rk}}}{4}$	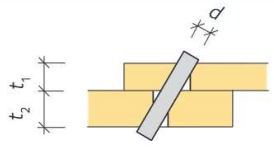
$* \quad F_{\mathrm{v,Rk}} = 1{,}05\,\frac{f_{\mathrm{h,1,k}} t_1 d}{2+\beta}\left(\sqrt{2\beta(1+\beta)+\frac{4\beta(2+\beta)M_{\mathrm{y,Rk}}}{f_{\mathrm{h,1,k}} d t_1^2}} - \beta\right) + \frac{F_{\mathrm{ax,Rk}}}{4}$	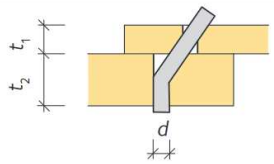
$* \quad F_{\mathrm{v,Rk}} = 1{,}05\,\frac{f_{\mathrm{h,1,k}} t_2 d}{1+2\beta}\left(\sqrt{2\beta^2(1+\beta)+\frac{4\beta(1+2\beta)M_{\mathrm{y,Rk}}}{f_{\mathrm{h,1,k}} d t_2^2}} - \beta\right) + \frac{F_{\mathrm{ax,Rk}}}{4}$	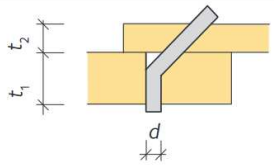
$* \quad F_{\mathrm{v,Rk}} = 1{,}15\sqrt{\frac{2\beta}{1+\beta}}\sqrt{2M_{\mathrm{y,Rk}} f_{\mathrm{h,1,k}} d} + \frac{F_{\mathrm{ax,Rk}}}{4}$	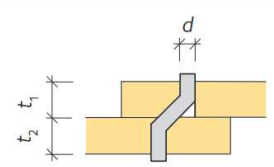

Figure 2.20: EN 1995-1-1 shear resistances for single shear (Kliger et al., 2022).

$F_{v,Rk} = f_{h,1,k} t_1 d$	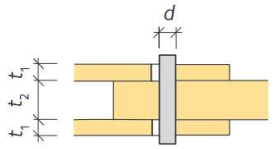
$F_{v,Rk} = 0{,}5 f_{h,2,k} t_2 d$	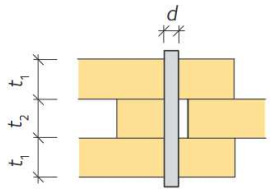
$* \quad F_{v,Rk} = 1{,}05 \frac{f_{h,1,k} t_1 d}{2+\beta} \left(\sqrt{2\beta(1+\beta) + \frac{4\beta(2+\beta) M_{y,Rk}}{f_{h,1,k} d t_1^2}} - \beta \right) + \frac{F_{ax,Rk}}{4}$	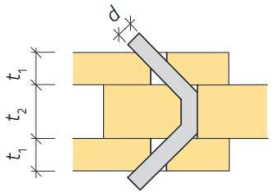
$* \quad F_{v,Rk} = 1{,}15 \sqrt{\frac{2\beta}{1+\beta}} \sqrt{2 M_{y,Rk} f_{h,1,k} d} + \frac{F_{ax,Rk}}{4}$	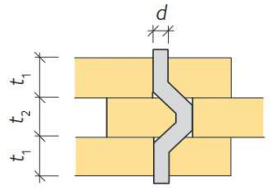

Figure 2.21: EN 1995-1-1 shear resistances for double shear (Kliger et al., 2022).

It can be seen that the equations show close resemblance to the solutions derived in Sections 2.2.3.1 to 2.2.3.3, as they are based on them. For example, the equations for modes (c), (d), and (f) are similar to Equations (2.28), (2.37) and (2.43) respectively. However, the following differences can be observed:

- There are additional constants introduced.
- In certain equations an additional term including $F_{\mathrm{ax,Rk}}$ is introduced.

The constants are a result of the combination of timber and steel. Safety factors of these materials differ, as well as additional factors such as k_{mod}, taking into account moisture contents for timber. However, the moisture content is not relevant for the yield moment of the fastener. Consequently, these additional constants are introduced to counter the negative effects of k_{mod} and γ_{M} on the yield moment of the fastener (H. J. Blaß and Sandhaas, 2017). The term including $F_{\mathrm{ax,Rk}}$ is a direct result of the so-called rope effect. This effect occurs when a fastener is deformed such that it becomes loaded (partially) in tension, as shown in Figure 2.22. This provides additional resistance for the connection. H. J. Blaß and Sandhaas, 2017 derived the inclusion of the rope effect analytically, from this a friction coefficient μ resulted. In EN 1995-1-1, this is set at $\mu = 0.25$, resulting in the $\frac{1}{4}$. Moreover, there are limits specified to how much rope effect may be added. For screws, this is 100% of the other term, causing it to double at most. However, for dowels no contribution of the rope effect may be added.

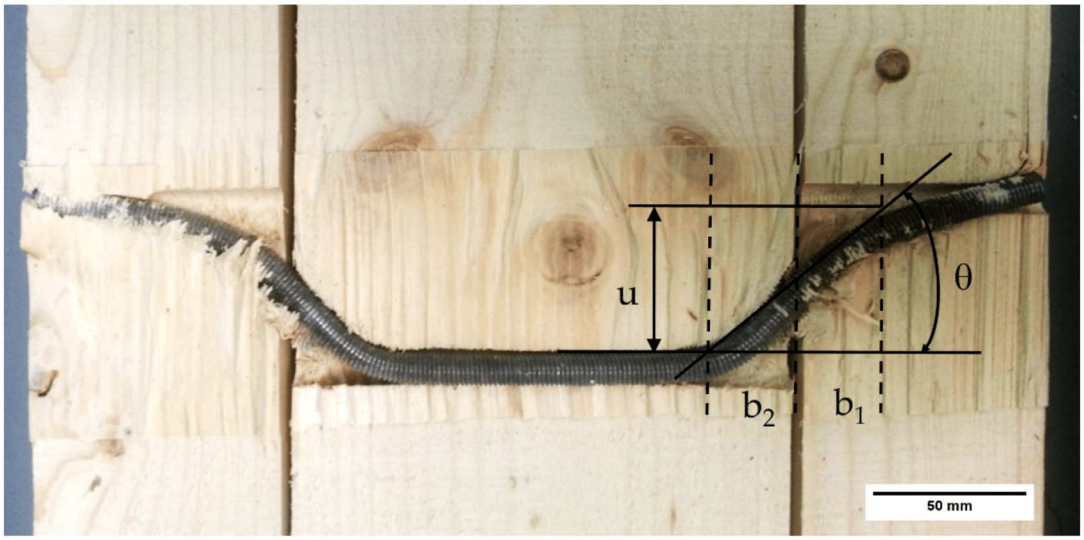

Figure 2.22: Rope effect due to large deformations causing additional tensile forces (Domínguez et al., 2021).

The fastener diameter is an important parameter in the calculation of yield moments. However, certain dowel-type fasteners do not have smooth shanks and are (partly) threaded. For these cases, EN 1995-1-1 prescribes the following:

> (2) For smooth shank screws, where the outer thread diameter is equal to the shank diameter, the rules given in 8.2 apply, provided that:
>
> - The effective diameter d_{ef} is taken as the smooth shank diameter;
> - The smooth shank penetrates into the member containing the point of the screw by not less than $4\,d$.
>
> (3) Where the conditions in (2) are not satisfied, the screw load-carrying capacity should be calculated using an effective diameter d_{ef} taken as 1.1 times the thread root diameter.

This essentially states that one uses the shank diameter as long as it penetrates sufficiently deep in the shear connection. However, if that is not the case, a multiplication of the inner thread diameter must be taken. This is as the thread does not contribute to the lateral loading capacity. However, the outer thread diameter may be used when the withdrawal strength of axially loaded screws is required (CSA Group, 2019).

2.2.3.5 Single Lap Connections

A case study is performed on a laterally loaded single lap joint with one fastener. The timber has a density of $\rho_k = 420\,\mathrm{kg/m^3}$, the fastener has an effective diameter of $d_{ef} = 6.49\,\mathrm{mm}$ and yield moment of $M_{y,Rk} = 27.2\,\mathrm{Nm}$. The shear resistance of the connection for various combinations of member thicknesses is shown in Figure 2.23.

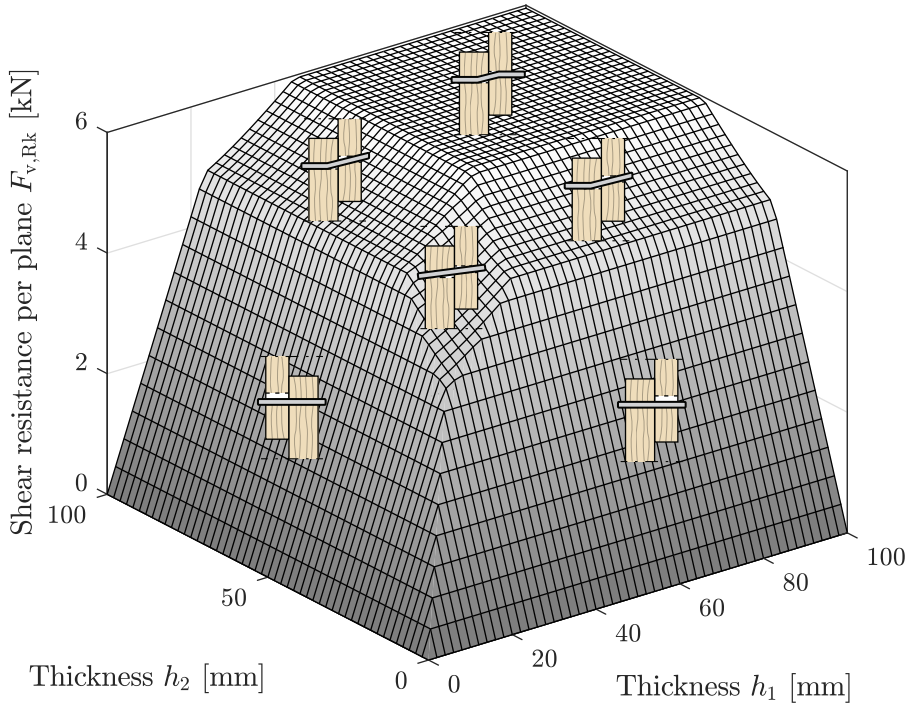

Figure 2.23: Shear resistance $F_{v,Rk}$ of a single lap connection ($\rho_k = 420\,\mathrm{kg/m^3}$, $d_{ef} = 6.49\,\mathrm{mm}$, $M_{y,Rk} = 27.2\,\mathrm{Nm}$).

From the results a clear pattern can be seen, if one member is significantly thinner than the other embedment failure occurs. In case the members are of roughly equal thickness, and they are of an intermediate thickness, rotation of the dowel occurs. When the members become significantly thick with respect to the fastener diameter, two plastic hinges develop in the fastener resulting in ductile failure. For the intermediate zones failure occurs due to the formation of a single plastic hinge. The initial offset of the shear resistance is caused by the rope effect, providing an additional increase in shear resistance in case the dowel rotates (not for the pure embedment failures).

2.2.3.6 Double Lap Connections

Another case study is performed on a laterally loaded double lap joint with one fastener. The timber has a density of $\rho_k = 420\,\mathrm{kg/m^3}$, the fastener has an effective diameter of $d_{ef} = 6.49\,\mathrm{mm}$ and yield moment of $M_{y,Rk} = 27.2\,\mathrm{Nm}$. The shear resistance of the connection for various combinations of member thicknesses is shown in Figure 2.24.

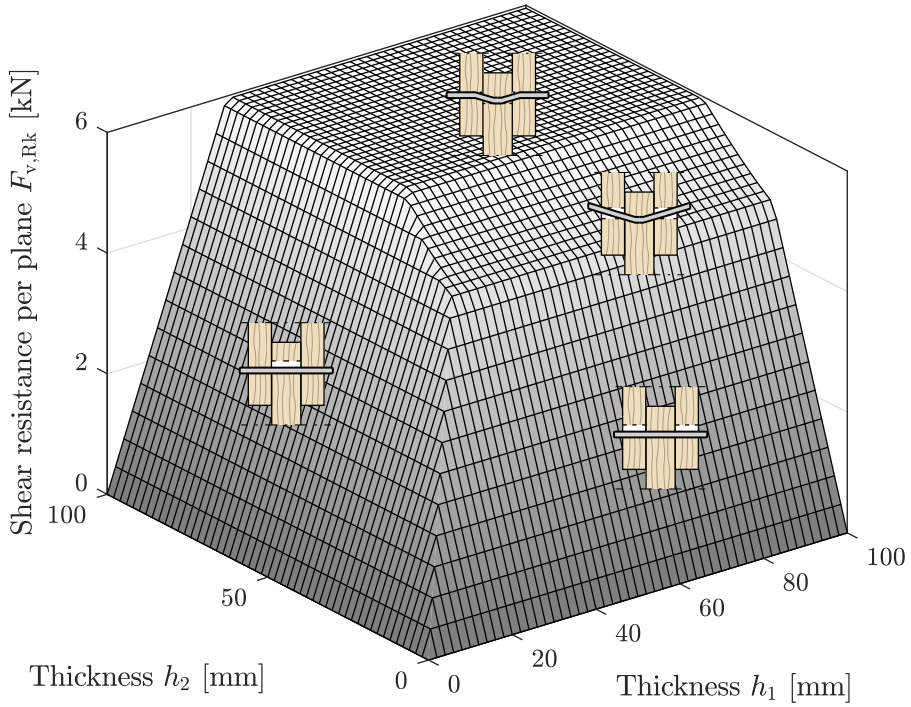

Figure 2.24: Shear resistance $F_{v,Rk}$ of a double lap connection ($\rho_k = 420\,\mathrm{kg/m^3}$, $d_{ef} = 6.49\,\mathrm{mm}$, $M_{y,Rk} = 27.2\,\mathrm{Nm}$).

The results show a similar pattern to that of the single lap joint, but two key differences can be observed. First, failure due to dowel rotation is absent. This failure mode cannot occur due to the symmetry of the connection. Second, for failure mode II the plastic hinge that develops can only do so in the middle member due to symmetry. Therefore, this failure mode is absent for the outer members.

2.2.3.7 Multiple Lap Connections

In case that there are more than three members in laterally loaded connections, the connection is split into combinations of members that are covered by the original equations in the EYM (H. J. Blaß and Sandhaas, 2017). Only the modes that can physically occur need to be taken into account, some modes cannot occur due to geometric or material reasons. For every shear plane, all the EYM modes that can occur are calculated and the lowest shear resistance is governing. This procedure is performed for all shear planes, after which these governing shear resistance per shear plane are summed to obtain the total shear resistance of the connection. This procedure is visualized in Figure 2.25.

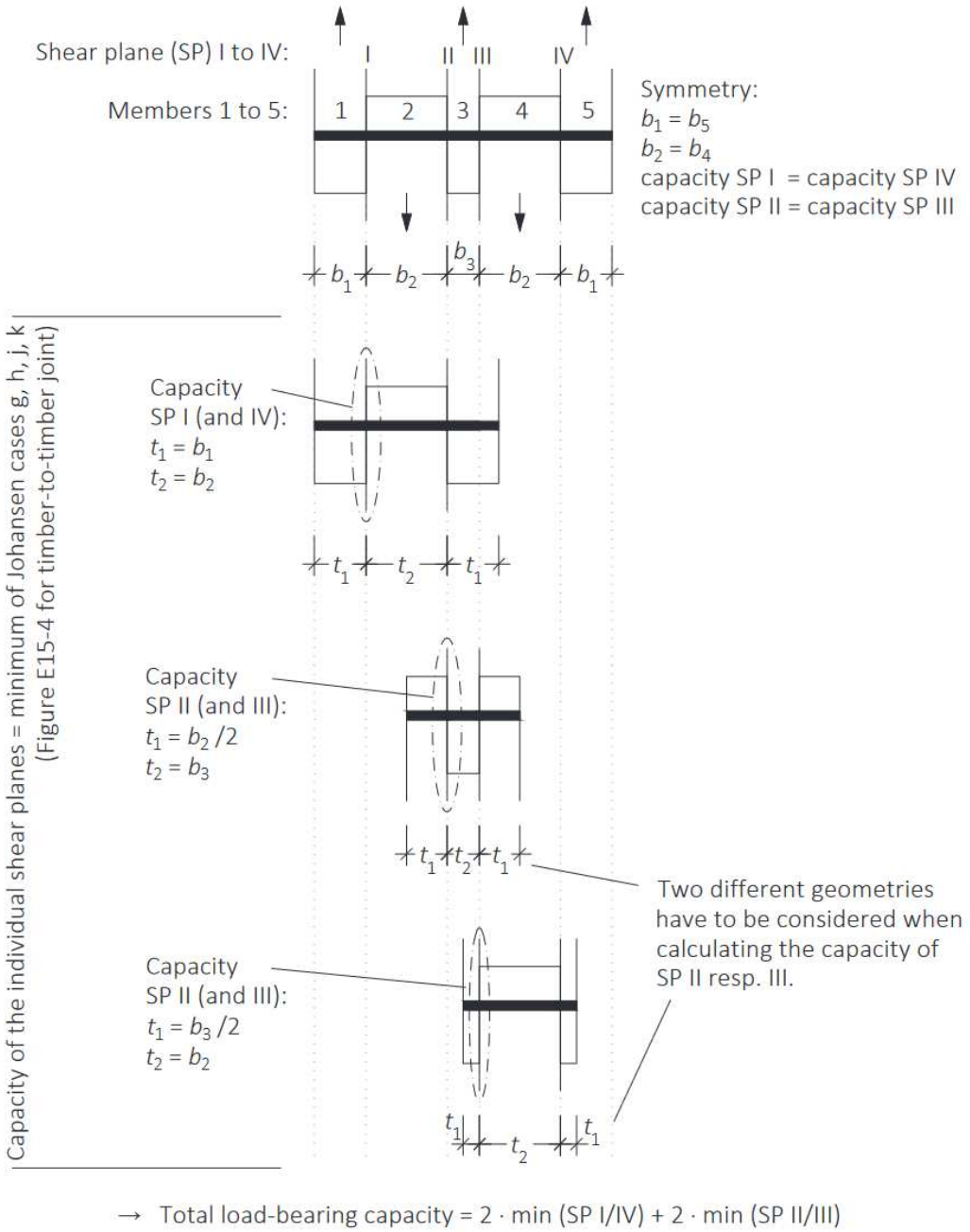

Figure 2.25: Procedure to determine the shear resistance of laterally loaded connections with more than three members (H. J. Blaß and Sandhaas, 2017).

2.3 Multiple Fasteners

The shear resistance as discussed in Section 2.2 holds for one single fastener. In principle, the shear resistance of the entire connection may be multiplied by the amount of fasteners. However, in case of multiple fasteners additional phenomena need to be taken account. When fasteners are in close proximity, the load distribution is not necessarily equal over all fasteners. Not all fasteners are contributing equally, and therefore an effective number of fasteners n_{ef} is considered. Moreover, new types of failure can occur where the whole fastener group fails. In this section these concerns are discussed and presented.

2.3.1 Group Patterns

As space is often limited in connections, it is important to choose a fastener pattern that fits the required amount of fasteners while keeping sufficient spacing. Often this results in parallel rows of fasteners, these can also be staggered. In case of staggered rows, the US NDS sets certain limits for the spacing between adjacent rows (AWC Wood Design Standards Committee, 2023). This standard states, that when the spacing is relatively low, the staggered row cannot be seen as an independent row but needs to be added to the other adjacent row. This not only holds for which parallel spacing a_1 must be used but also for how the effective number of fasteners n_{ef} must be calculated.

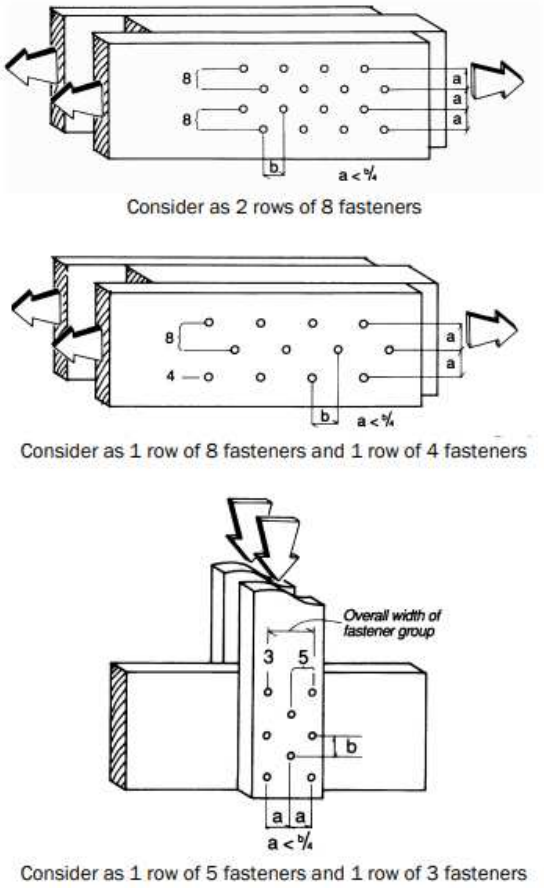

Figure 2.26: Spacing rules in the US NDS for staggered fastener patterns (AWC Wood Design Standards Committee, 2023).

2.3.2 Group Failure Mechanisms

In addition to the failure modes considered in EYM, it is possible that groups of fasteners cause splitting and thereby causing brittle failure. The four group failure mechanisms considered are shown in Figure 2.27. Which of these can occur varies greatly per fastener. For nails, row shear barely occurs due to the small diameters. Block shear also rarely occurs for nails as they often do not protrude the entire timber. On the other hands, for dowels block shear must be checked. Once again, row shear is not likely to occur as this requires more shear planes to split compared to block shear.

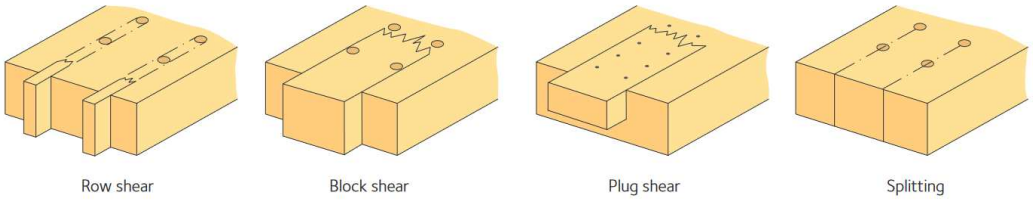

Figure 2.27: Failure modes of groups of fasteners (Kliger et al., 2022).

Block shear for dowel-type fasteners can be calculated using

$$F_{\mathrm{bs,Rd}} = \max \begin{cases} 1.5\, A_{\mathrm{net,t}}\, f_{\mathrm{t,0,d}} \\ 0.7\, A_{\mathrm{net,v}}\, f_{\mathrm{v,d}} \end{cases} \tag{2.44}$$

The net areas required are the ones corresponding to the checked resistances. $A_{\mathrm{net,t}}$ is the area of the end surface loaded in tension, $A_{\mathrm{net,v}}$ are the sides loaded in shear. For plug shear failure this procedure can be used as well, the difference is that the $A_{\mathrm{net,v}}$ is larger as the bottom side of the plug is also loaded in shear and must be included.

2.3.3 Minimum Spacing

Fasteners must be spaced sufficiently from each other and the timber ends to avoid splitting. The distances considered are shown in Figure 2.28. A loaded end or edge is one where the load transferred by the fastener has a component in the direction of that end or edge. These generally require larger spacing due to the increased risk of splitting. The distances vary per fastener, nails for example require smaller distances as the risk of splitting is reduced due to its smaller diameter compared to other fastener types. For dowels the required spacing is given in Table 2.2. For screws the outer thread diameter must be used to determine these distances.

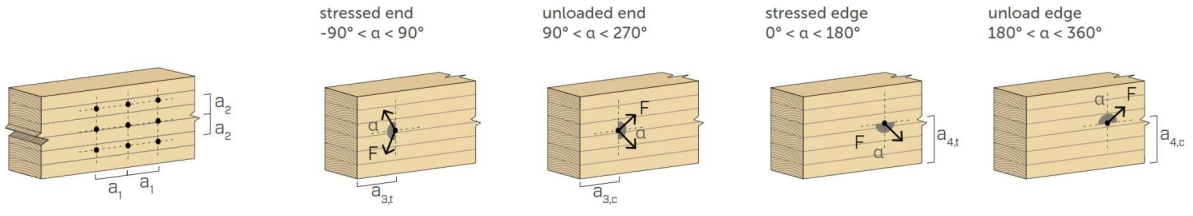

Figure 2.28: Fastener spacing and edge and end distances (Appendix E.2).

Table 2.2: Dowel minimum spacing and end and edge distances.

Distances and spacing	Angle	Minimum values
Parallel spacing a_1	-	$(3 + 2\ \cos\alpha)\, d$
Perpendicular spacing a_2	-	$3\, d$
Loaded end $a_{3,\mathrm{t}}$	-	$\max(7\, d; 80\ \ \mathrm{mm})$
Unloaded end $a_{3,\mathrm{c}}$	$\alpha < 30°$	$\max(3.5\, d; 40\ \ \mathrm{mm})$
	$30° \leq \alpha \leq 90°$	$a_{3,\mathrm{t}}\ \sin\alpha$
Loaded edge $a_{4,\mathrm{t}}$	-	$\max[(2 + 2\ \sin\alpha)\ d; 3\, d]$
Unloaded edge $a_{4,\mathrm{c}}$	-	$3\, d$

2.3.4 Group Effect

For groups of fasteners, Lantos, 1969 has researched how the force distribution is over the fasteners. It has been revealed that it is not evenly distributed due to imperfections of the timber and fastener placement. In reality, the first and last fastener receives the highest load. This behavior is schematized in Figure 2.29. Consequently, the shear resistance of the entire joint is not simply the multiplication of all the fasteners. This effect is especially relevant for larger-diameter fasteners, as these behave mostly linear elastic. Fasteners with a smaller diameter often allow for plasticity, and in turn enables redistribution of the forces.

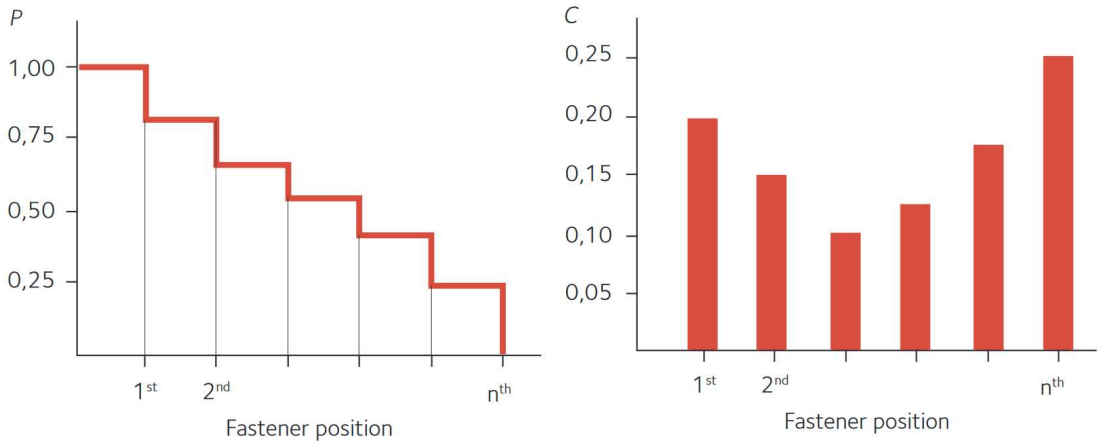

(a) Force along timber member. (b) Force distribution over fasteners.

Figure 2.29: Group effect fastener behavior (Kliger et al., 2022).

To take the group effect into account, a so-called effective number of fasteners n_{ef} is included in EN 1995-1-1, which can be calculated using

$$n_{\mathrm{ef}} = n^{k_{\mathrm{ef}}} \qquad \text{(screws } d \leq 6\,\mathrm{mm}\text{, nails, and staples)} \tag{2.45}$$

$$n_{\mathrm{ef}} = \min \begin{cases} n \\ n^{0.9}\ \sqrt[4]{\dfrac{a_1}{13\, d}} \end{cases} \qquad \text{(screws } d > 6\,\mathrm{mm}\text{, bolts, and dowels)} \tag{2.46}$$

The factor k_{ef} for fasteners with a small diameter depends on the spacing. For large spacing $k_{\mathrm{ef}} = 1$, while for dense spacing where $a_1 = 7\, d$ the factor becomes $k_{\mathrm{ef}} = 0.7$ (CEN, 2014).

3 Adhesive Shear Connections

Adhesive connections are commonly used in manufactured products such as CLT and glulam. However, they are less frequently applied as conventional joining techniques. Adhesive joints are typically chosen for specific applications, such as renovations using epoxies or glued-on plates for reinforcement. The limited use of adhesive connections can be attributed to several factors:

- Lack of design rules and standards.
- Difficulties and uncertainties in strength calculations.
- The need for a controlled environment and process to produce reliable adhesive connections.

The simplest form of a shear lap joint is a single lap joint (SLJ). In these joints, the primary load transfer occurs through shear. However, there is also a significant peeling effect normal to the adhesive plane that must not be overlooked. Both types of stresses are visualized in Figure 3.1. The peeling effect is a result of the asymmetry of the connection and the resulting bending.

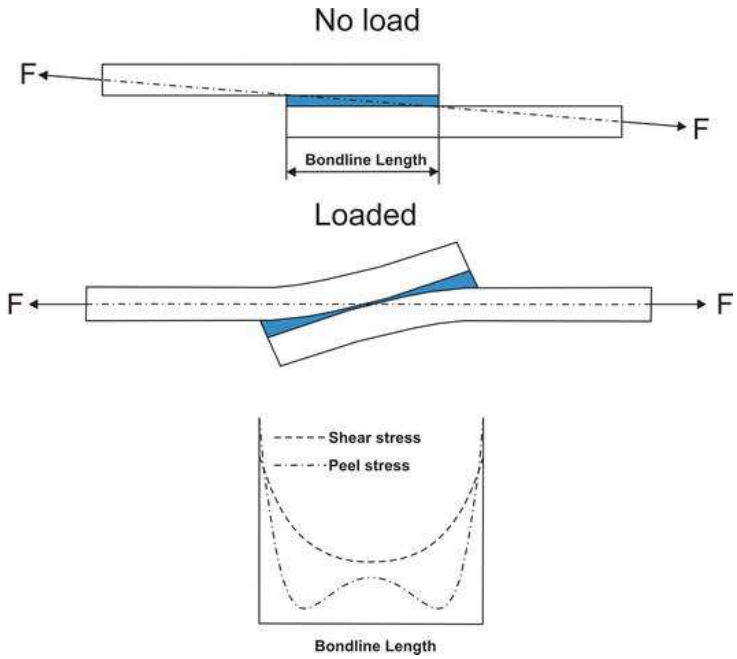

Figure 3.1: Single lap joint and its shear and peel stress distribution (Özer, 2018).

o enhance the efficiency of load transfer in a single lap joint, various types of laps can be utilized. A range of options is illustrated in Figure 3.2. These configurations aim to minimize peeling effects by making the joints more symmetric, thereby creating a more direct load path. Additionally, certain lap types increase the area loaded in shear, further improving performance. Another effective option is the double lap joint (DLJ). Due to its symmetric nature, the peeling stresses are significantly lower compared to SLJs.

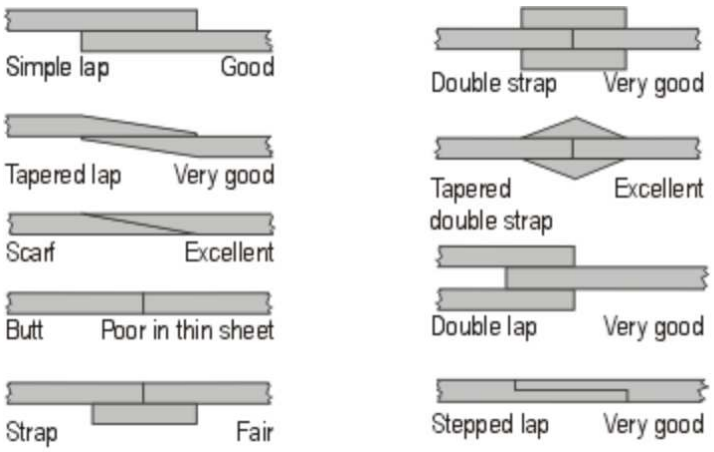

Figure 3.2: Lap joints can be executed in a variety of types (Özer, 2018).

This chapter further lays out the different structural adhesives and their characteristics. Once these are known, analytical and FEM calculation methods for stresses in adhesive lap connections are analyzed and compared.

3.1 Adhesive Connections

Timber adhesive connections can be categorized into various groups, as classified in Figure 3.3. Hybrid wood joints use adhesives to connect different materials, often steel to timber. Well-known examples include glued-in rods or plates. Wood-to-wood joints can be further distinguished into continuous or local joints. Continuous joints are found in built-up elements or products such as CLT and glulam. Local joints transfer forces at specific points and include examples such as lap joints, glued-on gusset plates, and finger joints.

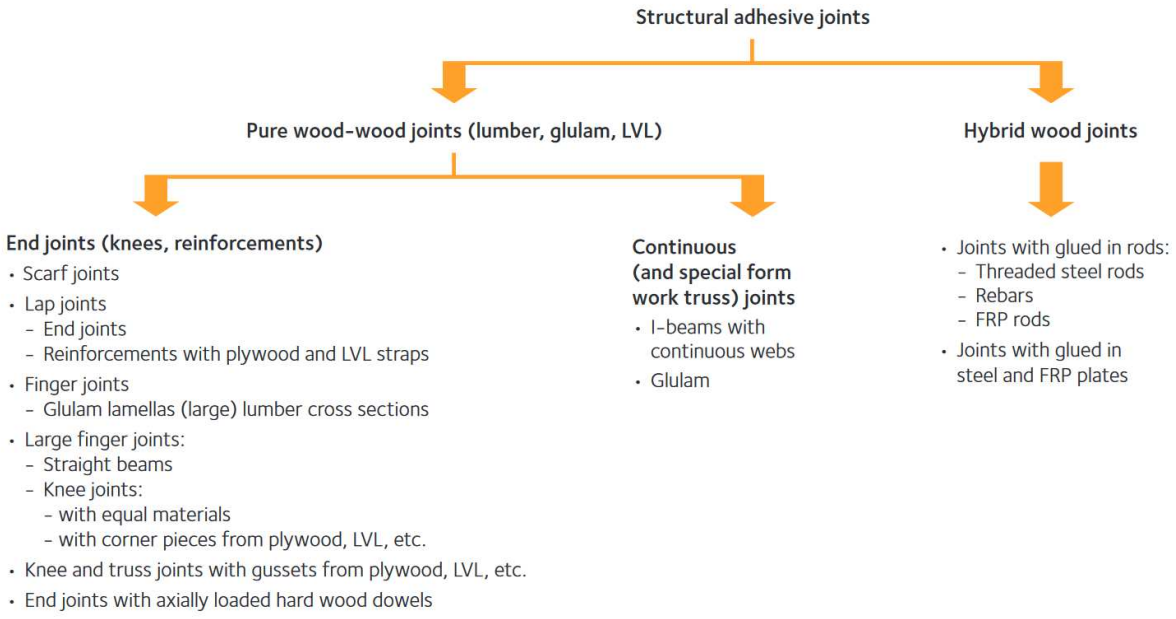

Figure 3.3: Different categories of adhesive joints (Kliger et al., 2022).

3.2 Adhesive Types

For structural applications, adhesives with exceptional load-bearing qualities are required. Within this category, various subgroups of structural adhesives can be chosen, depending on the specific application. The following considerations are important when selecting the optimal adhesive:

- The materials to be bonded.
- The environmental conditions, such as moisture content, temperature, UV exposure, or water contact.
- The chemical compatibility with other substances, such as liquids with high salt content or petroleum-based liquids.
- The type of load (static or dynamic) and whether fatigue is a factor.
- The joint configuration and corresponding load transfer through the joint.

Within structural adhesives, the following subgroups can be distinguished:

- **Epoxy adhesives:** Among the strongest adhesive bonds, these are generally two-part adhesives (though one-part variants exist that use heat curing). They work with various substrates and exhibit excellent gap-filling properties. They are also very durable, performing well under various environmental conditions such as heat and chemical exposure.
- **Resorcinol-formaldehyde adhesives:** These create strong adhesive bonds and come as a two-part adhesive. They have better UV resistance and heat stability compared to epoxy, making them more suitable for exterior applications. However, they lack gap-filling properties, requiring proper craftsmanship to ensure a tight fit.
- **Urethane adhesives:** Flexible yet strong, these adhesives are excellent for applications where impact resistance or vibration is important.
- **Polyurethane (PU) adhesives:** A subset of urethane adhesives, PU adhesives are rigid and firm, in contrast to the flexibility of urethane adhesives.
- **Cyanoacrylate adhesives:** Known as “super glue”, these adhesives are renowned for their fast curing properties and thin bond lines. They are commonly used for smaller applications but also exist within the structural adhesive category.
- **Polyvinyl acetate (PVAc) adhesives:** Commonly known as “carpenter’s glue”, this water-based adhesive has good strength, though lower than that of the previously mentioned adhesives. It is easy to handle but is reactive to solvents. It remains stable at lower temperatures but becomes unstable above 40°C and exhibits significant creep.

3.3 Adhesive Failure Mechanisms

In Chapter 2 it has been shown that mechanical fasteners can provide ductility, which results in failure mechanisms that show sufficient warning before failure. In contrast, adhesive joints do not exhibit this feature. While there are slight differences in the elasticity of adhesives, their failure modes are generally brittle, which is a concern for structural engineering applications. The different links that can fail in a lap joint are shown in Figure 3.4.

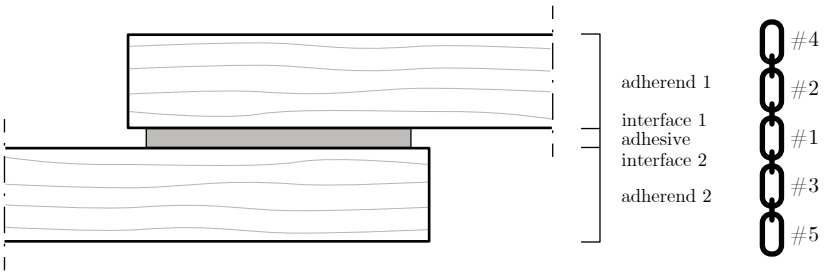

Figure 3.4: Different links that can fail in an adhesive timber connection.

Each of the links in the connection fails differently, of which the various failure types are shown in Figure 3.5. These can be described as follows:

- **Adhesion failure:** The interface between the adhesive and timber fails.
- **Cohesion failure:** The adhesive itself fails.
- **Adhesion/cohesion failure:** A combination of the two failure modes.
- **Adherend failure:** Failure of the timber itself.

The failure modes in which the adhesive (or part of it) fails are all brittle and occur very suddenly. Among these failure modes, the least brittle is the failure of the timber. Nevertheless, this still constitutes a very brittle failure mode. The failure of the timber becomes increasingly concerning when the lap joint is angled, causing one of the timber members to be loaded partially perpendicular to the grain.

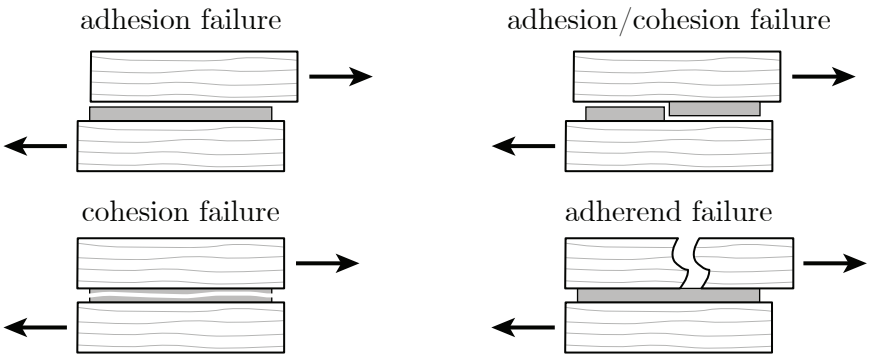

Figure 3.5: Different types of failure that can occur in an adhesive connection.

3.4 Stress Analysis

To design adhesive joints, analysis must be performed to assess the strength and deflections of such joints. Especially for strength considerations, the stresses in the joint are of importance. This section first compares four classical theories that are analytically derived. Next, finite element models (FEM) are derived to determine the joint stresses as well. These are also compared to the analytical theories. Last, the cohesive zone model (CZM) is investigated, which is a method based on fracture mechanics.

Many theories can be found in literature that describe stress analysis of adhesive joints. Figures D.1 to D.3 in Appendix D show an extensive summary of many linear and non-linear analyses (Campilho, 2017). These theories vary from the most simplest cases of the single lap joint in 2D to 3D theories. Theories are not limited to flat members, but there exist theories for tubular connections.

In this section four of these theories are chosen to elaborate. First, Volkersen, 1938 is evaluated as this is the most basic case of a single lap joint. Second, Goland and Reissner, 1944 is evaluated as Volkersen assumes pure shear, but a single lap joint in reality exhibits bending causing a bending moment that is taken into account by Goland and Reissner. Third, Ojalvo and Eidinoff, 1978 is chosen as this expands upon Goland and Reissner by providing a more complete description of the stress distribution. Last, Hart-Smith, 1973 is chosen as this theory includes plasticity of the adhesive layer. The geometry of a standard single lap joint is shown in Figure 3.6

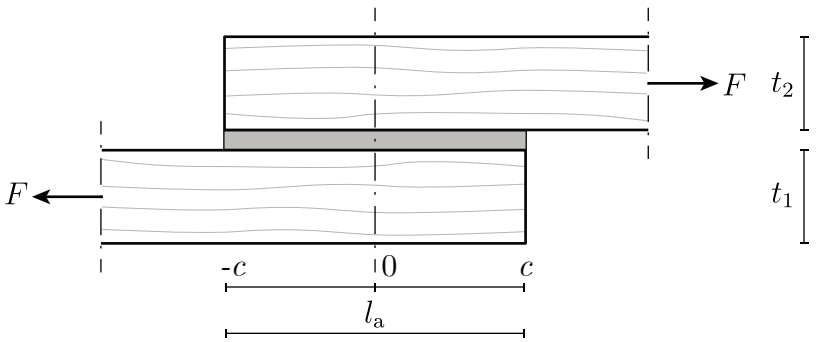

Figure 3.6: Geometry of the SLJ considered in the various stress analyses.

3.4.1 Analytical Methods

3.4.1.1 Volkersen

The conditions of the Volkersen model are shown in Figure 3.7 (Volkersen, 1938). In the Volkersen model, adherends are assumed to transfer the forces in tension while the adherend is acting fully in shear. Both the adherend and adhesive are assumed to behave elastically. This resulted in a closed-form solution that gives the shear stress distribution over the overlap length. The assumptions made by Volkersen make the model more suitable for adherends with a high stiffness compared to the adhesive.

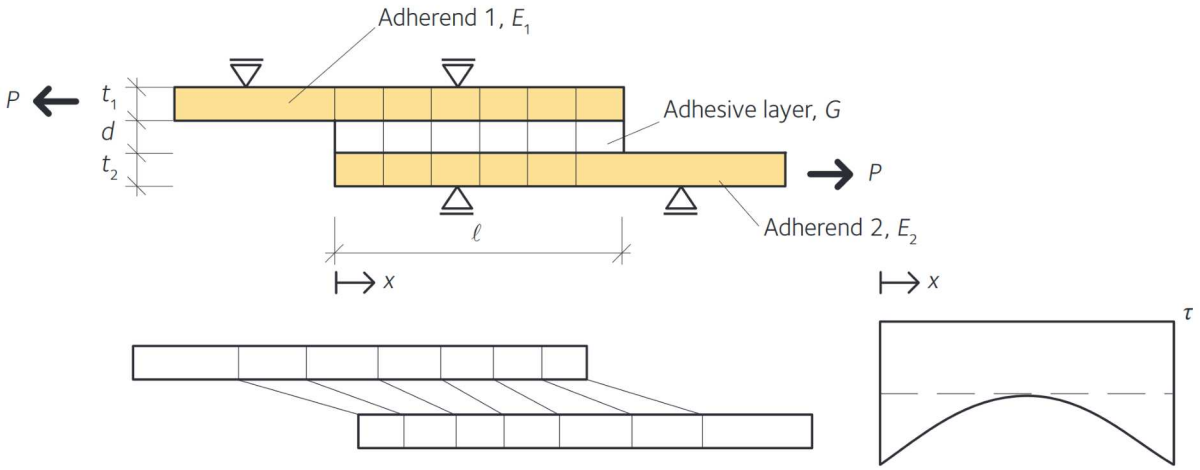

Figure 3.7: Volkersen adhesive stress model (Kliger et al., 2022).

The shear stress as derived by Volkersen is given by

$$\tau = \frac{F\,\omega}{2\,w}\,\frac{\cosh(\omega\,x)}{\sinh\left(\omega\,\frac{l_a}{2}\right)} + \frac{t_2 - t_1}{t_2 + t_1}\,\omega\,\frac{l_a}{2}\,\frac{\sinh(\omega\,x)}{\cosh\left(\omega\,\frac{l_a}{2}\right)} \tag{3.1}$$

where $$\omega = \sqrt{\frac{G_a}{E\,t_2\,t_a}\,\frac{1+t_2}{t_1}} \tag{3.2}$$

G_a is the adhesive shear modulus

l_a is the overlap length

E is the adherend modulus of elasticity

3.4.1.2 Goland and Reissner

Goland and Reissner, 1944 improved the model of Volkersen by including the effects caused by bending of the joint and the corresponding eccentricities causing bending moments. The model is shown in Figure 3.8.

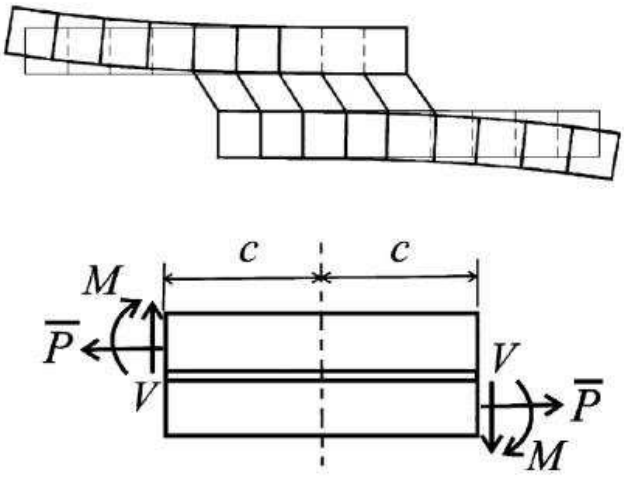

Figure 3.8: Goland and Reissner adhesive stress model (Quispe Rodríguez et al., 2011).

The bending is taken into account by the so-called bending moment factor k. For the Goland

and Reissner analysis this is defined as

$$k = \frac{1}{1 + 2\sqrt{2}\,\tanh(u_{2c})} \tag{3.3}$$

$$\text{where} \qquad u_{2c} = \sqrt{3\frac{1-\nu^2}{2}}\frac{c}{t}\sqrt{\frac{F}{t\,w\,E}} \tag{3.4}$$

t is the adherend thickness

ν is the adherend Poisson's ratio

E is the adherend elasticity

The shear stress in the adhesive layer is found by solving the corresponding differential equations and using their boundary conditions, this results in

$$\tau(x) = \left[\frac{\beta\,c}{t}\,(1+3\,k)\,\frac{\cosh\left(\frac{\beta}{t}x\right)}{\sinh\left(\frac{\beta\,c}{t}\right)} + 3\,(1-k)\right]\frac{F}{w\,t_a}\,\frac{t}{8\,c} \tag{3.5}$$

$$\text{where} \qquad \beta = \sqrt{8\frac{G_a}{E}\frac{t}{t_a}}$$

Similarly, the (normal) peal stress in the adhesive layer is calculated by

$$\sigma(x) = H\left[\left(R_2\,\lambda^2\,\frac{k}{2} - \lambda\,k'\,\cosh(\lambda)\,\cos(\lambda)\right)\cosh\left(\lambda\frac{x}{c}\right)\,\cos\left(\lambda\frac{x}{c}\right) + \left(R_1\,\lambda^2\,\frac{k}{2} - \lambda\,k'\,\sinh(\lambda)\,\sin(\lambda)\right)\sinh\left(\lambda\frac{x}{c}\right)\,\sin\left(\lambda\frac{x}{c}\right)\right] \tag{3.6}$$

$$\text{where} \qquad \gamma = \sqrt[4]{6\frac{E_a}{E}\frac{t}{t_a}} \tag{3.7}$$

$$\lambda = \gamma\,\frac{c}{t} \tag{3.8}$$

$$A = \frac{1}{2}\left(\sinh(2\,\lambda) + \sin(2\,\lambda)\right) \tag{3.9}$$

$$R_1 = \cosh(\lambda)\,\sin(\lambda) + \sinh(\lambda)\,\cos(\lambda) \tag{3.10}$$

$$R_2 = \sinh(\lambda)\,\cos(\lambda) - \cosh(\lambda)\,\sin(\lambda) \tag{3.11}$$

$$H = \frac{1}{A}\left(\frac{t}{c}\right)^2\frac{F}{w\,t} \tag{3.12}$$

$$k' = k\,\frac{c}{t}\sqrt{3\,(1-\nu^2)\,\frac{F}{w\,t\,E}} \tag{3.13}$$

3.4.1.3 Hart-Smith

Hart-Smith, 1973 tried to improve upon the model provided by Goland and Reissner. One of the aspects that changed is the bending moment factor k. However, not all research is in agreement whether this actually improves the results (van Ingen and Vlot, 1993). Another aspect that Hart-Smith does completely different is the inclusion of plastic behavior. Up until this point all theories were elastic, but Hart-Smith considers that the most heavily-loaded parts of the adhesive behave plastically. This model is shown in Figure 3.9.

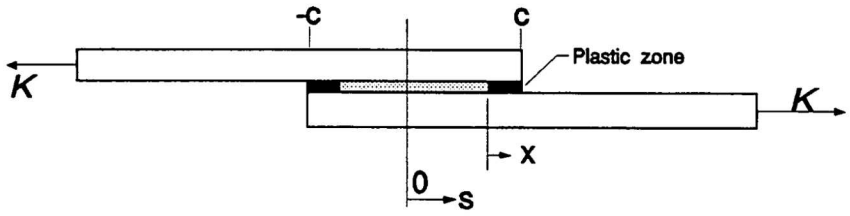

Figure 3.9: Hart-Smith adhesive stress model (van Ingen and Vlot, 1993).

The bending moment factor is determined by

$$k = \frac{1}{1 + k_{s1}\, c + \frac{1}{6}\,(k_{s1}\, c)^2} \tag{3.14}$$

$$\text{where} \qquad k_{s1} = \sqrt{\frac{F}{w\, t}\frac{1}{D}} \tag{3.15}$$

$$D = \frac{E\, t^3}{12\,(1-\nu^2)} \tag{3.16}$$

The bending moment per unit width is now defined by

$$M_0 = k\,\frac{F}{w\, t}\frac{t}{2}\left(1 + \frac{t_a}{t}\right) \tag{3.17}$$

The shear stress is given by

$$\tau(x) = A_2\, \cosh(2\,\lambda\, x) + C_2 \tag{3.18}$$

$$\text{where} \qquad \lambda = \sqrt{\frac{2\, G_a}{E\, t\, t_a}} \tag{3.19}$$

A_2, C_2 are constants derived from the boundary conditions

The unknown constants are derived using the boundary conditions as specified in Hart-Smith, 1973. Additionally, from this derivation the length of the elastic region r is derived. The shear stress given by Equation (3.18) is valid in this region. In the plastic region the shear stress is bounded by the plastic strength of the adhesive.

The normal stress is given by

$$\sigma(x) = A\, \cos(Z\, x)\cosh(Z\, x) + B\sin(Z\, x)\sinh(Z\, x) \tag{3.20}$$

$$\text{where} \qquad Z = \sqrt[4]{\frac{E_a}{2\, t_a\, D}} \tag{3.21}$$

D is the flexural rigidity of the adherends

A, B are constants derived from the boundary conditions

3.4.1.4 Ojalvo and Eidinoff

Ojalvo and Eidinoff, 1978 also built upon the theory provided by Goland and Reissner. The difference is that this theory is able to assume a linear variation of the shear stress over the adhesive thickness. This is done by expanding the shear-displacement relationship, of which the following was used by Goland and Reissner:

$$\gamma(x)_a = \frac{u(x)_u - u(x)_l}{d} \tag{3.22}$$

However, the following form was used by Ojalvo and Eidinoff:

$$\gamma(x)_{\mathrm{a}} = \frac{u(x)_{\mathrm{u}} - u(x)_{\mathrm{l}}}{d} + w_i \qquad \text{where } i = \mathrm{u,l} \tag{3.23}$$

In this equation, u_i are the longitudinal displacements and w_i the transverse displacements. By defining the shear strain at the upper and lower interface, a linear shear stress distribution can be defined between those two bounds.

As the theory builds upon Goland and Reissner, the model looks the same as what was presented in Figure 3.8. For the bending moment factor it can be chosen to use that of Goland and Reissner, but also the one provided by Hart-Smith. It is chosen to use the one of Hart-Smith within this analysis, given by Equation (3.14), as in general researchers believe it is an improvement upon Goland and Reissner (van Ingen and Vlot, 1993).

The shear stress is given by

$$\tau(x) = \left(A \cosh\left(\varphi \frac{x}{c}\right) + B\right) \frac{F}{w\, l_{\mathrm{a}}} \tag{3.24}$$

$$\text{where} \qquad \lambda = \sqrt{\frac{G_{\mathrm{a}}\, c^2 \left(1 - \nu^2\right)}{E\, t\, t_{\mathrm{a}}}} \tag{3.25}$$

$$\beta = \frac{t_{\mathrm{a}}}{t} \tag{3.26}$$

$$\varphi = \lambda \sqrt{2 + 6\, (1+\beta)^2} \tag{3.27}$$

$$A = \frac{2\,\lambda^2 \left(1 + 3\,(1+\beta)^2\, k\right)}{\varphi \sinh(\varphi)} \tag{3.28}$$

$$B = 1 - \frac{A}{\varphi} \sinh(\varphi) \tag{3.29}$$

The normal stress is given by

$$\sigma(x) = \left(C \sinh\left(a_1 \frac{x}{c}\right) \sin\left(a_2 \frac{x}{c}\right) + D \cosh\left(a_1 \frac{x}{c}\right) \cos\left(a_2 \frac{x}{c}\right)\right) \frac{F}{w\, l_{\mathrm{a}}} \tag{3.30}$$

$$\text{where} \qquad \rho = \sqrt{\frac{24\, E_{\mathrm{a}}\, c^4 \left(1 - \nu^2\right)}{E\, t_{\mathrm{a}}\, t^3}} \tag{3.31}$$

$$a_1 = \sqrt{3\,\beta\, \frac{\lambda^2}{2} + \frac{\rho}{2}} \tag{3.32}$$

$$a_2 = \sqrt{\text{-}3\,\beta\, \frac{\lambda^2}{2} + \frac{\rho}{2}} \tag{3.33}$$

The constants C and D can be derived by solving the boundary conditions given by

$$\begin{cases} \mathrm{d}^3\sigma - 6\,\beta\,\lambda^2\ \mathrm{d}^1\sigma = \text{-}k\,\gamma\,\rho^2\,(1+\beta) \\ \mathrm{d}^2\sigma = k\,\gamma\,\rho^2\,(1+\beta) \end{cases} \tag{3.34}$$

3.4.1.5 Analytical Comparison

The closed-form solutions are compared using the case study shown in Figure 3.10. The Hart-Smith analysis uses an adhesive plastic stress of $\tau_p = 3\,\mathrm{N/mm^2}$.

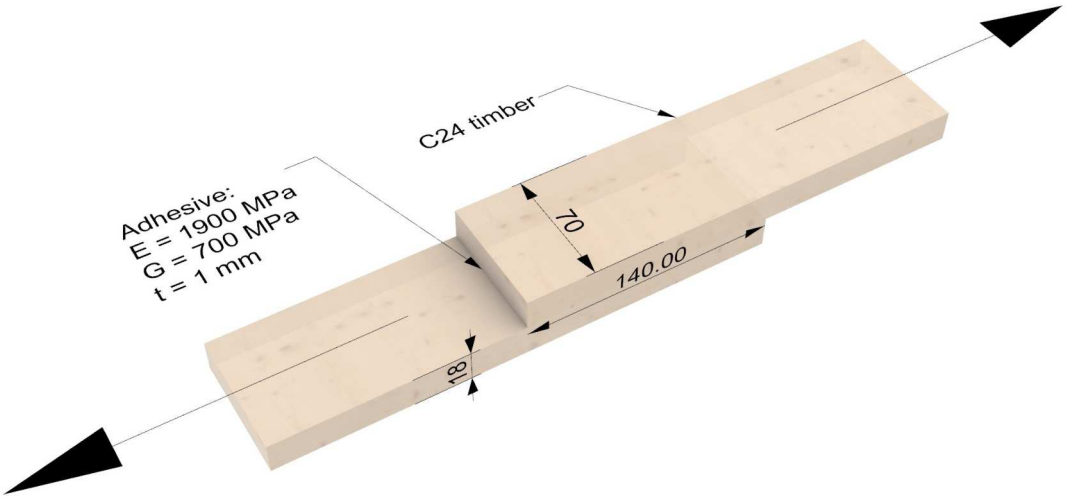

Figure 3.10: SLJ case study and its parameters.

In Figure 3.11, the shear stresses along the adhesive bond are shown. It shows clear stress peaks near the ends of the joint, whereas shear stresses are almost negligible in the middle of the joint. These shear stress peaks at the ends of the joint are not realistic, as in reality, the shear stress should drop to zero since there is no material to shear against. Other analytical solutions have addressed this phenomenon. It can be seen that the theories generally agree. Goland and Reissner, Ojalvo and Eidinoff, and Hart-Smith differ only slightly. Hart-Smith's model shows an early cutoff near the ends due to the plasticity that is taken into account. Volkersen's theory predicts slightly lower stresses near the ends but higher stresses toward the middle compared to the other theories.

The peel stresses for the case study are shown in Figure 3.12. Volkersen's theory is evidently absent, as it does not account for the peel stresses caused by the bending of the joint. The other three theories almost perfectly agree for this case study. The peel stresses are relatively high near the joint ends and quickly decrease. The peel stresses decrease to the point where a zone is in compression. Near the middle of the joint, the peel stresses become stable and almost zero. Once again, the stresses are almost negligible in the middle, indicating that increasing the bond length beyond a certain point is not beneficial.

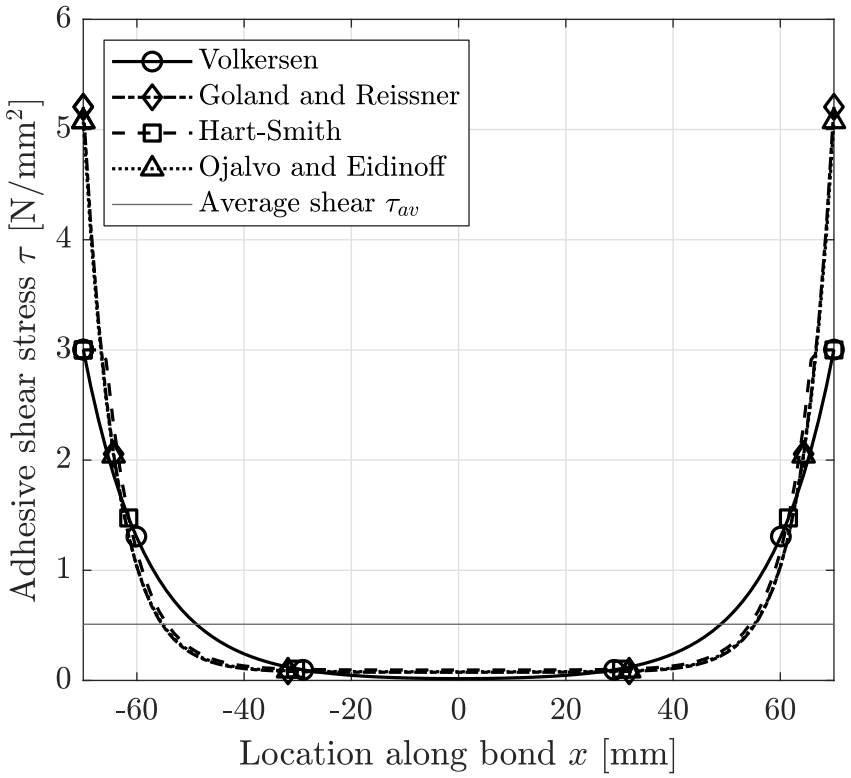

Figure 3.11: Shear stress τ in adhesive along bond length.

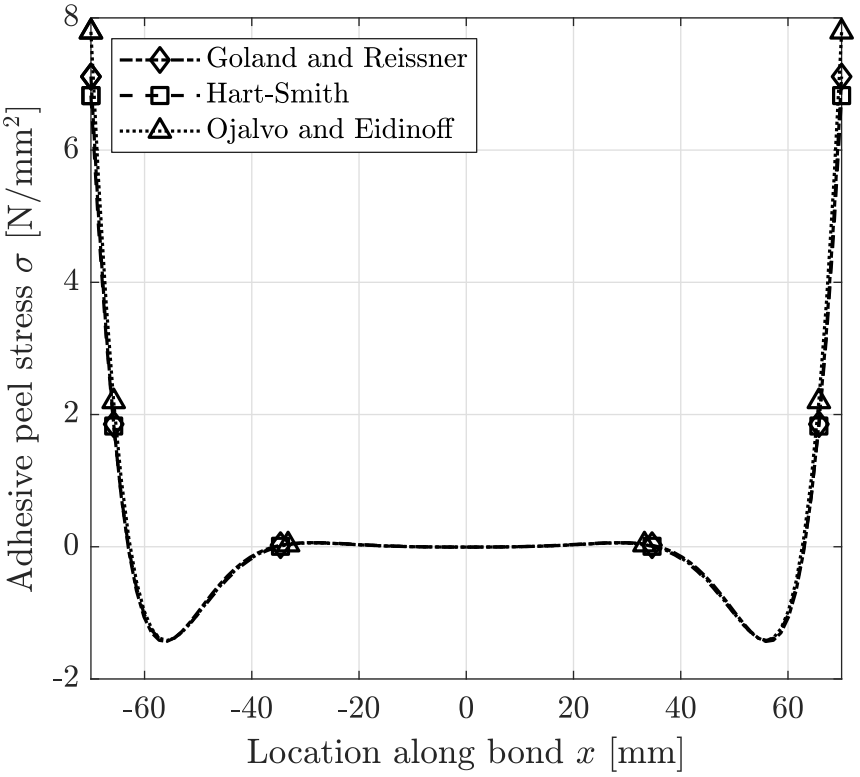

Figure 3.12: Normal (peel) stress σ in adhesive along bond length.

As explained in Section 3.4.1.3, the Hart-Smith solution includes plasticity of the adhesive. This is shown in the zoomed-in shear stresses at the joint end in Figure 3.13. It can be seen that at around 67 mm the shear stresses level out, which indicates that the adhesive reached the stress at which it behaves plastically.

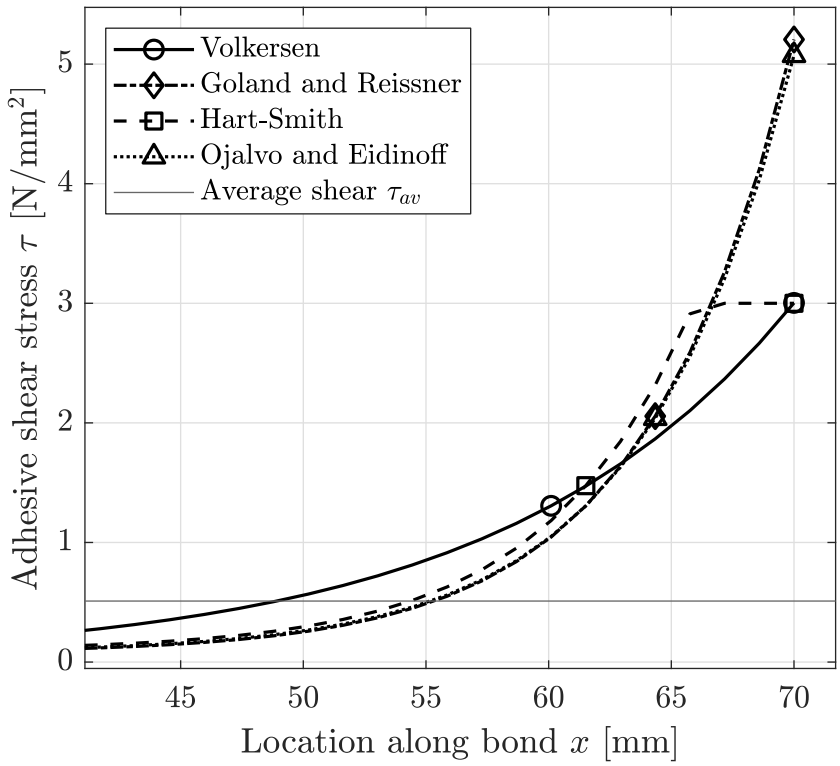

Figure 3.13: Shear stress τ in adhesive near joint ends.

3.4.2 Finite Element Model

The presented theories in Sections 3.4.1.1 to 3.4.1.4 show a fundamental problem with the closed-form solutions for designers. This is them only being suitable for very specific cases of the adhesive joint. In case of more complex joints and boundary conditions, many of these theories cannot be used for stress analysis or become very time and computationally expensive. In the case that a specific design cannot be assessed using a closed-form solution, or a more precise stress analysis is required, a finite element model (FEM) can be made of the joint.

The case study presented in Figure 3.10 is modeled in ABAQUS, of which the model is shown in Figure 3.14. The boundary conditions are fully gripped at the left end, while the joint is allowed to move horizontally at the right end. Once again a load of 5 kN is applied at the end that is free to move horizontally. The adhesive is connected to the timber by means of a surface constraint, which is visualized in Figure 3.15.

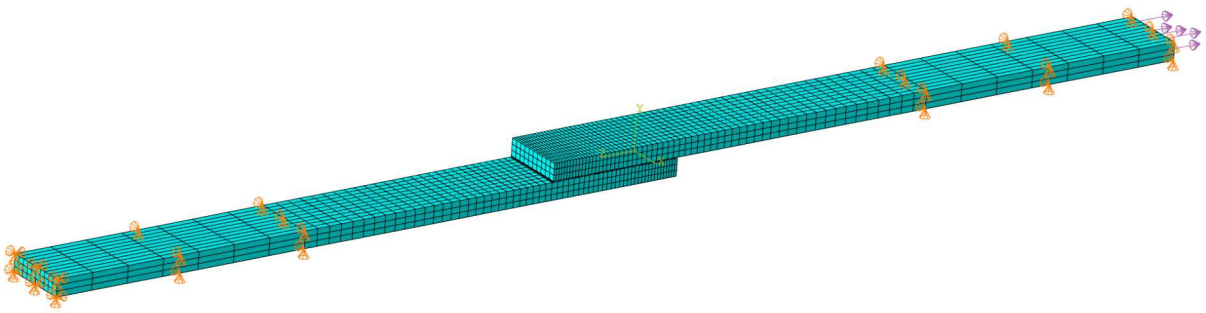

Figure 3.14: Case study ABAQUS model and its boundary conditions.

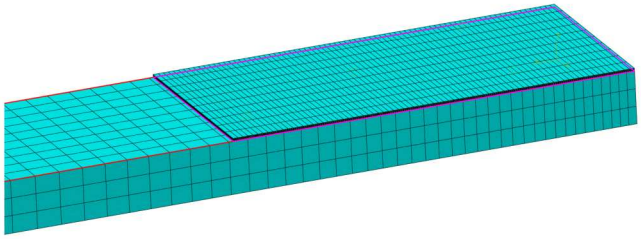

Figure 3.15: Case study ABAQUS adhesive to timber contact surface.

The results of the simulation can be seen in Figure 3.16. The bending causing additional peel stresses can be seen very clearly. The maximum shear and peel stresses along the bond length are extracted from this model.

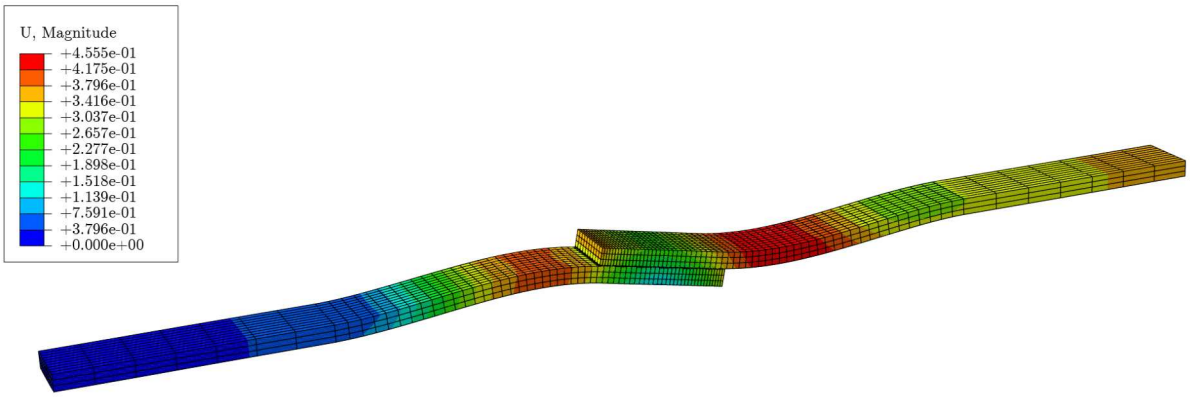

Figure 3.16: Case study ABAQUS deflection results.

The analytical results in Figures 3.11 and 3.12 are compared to the stresses extracted from the ABAQUS model in Figures 3.17 and 3.18. The shear stresses show an almost perfect agreement with the Goland and Reissner and Ojalvo and Eidinoff solution. The peel stresses also show nearly perfect agreement. There is a slight discrepancy where the peel stress drops in the compressive region. However, this can explained by the fact that the FEM model can be modeled much more accurately. For this purpose, it was a relatively crude model. However, with improvements to the meshing (including a finer mesh near stress peaks) and parameter tuning a more accurate stress analysis is expected.

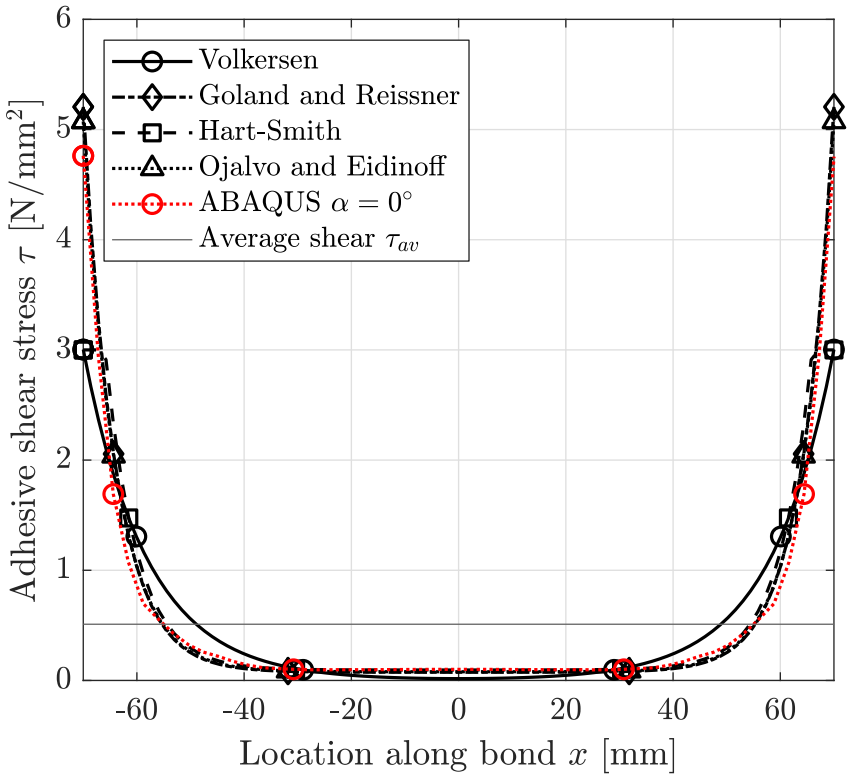

Figure 3.17: Shear stress τ in adhesive along bond length.

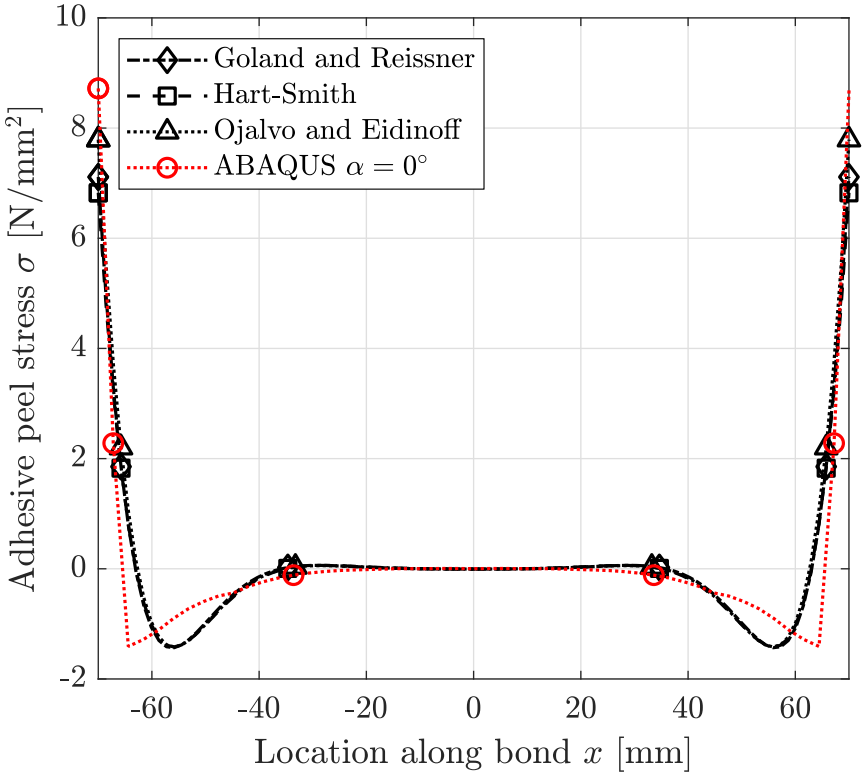

Figure 3.18: Normal (peel) stress σ in adhesive along bond length.

The analytical solutions were limited to parallel SLJ configurations. However, FEM allows for the analysis of more complex configurations. In Figure 3.19 a SLJ with an angle of $\alpha = 55°$ is modeled. The boundary conditions are the same, and an additional gripper is added to the bottom chord, which is considered to be continuous as it would be in a truss.

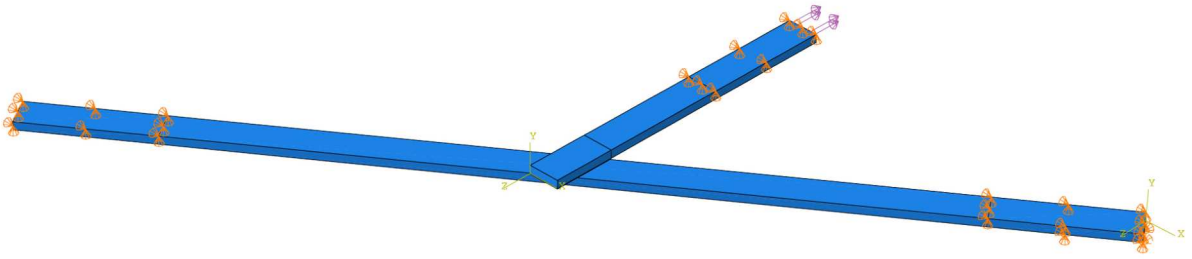

Figure 3.19: Angled case study ABAQUS model and its boundary conditions.

The results of the analysis are shown in Figure 3.20, once again the bending behavior can be clearly seen. However, what is more important is the stress distribution in the adhesive. Due to the vastly different boundary conditions compared to the parallel SLJ, the stresses are also much more complex. Analyzing the stresses and comparing them to the parallel case confirms this, as they are in no way correlated.

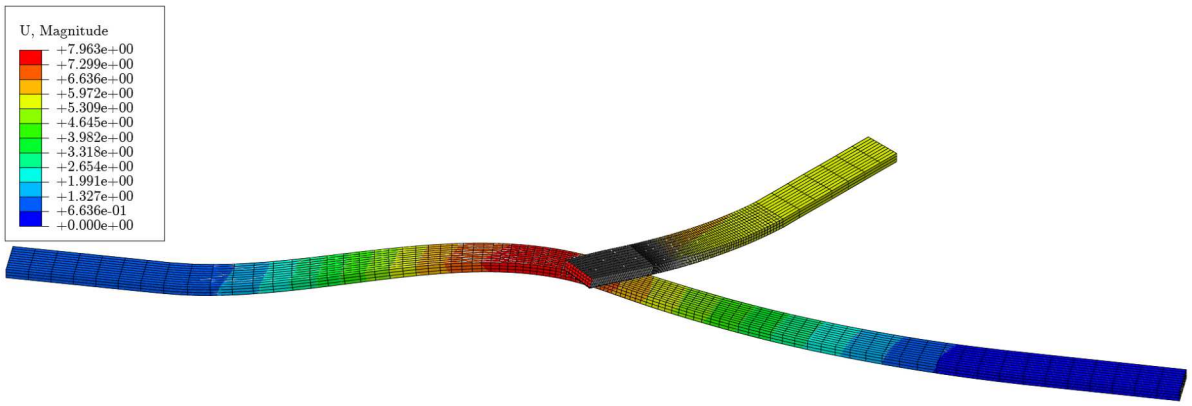

Figure 3.20: Angled case study ABAQUS deflection results.

Last, the differences between a SLJ and DLJ are investigated. The ABAQUS model of the DLJ is shown in Figure 3.21. There are two differences: First, the outer members have half the thickness of the middle member, the total joint thickness remains equal to that of the SLJ. Second, there are two adhesive layers instead of a single one. The boundary conditions remain exactly the same.

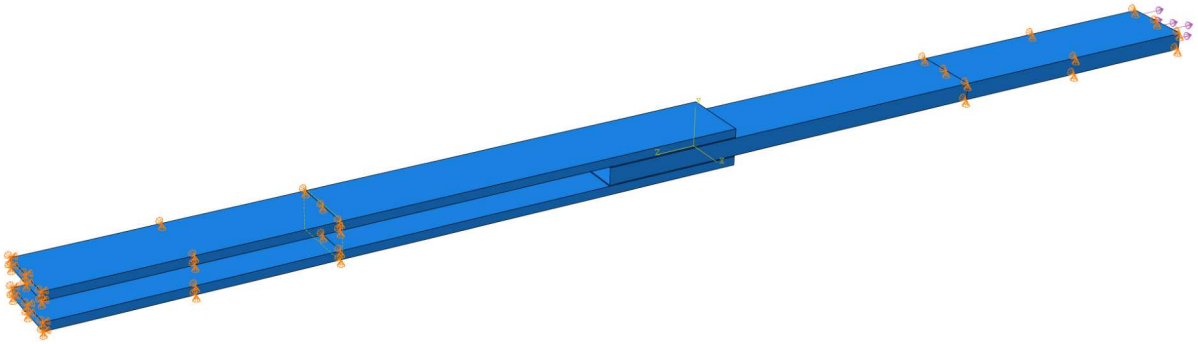

Figure 3.21: DLJ case study ABAQUS model and its boundary conditions.

The peel stresses are of primary interest, of which the deformed results are shown in Figure 3.22. The shear and peel stresses of both the SLJ and DLJ configuration are shown in Figures 3.23 and 3.24 respectively. The following observations can be made:

- The maximum shear stresses in the DLJ are lower than in the SLJ. However, there are locations in the adhesive where the shear is slightly higher in the DLJ than in the SLJ.
- The peel stresses in the DLJ are significantly lower than in the SLJ. The peel stresses at the side of the outer members is purely consisting of a small compressive stress. The peel stresses at the middle member side are only a fraction of the peel stresses in the SLJ. Moreover, the small peel stresses at the ends quickly level out to zero peel stress in the adhesive.
- The deformations in Figure 3.22 explain the peel stresses as shown in Figure 3.24. Due to the elasticity of the outer thinner members, the left side of the adhesive is being compressed. On the other hand, the thin side members can be seen to slightly curve upwards on the right side of the adhesive, causing the tensile peel stresses.

These results show that it is beneficial to design shear connections using a DLJ instead of a SLJ. The most important reason being the significant reduction in peeling stresses in the adhesive layer, while also slightly lowering the shear stress peaks. The total volume of adherend remains constant, whereas the only cost is the doubling of the required adhesive.

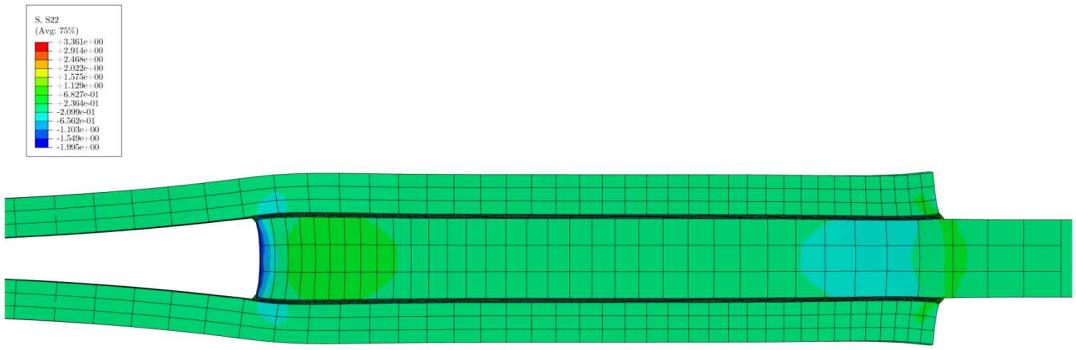

Figure 3.22: Angled case study peel stresses (S22) results.

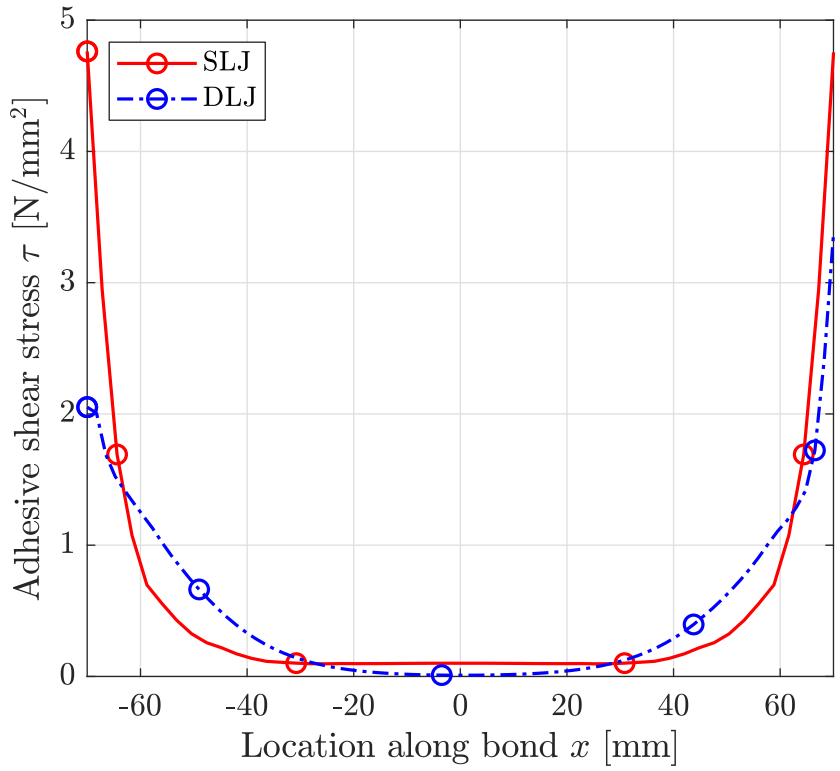

Figure 3.23: Shear stress τ in an adhesive layer along bond length.

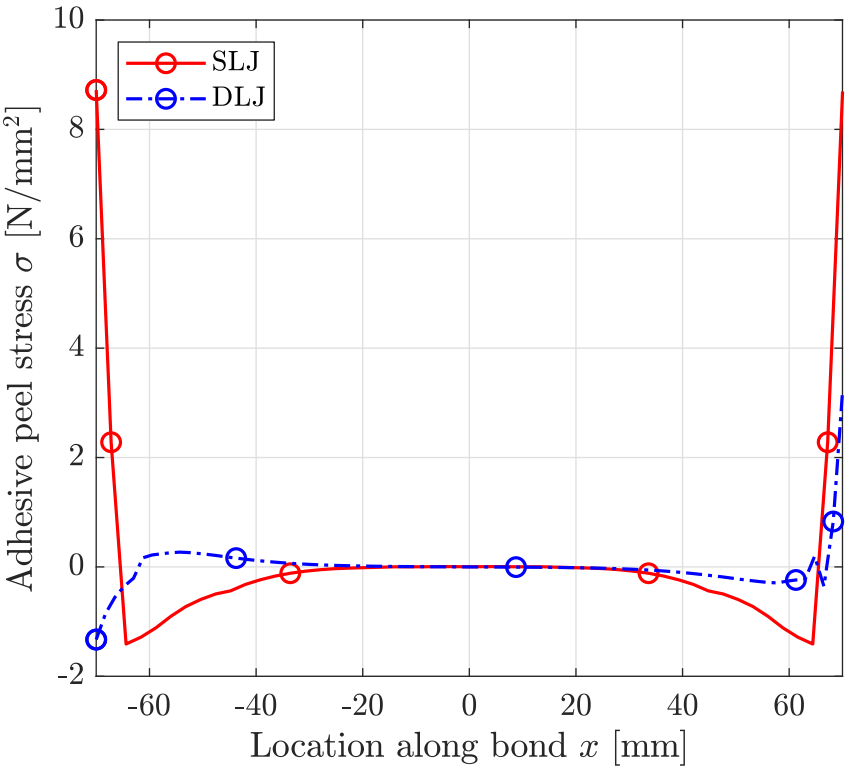

Figure 3.24: Normal (peel) stress σ in an adhesive layer along bond length.

3.4.3 Cohesive Zone Model

The FEM method presented in Section 3.4.2 cannot directly predict failure. It enables a more detailed stress analysis, which can potentially be compared to the material strengths, but it does not indicate failure. For this purpose, the cohesive zone model (CZM) can be used. This method, based on fracture mechanics, can predict crack propagation through the failing adhesive.

The concept of CZM is shown in Figure 3.25, which distinguishes two main phases: elastic behavior and damage evolution. This is often represented in a traction-separation diagram. Up until a certain traction t_{m}^{0}, the joint behaves elastically. However, after a certain traction damage initiates and starts propagating throughout the adhesive until failure. The real traction-separation behavior is simplified to a bi-linear shape in this example. The area of this graph is the fracture energy G before failure.

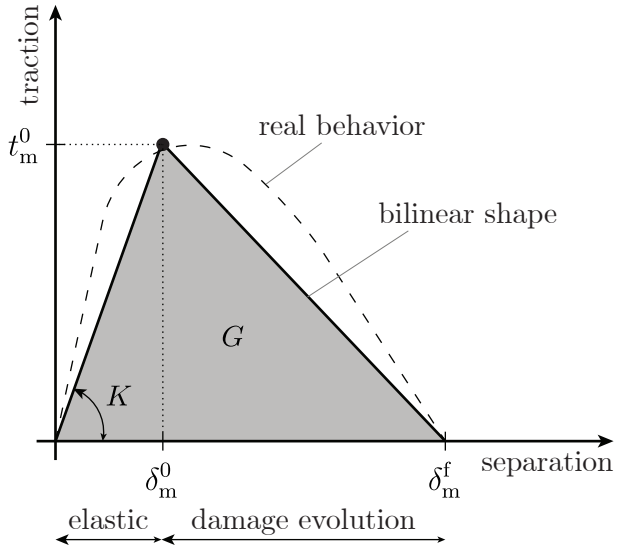

Figure 3.25: Bi-linear traction-separation behavior used in the CZM.

The choice of a bi-linear relationship is not arbitrary, as it often does not provide any significant benefits to choose a different curve, but there are other options. Examples of this are given in Figure 3.26, but for simplicity this section uses the bi-linear approximation.

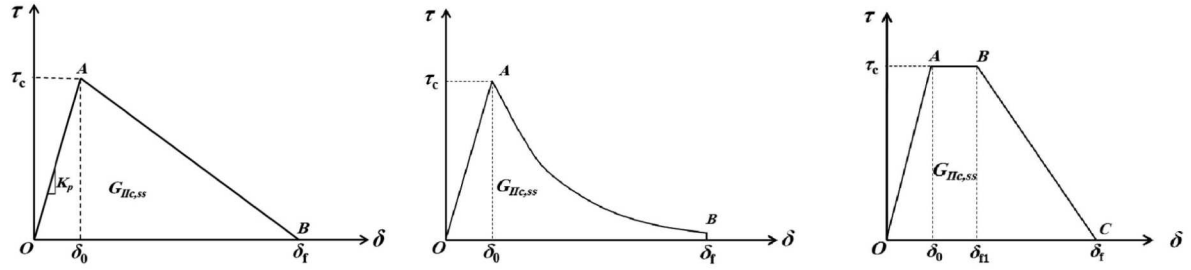

Figure 3.26: Shapes for the traction-separation curve (Heidari-Rarani and Ghasemi, 2017).

The presented behavior in Figure 3.25 is slightly more complex, as there are two modes: shear or normal response. It can also be a combination of these two, which is visualized in Figure 3.27.

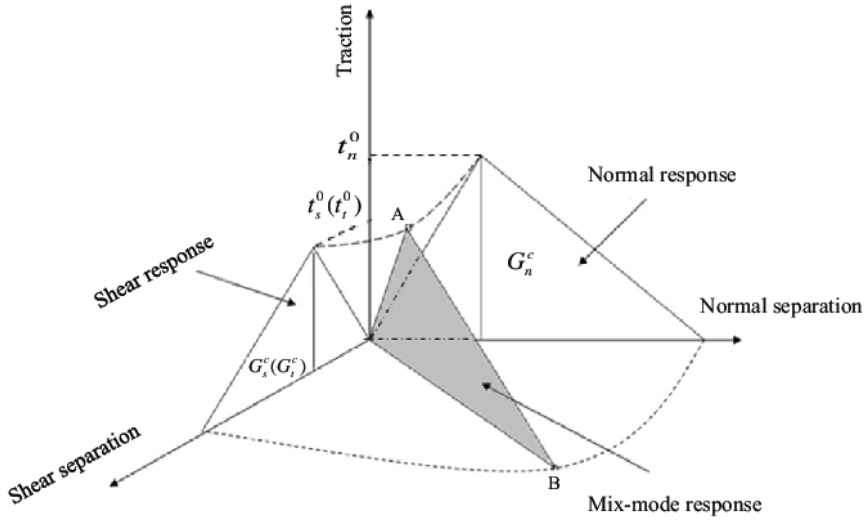

Figure 3.27: Mixed-mode behavior in CZM models (Zhang et al., 2015).

This also highlights one of the challenges of using a cohesive zone model (CZM). Although it provides a very accurate description of the failure mode, it requires numerous material properties. For example, the adhesive supplier 3M offers a service to perform all the necessary tests to obtain these properties, as listed in Figure 3.28.

Physical Effect	Test Name	Test Sketch	Material Parameter	Description	Symbol	Unit
Elasticity	Uniaxial Tension Test		Young's Modulus and Poisson's Ratio	Resistance to elastic deformation and transverse contraction in tension	K_I, K_{II}, K_{III}	MPa
Damage Initiation	Thick Adherend Butt Joint Tension Test		Tensile Strength	Maximum stress in laterally constrained tension	σ_I	MPa
	Thick Adherend Shear Test		Shear Strength	Maximum stress in shear	$\sigma_{II} = \sigma_{III}$	MPa
Damage Evolution	Tapered Double Cantilever Beam (TDCB) Test		Mode I Fracture Energy (Critical Energy Release Rate)	Resistance to crack propagation in Mode I (opening mode)	G_{IC}	$\frac{N}{mm} = \frac{kJ}{m^2}$
	End-Notched Flexure (ENF) Test		Mode II Fracture Energy (Critical Energy Release Rate)	Resistance to crack propagation in Mode II (shear mode)	$G_{IIC} = G_{IIC}$	$\frac{N}{mm} = \frac{kJ}{m^2}$

Figure 3.28: Tests required to obtain al CZM parameters (3M, n.d.).

An adhesive of which these properties are known, but different from the adhesive used in Figure 3.10, is modeled in ABAQUS. The CZM allows to see the crack growth in the adhesive, of which a time step is shown in Figure 3.29. Once crack growth is initiated in an element, and the fracture energy is reached, it is removed from the model. From Figure 3.29 this is clearly visible near the ends of the adhesive bond. This continues until the entire adhesive layer is damaged and thereby resulting in failure of the joint.

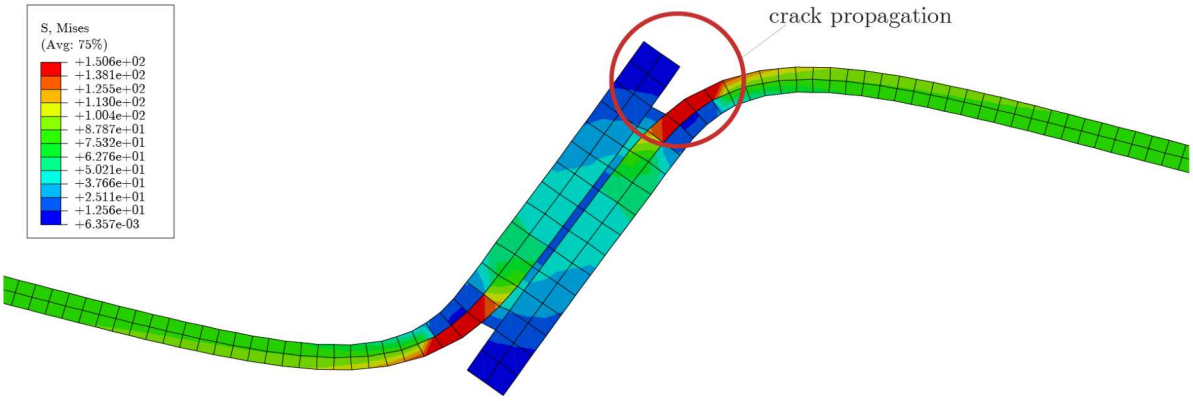

Figure 3.29: Crack propagation in an adhesive single lap joint using a CZM.

3.4.4 Stress Analysis Considerations

In the previous sections, three important methods for determining stresses in adhesive bonds have been discussed: closed-form analytical solutions, 3D FEM analysis, and the cohesive zone model. Each of these methods comes with its own set of advantages and disadvantages.

There are many closed-form theories for SLJ configurations, each approaching the problem slightly differently. For example, Volkersen's method ignores normal stresses and only considers shear stress, whereas Goland and Reissner's method includes the normal stresses caused by the rotation of the joint configuration. However, both methods fully ignore any plasticity of the adhesive. Hart-Smith expands on existing theories by considering the plasticity of the adhesive near the bond ends. However, here the optimal joint parameters are obtained through boundary conditions, which requires an iterative process.

A significant disadvantage is that all these theories are only valid for specific boundary conditions in parallel joints. Moreover, closed-form analyses cannot reliably predict adhesive joint strength and are only accurate for low loads (van Ingen and Vlot, 1993). An alternative solution is the application of a FEM model, which provides more detailed information on the stress distribution. However, this requires a complex FEM model. For even more accurate results, FEM modeling using a CZM can be chosen, as it includes crack propagation through the joint. This approach, however, necessitates obtaining a large number of material properties through a variety of tests.

4 Methodology

4.1 Design Toolbox

4.1.1 Overview

The design toolbox is a parametric design tool in which lap shear connections can be designed and analyzed. It is implemented using a truss as case study, but can also assess singular joints. It allows the designer to quickly assess different joint and truss variants, in which the tool also provides the shear resistance of the joint in case mechanical fasteners are used. Another purpose of the design toolbox is the direct link to a robotic fabrication process, as robot code for an ABB robot setup can be extracted as well. Additionally, the tool offers various optimization possibilities, such as minimizing material use, minimizing deflections, or other criteria.

This section is divided into two parts: Section 4.1.2 explains the truss parametric model, including its structural modeling. Section 4.1.3 presents the joint generation process and the calculation of the shear resistance.

4.1.2 Truss Design

4.1.2.1 Parametric Design

The design toolbox can design either singular joints or trusses, within the truss category it can generate Warren, Pratt, or Howe trusses. The trusses are double lap joints in which the diagonals are the middle member and the chords are the outer members. The parameters that can be controlled are shown in Figure 4.1, and listed below:

- **Truss type:** Determines the layout of the diagonals.
- **Width w and height h:** The global span and height of the truss.
- **Number of subdivisions n:** The number of bays (and thereby diagonals) the truss has.
- **Node offset p:** The horizontal offset of the diagonals from the subdivision node.
- **Cross-sectional properties:** All properties of the timber members can be set, both the dimensions and material properties.
- **Fastener properties:** Any fastener type and its properties can be chosen, as well as the fastener layout that will be used in the upcoming sections.

The truss is designed as a double lap joint, with the chords acting as the double members while the diagonals serve as the single middle members. This configuration is chosen because placing more material away from the neutral axis increases the stiffness of the truss. Additionally, the increased amount of material in the chords reduces the possibility of buckling in the longer chords.

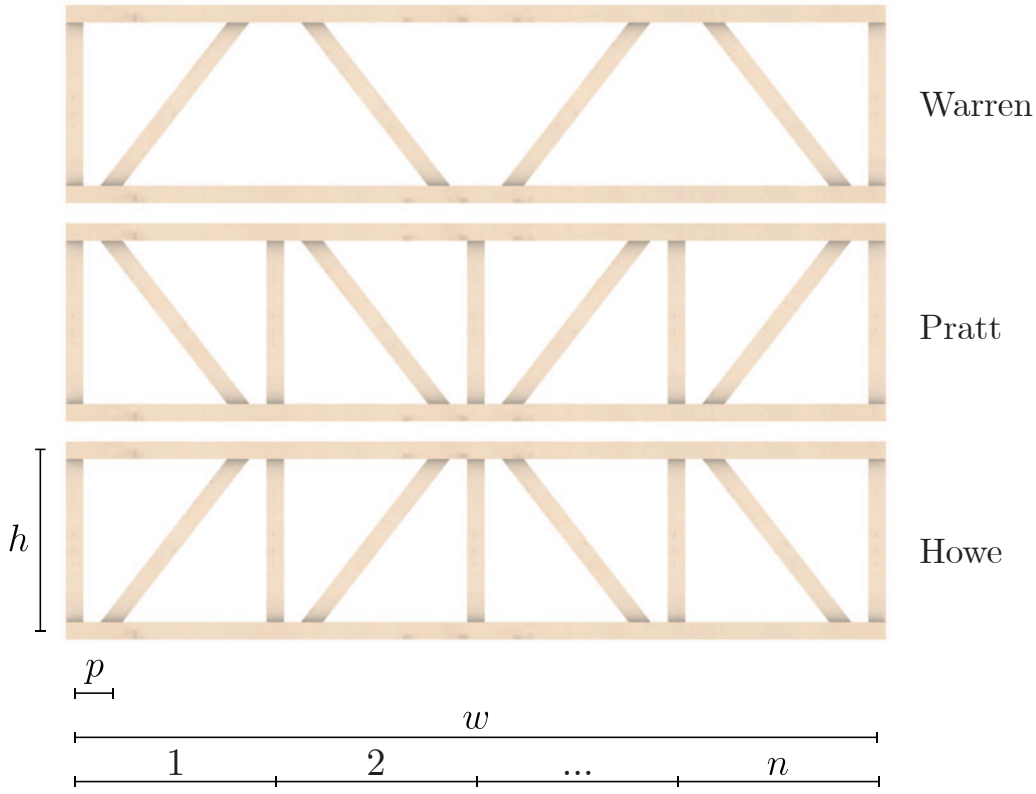

Figure 4.1: The three truss variants and their parameters.

The node offset parameter p influences how the ends of the diagonals are sawn. If the node offset is low, a significant portion of the end face can be sawn off, as shown in Figure 4.2. This influences the fastener layout in two important ways:

- The available overlap area in which the joint can be realized reduces.
- The (vertical) sawing of the end creates an additional face that is considered an end face. End faces have larger spacing requirements than edge spacing. In turn, the available joint area after subtraction of the end and edge distances reduces.

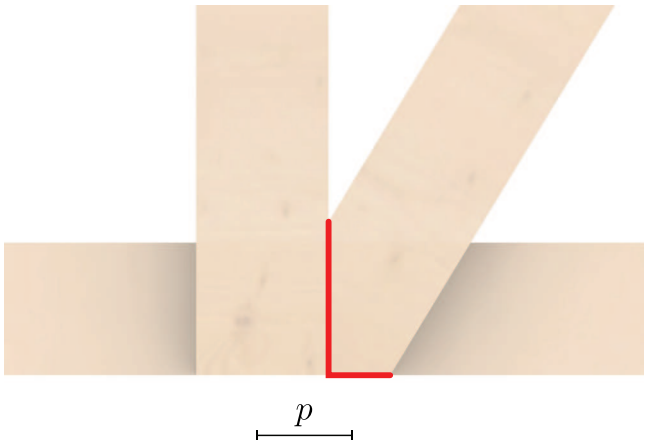

Figure 4.2: For low node offsets p, the diagonal is sawn off where it overlaps.

4.1.2.2 Structural System

The structural behavior of the truss is analyzed in GSA, of which the mechanical scheme is shown in Figure 4.3. It is a simply supported truss, which is fully supported in the out-of-plane direction (because it is a 3D model, but it is considered to be sufficiently supported by the other structural members in the total structural system). Similarly, rotation about members their own axis is restrained. The diagonals are modeled as bars only transferring axial loads. The external loads are applied as point loads, to represent the loads transferred by girders.

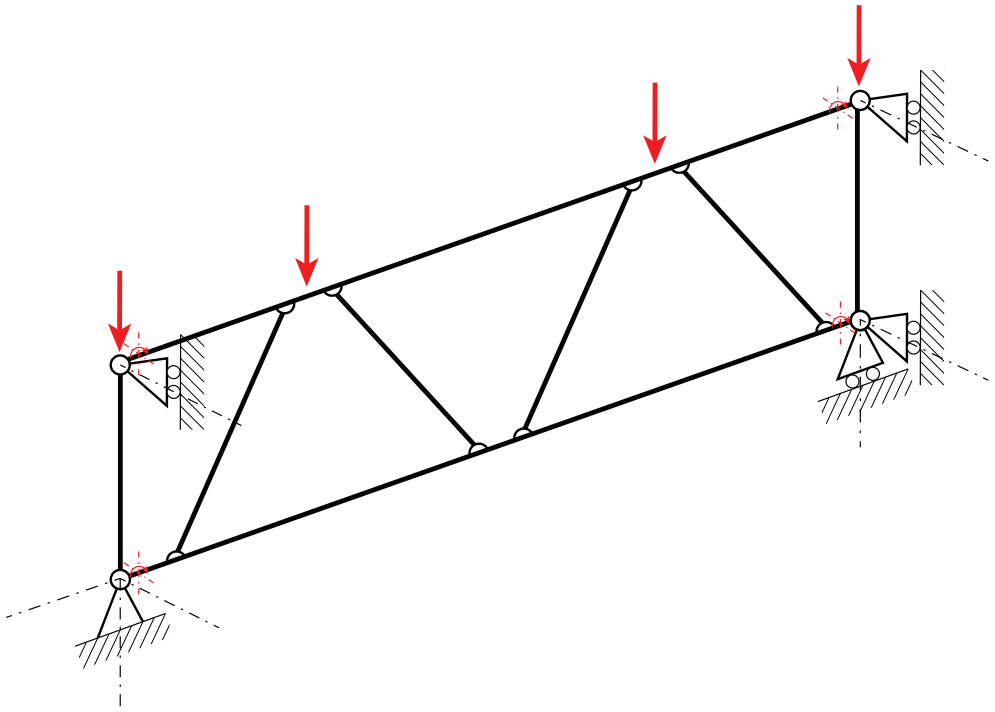

Figure 4.3: Mechanical scheme of the truss.

This model in GSA is shown in Figure 4.4. Moreover, it is shown how the nodal loads are determined. The nodal loads are based on the shortest distance, resulting in the center nodes being more heavily loaded than the two outer ones.

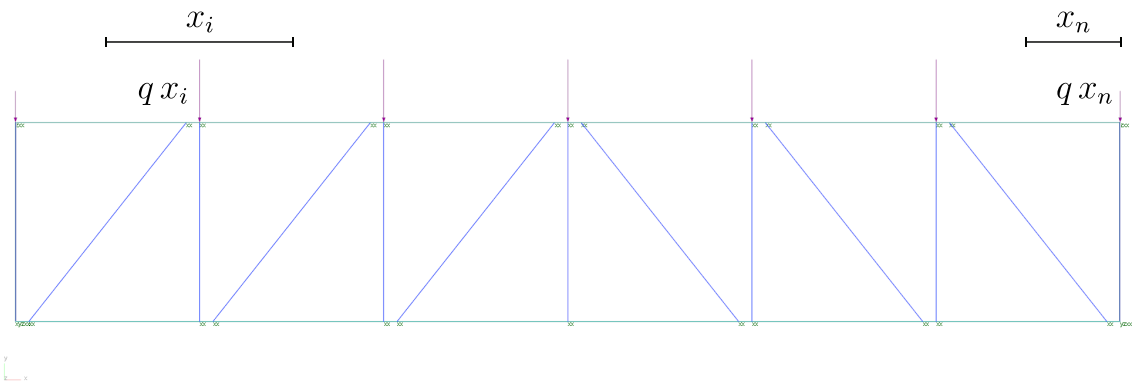

Figure 4.4: Structural model in GSA and point load determination.

Any load case or combinations thereof can be added to this structural model. During this research

the following load case is used:

$$1.2P + 1.5Q \tag{4.1}$$

In which the permanent load (P) is the material self weight and the variable load (Q) is equal to $Q = 1.5\,kN/m^2$. The algorithm is capable of handling any type of load combination, but it is important to be aware of reversed loads (such as uplift). This can affect the ends that are stressed and thereby influencing the required end distances. A conservative approach is to always use the stressed end distances.

4.1.2.3 Axial Forces

To determine the minimum spacing, it must be known whether a diagonal or vertical is acting in compression or tension, as this influences whether an end face is stressed or unstressed. Therefore, the GSA model runs in Grasshopper, directly calculating the model. The results can be used to determine whether a diagonal or vertical acts in compression or tension (or possibly both can occur, in which case the worst case is taken). The results of such an analysis for a single load combination are shown in Figure 4.5.

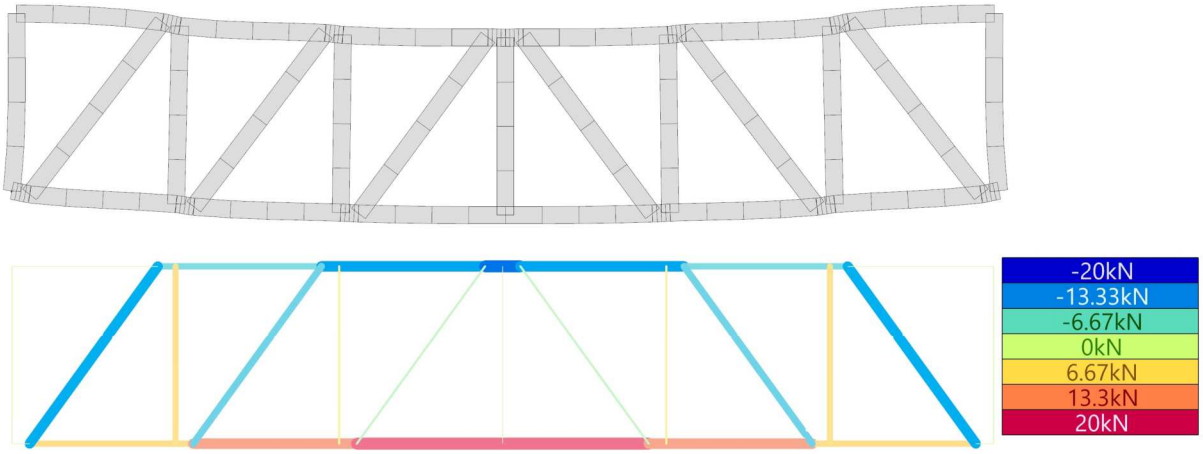

Figure 4.5: Axial forces of truss members in Grasshopper.

4.1.2.4 Bending Moments

The truss is modeled such that the diagonals and verticals are only loaded axially. However, depending on the fastener group, there can be some moment resistance in these joints. This section briefly investigates the effects of these bending moments on the resistance of the truss. In Figure 4.6 the bending moments for the used load combination are shown, in this case the diagonals are modeled as beams instead of bars and can thus transfer bending moments. The bending moments acting are in plane of the truss.

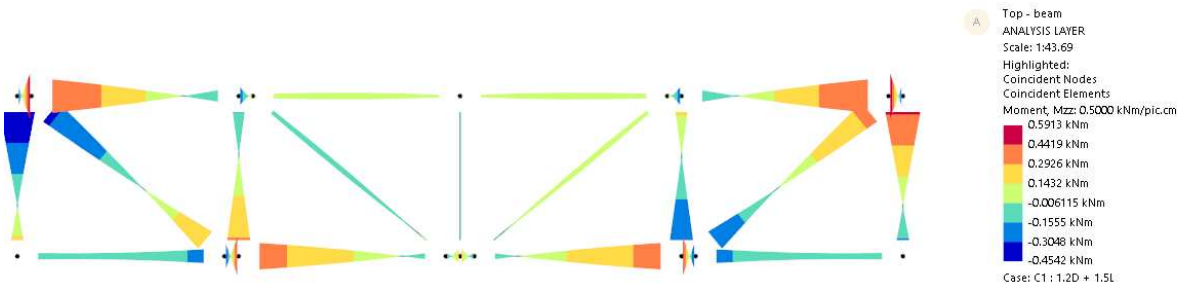

Figure 4.6: Bending moments in the truss when the diagonals are modeled as beams.

Continuing with this, it is assessed whether the simplest form of two fasteners can resist the maximum bending moment observed. This situation is illustrated in Figure 4.7, the moment resistance of the node is based on the shear resistance of the individual fasteners. This results in the following resistance:

$$M_{\mathrm{Rd}} = 8 \cdot \frac{133}{1000} = 1.064 \text{ kNm} \tag{4.2}$$

Comparing this to the maximum bending moment gives a unity check of

$$\mathrm{UC} = \frac{0.3217}{1.064} = 0.3 \tag{4.3}$$

Therefore, the joint while not being designed as a moment resisting joint would still be more than sufficient to carry the bending moment. However, it must be considered that the joint is loaded in both shear and bending and therefore that combination should be checked as well.

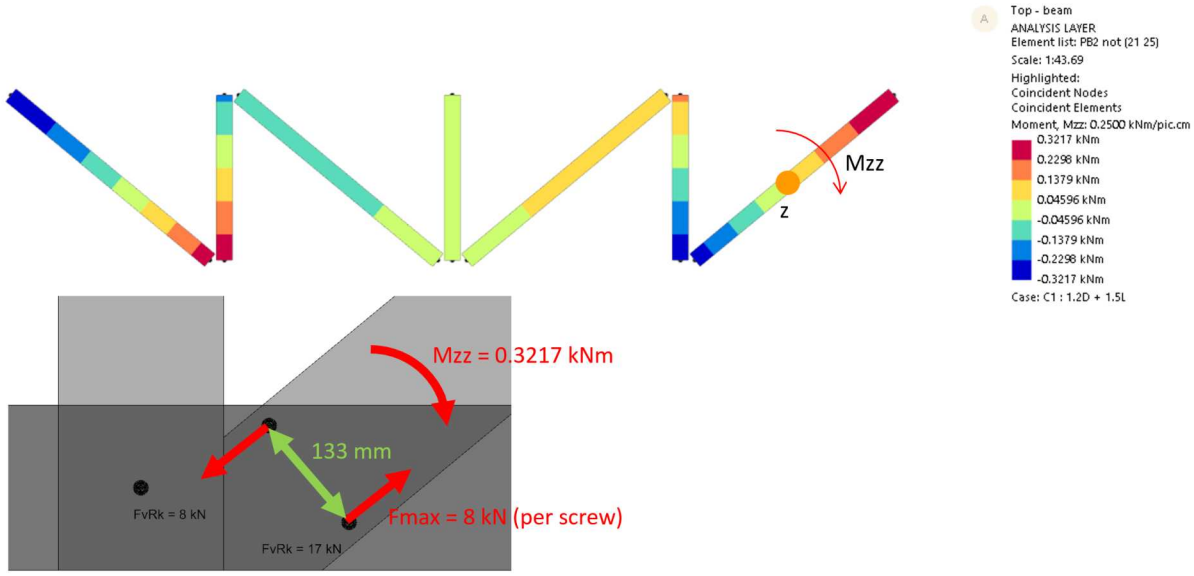

Figure 4.7: Bending moments in the truss and the moment resistance of two fasteners.

Important to note is that these joints never come close to full moment-resisting joints. Therefore, the resistance of each fastener group is calculated individually. The stiffness of a single fastener of 6 mm is

$$K_{\mathrm{u}} = \frac{2}{3} K_{\mathrm{ser}} = \frac{2}{3} \cdot \frac{d\,\rho_{\mathrm{m}}^{1.5}}{23} = \frac{2}{3} \cdot \frac{6 \cdot 420^{1.5}}{23} = 1497\,\mathrm{N/mm} \tag{4.4}$$

Using this information, the rotational stiffness of the joints can be calculated using

$$K_{\mathrm{j}} = 2\,K_{\mathrm{u}} \sum r^2 \tag{4.5}$$

These rotational stiffnesses are calculated for each joint, which is then used in the structural model in GSA. The bending moments corresponding to this are shown in Figure 4.8. It can be seen that the bending moments are only a fraction of the case where full moment-resisting joints are assumed. Therefore, it is safe to assume that the joints will not transfer any meaningful moments and act as hinges for the materials and situations considered in this research.

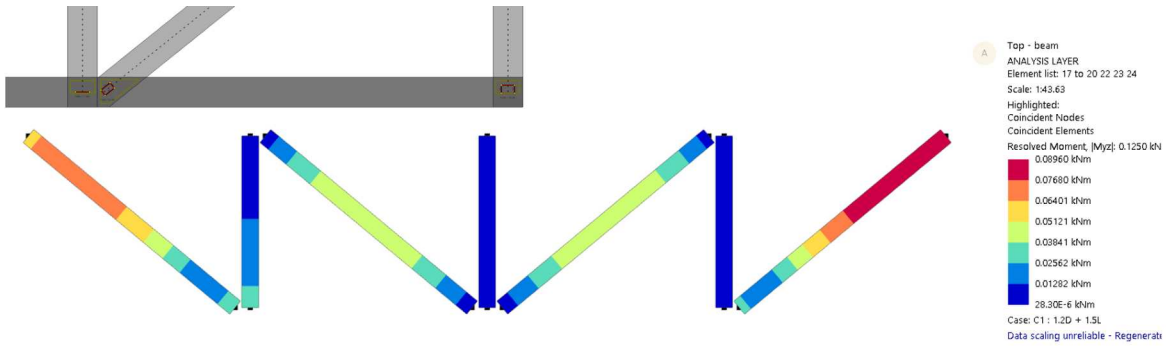

Figure 4.8: Bending moments in the truss using the actual joint stiffness.

4.1.3 Mechanical Joint Generation

4.1.3.1 Fastener Placement Procedure

Considering the minimum end and edge distances as presented in Section 2.3.3, the overlap area of timber members cannot be fully utilized and must be reduced accordingly to provide sufficient distance from the member sides. Next, within this suitable area, the fasteners must be arranged to avoid unnecessary eccentricities that could cause additional stresses on the connection. Moreover, the connection is preferably in-line with the member introducing the load, for the same reason. This process can be distinguished in five main steps, which are visualized in Figure 4.9:

- **Stress state determination:** Section 4.1.2.3 explains how the load of a member can be extracted. Using this information, each joint is given a plane that indicates the load direction. Using this information, each edge or end is given a tag that indicates whether it is a stressed or unstressed face of the member. Moreover, it is important to note that this process is performed for all members in the joint through which the fastener passes. This is important as the load transfer between chords and diagonals has opposite effects.
- **Governing end and edge spacing:** For every end and edge the offset is computed for the correct stress state (shown in Figure 2.28). Using all these offsets, the outline is constructed in which the fasteners can be located while adhering to all the prescribed end and edge distances. This is shown in Figure 4.9a.
- **Minimum perpendicular spacing:** First, the centerline of the diagonal is constructed so that the joint has no eccentricity. Next, this centerline is offset so that the minimum perpendicular spacing a_2 is guaranteed. This process is shown in Figure 4.9b.
- **Parallel spacing optimization:** With the minimum perpendicular spacing ensured, the goal is to eliminate any strength reductions due to the group effect. Parallel to the centerline, starting at the previously determined perpendicular ends, the parallel spacing a_1 is checked to ensure no group effects occur. If possible, the parallel spacing is chosen to fall between that distance and the end and edge distances. This ensures it never sits exactly on one of the boundaries and allows the fasteners to be spread more evenly throughout the joint, as shown in Figure 4.9c. Additionally, the center of the current area is moved as much as possible to the center of the joint node.
- **Perpendicular spacing optimization:** Next, the perpendicular distance is once again evaluated now that the parallel spacing is determined. If there is space left in the

perpendicular direction, a_2 is chosen such that it falls exactly in between the minimum required a_2 and the outer end and edge distances. This process is shown in Figure 4.9d, and is similar to how a_1 is optimized.

- **Fastener insertion:** Last, the constructed area in the previous step is used to fit in the fastener pattern of choice. It spreads the fasteners evenly over the suitable area. This process is shown in Figure 4.9d.

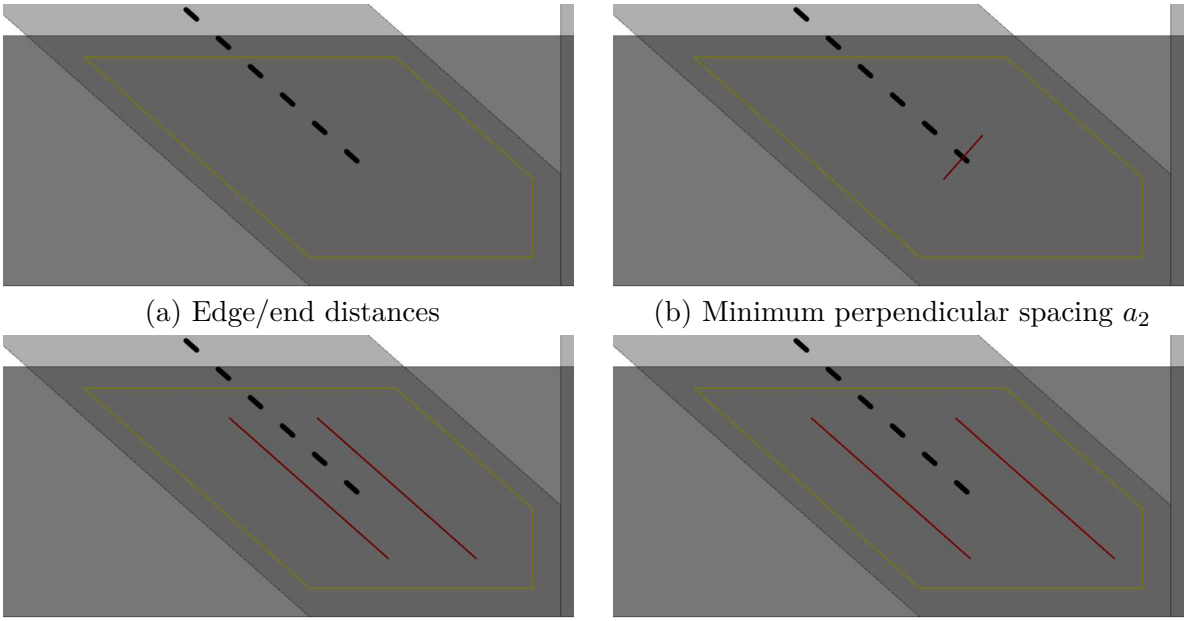

(a) Edge/end distances

(b) Minimum perpendicular spacing a_2

(c) Parallel spacing optimization a_1

(d) Perpendicular spacing optimization a_2

Figure 4.9: Step-by-step procedure of the fastener layout generation.

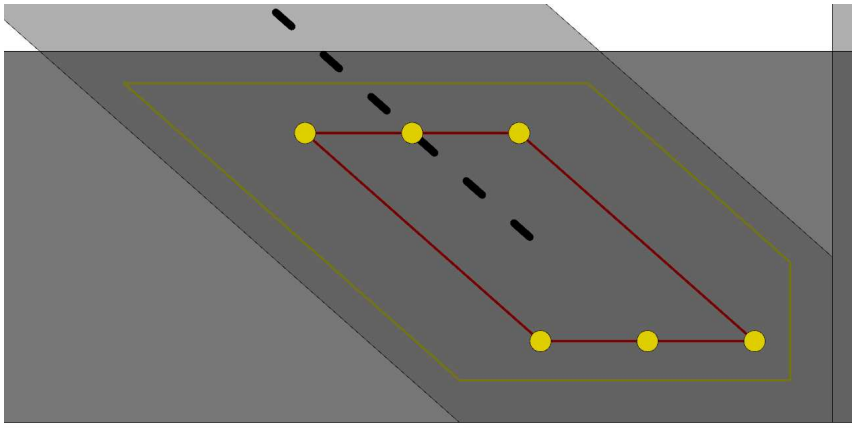

Figure 4.10: Fastener insertion within the optimized fastener area.

Using this process, the minimum required end distances and spacing are guaranteed. Moreover, it tries to optimize the area such that group effect reductions are reduced as much as possible. This is all while organizing the fasteners as centrally as possible while utilizing the space as efficiently as possible. There are various parameters that can be adjusted so that the joint meets all configurations, such as increasing the node offset p or using a different fastener pattern.

The algorithm also offers the possibility to choose between a square or parallel placement configuration, which are both shown in Figure 4.11. In general, they both result in equal strengths as the algorithm guarantees that spacing requirements are met while avoiding group effect reductions. However, due to the greater spacing of the parallel placement it can place larger groups of fasteners. Moreover, parallel placement spaces the fasteners in general further from each other. This gives the joint a small moment-carrying capacity which is significantly smaller for the square placement. This moment-carrying capacity can be required to absorb small eccentricies. Therefore, it is advised to utilize the parallel placement.

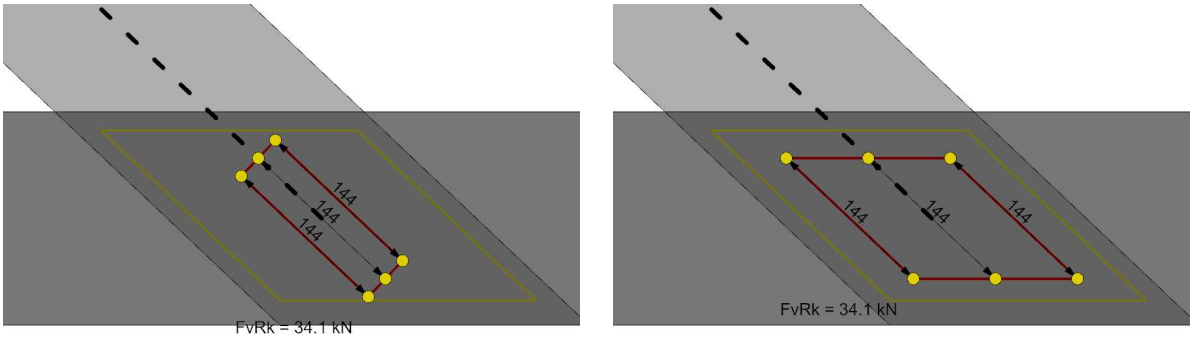

(a) Square placement (b) Parallel placement

Figure 4.11: Square and parallel placement algorithm results.

4.1.3.2 Fastener Placement Cases

Four fastener patterns can be distinguished: single, one row, side-by-side, or grids. For each of these patterns the algorithm varies slightly. For a fastener grid the placement rules of the former cases are combined.

For single fasteners the placement rules are shown in Figure 4.12, there are two cases:

1. If the fastener can be placed exactly on the joint node, it is done so.
2. If the joint node falls outside the boundary edges, the fastener is placed at the first possibility on the centerline that falls within the boundary edges.

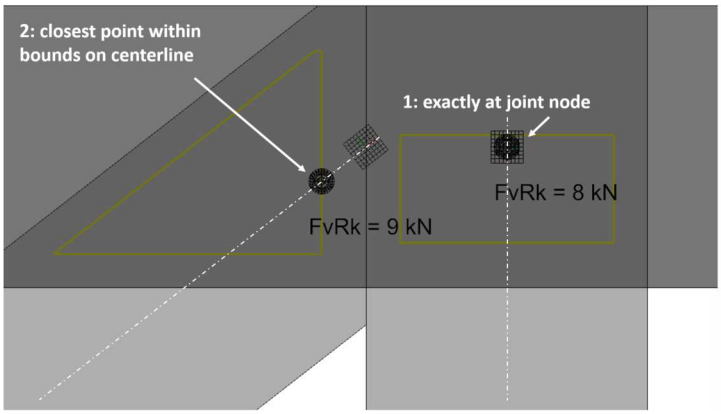

Figure 4.12: Single fastener placement rules.

For a row of fasteners the placement rules are shown in Figure 4.13, there are three cases:

1. If the length of the centerline that falls within the boundaries is not sufficient to fully avoid group effects, then that part of the centerline within the boundaries is fully utilized to space the fasteners.

2. If the length of the centerline is sufficient to fully avoid the group effects, then the length utilized is exactly in between the boundaries and this minimum distance. In this case this pattern can be centered fully over the joint node.

3. This case is equal to that of the previous case. However, in this case it cannot be centered fully over the joint node without moving the fastener group outside the boundaries. In this case, the group is moved to the boundary such that it is centered as much as possible over the joint node while not crossing the bounds.

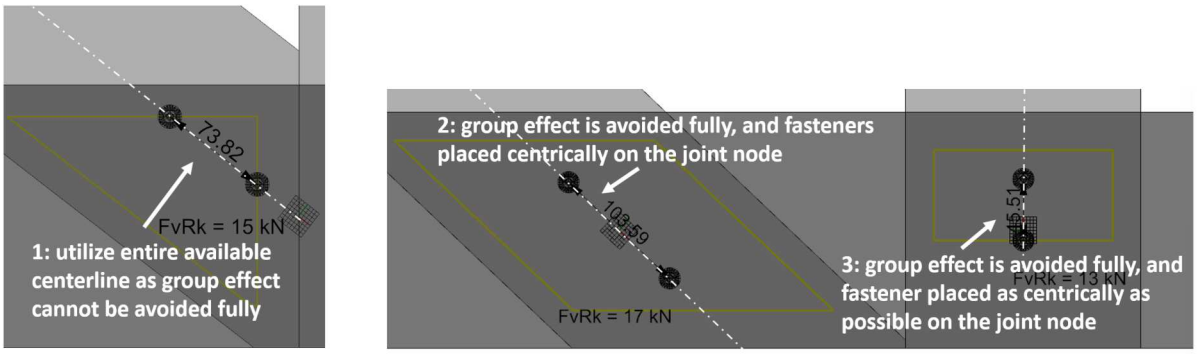

Figure 4.13: Row of fasteners placement rules.

For side-by-side fasteners the placement rules are shown in Figure 4.14, there are two cases:

1. If the node lies within the boundaries, and there is sufficient space in perpendicular direction, then the fasteners are placed in between the minimum perpendicular spacing and boundaries.

2. If the node falls outside the boundaries, it is searched along the centerline where the perpendicular spacing is the largest. The fasteners are placed here, spaced in between the minimum perpendicular distance and the boundaries once again.

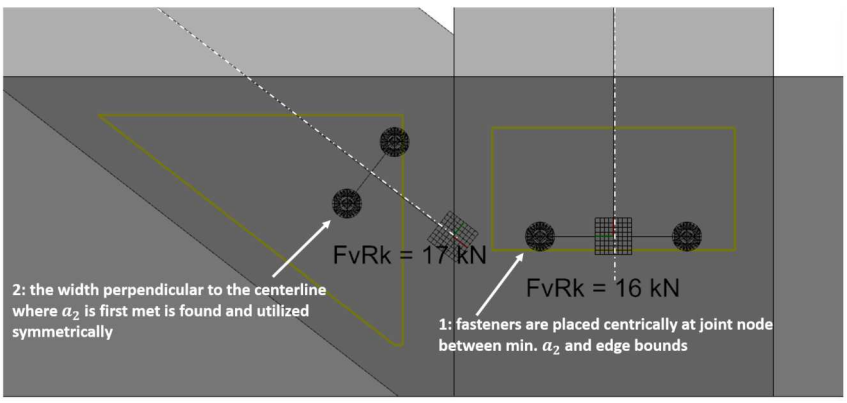

Figure 4.14: Side-by-side fasteners placement rules.

For a grid of fasteners the placement rules are shown in Figure 4.15, there are three cases:

1. The perpendicular distance is met, but there is not sufficient space to fully avoid group effect reductions. The entirety of parallel spacing is utilized.
2. The same as in the first case, but in this case there is space in the perpendicular distance left where the a_2 distance is once again optimized by placing it exactly in between the minimum required spacing and the boundary.
3. In the last case the perpendicular distance is met and the group effect can be fully avoided. The algorithm tries to center the fastener group as much as possible over the joint node.

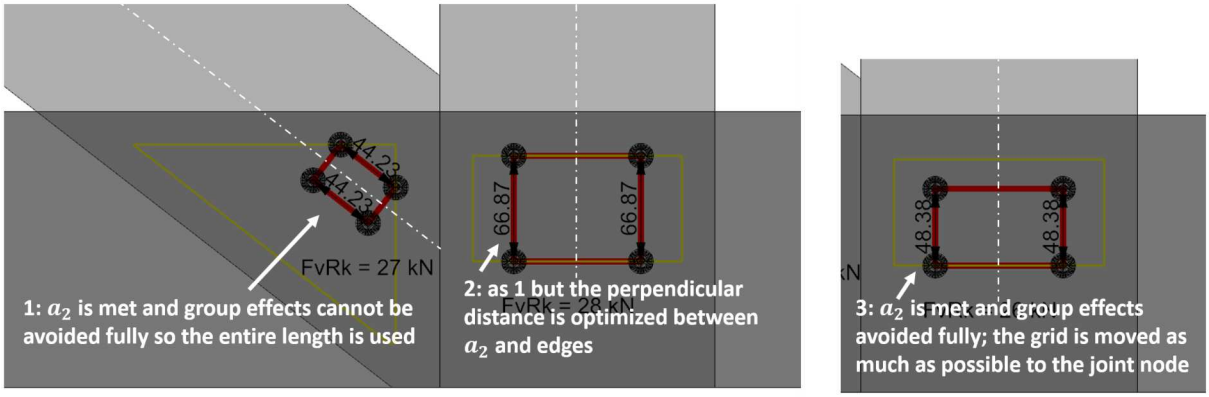

Figure 4.15: Grid of fasteners placement rules.

4.1.3.3 Shear Resistance

Now the fastener distribution has been determined, the shear resistance of each joint is calculated. For this, the number of fasteners and their parallel spacing a_1 are required. The parallel spacing plays an important role in the determination of the effective number of fasteners n_{ef}, as discussed in Section 2.3.4. The parameters for a given scenario are shown in Figure 4.16, in which these shear resistances can be compared to the member axial results of the structural model presented in Section 4.1.2.3. The calculation procedure is based on the EN 1995-1-1 design rules, as presented in Section 2.2.3.4. The Python code responsible for this is shown in Appendix C.

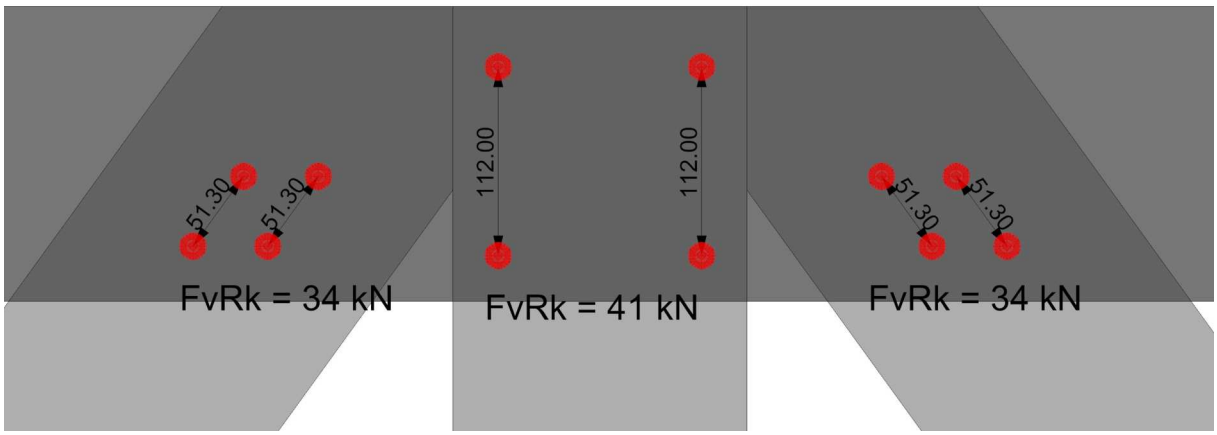

Figure 4.16: Shear resistance calculated for each joint including group effects.

Observations from the results shown in Figure 4.16 are:

- The effect of a stressed end is clearly visible in the diagonals. As the diagonals are acting in compression, their ends are stressed. Consequently, these ends required a significantly larger end distance compared to the vertical that is acting in tension (and thereby its end is unstressed).
- As a result of the compression in the diagonals (and corresponding loaded end distance), in combination with the partly sawn end due to the low node offset distance p, the available joint area is relatively low. Consequently, the group effect becomes more present and results in a 25% decrease in strength compared to the vertical member joint that has better spacing.

4.1.3.4 Optimization Algorithm

Using the tools developed in the previous sections, the model is expanded to a fully automatic optimization algorithm. In this tool the designer can design the truss using the parameters shown in Section 4.1.2. Next, a multi-objective optimization algorithm using Octopus will generate the most ideal fastener configuration for all the nodes in the model simultaneously. The following objectives are optimized:

- **Minimize residual strength:** Which means that the shear resistance of each joint must be as close as possible to the actual load it must transfer, so that joints are not overdimensioned.
- **Minimize material use:** Minimize the amount of material used by calculating the total volume of the fasteners.
- **Prioritize rows or side-by-side:** The designer can choose whether rows of fasteners or side-by-side fasteners are preferred.

While doing so, all designs must meet the following requirements as well:

- Shear resistance must be larger than the applied load.
- End and edge distances must be met.
- Parallel and perpendicular fastener spacing must be met.

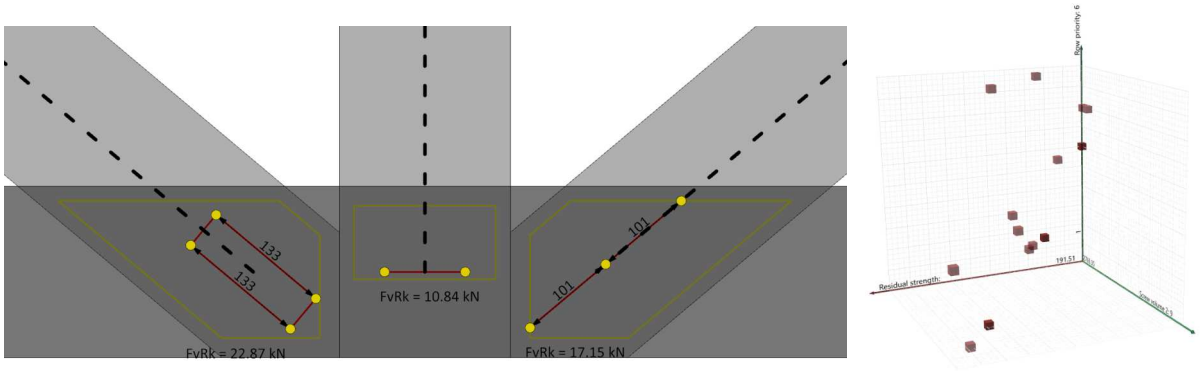

(a) Generated nodes (b) Performance

Figure 4.17: Optimization algorithm of the truss joints using Octopus.

4.2 Robotic Setup

The robotic setup consists of multiple components, an overview of the setup can be seen in Figure 4.18. The following components can be distinguished:

- **ABB IRB 1200-5/0.9 and IRB 1600-10/1.45 robots**: The two robots to which the subsystems are connected. The IRB 1200 is responsible for pick-and-place tasks whereas the IRB 1600 is equipped with the fastening tools.
- **Parallel gripper**: The IRB 1200 is equipped with a 240 mm wide parallel gripper for pick-and-place tasks.
- **Qdos 30 peristaltic pump**: The peristaltic pump is responsible for pumping of the adhesive to the nozzle.
- **Rodac RC3460 screwdriver**: The Rodac screwdriver is pneumatically controlled and attached to the IRB 1600.
- **AMB (Kress) 1050 FME-P milling motor**: The milling motor has its own stationary location.

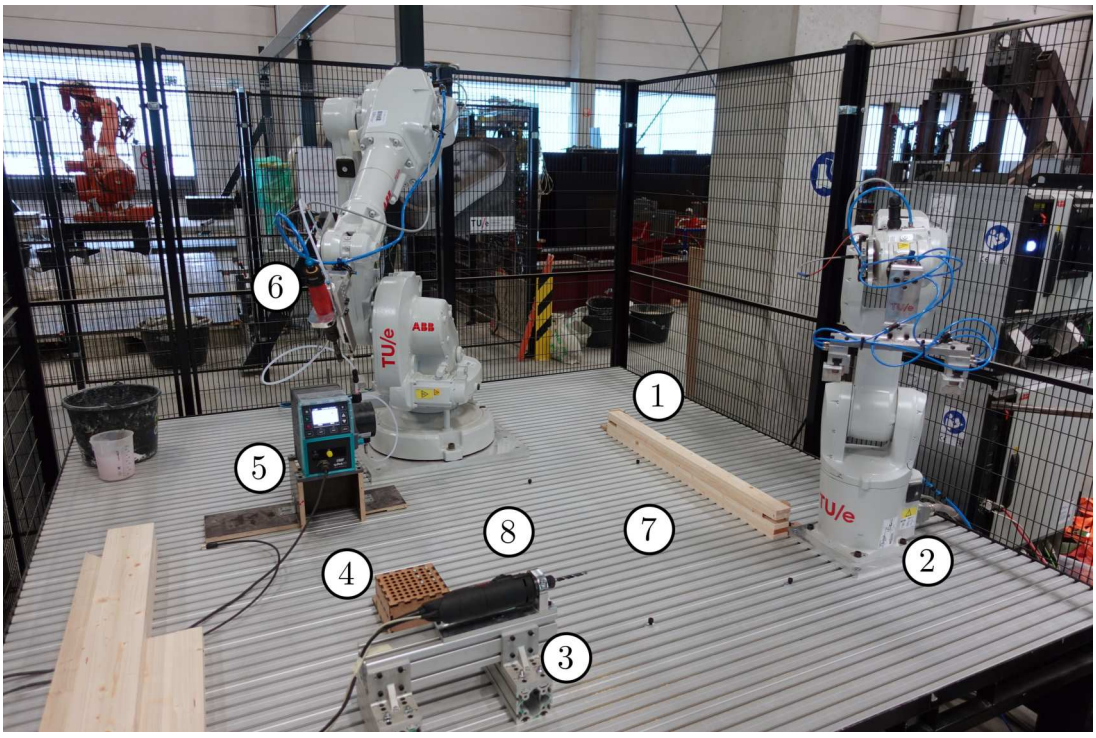

Figure 4.18: The complete robotic setup to fabricate shear connections.

In the robotic setup in Figure 4.18 the following subsystems and locations can be distinguished:

1. Pickup location of the timber members, which are vertically stacked in order of placement.
2. IRB 1200 robot equipped with a parallel gripper responsible for pick-and-place actions.
3. The stationary drilling station for the AMB milling motor.
4. Pickup location of the screws.
5. Adhesive dispensing system using the Qdos peristaltic pump.

6. IRB 1600 robot that is responsible for all fastening tasks, with a dedicated end-effector for both gluing and screwing.
7. Work object location where the truss elements are fabricated.
8. Reorientation location where the members can be temporarily placed when the gripper needs to be relocated.

The pickup location of the timber members is shown in Figure 4.19. The members are stacked vertically in order of appearance. The MDF brackets are calibrated and ensure that the members are always aligned properly.

Figure 4.19: Pickup location of the timber members.

The parallel gripper is shown in Figure 4.20, it consists of the following components:

1. MDF backstop blocks prevent the timber piece from being pushed too far in the gripper (e.g. when being drilled). The timber members are gripped so that there is 3 mm of free vertical space left.
2. The parallel gripper is spaced 240 mm apart. The brackets are aligned such that there is 4 mm of free horizontal space left.
3. The parallel gripper is operated pneumatically. The pneumatic system is connected via a relay, which can be controlled using a digital signal.

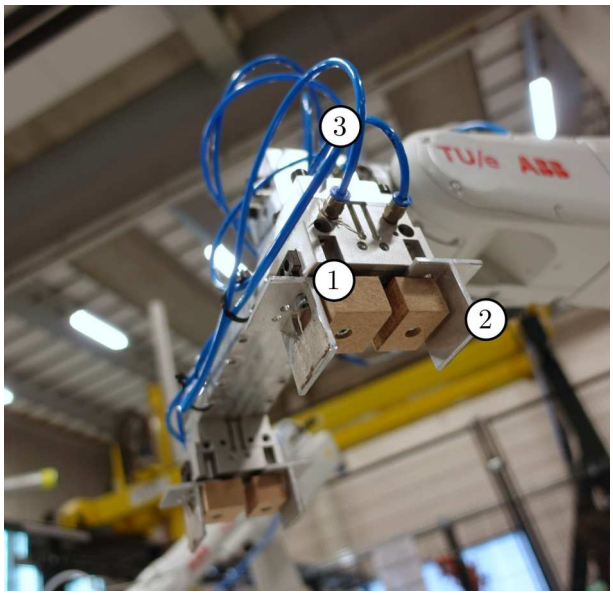

Figure 4.20: Parallel gripper setup.

4.2.1 Adhesive Dispensing

The adhesive dispensing system is shown in Figure 4.23, the following components can be distinguished:

1. **Qdos 30 peristaltic pump**: A peristaltic pump has been chosen, of which the operating principle is shown in Figure 4.21. These pumps are capable of handling relatively high viscosities, a characteristic frequently encountered with adhesives. Given that the fluid remains entirely separate from the pump and is fully contained within the tubing, maintenance is straightforward and damage to the pump itself is uncommon. Moreover, peristaltic pumps are known for their precise metering capabilities, a crucial feature for achieving accurate control over the quantity of adhesive dispensed, essential for ensuring proper connections. Furthermore, peristaltic pumps are self-priming eliminating the necessity for additional equipment, and they can run dry without damaging the pump.

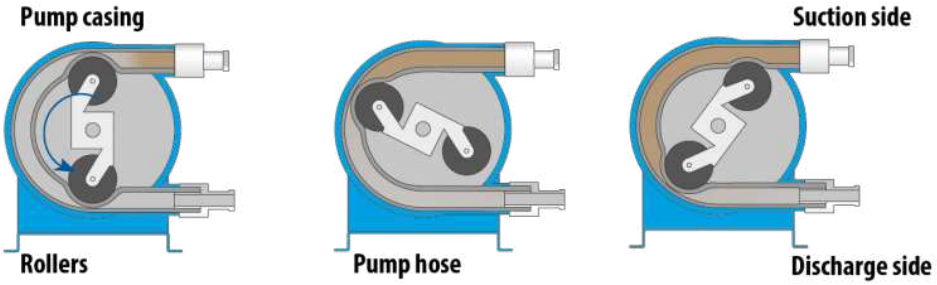

Figure 4.21: A peristaltic pump operates on the following principle: Multiple rollers rotate to compress the internal tubing. In doing so, they create a separation between the suction and discharge sides. When the pressure is released and the tube returns to its initial state, a vacuum is generated, drawing the fluid through the system ("Tapflo", n.d.).

2. **PROFIBUS M12 input connector**: The peristaltic pump can be controlled using digital or analog signals. These signals are provided by the IMPACT67 I/O system, which is controlled by the RAPID code. With a digital signal, the pump can be activated or deactivated at a manually defined speed. Alternatively, with an analog signal, it is possible to directly control the pump flow rate within a 4-20 mA range, which correlates directly with the minimum and maximum flow rates of the pump.

3. **Nozzle**: A custom 3D-printed nozzle is used, which matches the tubing diameters so that it ensures proper output flow. It includes a printed G1/8 thread to which a FESTO QS-G1/8-4 connector can be connected which in turn connects to the 4 mm tubing. A single opening is chosen, as the intended application is on a small scale. For larger-scale applications, more complex nozzles can be designed with multiple openings or additional features to effectively distribute the adhesive. The nozzle and its dimensions is shown in Figure 4.22. For the robotic setup a longer version is printed, shown in Figure 4.22c, as it is tuned to the length of the screwdriver and the end-effector.

(a) Dimensions (b) Nozzle (c) Long nozzle

Figure 4.22: The 3D-printed dispensing nozzle.

Figure 4.23: Adhesive dispensing subsystem.

The amount of adhesive dispensed per area ρ_{a} is based on the system parameters, which must meet the requirements as specified by the adhesive supplier ρ_{req}. To control the dispensed adhesive, the parameters of the dispensing process shown in Figure 4.24 must be determined. This results in the following condition:

$$\rho_{\mathrm{req,min}} \leq \rho_{\mathrm{a}} = \frac{Q}{v\,s} \leq \rho_{\mathrm{req,max}} \tag{4.6}$$

where
- ρ_{a} is the adhesive dispensed per area [g/mm^2]
- Q is the system flow rate [g/s]
- v is the robot speed [mm/s]
- s is the adhesive spread [mm]
- ρ_{req} are the supplier requirements [g/mm^2]

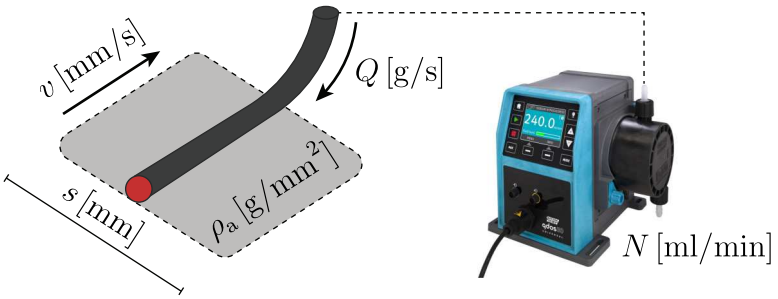

Figure 4.24: The parameters of the adhesive dispensing process.

The system flow rate Q is directly influenced by the pump rate N. However, due to the high viscosity of the adhesive, not all pump rates are capable of effectively transferring the adhesive. Consequently, the dispensed adhesive exhibits discontinuities, resulting in gaps. Tests are conducted at various pump rates to measure coverage, which is considered 100% when a continuous adhesive line without gaps is dispensed. The results are shown in Figure 4.25 and provided in Appendix A.1. It can be seen that for a pump rate of $N = 250$ ml/min or higher 100% coverage is achieved. Therefore, the system pump rate is set at $N = 250$ ml/min. Higher pump rates are avoided to reduce system wear.

Due to the adhesive's higher viscosity, the pump rate N is not equal to the system flow rate Q. Therefore, measurements were conducted to determine the system flow rate Q at the selected pump rate of $N = 250$ ml/min. This yielded a system flow rate of $Q = 0.15$ g/s, of which the results are provided in Appendix A.2.

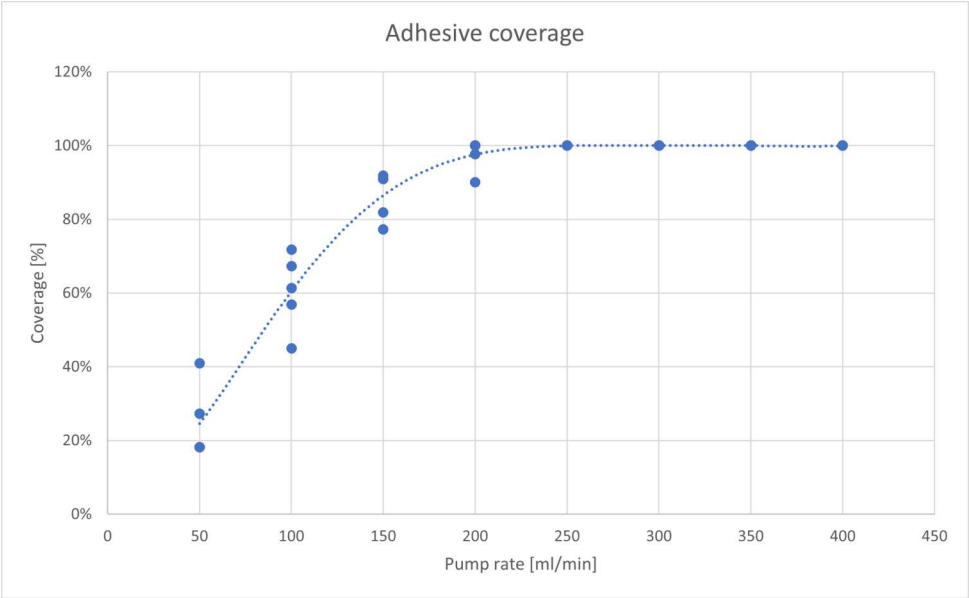

Figure 4.25: The coverage of adhesive lines at varying pump rates, where a 100% coverage means that no gaps are observed in the disposed adhesive lines.

For a constant flow rate Q, the adhesive spread s is depends only on the robot speed v. Higher speeds lead to less material being dispensed, resulting in reduced spread. For the selected pump speed of $N = 250$ ml/min, the adhesive spread is measured at various robot speeds. The results are shown in Figure 4.26 and provided in Appendix A.3. A curve is fitted to the measurements, yielding the following relationship:

$$s(v) = 61.322\, v^{-0.245} \tag{4.7}$$

where s is the adhesive spread [mm]
v is the robot speed [mm/s]

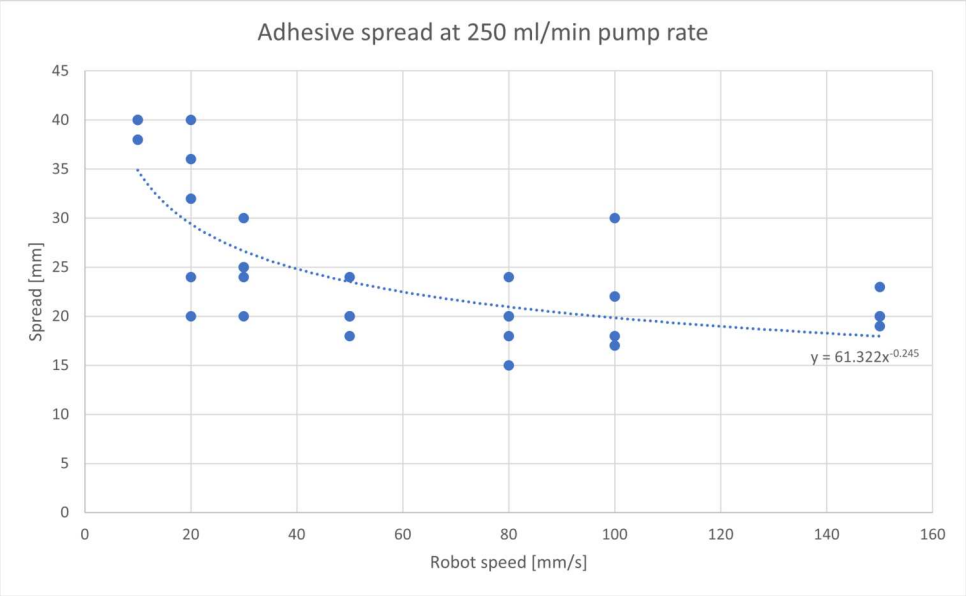

Figure 4.26: The spread of an adhesive line after being clamped when disposed at a constant pump rate of 250 ml/min but with varying robot speeds.

The only variable system parameter is the robot speed, which must be adjusted to meet the specified adhesive requirements. Rewriting Equation (4.6) and substituting Equation (4.7) yields the following definition:

$$v = \frac{Q}{\rho_{\text{req}}\, s} = \frac{0.15}{\rho_{\text{req}}\, 61.322\, v^{-0.245}} \tag{4.8}$$

$$v = \sqrt[0.755]{\frac{0.15}{61.322\, \rho_{\text{req}}}} \tag{4.9}$$

In the experimental setup Griffon D3 carpenter's glue will be used, which requires 5-7 m^2/kg of adhesive as provided by Appendix E.3. The average value of 6 m^2/kg is adopted and converted to grams per square millimeter [g/mm^2]. This is inserted in Equation (4.9), giving a robot speed of $v = 33.55$ mm/s. Inserting in Equation (4.7) gives a spread of $s = 25.93$ mm/s.

The adhesive pattern employs either perpendicular or parallel lines to the timber. Perpendicular lines can be chosen for the reason that it allows air to escape from multiple sides easier, thereby reducing the possibility of air gaps in the connection. The parallel lines are spaced using the spread determined before, of which 80% of the calculated spread is used to achieve partial overlap which ensures adequate coverage. This yields a spread of $s = 20$ mm/s. In situations where exactly 20 mm spacing is not possible, the spacing is rounded down, resulting in slightly more overlap. The adhesive pattern using this approach is shown in Figure 4.27.

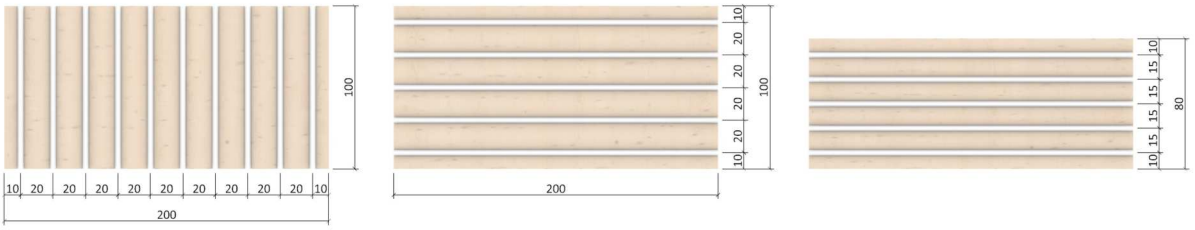

Figure 4.27: The perpendicular and parallel adhesive pattern using a $s = 20\,\text{mm}$ spread.

4.2.2 Drilling

The predrilling is performed using the AMB Kress 1050 FME-P milling motor. This is used to predrill clearance holes in the upper timber members. The milling motor is oriented horizontally in a custom-made station, which is shown in Figure 4.28. The robot approaches the drill horizontally at a speed of 2 mm/s, it predrills the clearance holes using an $\varnothing = 8\,\text{mm}$ drill. The following components can be distinguished:

1. The AMB milling motor is clamped in the stationary station and operated at a constant speed of 3500 RPM [rev/min].
2. A timber drill with a diameter of 8 mm is used.
3. The backstops in the gripper prevent the timber from slipping further in the gripper. This ensures that the drilling depth is equal in all situations, and that the timber member cannot tilt with respect to the other side of the gripper.
4. Preferably, holes are drilled in between the two grippers. However, for holes at the ends of the members this is not possible, as this would mean holes must be drilled at the location of the gripper. For these situations, holes are drilled outside of the gripper, with a safety offset of 20 mm. It has been tested that up until an offset of about 100 mm the gripper is capable of drilling the holes without the timber member moving. However, beyond this distance the timber member is pushed out of the grippers.

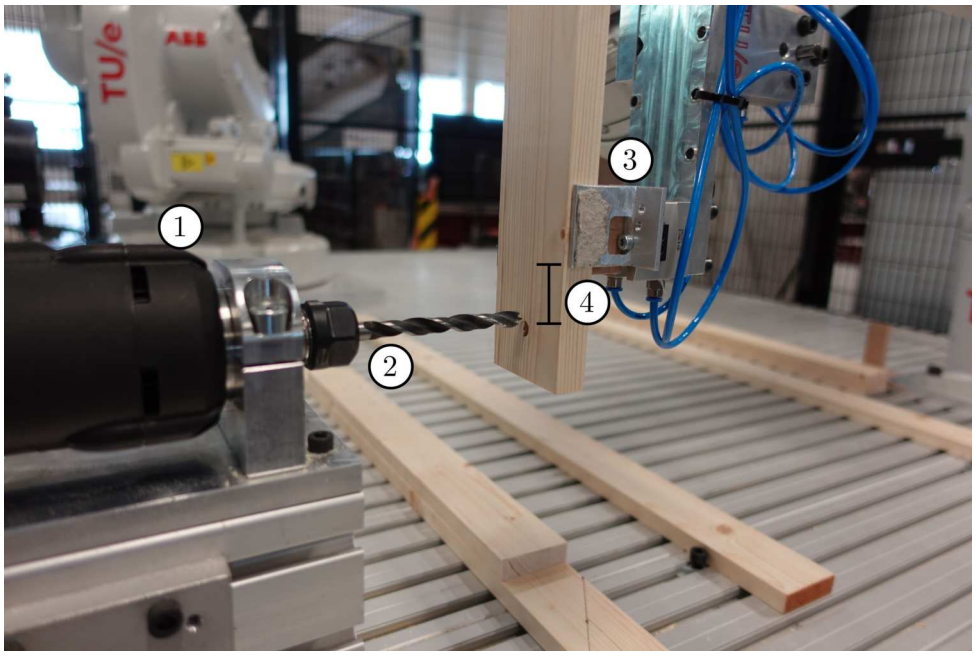

Figure 4.28: The station for the milling motor.

As the truss case study requires holes mostly at the outer ends of the members, the gripper must be re-positioned multiple times to adhere to the 20 mm offset. This causes that, for long members, relatively large turning radii are required, as shown in Figure 4.29. To do this safely, a turning point in the middle of the open space is used. Consequently, the robot first carefully moves to that location, then re-orients the gripper for the next operation, and only after that starts moving in that specific direction.

Figure 4.29: A long member gripped at one of its ends.

4.2.3 Screwing

Screwing uses the system developed by Vrenken, 2023 as a basis. The pickup location remains unchanged, and is shown in Figure 4.30. It is important to choose screws that have a sloped head so that the screws center themselves in the hole. This makes pickup more accurate. During pickup, the screwdriver moves slowly towards the screw, and rotates 90° so that the screw can snap onto the magnetic bit holder properly.

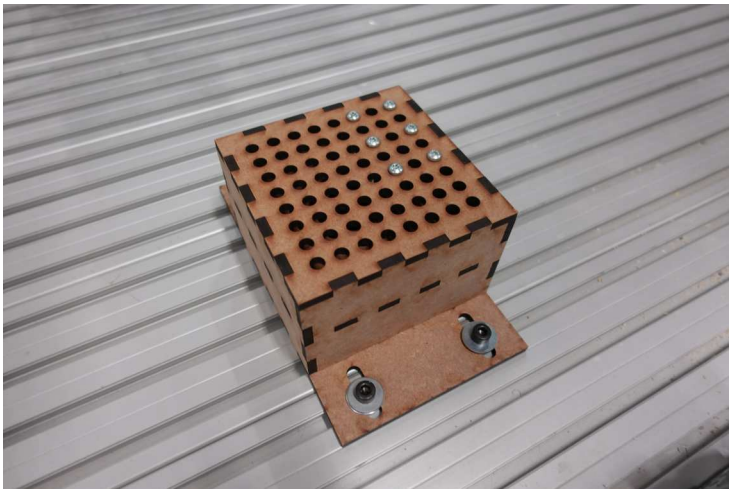

Figure 4.30: Screw pickup location.

The end-effector used combines the dispensing nozzle and the screwdriver, and is shown in Figure 4.31. It consists of the following components:

1. Magnet bit holder suitable for large screws.
2. Pneumatically (7 bars) activated screwdriver that is operated at an RPM of 550 rev/min.
3. AC006 capacitive sensor with a range of 2 mm.
4. The sensor provides a digital input that is used to detect the final screwing distance and stops the screwing process.
5. The dispensing nozzle is located next to the screwdriver, and is located in height above the screwdriver and sensor.

After picking up the screw, the end-effector moves to the screw destination. The end-effector moves down slowly until the screw is just above the timber. Next, the end-effector moves down with a constant speed calculated using

$$v = \frac{\text{RPM}}{60} \cdot l_{\text{lead}} = \frac{550}{60} \cdot 0.55 \approx 5 \text{ mm/s} \tag{4.10}$$

where RPM is the screwdriver speed [rev/min]
l_{lead} is the screw lead [mm]

The height of the sensor is calibrated so that it sends out a signal when the screw's head is touching the upper timber member. Once the signal is sent, the robot stops its movement and moves back upward. During this whole process, the parallel gripper keeps the timber piece gripped so that the members do not start rotating and that while moving back upwards the pieces are not pulled upwards due to the strong magnet.

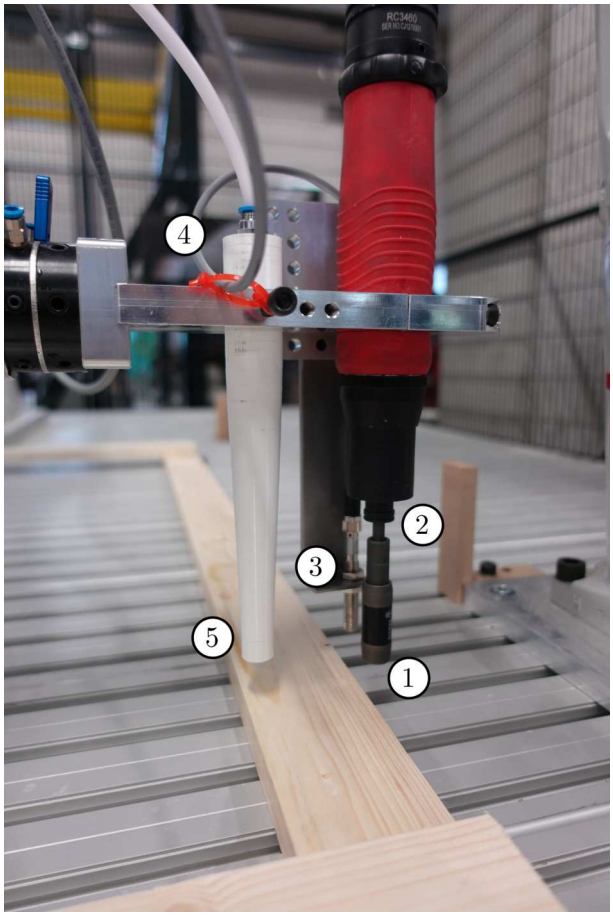

Figure 4.31: Fastening end-effector with the screwdriver and the nozzle.

4.2.4 Robot Collaboration

The robots collaborate using MultiMove operations, where one robot waits until the other one is finished with its task. This is achieved using waiting signals that are only send when a robot is fully done with its current operation. This ensures that the robots do not clash or interfere with each other, and the tasks are performed sequentially. All the steps presented in the previous sections are combined in a continuous process, of which all the individual steps are shown in Figure 4.32. The process currently requires 35 minutes to complete. However, there are many aspects of the process that can be improved to increase the fabrication speed.

Before the program is executed using the physical robots, digital checks have been performed using the ABB RobotStudio software. In these checks, singularity errors or restricted movements are removed. Collision checks between robots, the surroundings, and the work pieces are performed as well.

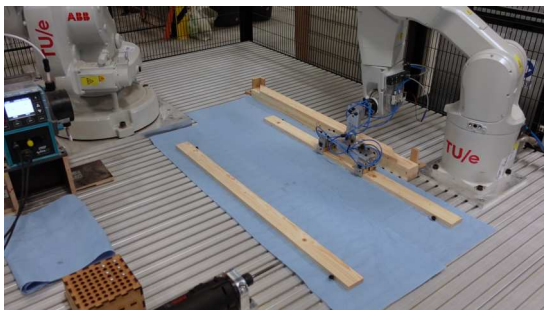

(a) Place bottom chords

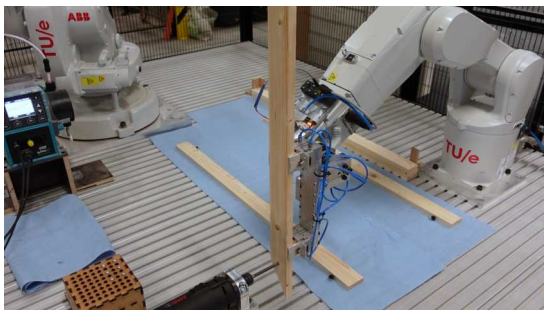

(b) Drill all member holes

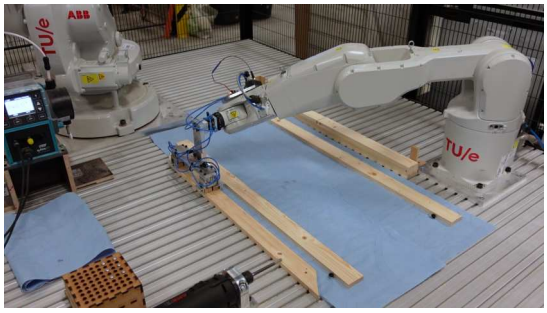

(c) Reorient members where required

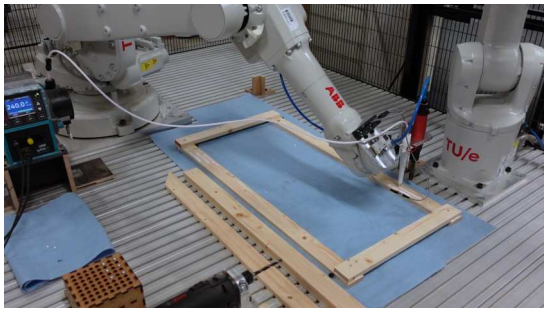

(d) Glue verticals and diagonals

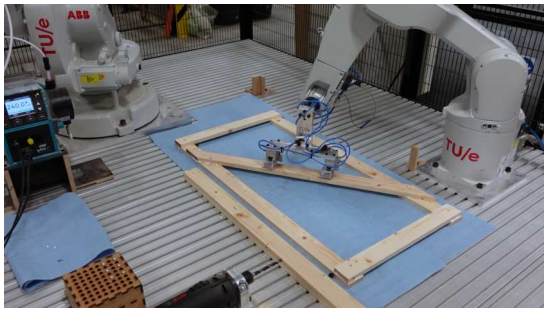

(e) Place verticals and diagonals

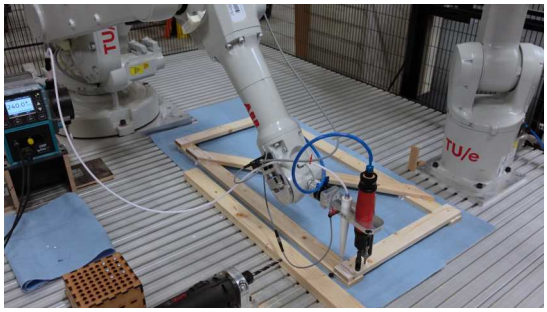

(f) Glue upper chords

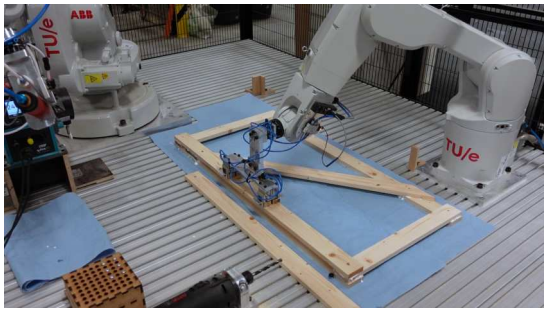

(g) Place and hold upper chord

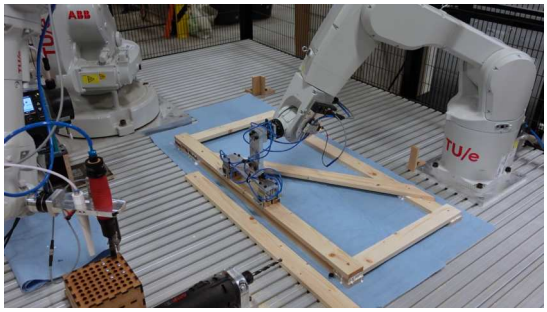

(h) Pick up screw

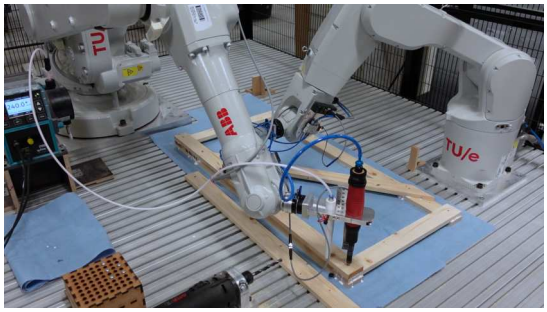

(i) Drill screws

(j) Final product

Figure 4.32: Steps in the robotic fabrication process.

4.3 Experimental Setup

The experimental setup to evaluate the robotic fabrication process tested various samples, each addressing different aspects of the fabrication process. Each sample underwent testing five times. Table 4.1 presents the tests conducted and the parameters investigated.

Initially, the robotic dispensing process was examined. In this phase, the PVAc was diluted with 5% water, as tested in sequence R2. Subsequently, the diluted PVAc was utilized in the robotic dispensing process, employing the method outlined in Section 4.2.1.

Following this, clamping methods for applying curing pressure using screws were investigated in tests R4 and R5. Test R4 involved screws with only predrilled holes, while test R5 explored the use of clearance holes in the upper members. Both tests were conducted without the screws, as their sole purpose was to introduce clamping pressure. Finally, in test R6, the screws were left in during testing to observe the interaction between the adhesive and screws.

Table 4.1: The different test sequences and the investigated parameters.

Description	ID	Adhesive	Application method	Clamping	Test situation
Benchmark	R1	Regular	Spread out using a comb	F-clamps	Normal
Watered-down	R2	5% watered down	Spread out using a comb	F-clamps	Normal
Robotic dispensing	R3	5% watered down	Robotic; linear pattern	F-clamps	Normal
Predrilled screw clamping	R4	Regular	Spread out using a comb	Screws; predrilled	Normal
Clearance hole screw clamping	R5	Regular	Spread out using a comb	Screws; clearance holes	Normal
Secondary load path	R6	Regular	Spread out using a comb	F-clamps	Including screws

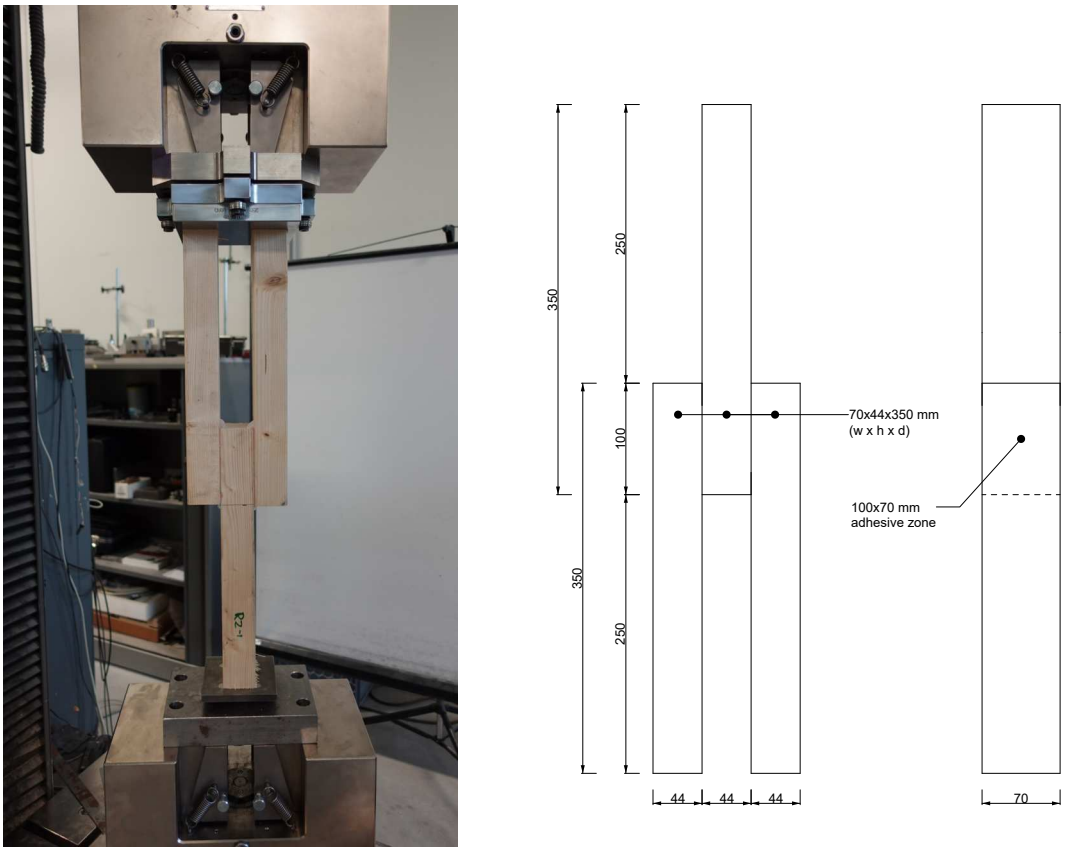

(a) Setup (b) Dimensions

Figure 4.33: The experimental setup used and sample dimensions.

The experimental setup is shown in Figure 4.33, of which the dimensions of the samples are given in Figure 4.33b. The samples are hinged on both sides using ball hinges. The middle member is placed on the bottom plate and the hinges allow the sample to center. The (compressive) load is applied using displacement control at a rate of 1 mm/min.

All the samples are prepared using an identical process, the only differences are the ones described in Table 4.1. The procedure is as follows:

- The adhesive areas are sanded using 150P grit paper.
- These areas are made dust free using a dry cloth.
- Using a damp cloth the areas are cleaned.
- The adhesive is applied one-sided to each joint.
- The three members are aligned using a guide to ensure exact overlap dimensions.
- The members are left undisturbed for at least 24 hours at room temperature. The clamping measures are not removed during this time.

The robotic dispensing of the adhesive in set R3 is performed using the developed method in Section 4.2.1. The adhesive is applied perpendicular to the grain, as shown in Figure 4.34.

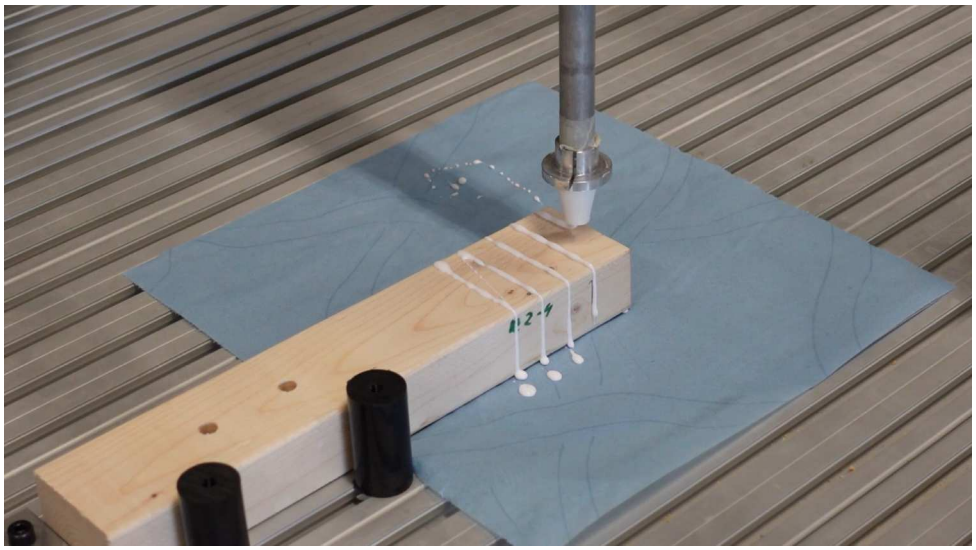

Figure 4.34: Robotic dispensing of the adhesive.

The sample sets where screw clamping is utilized to introduce the clamping pressure use Dynaplus 6x120 mm screws with a root diameter of 4 mm. These screws are long enough to penetrate the full assembly, and have a one-third smooth shank, which is shown in Figure 4.35a. Ideally, screws with a smooth shank of at least 88 mm are used, as these only screw in the bottom member. However, this ratio of thread to smooth shank for a 120 mm was not common and therefore this alternative was chosen. For the screws two different predrilled holes are used: For R4 predrilled holes of 4 mm are used, which is equal to the inner thread of the screws. For R5 clearance holes of 7 mm are used which is 1 mm larger than the smooth shank. These situations are shown in Figure 4.35b.

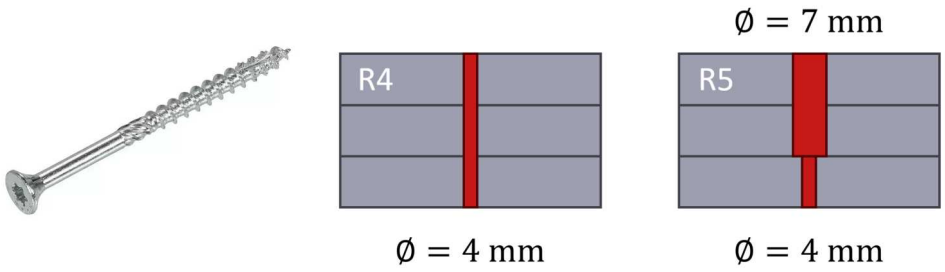

(a) Screws (b) Predrilled holes

Figure 4.35: Dynaplus $\varnothing = 6$ mm and $\varnothing_r = 4$ mm screws used and the corresponding predrilled holes.

The analytical stresses are derived from the model presented by Her and Chan, 2019. The relationships for the shear and peel stresses are shown in Equations (4.11) and (4.12). The scheme is shown in Figure 4.36.

$$\begin{aligned}\tau(x) = {} & K_1 + K_2 \sinh(m_2\, x) + K_3 \cosh(m_2\, x) + \\ & K_4 \sinh(\mathrm{Re}\{m_3\}\, x) \cos(\mathrm{Im}\{m_3\}\, x) + K_5 \sinh(\mathrm{Re}\{m_3\}\, x) \cos(\mathrm{Im}\{m_3\}\, x) + \\ & K_6 \cosh(\mathrm{Re}\{m_3\}\, x) \cos(\mathrm{Im}\{m_3\}\, x) + K_7 \cosh(\mathrm{Re}\{m_3\}\, x) \sin(\mathrm{Im}\{m_3\}\, x)\end{aligned} \tag{4.11}$$

$$\begin{aligned}\sigma(x) = {} & A_1 \sinh(m_2\, x) + A_2 \cosh(m_2\, x) \\ & + A_3 \sinh(\mathrm{Re}\{m_3\}\, x) \cos(\mathrm{Im}\{m_3\}\, x) + A_4 \sinh(\mathrm{Re}\{m_3\}\, x) \sin(\mathrm{Im}\{m_3\}\, x) \\ & + A_5 \cosh(\mathrm{Re}\{m_3\}\, x) \cos(\mathrm{Im}\{m_3\}\, x) + A_6 \cosh(\mathrm{Re}\{m_3\}\, x) \sin(\mathrm{Im}\{m_3\}\, x)\end{aligned} \tag{4.12}$$

The constants of these equations can be found by solving the boundary conditions. The parameters for the experimental setup and the corresponding constants are given in Table 4.2.

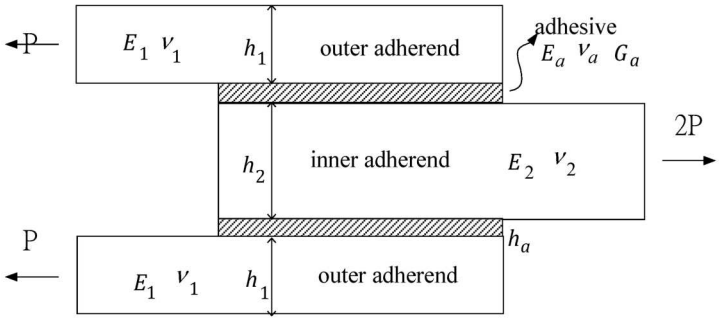

Figure 4.36: Analytical model scheme and parameters (Her and Chan, 2019).

Table 4.2: Geometry and material properties and solved shear and peel stress constants.

Property	Symbol	Value	Unit
Timber elasticity	$E_1 = E_2$		N/mm^2
Adhesive elasticity	E_a		N/mm^2
Timber Poisson's ratio	ν	0.3	
Adhesive Poisson's ratio	ν	0.4	
Thickness	$h_1 = h_2$	44	mm
Width	w	70	mm
Adhesive thickness	h_a	0.1	mm
Shear stress constants	K_1	3.51E-13	
	K_2	1.35E-42	
	K_3	4.05E-42	
	K_4	-6.03E-04	
	K_5	-1.93E-03	
	K_6	-1.81E-03	
	K_7	-6.43E-04	
Peel stress constants	A_1	1.52E-43	
	A_2	5.05E-44	
	A_3	2.42E-04	
	A_4	-1.97E-03	
	A_5	7.95E-05	
	A_6	-1.97E-03	

The results of the experiments are compared with the analytical as well as FEM results, which is shown in Figure 4.37. The model is built up as follows:

- It is a 3D continuum model using HEX/brick elements.
- The adhesive uses quadratic interpolation and the bricks have 20 nodes. In the timber less precision is required, so 8-node brick elements are used. The intermediate zone in the timber near the adhesive is also quadratic.
- The sample is symmetric, so the model is cut in half and the corresponding boundary conditions are applied at the cut section.
- The side of the single member is restrained in X, Y and Z. The side of the double members is only restrained in X and Y and can slide in Z.
- The load is introduced as a surface pressure in this Z direction.
- The timber elasticity is determined using additional tests.
- The adhesive properties are derived from the DLJ experiment results.

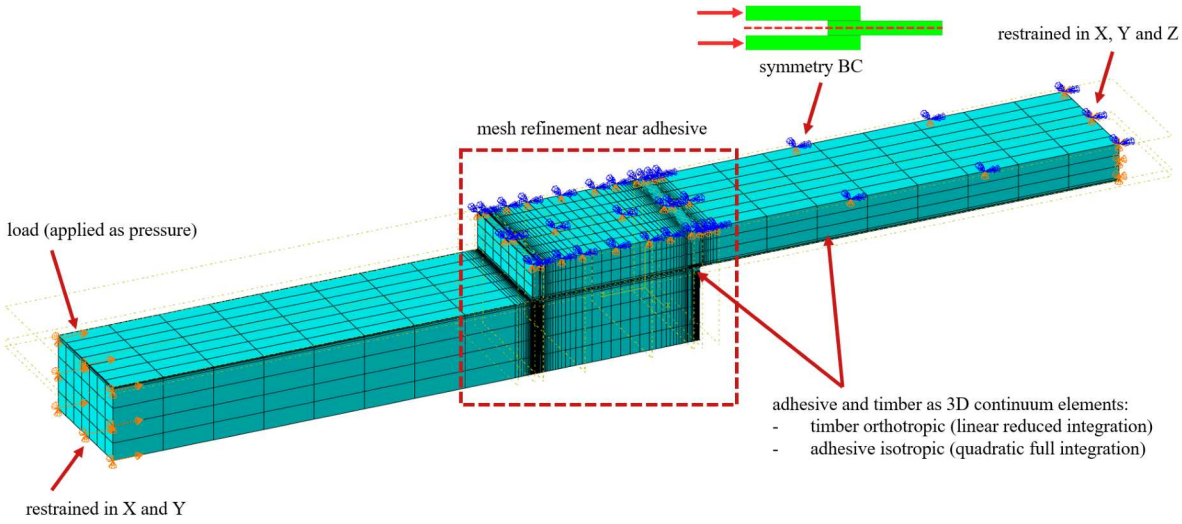

Figure 4.37: The 3D continuum FEM model to assess stresses in the adhesive layer. The dimensions are equal to that of the samples used, shown in Figure 4.33b.

An explorative study is performed for loads at an angle, which is the situation as in a truss node. The model used for these cases is shown in Figure 4.38 which is under a 45° angle. The only difference with respect to the parallel joint is that the outer member is restrained at its both ends in X, Y, and Z direction.

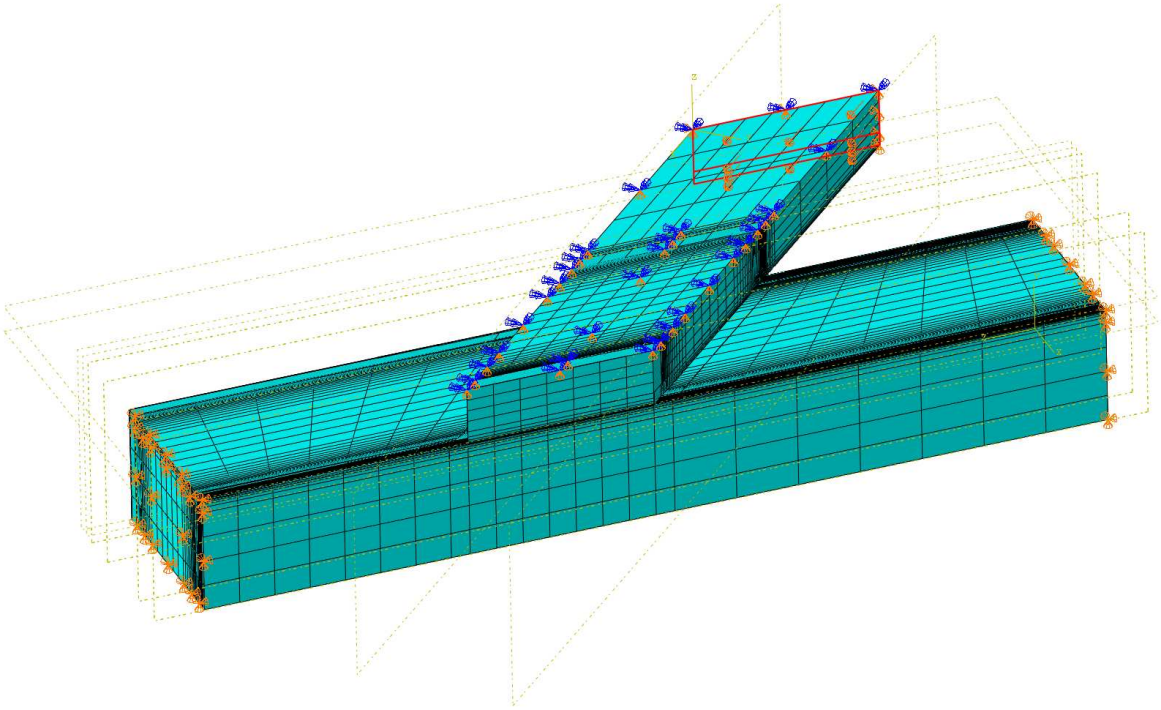

Figure 4.38: The 3D continuum FEM model for a 45° angled joint.

To determine the elasticity of the timber parallel to the grain, additional compressive tests parallel and perpendicular to the grain are performed. The tests are performed conform the procedure specified by EN 408 (CEN, 2012). The dimensions of the timber are slightly adjusted

as this was the available timber stock. The members have a cross section of 44x70 mm and a length of 200 mm. The strain is measured using LVTD sensors over a length of 100 mm on both sides of the member. The experimental setup is shown in Figure 4.39.

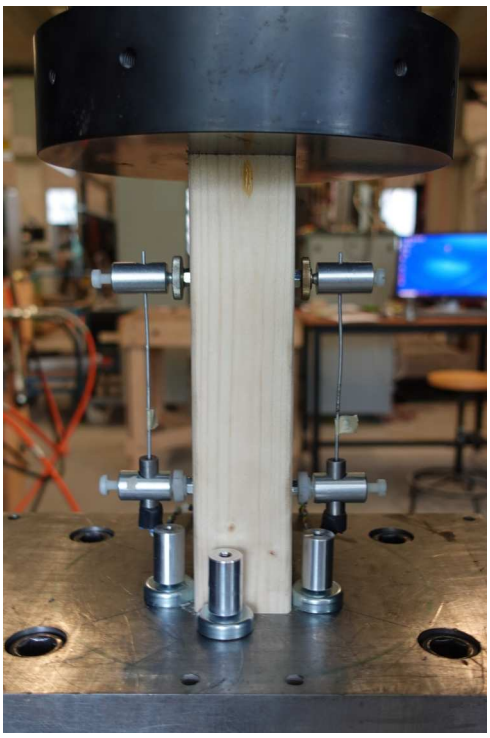

Figure 4.39: Setup to determine the compressive elasticity parallel to the grain.

The load is introduced at 6 mm/min, after which the elasticity is determined using the 10% and 40% loads of the maximum load at failure. The compressive elasticity is calculated using

$$E = \frac{\sigma_{40\%} - \sigma_{10\%}}{\varepsilon_{40\%} - \varepsilon_{10\%}} \tag{4.13}$$

The corresponding elasticities of the seven samples are listed in Table 4.3. This results in an average elasticity of $E_{c,0} = 13779.71$ N/mm^2. This is the elasticity used in the FEM model.

Table 4.3: Compressive elasticity of the timber batch.

Sample	Parallel compressive elasticity	Unit
C1	15464.40	N/mm^2
C2	12843.47	N/mm^2
C3	15180.23	N/mm^2
C4	10218.08	N/mm^2
C5	14256.79	N/mm^2
C6	14840.80	N/mm^2
C7	13654.25	N/mm^2
Mean	13779.71	N/mm^2

The shear modulus of the adhesive is determined using the following relationship:

$$G_{\mathrm{a}} = \frac{F_{40\%} - F_{10\%}}{d_{65\%} - d_{40\%}} \tag{4.14}$$

The values are taken from the average load-displacement result of the double lap experiment. The range is chosen between 40% and 65% of the maximum load as it is most representative of the behavior. Especially the lower limit is increased, as the initial part of the graph is not fully representative due to the initial settlement. The region used for this is shown in Figure 4.40.

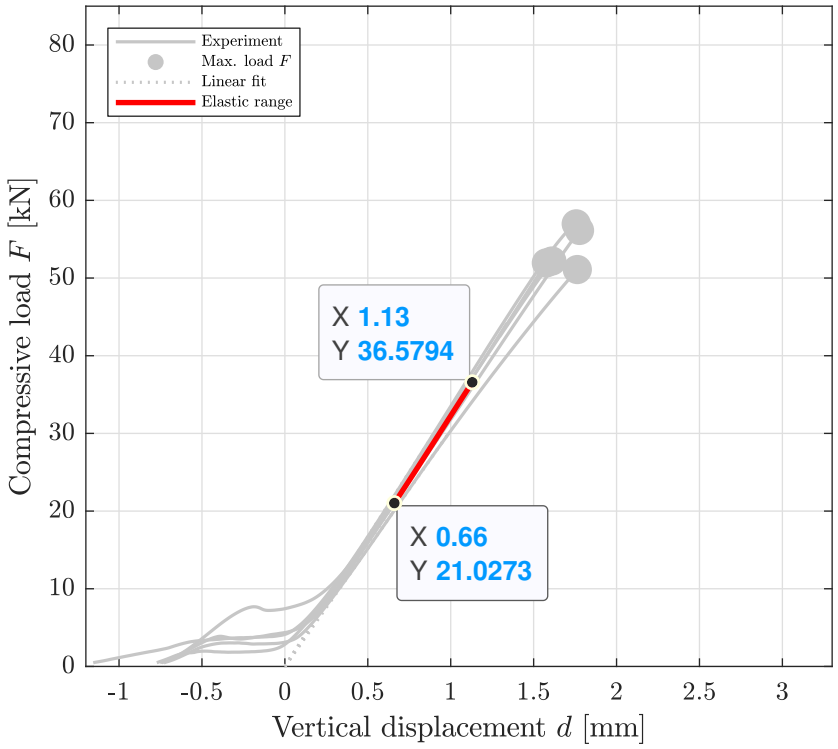

Figure 4.40: Load-displacement result of double lap joint compressive test and the zone utilized to determine the shear modulus of the adhesive.

Important to consider is that not the full vertical displacement d comes from the adhesive. Part of this is due to the timber compressing. This part is subtracted from the displacement in the determination of the shear modulus. As there is an intermediate zone where the timber is not fully loaded in compression, only 200 mm of the members is considered compressed, which is shown in Figure 4.41. The corresponding vertical displacements attributed to the adhesive d_{a} are shown in Table 4.4.

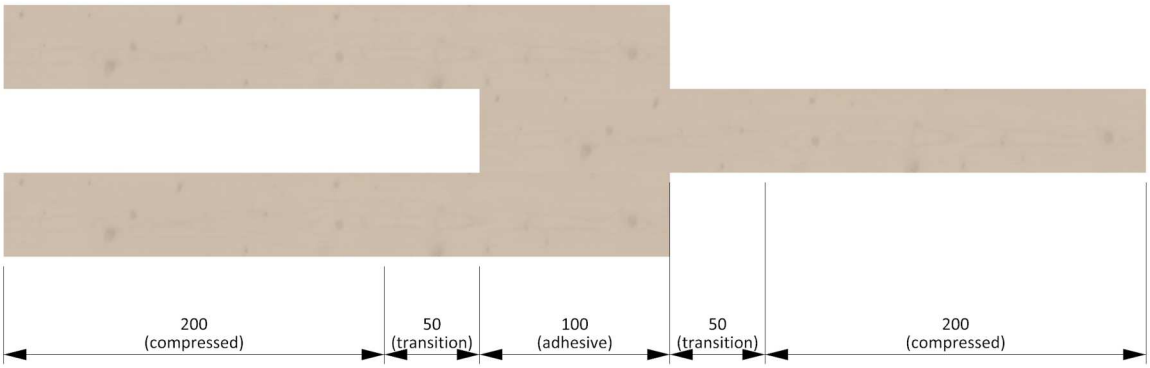

Figure 4.41: Of the timber, 200 mm is considered compressed on both sides as the last 50 mm near the adhesive acts as a transition zone where the stresses are not purely axial.

Table 4.4: Actual adhesive vertical (shear) displacement d_{a} after subtraction of the compressed timber contributions.

Load F [kN]	Displacement d [mm]	Stress σ [N/mm^2]	Strain ε [-]	Compression ΔL [mm]	Adhesive displacement d_{a} [mm]
21.03	0.66	7.10	0.00052	0.21	0.45
36.58	1.13	11.54	0.00084	0.34	0.79

The shear modulus of the adhesive is

$$G_{\mathrm{a}} = \frac{F_{40\%} - F_{10\%}}{d_{65\%} - d_{40\%}} = \frac{36.58 - 21.03}{0.45 - 0.79} = 45.59 \text{ kN/mm}^2 \tag{4.15}$$

The elasticity of the adhesive follows from

$$E_{\mathrm{a}} = 2\,G_{\mathrm{a}}\,(1 + \nu) = 2 \cdot 45.59 \cdot (1 + 0.4) = 127.65 \text{ kN/mm}^2 \tag{4.16}$$

5 Results

In this section, the various results obtained are discussed. First, the results obtained by utilizing the design toolbox developed in Section 4.1 are presented, focusing on mechanical fasteners and their possible configurations. Second, the experimental results are presented. The results of the shear DLJs are presented in Section 5.2.1 and those of the timber elasticity in Section 5.2.2. Third, the stresses in the DLJs are assesed using analytical and FEM models in Section 5.3. Fourth, the results of a parallel joint are compared to an angled adhesive joint in Section 5.4. Last, the fabricated prototype is presented in Section 5.5.

5.1 Design Toolbox Analysis

Using the design toolbox developed in Section 4.1, various configurations of mechanical fasteners are studied. A selection of parameters is varied to see the effects on the ultimate shear strength.

In Figure 5.1 different fastener groups are compared for a varying overlap length. Three distinct zones can be distinguished:

- Zero shear strength occurs when the overlap length is too small for the fasteners to be placed while also meeting the end distances.
- An increasing shear resistance where the overlap length is sufficient to meet the minimum end distances, but where the group effect causes a reduction in strength. It can be seen that this zone is absent for a single fastener.
- A constant shear strength when sufficient overlap is provided so no group reductions occur.

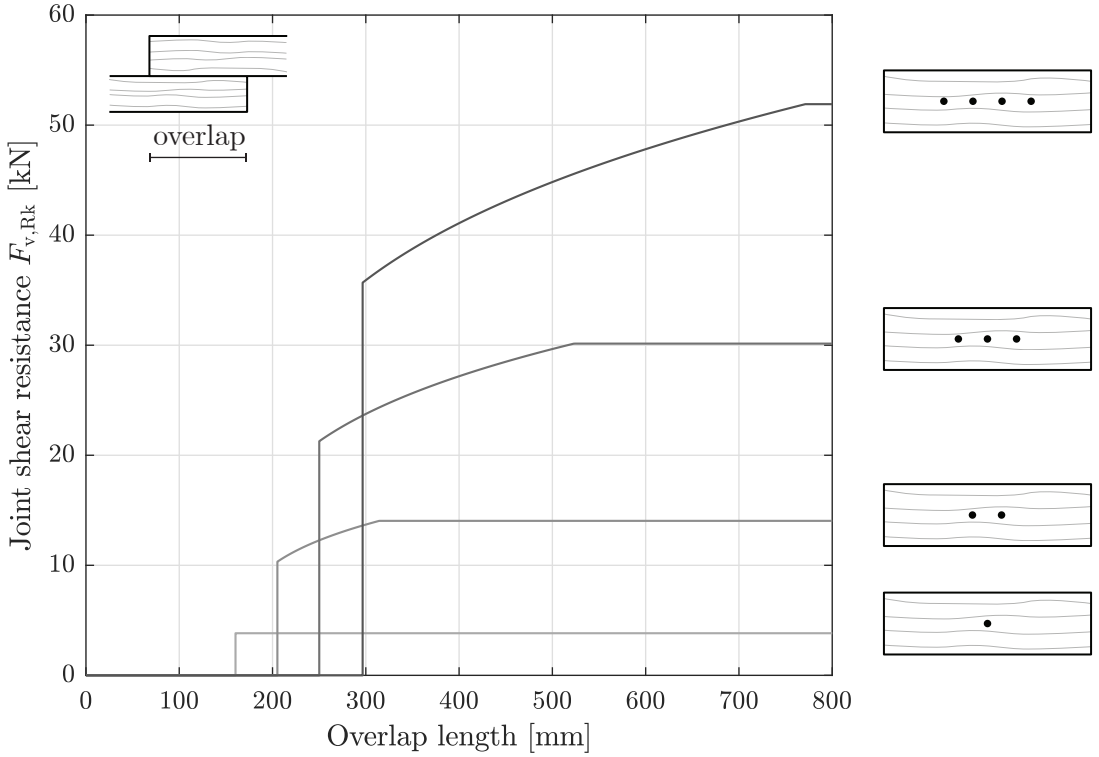

Figure 5.1: SLJ shear resistance for different amounts of fasteners and varying overlap.

In Figure 5.2, SLJs and DLJs are compared where the outer and inner member thickness ratios are varied. This is performed for a variety of fastener configurations. The following can be observed:

- The highest shear resistances are obtained when the member ratio is one.
- Constant shear resistances are observed when fastener failure occurs, while a sloped shear resistance indicates timber embedment failure.
- Depending on the combination of material properties, geometry, and fastener layout, either timber embedment or fastener failure can occur. When only the fastener group is varied while keeping other parameters constant, the failure mode can also shift.
- In case of fastener failure, a SLJ will have halve the strength of a DLJ as there is only one shear plane. For timber embedment failure, the DLJ and SLJ have equal strength as the total member thickness are equal in either joint.
- For joints where the thickness ratio is not equal to one, but for example three, the SLJ reaches a plateau while the DLJ continues to increase in strength. This is because the corresponding failure mechanism for the SLJ is fastener failure. However, the same fastener failure in the DLJ requires twice as much load because there are two plastic hinges instead of one. Consequently, the DLJ has a longer trajectory before failing in fastener failure instead of embedment failure for smaller fastener groups, demonstrating an effect similar to the former point.

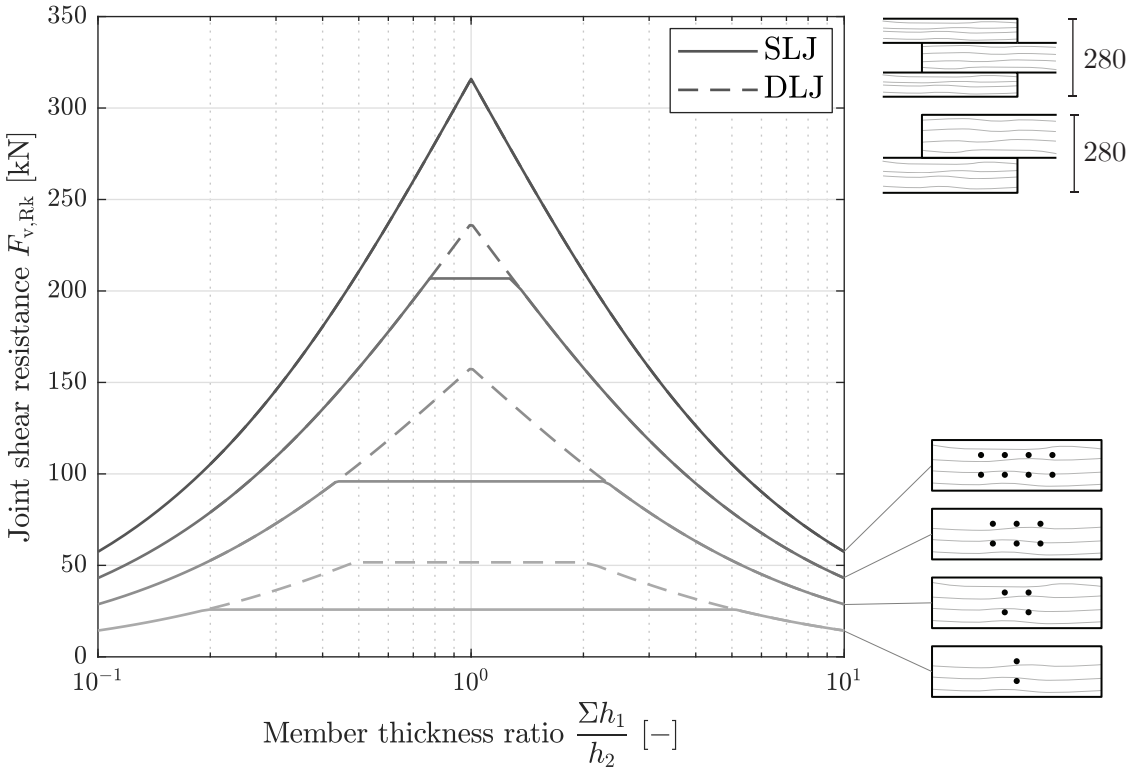

Figure 5.2: SLJ and DLJ shear resistance for different fastener patterns and a varying member thickness ratio.

In Figure 5.3, both a SLJ and DLJ are compared, with the load angle increased by rotating one of the members. This comparison is conducted for various fastener configurations. The following observations can be made:

- For small fastener groups, the load angle has no significant effect, as fastener failure governs in all cases, even when the load is perpendicular to the grain.
- For large fastener groups, it can be seen that by increasing the load angle, the strength of the joint significantly reduces as embedment failure governs. Comparing the strength of a parallel joint to a perpendicular one, the strength is halved.
- For intermediary fastener groups, a combination of the two effects can be observed. Initially, the joint strength remains constant as fastener failure governs. However, as the timber is increasingly loaded perpendicular to the grain, embedment failure becomes governing, leading to a reduction in strength.

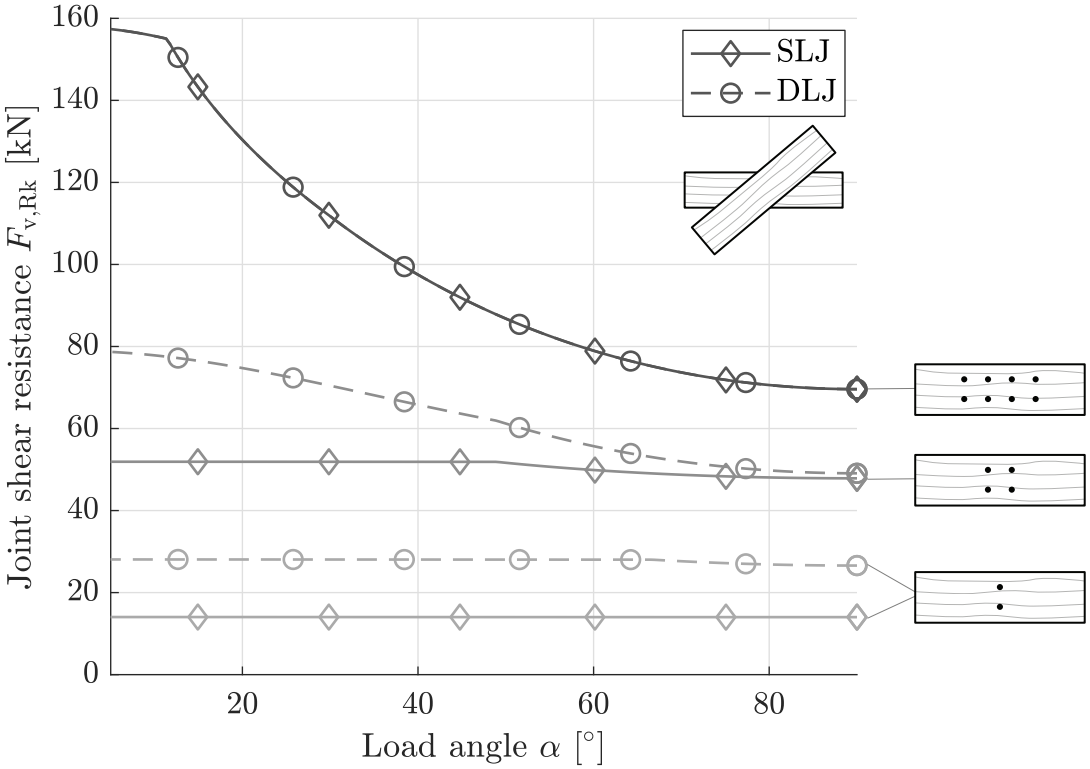

Figure 5.3: SLJ and DLJ shear resistance for different fastener patterns and a varying load angle.

In Figure 5.4, both a SLJ and DLJ are compared with an increasing load angle achieved by rotating one of the members. However, in this scenario, the ends of the timber are not continuous but sawn off, affecting the end distance. This comparison is performed for various fastener configurations. The following observations can be made:

- Due to the sawn end, there is less space for the fasteners. Consequently, the fasteners are spaced closer together, which increases the effects of the group effect. Up until an angle of roughly 30°, this results in a lower shear resistance of the joint compared to the continuous joint.
- At a certain angle, the available area of the joint becomes so small that the fasteners cannot be placed anymore due to spacing requirements. Beyond this point, the shear resistance of the joint is zero because it does not meet the spacing requirements.

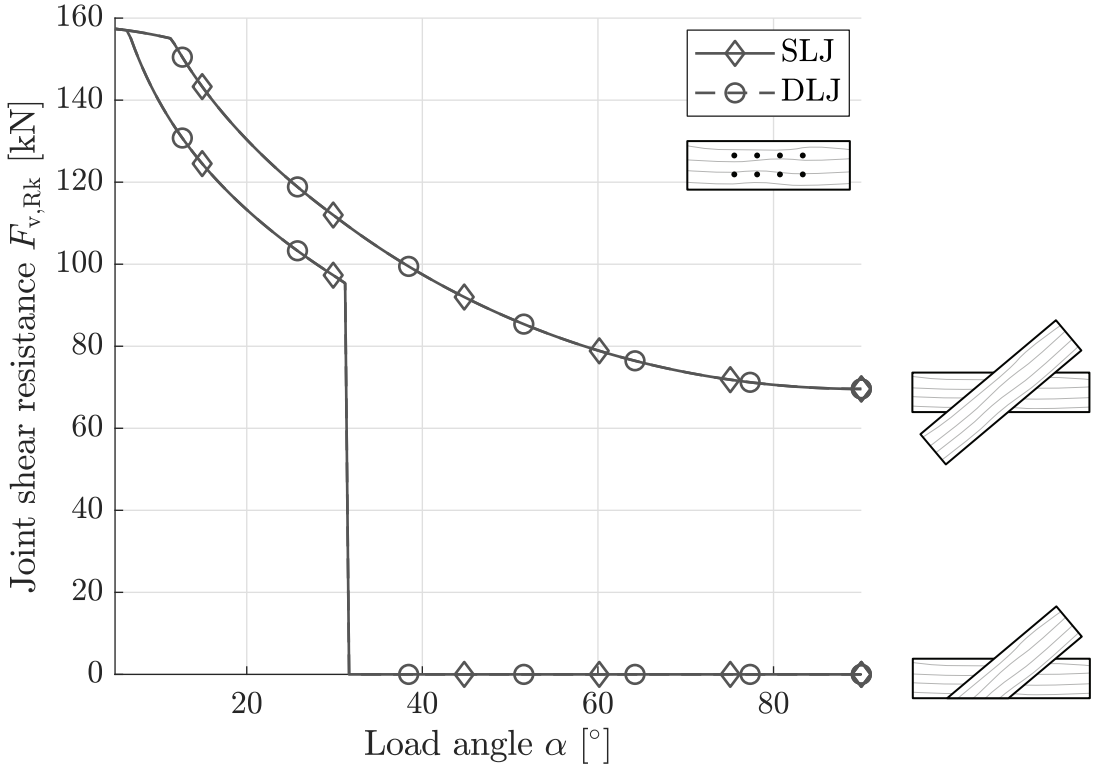

Figure 5.4: SLJ and DLJ shear resistance for different fastener patterns and a varying load angle where the diagonal member is sawn off.

In Figure 5.5, DLJ is assessed at a constant load angle of 45°. The node offset of the diagonal from a vertical member is increased. A low node offset means that the diagonal is very close to a vertical member, whereas it moves away for increasing node offsets. For small node offsets, a significant portion of the diagonal must be sawn off as the vertical and diagonal cannot overlap, affecting the available joint area. This is performed for a variety of fastener configurations. The following observations can be made:

- For large fastener groups, a minimum node offset is required, otherwise there is insufficient space to meet all the spacing requirements, resulting in a zero joint strength.
- Once the node offset is barely sufficient, the group effect reductions become clearly visible. Starting at a node offset that meets the minimum spacing requirements, the joint strength increases along a curve as the spacing increases. At a certain point, the strength no longer increases, indicating that the node offset is sufficiently large to prevent group effect reductions.
- If the node offset is sufficiently large, the joint strength remains constant as no group effect reductions occur. However, it can be seen that the strength very slowly decreases for larger node offsets. This is because, by increasing the node offset, the angle of the diagonal member changes. Consequently, the embedment strength of the timber slightly decreases as the load angle increases.

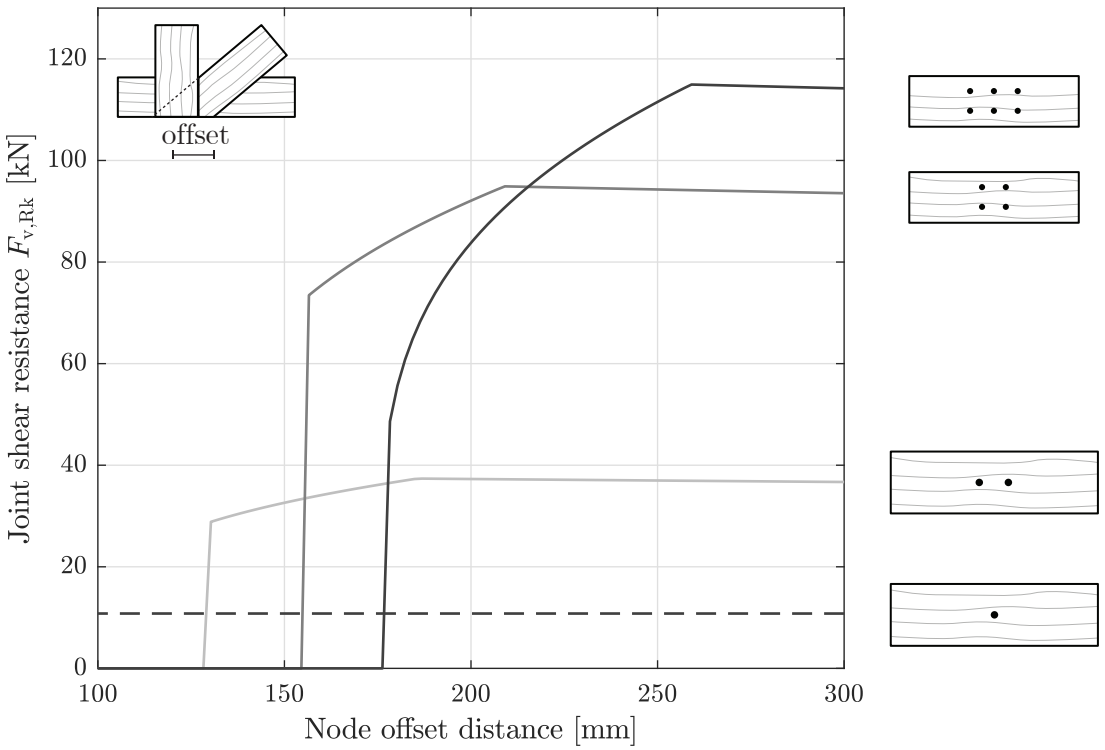

Figure 5.5: DLJ shear resistance for different fastener patterns and a varying diagonal offset.

5.2 Experimental Results

5.2.1 Double Lap Joints

The results of the experimental setup, as presented in Section 4.3, are discussed in this section. The purpose of the experiments is to assess the performance of different parameters in the gluing process. During the tests, three failure modes were distinguished:

- **Adhesion failure:** A small portion of samples failed in adhesion, as shown in Figure 5.6. There were no significant pieces of timber torn off, and delamination was limited to very minor areas. The failure was explosive, with the failed adherend springing away.
- **Timber shear failure:** The majority of samples failed in timber shear, of which two cases are shown in Figure 5.7. These samples exhibited clear pieces of timber torn off, with the amount varying between samples. The failure was explosive, causing the failed adherend to spring away with bits of timber.
- **Timber splitting failure:** A group of samples failed by splitting of the middle member, as shown in Figure 5.8. Stresses perpendicular to the timber grain initiated a crack in the middle member, which started propagating during the test. These samples did not result in explosive failure. Instead, the middle member simply continued to split and the test was stopped after excessive splitting.

Figure 5.6: Samples failed in adhesion of the adhesive layer.

Figure 5.7: Samples failed in timber shear near the joint.

Figure 5.8: Samples failed by splitting of the middle member.

The results of the benchmark set are shown in Figure 5.9, it can be seen that the stiffness of the joint is very similar for all samples. The maximum vertical displacement only reaches about 1.75 mm. There is relatively little spread, and a relatively constant failure load.

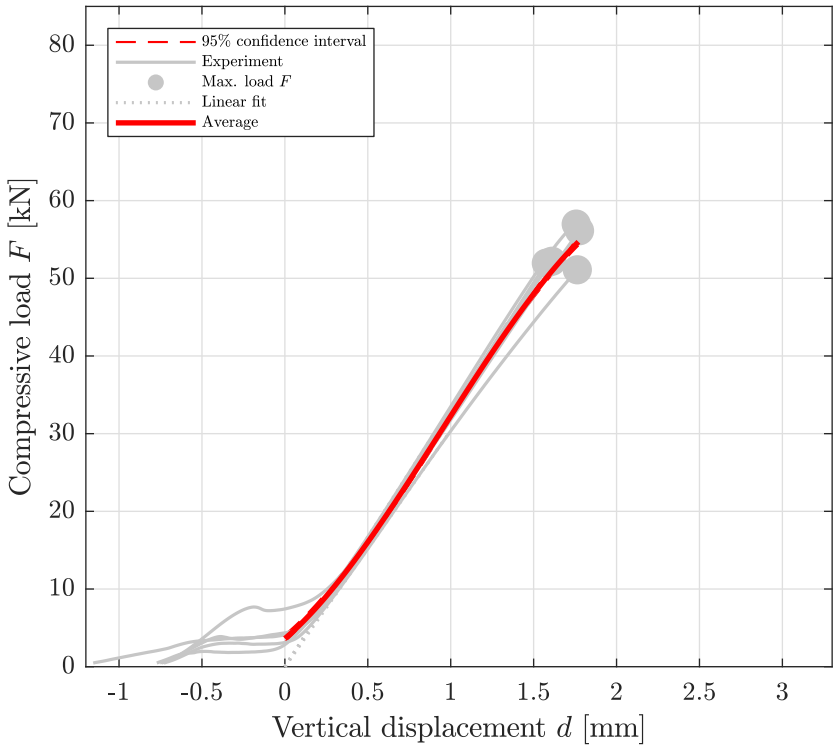

Figure 5.9: Load-displacement results of the benchmark samples R1 (**red**).

A 5% watered-down adhesive mixture is used for the pumping process, and the results are compared to the benchmark set in Figure 5.10. The joint stiffness is almost equal to the benchmark, and the maximum shear strength is roughly the same. Some samples reached slightly lower strengths, whereas one was significantly stronger.

The robotic fabrication process applies the adhesive using a nozzle and predetermined settings, as presented in Section 4.2.1. The results of these samples are shown in Figure 5.11. Once again, the stiffness of the joint is almost equal to the benchmark set. Moreover, three of the samples reached significantly higher joint strengths, while only one performed slightly worse, and one was equally strong.

Two cases were investigated where the method of introducing the clamping pressure varied. Both cases utilized screws: One case had predrilled holes (screw root diameter), and the other case had clearance holes in the upper two members. The results of these samples are shown in Figures 5.12 and 5.13 respectively. Using predrilled holes proved unreliable, with strengths varying significantly, and two samples barely reached any meaningful strength. Investigations of the failure modes showed large sections of the adhesive were poorly bonded. On the other hand, using clearance holes demonstrated performance similar to the benchmark set. The stiffness was roughly equal, and all samples were either almost equally strong or significantly stronger, with one achieving the highest resistance of 80 kN overall.

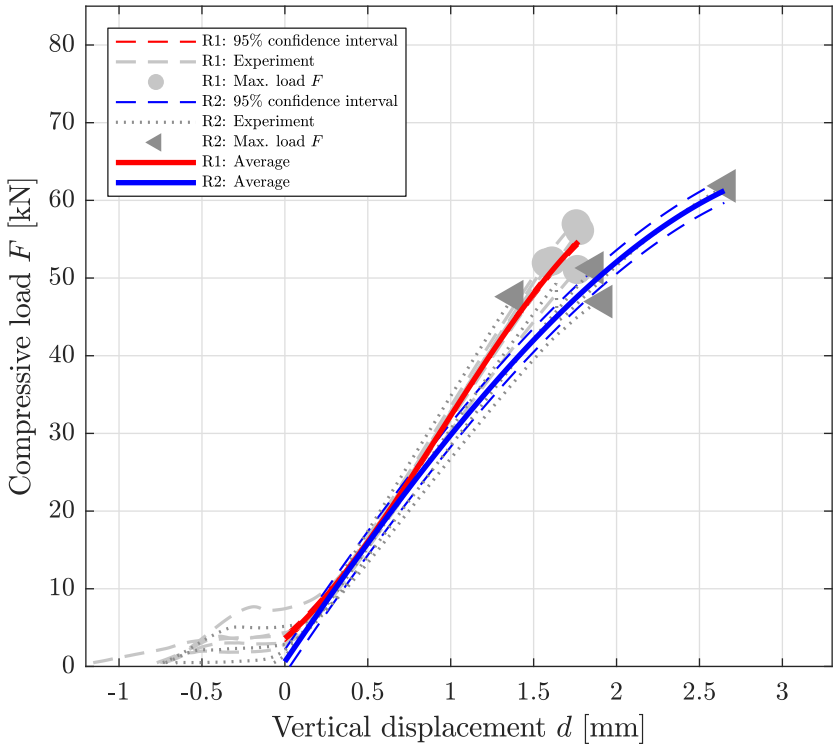

Figure 5.10: Load-displacement results of 5% watered-down samples R2 (**blue**) compared to the benchmark samples R1 (**red**).

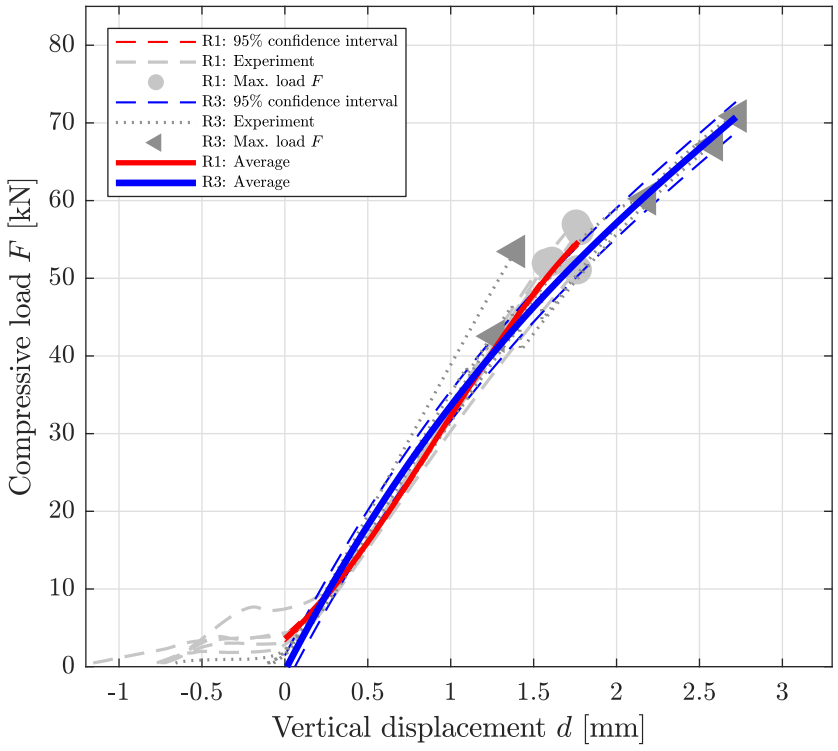

Figure 5.11: Load-displacement results of robotic dispensing samples R3 (**blue**) compared to the benchmark samples R1 (**red**).

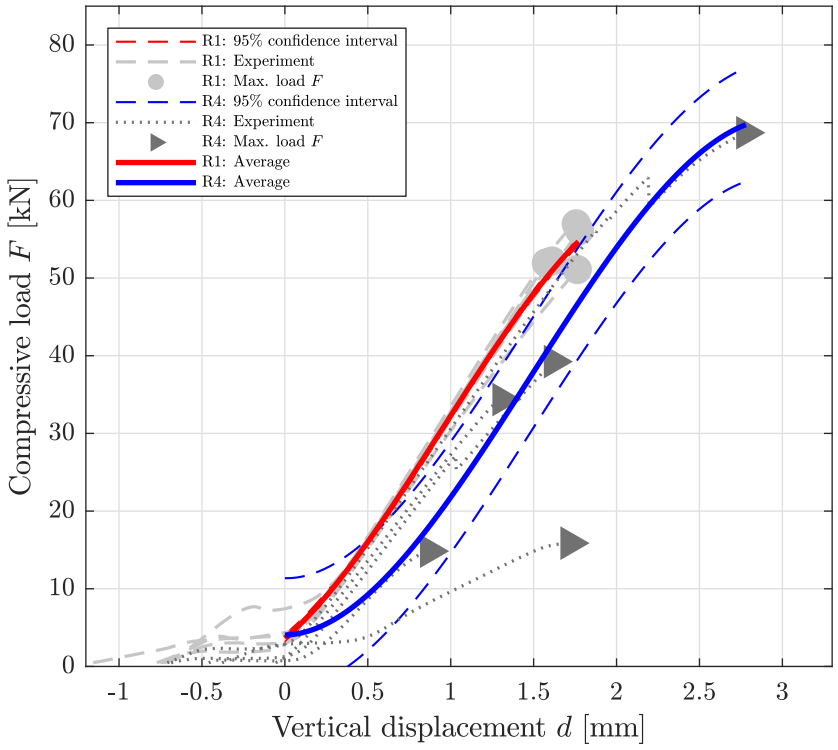

Figure 5.12: Load-displacement results of predrilled screw clamping samples R4 (**blue**) compared to the benchmark samples R1 (**red**).

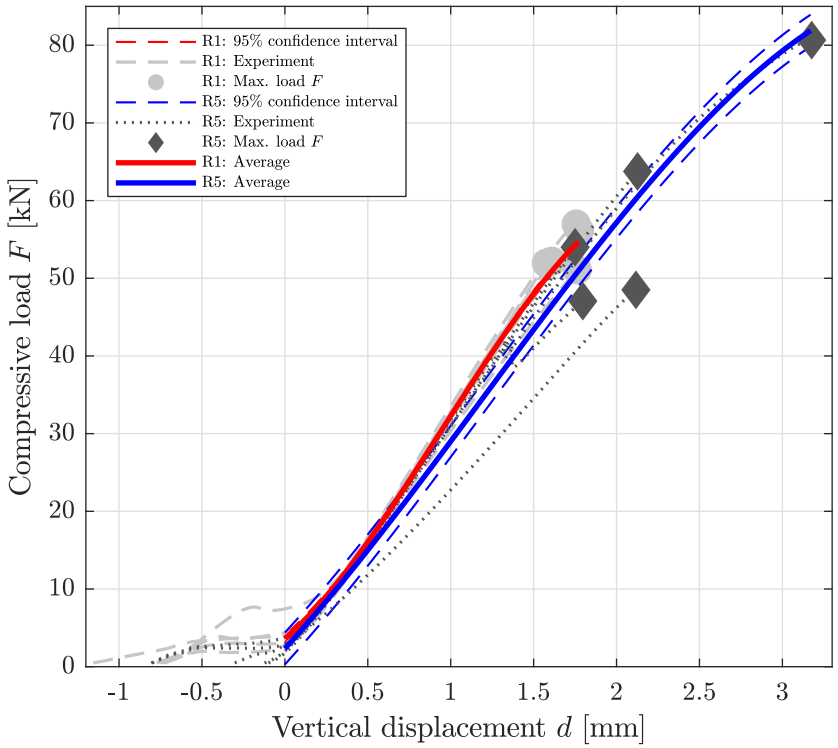

Figure 5.13: Load-displacement results of clearance hole screw clamping samples R5 (**blue**) compared to the benchmark samples R1 (**red**).

Last, the adhesive-screw hybrid joints were assessed. In these samples, the screws used for introducing the clamping pressure were left in during testing. The results of these samples are shown in Figure 5.15. The joints reach strengths similar to that of the benchmark set until the failure of the first adhesive layer occurs. After this, the test continues, and the strength slowly increases again, though the stiffness of the joint decreases. The test was not continued until failure of the second adhesive because the hinges of the setup tilted, as shown in Figure 5.14. The load was not introduced centrically anymore, and due to the tilting of the hinges it could not be guaranteed that the bolts were sufficiently strong to withstand the loads.

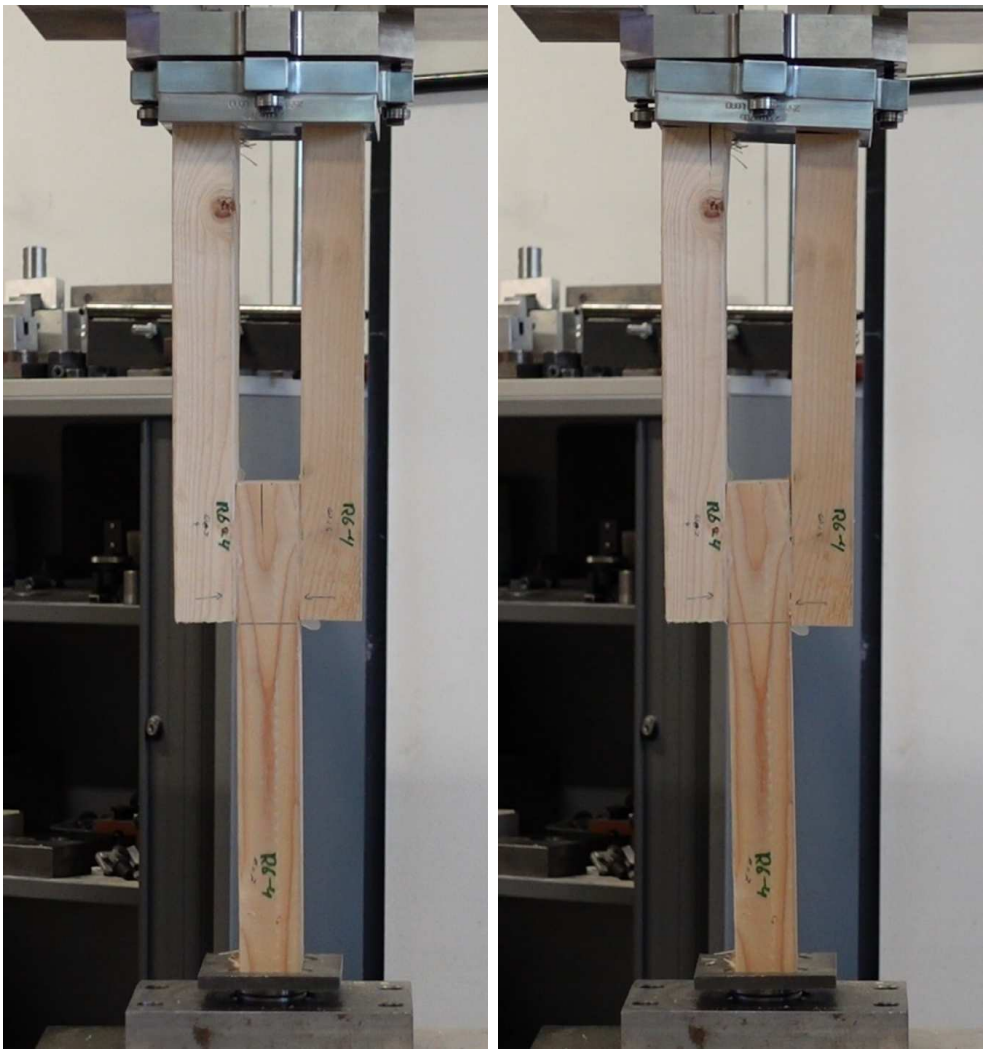

(a) Initial position (b) Eccentric position

Figure 5.14: Adhesive-screw hybrid samples during testing, where after failure of the first adhesive layer the sample becomes asymmetric.

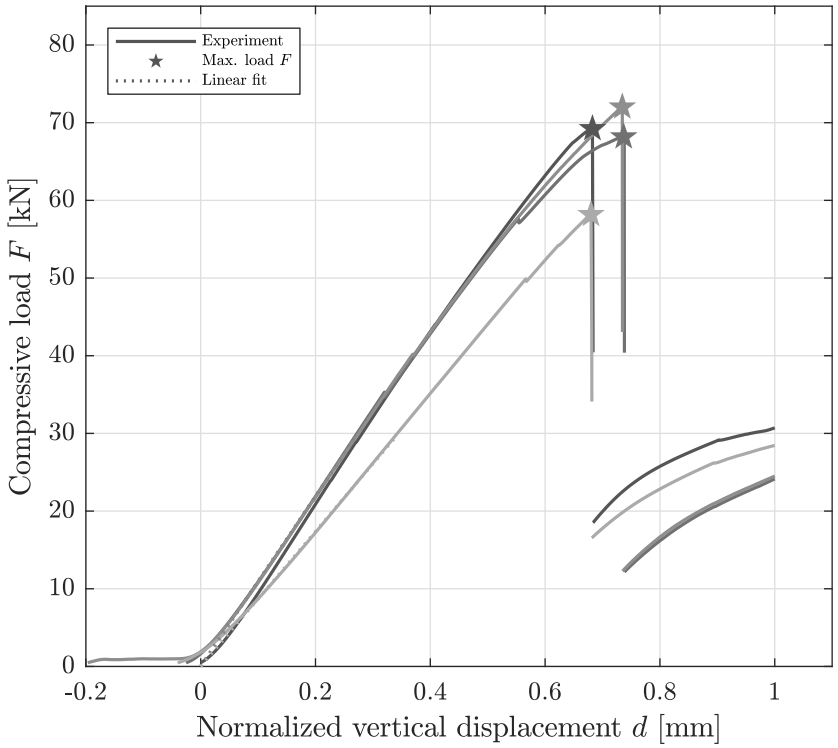

Figure 5.15: Load-displacement results of adhesive-screw hybrid connection samples R6.

5.2.2 Timber Elasticity

To create a representative FEM model of the experimental results, the elasticity of the timber was determined. Since the sample is primarily loaded in compression, the compressive elasticity parallel to the grain was measured. The result of one of the tests is shown in Figure 5.16, where the elasticity is calculated between 10% and 40% of the maximum load observed. The average elasticity of the seven samples is $E_{c,0} = 13\,779.71$ N/mm^2.

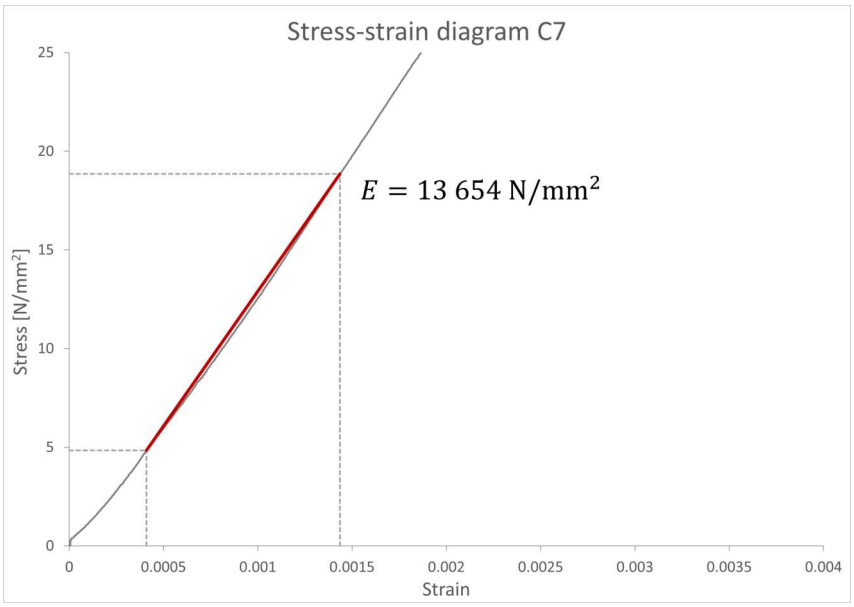

Figure 5.16: Stress-strain result of a compressive test, where the 10% to 40% range is indicated used in the calculation of the parallel compressive elasticity of sample C7 (the other results are shown in Appendix B).

5.3 FEM Verification

From literature, it is known that the stress distribution in adhesive bonds is extremely localized, as discussed in Chapter 3. Therefore, simply using the maximum load as an indicator of the strength may not suffice. Consequently, additional analytical and FEM verifications have been performed to assess the stresses in the tested samples. The analytically derived shear and peel stresses along the bond length are shown in Figures 5.17 and 5.18 respectively. It can be seen that the shear stresses exhibit large peaks near the adhesive ends, while the majority of the joint remains unstressed. Similarly, the peel stresses peak near the ends, showing a smaller local peak in the opposite direction, with the center of the adhesive remaining unstressed.

The analytical results are compared to the FEM model presented in Section 4.3, of which the stresses are shown in Figures 5.19 and 5.20. The maximum stresses found are presented in Table 5.1. It can be seen that the shear stresses have similar distributions in both models, with some differences in peak stresses near the ends. The peel stress also shows similar behavior, with a peak stress at the same location and no stress in the center. However, the local peaks indicated by the analytical model are not present in the FEM results.

The maximum stresses occur at the ends of the adhesive, with agreement between the analytical and FEM models. The magnitude of these maximum stresses varies between the two models, with the FEM simulations resulting in more conservative estimates. The shear and peel stresses are higher by 10% and 18%, respectively, at these locations.

The differences between the analytical and FEM results can be attributed to the assumptions made in the analytical model, which is a simplification of real behavior. Moreover, research on adhesive joints is often conducted for thin metallic compositions, as prescribed by ASTM D1002-10. However, this timber joint has significant differences in material properties, ratios, and dimensions compared to this test method, which can explain the different stress patterns observed in the FEM model. Additionally, adhesive stresses are highly sensitive to certain parameters. For example, the thickness of the adhesive layer (assumed to be 0.1 mm) greatly affects the stress magnitudes in the FEM model, whereas the analytical model does not consider the through-thickness stress distribution, which the FEM model does. These sensitivities can explain the differences between the results.

Table 5.1: Analytical and ABAQUS maximum stresses in the adhesive layer.

	Max. shear stress τ [N/mm^2]	Max. peel stress σ [N/mm^2]
Analytical	262.83	232.07
ABAQUS	292.31	274.89
Difference	11%	18%

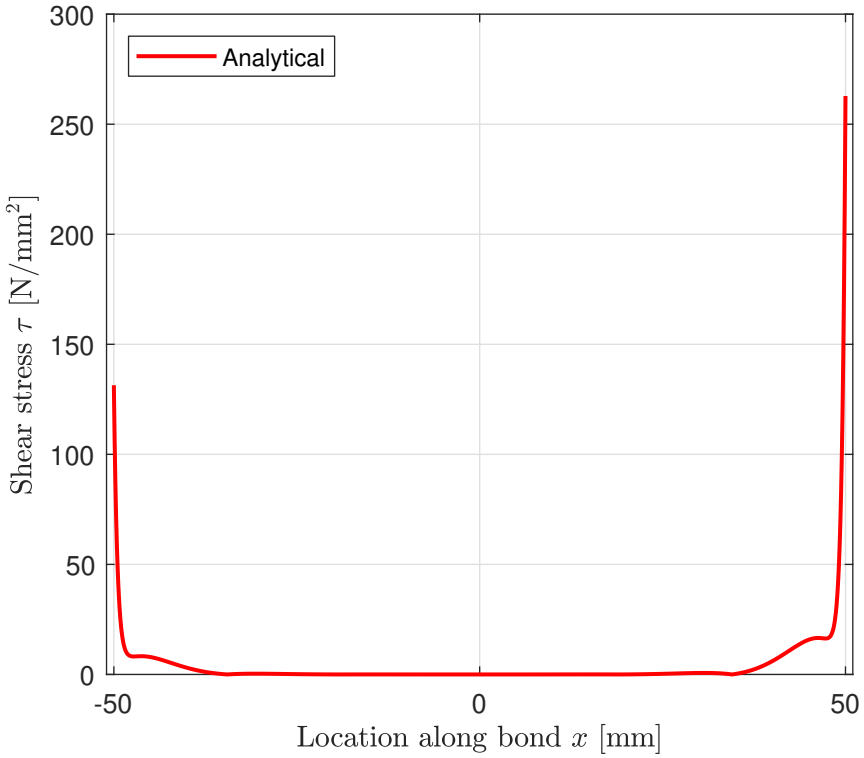

Figure 5.17: Analytical shear stresses τ along adhesive.

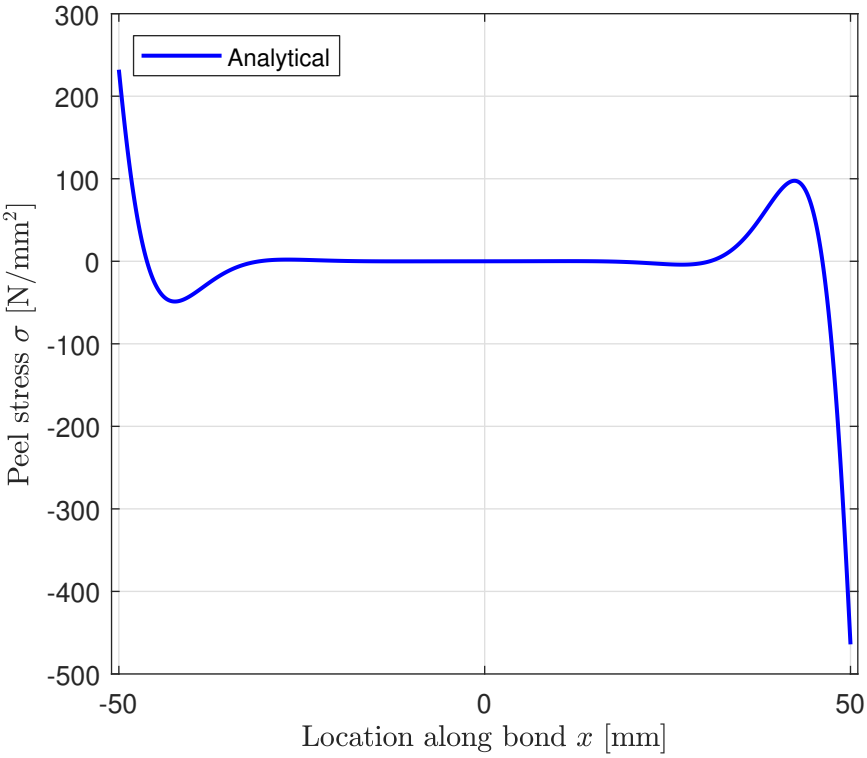

Figure 5.18: Analytical peel stresses σ along adhesive.

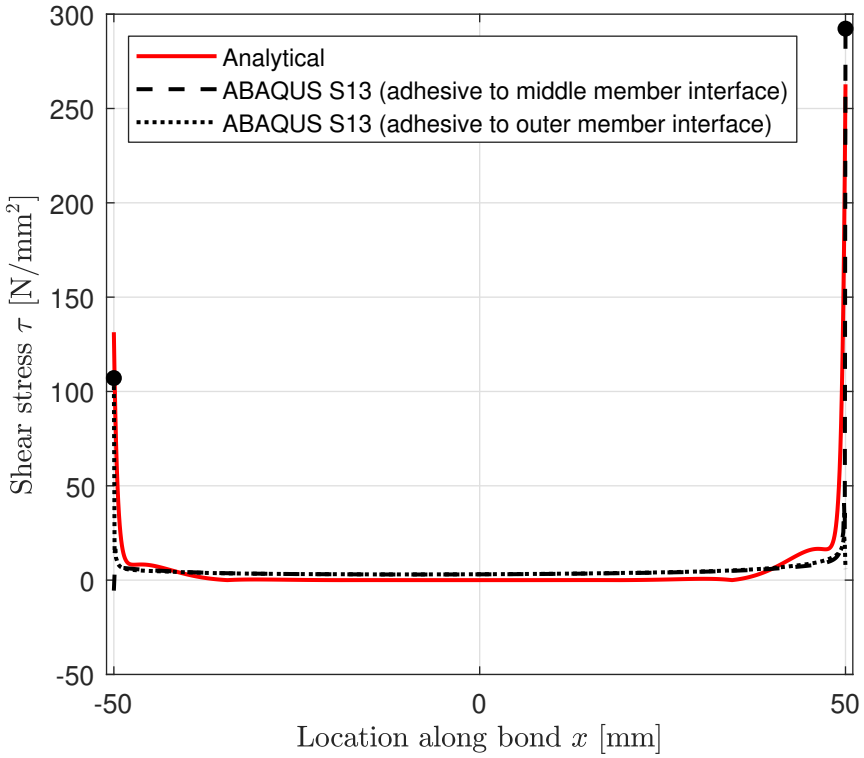

Figure 5.19: Analytical and ABAQUS shear stresses τ along adhesive.

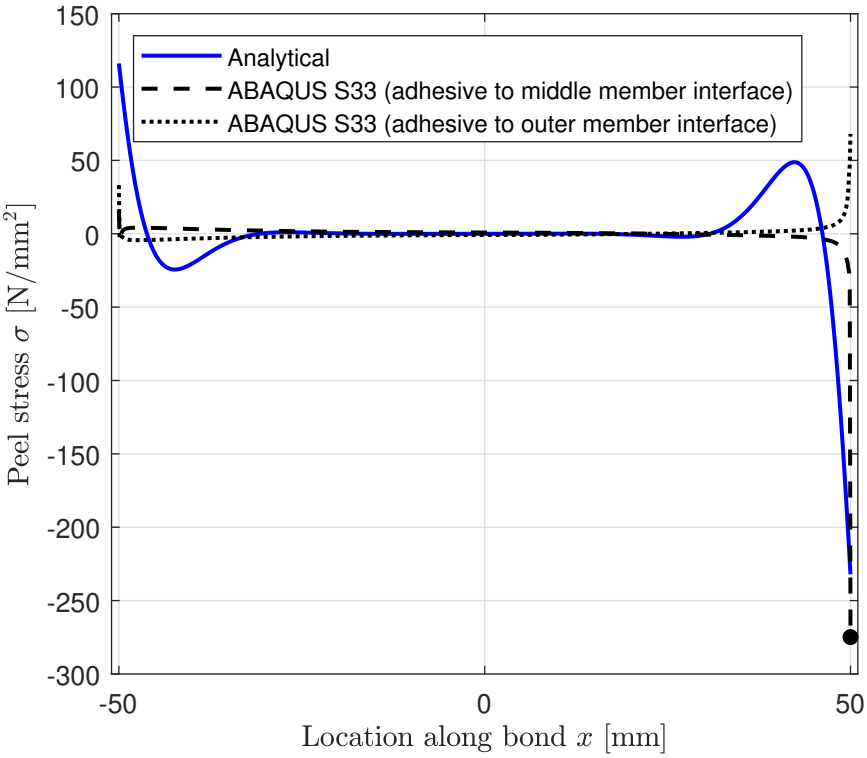

Figure 5.20: Analytical and ABAQUS peel stresses σ along adhesive.

5.4 Angled Adhesive Joint

In the previous sections, a parallel adhesive joint was discussed. This section compares the stresses in a parallel joint to those in an angled joint at a 45° angle. Not only is the parallel shear stress presented, but also the significant shear stresses experienced by the angled joint in other directions. The maximum stresses recorded for the parallel and angled joints are presented in Table 5.2.

Both joints are loaded with the same magnitude, but the peak stresses occurring in the material are significantly higher in the angled joint compared to the parallel joint. All stresses are at least doubled, and in some cases, the recorded peak stress is up to seven times higher. This indicates that loading the adhesive at an angle causes a substantial increase in stress peaks.

The peel stress distribution, shown in Figure 5.21, is similar to that of the parallel joint, but the maximum peel stress is significantly higher in the angled joint.

The three shear stresses are shown in Figures 5.22 to 5.24. It can be seen that the shear stresses S13 and S23 show similar distributions, in which their magnitudes differ significantly. Shear stress S12 was almost entirely absent for the parallel case, where it has a significant stress for the angled joint. The shear stresses are also compared using Tresca's stress, which shows a 200% increase in Tresca stresses for the angled case.

Table 5.2: ABAQUS maximum stresses in the adhesive layer for angled and parallel joint.

	Max. shear stress S12 [N/mm^2]	Max. shear stress S13 [N/mm^2]	Max. shear stress S23 [N/mm^2]	Max. Tresca stress [N/mm^2]	Max. peel stress S33 [N/mm^2]
Parallel 0°	37.66	292.31	59.61	673.8	274.887
Angled 45°	299.71	601.69	390.2	1609.17	802.9
Difference	696%	106%	555%	139%	192%

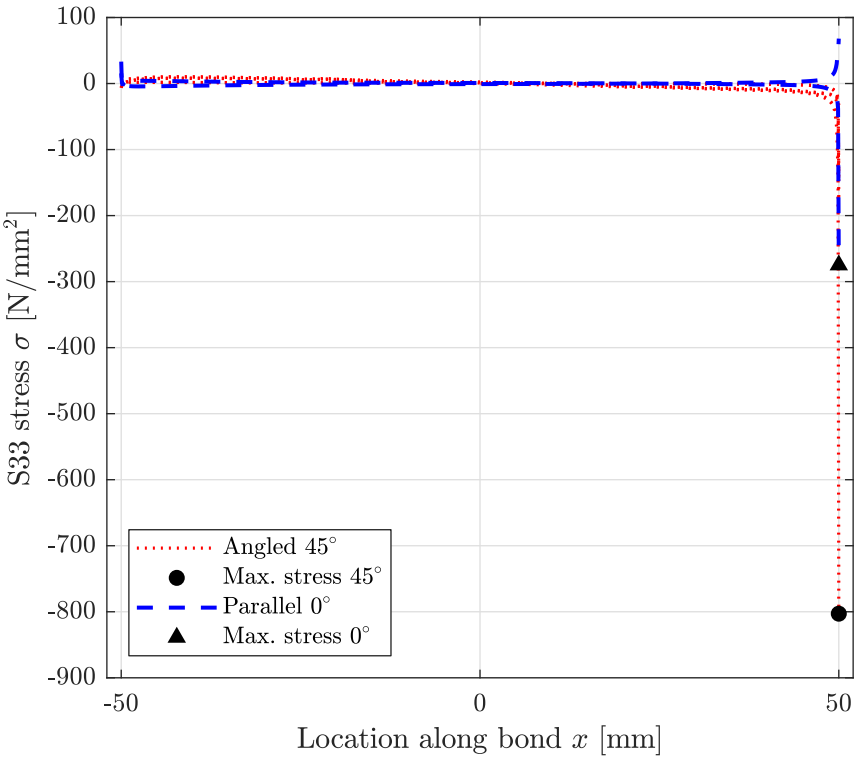

Figure 5.21: ABAQUS S33 peel stresses σ along adhesive for angled and parallel joint.

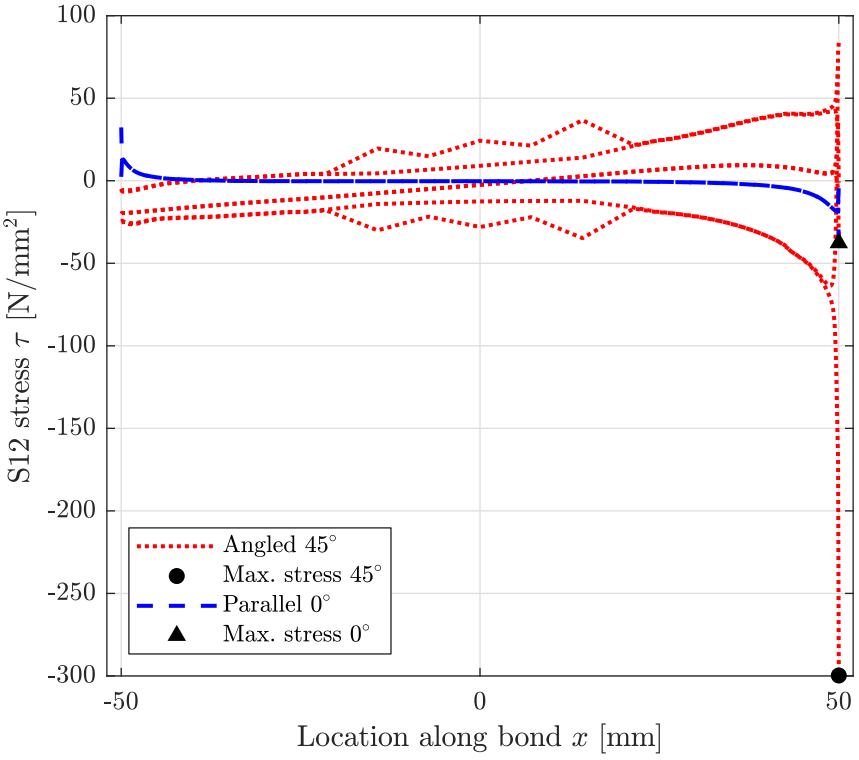

Figure 5.22: ABAQUS S12 shear stresses τ along adhesive for angled and parallel joint.

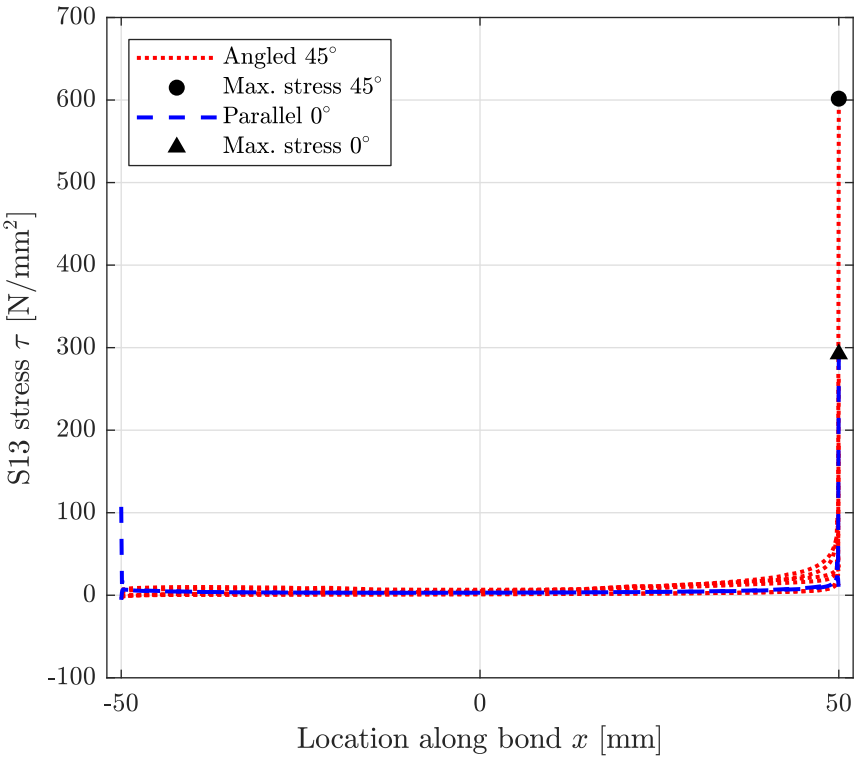

Figure 5.23: ABAQUS S13 shear stresses τ along adhesive for angled and parallel joint.

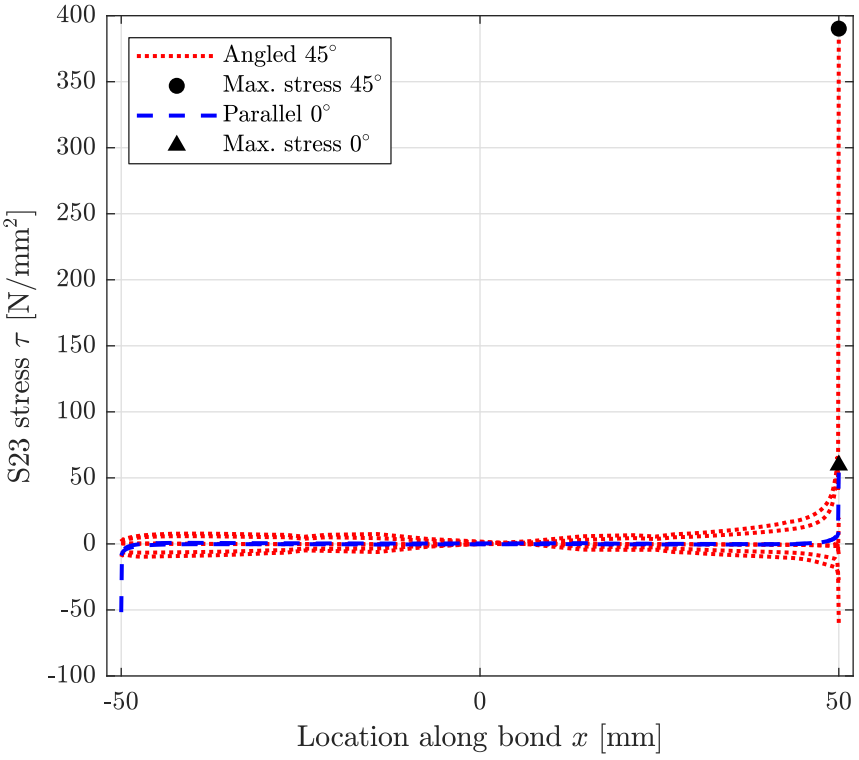

Figure 5.24: ABAQUS S23 shear stresses τ along adhesive for angled and parallel joint.

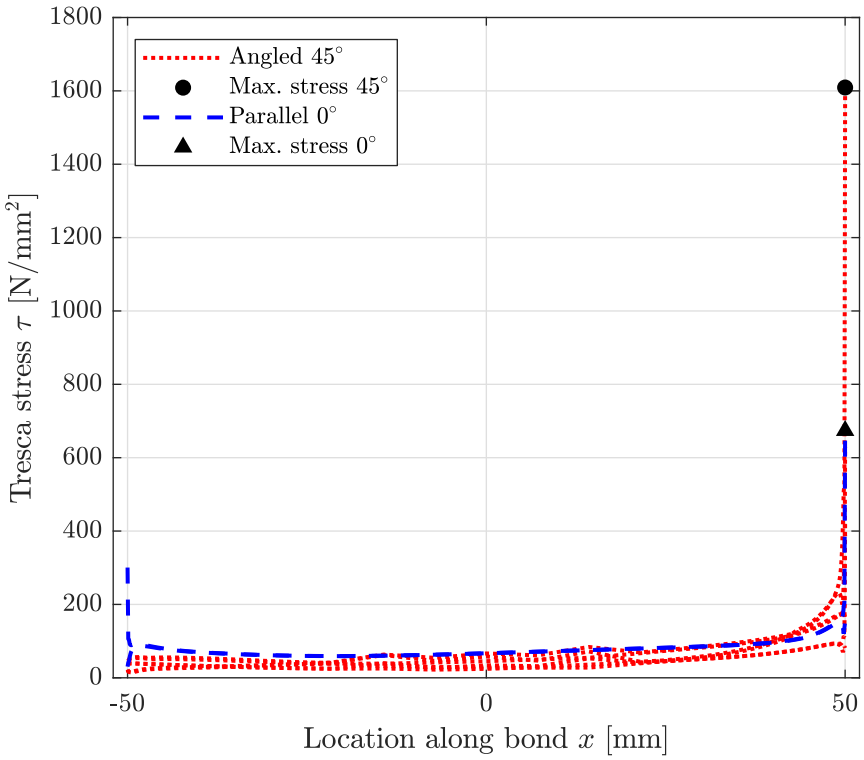

Figure 5.25: ABAQUS Tresca shear stresses τ along adhesive for angled and parallel joint.

5.5 Robotic Fabrication

The robotic fabrication process fabricates discretized elements that can be combined to form a complete truss. One of the members is shown in Figure 5.26. During the fabrication process the following observations were made:

- Careful calibration of all end effectors, ancillary elements, and workpieces is required. Small deviations can quickly accumulate, resulting in discrepancies of a few millimeters.
- The drilling process requires the parallel gripper to hold the elements at their ends. This sometimes proved challenging for larger pieces due to their weight. For example, the 1 m members were gripped at one end, leaving the other 800 mm extended (shown in Figure 4.29). On a few occasions, the member nearly fell out of the gripper due to its weight.
- Repositioning and turning the members to align them properly with the drill requires considerable time. The robot has to move relatively slowly to prevent vibrations from causing the member to shift or fall out of the gripper. Half of the fabrication time is attributed solely to predrilling the holes. Moreover, multiple repositioning steps increase the likelihood of errors and deviations in the final product.
- The current drill speed starts at an RPM of 3500 rev/min. However, operating the drill at higher speeds causes the relatively soft and low-density timber to burn.
- For these relatively small joints, it is crucial to carefully calibrate the adhesive dispensing timing. The start time of dispensing must be accurately timed to avoid moving too soon and thereby not dispensing adhesive on part of the joint.

- Screws must be chosen carefully to meet multiple criteria. One important criterion is ensuring that the bit magnet can easily snap to the screw head. For smaller heads, calibration and small discrepancies become more critical compared to larger heads.

Figure 5.26: One fabricated segment after the fully automated robotics fabrication process.

In general, the robotic process required very little to no manual intervention. However, in one instance, a long member that needed to be predrilled was not properly gripped. Due to its weight, it partly fell out of the gripper and had to be repositioned manually. Consequently, there was a slight discrepancy in the hole location, as shown in Figure 5.27a. When the screw was inserted at this location, it did not pass through the predrilled hole but screwed directly into the timber. As a result, the members were not properly clamped together, leading to an insufficient bond, as shown in Figure 5.27b.

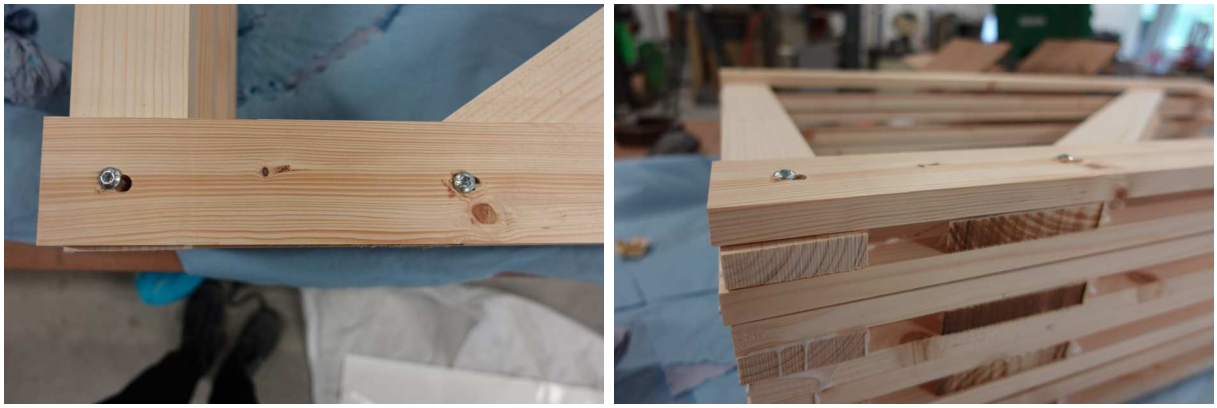

(a) Predrilled holes not properly aligned. (b) Clamping between members insufficient.

Figure 5.27: Fabrication error where manual intervention was required.

6 Discussion

Mechanical SLJ and DLJ joints
In Section 5.1, results of the design toolbox are presented, assessing various parameters and configurations of SLJs and DLJs using mechanical fasteners. It was demonstrated that DLJs are preferable over SLJs, as the failure modes of the fasteners in DLJs require more plastic hinges to form, thereby increasing the joint strength. Additionally, it was shown that joints (either SLJs or DLJs) are more effective when the member thickness ratios are equal: For SLJs, the members must be equally thick, and for DLJs, the sum of the outer members' thicknesses should equal that of the inner member.

Increasing the load angle negatively affects the strength of lap joints, as the timber is increasingly loaded perpendicular to its grain. This is particularly significant for failure modes where embedment failure governs, as the shear strength of the joint can be halved compared to its parallel configuration.

For practical reasons, it is often not possible to use continuous members, requiring sawn off member ends. Sawing off these ends increases the effects of required edge distances, often leaving less space for fasteners. This can result in fasteners being spaced closely together, leading to significant strength reductions due to the group effect. In the worst-case scenario, there is insufficient space for the fastener group to meet spacing requirements, resulting in zero strength.

Although these considerations provide valuable recommendations for designing mechanical lap joints, it is crucial to note that the type of failure mode is highly significant and can vary greatly. The goal is to achieve type III failure modes, characterized by two plastic hinges per shear plane in the joint, which is a ductile failure mode that provides ample warning before failure. However, even when considering the aforementioned factors, brittle embedment failure is still possible. This can occur, for example, when very large fastener groups are used, and the fasteners never fail but the timber always fails in embedment. Therefore, it is essential to always carefully assess the type of failure mode and its impact on joint strength.

Robotic fabrication of adhesive joints
In Section 5.2, various parameters of the robotic fabrication process for adhesive joints in timber structures are examined. The results demonstrate that the robotic process can achieve joints that are equally strong and reliable compared to a traditional adhesive process, provided the proper methods are used. One of the results covered the application of adhesive using a pump in a certain pattern, and then relying on the adhesive spread due to clamping pressure, which had proper distribution over the entire contact area of the joint. This approach is advantageous as it allows for more precise control over the amount of adhesive used. This precision is especially important for minimizing material waste, as very little excess adhesive is pressed out of the joint, while maintaining equal performance.

Traditionally, clamping pressure is introduced using tools such as F-clamps. In a robotic process, this is less desirable because it cannot be easily automated. Therefore, the method of introducing

clamping pressure using screws was investigated. This method proved successful, as equal performance was observed in the case of clearance holes. However, there are three important considerations when using screws:

- The type of screw used influences how the members are clamped together. Smooth shanks can guide the screw through the outer members while drilling only into the final member, thereby clamping the entire assembly. In contrast, fully threaded screws do not ensure proper clamping between the members, which can result in the adhesive not bonding correctly at certain points.
- Different types of screws result in different clamping pressures. For the relatively small joints investigated in this research, this was less critical. However, for larger assemblies, it is important to consider the area of effect of the chosen fastener and its clamping pressure. From this, the required minimum number of fasteners must be determined to introduce sufficient clamping pressure.
- The type of adherend preparation greatly influences the effectiveness of the screws. Proper clearance holes guarantee assembly pressure, whereas neglecting this step results in very unreliable joints due to a lack of clamping pressure.

Adhesive-fastener hybrid joints

A parallel joint was tested with the fasteners left in place after fabrication. This test was displacement-controlled. During the test, it was observed that once the first adhesive layer failed, the screws kept the assembly together, and the second adhesive layer carried the load. It was noted that the joint's stiffness decreased in this new configuration. The test was not conducted until failure of the second adhesive layer. However, the conceptual behavior of subsequent failures is illustrated in Figure 6.1.

With the reduced stiffness, the assembly will experience further loading. As displacement increases, the eccentricity of the assembly also increases, resulting in a further decreasing stiffness. After failure of the second adhesive layer, a significant drop in resistance will be measured, as the screws are considerably weaker and more flexible compared to the adhesive layer. With increasing displacements, the resistance will level out, and the fasteners eventually fail plastically.

Although the fasteners help maintain the assembly's integrity, it is challenging to use them as a proper secondary load path. The adhesive alone provides a very strong shear connection, and to match this strength, significantly larger fasteners would be required. Additionally, the rationale for using a hybrid connection when the strengths are nearly equal remains questionable. The primary consideration might be the increased stiffness of the joint due to the adhesive. However, the adhesive's rigidity compared to the fasteners poses additional challenges. This means that the fasteners will not be activated until the adhesive layers completely fail. When the adhesive fails, the load must be absorbed by the fasteners, which will also involve dynamic effects due to the sudden change, inducing additional stresses. This is particularly important considering that, in reality, the load is force-controlled, not displacement-controlled. This implies that if the first adhesive fails at a certain load, the second adhesive layer will fail immediately as well. For the fasteners to absorb the load, they must be designed to withstand the total load.

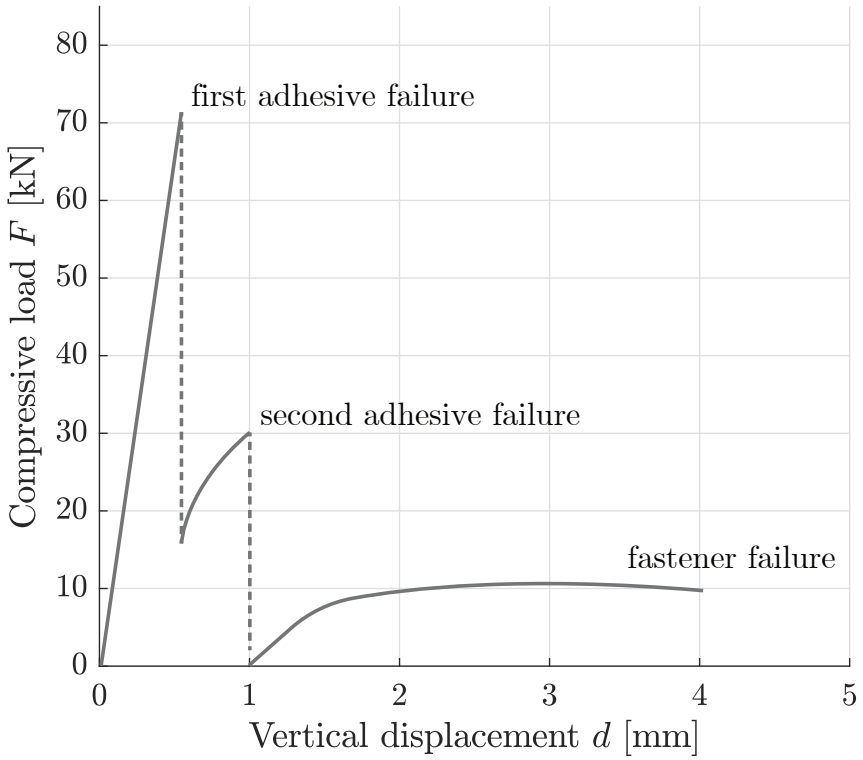

Figure 6.1: Conceptual load-displacement behavior of a hybrid connection until failure.

Adhesive strength prediction

Analytical and FEM models have been developed to assess the stresses in the adhesive samples. Both models indicate that the stress distribution peaks near the ends and zeros out in the middle of the adhesive, which aligns with observations in the literature. This suggests that the overlap length of the adhesive can be chosen economically if designed properly, as large portions of the adhesive are not engaged at failure. Therefore, it is important to carefully determine the required overlap length to avoid making it unnecessarily long.

The stress peaks that occur reach relatively high magnitudes, and at failure, explosive failure propagates through the entire bond instantly. These stress peaks can potentially be used to predict the strength of the adhesive bonds. An average shear stress is not suitable for this purpose due to the large inactivated portion of the adhesive, while the stress peaks do dictate the moment of failure. The analytical and FEM models produce varying stress peaks, but literature has shown that the models are sensitive to certain parameters that are currently assumed and difficult to measure accurately, which partly explains the differences. However, more in-depth analysis is required to better understand these differences. A better understanding of the origin of these variations can help develop a more accurate strength prediction criterion.

Angled adhesive joints

An angled adhesive joint was compared to a parallel joint. The angled adhesive joint experiences significantly higher stresses, indicating that failure occurs earlier in the angled joint. Furthermore, due to the angled load, the continuous timber member is loaded perpendicular to the grain, which may also result in earlier failure compared to the parallel joint. Considering that the diagonals in trusses are always loaded at an angle (and the verticals perpendicular) to the chords, it is crucial to account for this in the design and evaluation of truss strength.

Robotic fabrication process

A successful implementation of the robotic process has been achieved, resulting in a fully automated process capable of fabricating truss elements. However, observations during the process have identified areas for further improvement. The following aspects are recommended to improve:

- **Drilling station:** Currently, the drilling station is stationary, requiring the timber members to be moved to the station. Additionally, the members need to be reoriented multiple times to position the gripper close to the holes. Future implementations should investigate alternative drilling configurations. For instance, a large, possibly width-adjustable gripper could be designed to properly secure the timber members. Subsequently, a drilling end-effector could drill all holes in one operation, eliminating the need for continuous movement of the timber piece. This approach also opens up possibilities for other end-effectors to perform tasks on the timber members, such as milling or attaching components before assembly.
- **Work object area:** The current setup, with two stationary robots working together, limits the work area and consequently the size of the objects that can be fabricated. It is advisable to expand the robot setup to increase the work area, so that larger objects can be fabricated. This could be achieved by mounting robots on tracks on the ground or suspending them from the ceiling.
- **Weight restrictions:** The robots are relatively small, imposing limitations on the weight and type of elements they can handle. This significantly restricts the structural applicability of the fabricated objects. To address this, utilizing robots with higher handling capacities or creating more powerful grippers would allow for the use of larger and heavier elements.
- **Pick up station:** The existing pick-up station for timber elements relies on the calibration of MDF brackets. Future research should explore the development of smarter algorithms to improve the accuracy and versatility of picking up building blocks. Advanced systems could use cameras to identify objects, their locations, and dimensions, thereby eliminating the need for precise and cumbersome calibration sequences.

Figure 6.2: Fabricated truss segments assembled as a complete truss.

7 Further Research

This research investigated the robotic fabrication of mechanical and adhesive joints and the various parameters involved in this process. Given the scope of this research and its exploration of numerous aspects of the fabrication process, several paths for further study have emerged. The following topics require further investigation:

- **Prediction of stresses in adhesive joints:** Predicting stresses in adhesive joints is challenging for various reasons. While analytical models exist for parallel lap joints, they are sensitive to changes in parameters such as adhesive thickness, which are difficult to measure. Additionally, no closed-form theories exist for adhesive lap joints loaded at an angle, despite their potential frequency (e.g., in trusses). Future research could focus on developing methods to more accurately assess and predict the strength of these joints.
- **Structural behavior of robotically fabricated trusses:** The fabricated truss in this research serves as a validation of the robotic process itself. However, the detailed structural behavior of the entire truss has not been thoroughly investigated. While this study primarily focused on the individual components of the connections and the effects of the robotic process, further research could examine the structural behavior of a robotically fabricated truss composed of adhesive joints.
- **Design of adhesive-screw hybrid connections:** This research explored the use of adhesive-screw hybrid connections. However, designing a safe and reliable hybrid connection requires further attention. Future studies could investigate whether it is possible to create a hybrid connection with specific advantages over using either type of connection alone.
- **Continuous fabrication for longer assemblies:** The robotic fabrication process integrated various steps such as drilling, screwing, and gluing. However, for longer assemblies like the truss, the process had to be discretized. Research could focus on improving the robotic setup to enable the fabrication of continuous members, possibly through the use of external axes using e.g. robots on linear tracks. Other improvements to the efficiency of the robotic setup, such as enhancements to the adhesive pumping system, could also be explored.

By addressing these areas, future research can build on the findings of this study, advancing the field of robotic fabrication in the construction industry.

8 Conclusion

This research explored the robotic fabrication of shear connections in timber structures using adhesive, mechanical, or hybrid connections. The robotic setup was developed and validated through a case study involving the fabrication of a truss. Additionally, the research investigated and tested individual aspects of the robotic process to ensure that it performs as reliably as traditional fabrication methods.

The developed robotic system successfully integrated all steps into one workflow: picking and placing, drilling, gluing, and screwing. Experiments comparing these robotic tasks to traditional processes demonstrated that the adhesive joints produced by the robotic system are equally reliable and strong. Therefore, the robotic process can replace manual tasks and automate parts of the fabrication process.

The stresses in the adhesive layers were analyzed using experiments, analytical models, and FEM simulations. The results showed consistent stress distributions, with high stress peaks near the ends of the adhesive and minimal stress in the middle. However, accurately predicting failure loads remains challenging and requires further research.

In summary, this research successfully developed a robotic fabrication system for timber shear joints, such as those in trusses, using either adhesive or mechanical joints. These joints are as strong as those created by conventional methods, making them a suitable replacement and opening up new possibilities for further automation in the AEC industry.

References

3M. (n.d.). *Finite element analysis for 3m tapes and adhesives*. Retrieved January 31, 2024, from https://www.3m.com/wps/portal/en_US/3M/bonding-and-assembly-us/resources/full-story/~/fea-data-for-3m-psas/?storyid=ccd4a185-5e5b-4439-83ec-3ede3443231e

AWC Wood Design Standards Committee. (2023). 2024 national design specification (NDS) for wood construction.

Blaß, H. J., & Sandhaas, C. (2017). *Timber engineering - principles for design*.

Blaß, H., Bienhaus, A., & Krämer, V. (2000). *Effective bending capacity of dowel-type fasteners*.

Campilho, R. D. S. G. (Ed.). (2017). *Strength prediction of adhesively-bonded joints*. CRC Press, Taylor & Francis Group, a Science Publishers book.

CEN. (1991, February). EN 26891:1991: Timber structures - joints made with mechanical fasteners - general principles for the determination of strength and deformation characteristics.

CEN. (2007, January). EN 383:2007: Timber structures - test methods - determination of embedment strength and foundation values for dowel type fasteners.

CEN. (2009, April). EN 409:2009: Timber structures - test methods - determination of the yield moment of dowel type fasteners.

CEN. (2012). EN 408:2010: Timber structures - structural timber and glued laminated timber - determination of some physical and mechanical properties.

CEN. (2014, May). EN 1995-1-1:2004: Design of timber structures - part 1-1: General - common rules and rules for buildings.

CEN. (2022, April). EN 14592:2022: Timber structures - dowel-type fasteners - requirements.

CSA Group. (2019). *CSA o86:19: Engineering design in wood* (Eleventh edition) [OCLC: 1142750559]. CSA Group.

Dixit, S. (2020). Study of factors affecting the performance of construction projects in AEC industry. *Organization, Technology and Management in Construction: an International Journal*, *12*(1), 2275–2282. https://doi.org/10.2478/otmcj-2020-0022

Domínguez, M., Fueyo, J. G., Villarino, A., & Anton, N. (2021). Structural timber connections with dowel-type fasteners and nut-washer fixings: Mechanical characterization and contribution to the rope effect. *Materials*, *15*(1), 242. https://doi.org/10.3390/ma15010242

Goland, M., & Reissner, E. (1944). The stresses in cemented joints. *Journal of Applied Mechanics*, *11*(1), A17–A27. https://doi.org/10.1115/1.4009336

Gramazio Kohler Research. (2016). *Digital assembly of a complex roof structure*. Retrieved November 16, 2023, from https://gramaziokohler.arch.ethz.ch/web/e/projekte/201.html

Graser, K., Baur, M., Apolinarska, A., Dörfler, K., Hack, N., Jipa, A., Lloret, E., Sandy, T., Pont, D., Hall, D., & Kohler, M. (2020). DFAB HOUSE - a comprehensive demonstrator of digital fabrication in architecture, 130–139. https://doi.org/10.2307/j.ctv13xpsvw.21

Hart-Smith, L. (1973). Adhesive-bonded single-lap joints. *NASA CR 112236*.

Hasan, A., Baroudi, B., Elmualim, A., & Rameezdeen, R. (2018). Factors affecting construction productivity: A 30 year systematic review [Publisher: Emerald Publishing Limited]. *Engineering, Construction and Architectural Management*, *25*(7), 916–937. https://doi.org/10.1108/ECAM-02-2017-0035

Heidari-Rarani, M., & Ghasemi, A. (2017). Appropriate shape of cohesive zone model for delamination propagation in ENF specimens with r-curve effects. *Theoretical and Applied Fracture Mechanics*, *90*, 174–181. https://doi.org/10.1016/j.tafmec.2017.04.009

Her, S.-C., & Chan, C.-F. (2019). Interfacial stress analysis of adhesively bonded lap joint [Number: 15 Publisher: Multidisciplinary Digital Publishing Institute]. *Materials*, *12*(15), 2403. https://doi.org/10.3390/ma12152403

Hübner, U., Bogensperger, T., & Schickhofer, G. (2008). Embedding strength of european hardwoods. *Working commission W18 Timber structures*.

Järvholm, B., Stattin, M., Robroek, S. J., Janlert, U., Karlsson, B., & Burdorf, A. (2014). Heavy work and disability pension — a long term follow-up of swedish construction workers [Publisher: Scandinavian Journal of Work, Environment & Health]. *Scandinavian Journal of Work, Environment & Health*, *40*(4), 335–342. Retrieved November 15, 2023, from https://www.jstor.org/stable/43188027

Johansen, K. (1949). Theory of timber connections. *Publications of International Association for Bridge and Structural Engineering*, (9), 249–262.

Jorissen, A., & Blaß, H. (1998). The fastener yield strength in bending. *Proceedings CIB-W18 meeting*.

Kliger, R., Johansson, M., Crocetti, R., Annika, M., Lidelöw, H., Norlin, B., & Pousette, A. (2022). *Design of timber structures - structural aspects of timber construction* (3rd ed., Vol. 1). Swedish Forest Industries Federation.

Lantos, G. (1969). Load distribution of a row of fasteners subjected to lateral load. *Wood Science*, *1*(3), 129–136.

Maskuriy, R., Selamat, A., Ali, K. N., Maresova, P., & Krejcar, O. (2019). Industry 4.0 for the construction industry—how ready is the industry? [Number: 14 Publisher: Multidisciplinary Digital Publishing Institute]. *Applied Sciences*, *9*(14), 2819. https://doi.org/10.3390/app9142819

Ojalvo, I. U., & Eidinoff, H. L. (1978). Bond thickness effects upon stresses in single-lap adhesive joints. *AIAA Journal*, *16*(3), 204–211. https://doi.org/10.2514/3.60878

Özer, H. (2018, February 21). *Applied adhesive bonding in science and technology*. https://doi.org/10.5772/intechopen.68926

Quispe Rodríguez, R., Sollero, P., Bertoni Rodrigues, M., & Lima de Albuquerque, É. (2011). Stress analysis and failure criteria of adhesive bonded single lap joints. *COBEM 2011*.

Sandhaas, C., Ravenshorst, G. J. P., Blass, H. J., & Van De Kuilen, J. W. G. (2013). Embedment tests parallel-to-grain and ductility aspects using various wood species. *European Journal of Wood and Wood Products*, *71*(5), 599–608. https://doi.org/10.1007/s00107-013-0718-z

Tapflo pumps UK. (n.d.). Retrieved March 3, 2024, from https://www.tapflopumps.co.uk/blog/peristaltic-pump-guide/

Thoma, A., Adel, A., Helmreich, M., Wehrle, T., Gramazio, F., & Kohler, M. (2019). Robotic fabrication of bespoke timber frame modules. In J. Willmann, P. Block, M. Hutter, K. Byrne, & T. Schork (Eds.), *Robotic fabrication in architecture, art and design 2018* (pp. 447–458). Springer International Publishing. https://doi.org/10.1007/978-3-319-92294-2_34

van Ingen, J., & Vlot, A. (1993, April). *Stress analysis of adhesively bonded single lap joints* (LR-740). Delft University of Technology.

Volkersen, O. (1938). Die nietkraftverteilung in zugbeanspruchten nietverbindungen mit konstanten laschenquerschnitten. *Luftfahrtforschung*, *15*, 41–47.

Vrenken, L. (2023, May 9). *The parametric design and robotic assembly of a timber column* [Doctoral dissertation, TU/e].

Wagner, H. J., Alvarez, M., Groenewolt, A., & Menges, A. (2020). Towards digital automation flexibility in large-scale timber construction: Integrative robotic prefabrication and co-design of the BUGA wood pavilion. *Construction Robotics*, *4*(3), 187–204. https://doi.org/10.1007/s41693-020-00038-5

Zhang, C., Li, N., Wang, W., Binienda, W. K., & Fang, H. (2015). Progressive damage simulation of triaxially braided composite using a 3d meso-scale finite element model. *Composite Structures*, *125*, 104–116. https://doi.org/10.1016/j.compstruct.2015.01.034

Appendices

A Process Parameters Adhesive Dispensing

A.1 Pump Rate

Test					Criteria	
Pump rate [ml/min]	Samples [-]	ID [-]	Gap [mm]	Excess [mm]	Coverage [%]	Excess [%]
50		PS50-1	130	0	41%	0%
50		PS50-2	180	20	18%	9%
50	5	PS50-3	180	90	18%	41%
50		PS50-4	180	90	18%	41%
50		PS50-5	160	90	27%	41%
100		PS100-1	62	93	72%	42%
100		PS100-2	85	10	61%	5%
100	5	PS100-3	95	10	57%	5%
100		PS100-4	121	13	45%	6%
100		PS100-5	72	5	67%	2%
150		PS150-1	20	13	91%	6%
150		PS150-2	18	80	92%	36%
150	5	PS150-3	50	10	77%	5%
150		PS150-4	20	20	91%	9%
150		PS150-5	40	10	82%	5%
200		PS200-1	0	24	100%	11%
200		PS200-2	22	93	90%	42%
200	5	PS200-3	0	20	100%	9%
200		PS200-4	0	20	100%	9%
200		PS200-5	5	20	98%	9%
250		PS250-1	0	20	100%	9%
250		PS250-2	0	20	100%	9%
250	5	PS250-3	0	90	100%	41%
250		PS250-4	0	90	100%	41%
250		PS250-5	0	60	100%	27%
300		PS300-1	0	20	100%	9%
300		PS300-2	0	90	100%	41%
300	5	PS300-3	0	20	100%	9%
300		PS300-4	0	60	100%	27%
300		PS300-5	0	20	100%	9%
350		PS350-1	0	90	100%	41%
350		PS350-2	0	20	100%	9%
350	5	PS350-3	0	20	100%	9%
350		PS350-4	0	20	100%	9%
350		PS350-5	0	100	100%	45%
400		PS400-1	0	30	100%	14%
400		PS400-2	0	90	100%	41%
400	5	PS400-3	0	30	100%	14%
400		PS400-4	0	90	100%	41%
400		PS400-5	0	80	100%	36%

Constants				
Adhesive supply [g]	Adhesive length [mm]	Water content [%]	[g]	Robot speed [mm/s]
750	220	5%	37.5	30

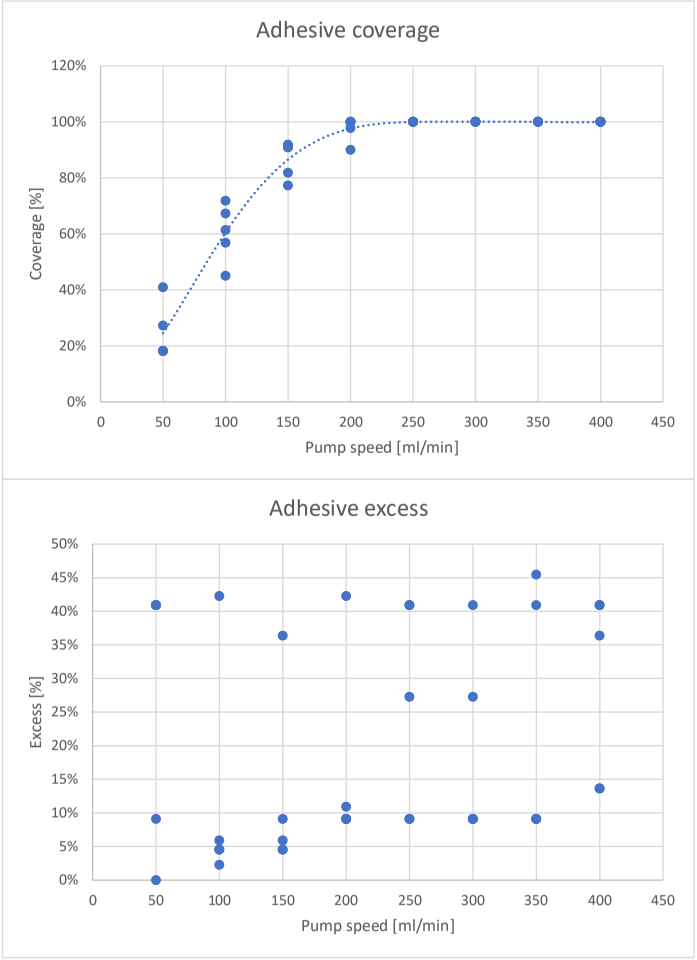

A.2 Dispensing Flow Rate

Test			Constants		Outcome
ID	Mass	Flow rate	Pump rate	Time	Flow rate
[-]	[g]	[g/s]	[ml/min]	[s]	[g/s]
FR250-1	6.00	0.15	250	40	0.15
FR250-2	6.00	0.15			
FR250-3	7.00	0.175			
FR250-4	6.00	0.15			
FR250-5	5.00	0.125			
FR250-6	6.00	0.15			
FR250-7	6.00	0.15			
FR250-8	6.00	0.15			
FR250-9	6.00	0.15			
FR250-10	4.00	0.1			
Mean	5.80				
Standard deviation	0.75				
5%-value	4.57				

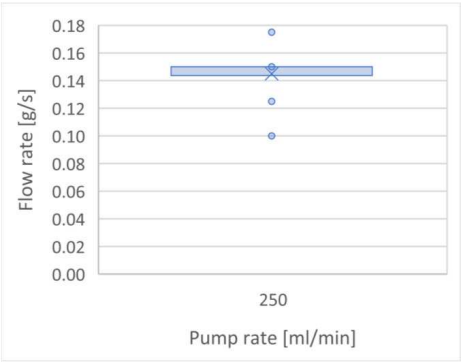

ID	Mass	Flow rate	Pump rate	Time	Flow rate
[-]	[g]	[g/s]	[ml/min]	[s]	[g/s]
FR300-1	6.00	0.15	300	40	0.15
FR300-2	5.00	0.125			
FR300-3	7.00	0.175			
FR300-4	5.00	0.125			
FR300-5	6.00	0.15			
FR300-6	6.00	0.15			
FR300-7	6.00	0.15			
FR300-8	6.00	0.15			
FR300-9	7.00	0.175			
FR300-10	7.00	0.175			
Mean	6.10				
Standard deviation	0.70				
5%-value	4.95				

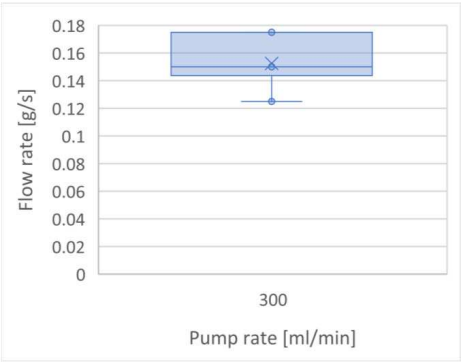

ID	Mass	Flow rate	Pump rate	Time	Flow rate
[-]	[g]	[g/s]	[ml/min]	[s]	[g/s]
FR350-1	8.00	0.2	350	40	0.18
FR350-2	7.00	0.175			
FR350-3	7.00	0.175			
FR350-4	6.00	0.15			
FR350-5	7.00	0.175			
FR350-6	7.00	0.175			
FR350-7	7.00	0.175			
FR350-8	8.00	0.2			
FR350-9	8.00	0.2			
FR350-10	8.00	0.2			
Mean	7.30				
Standard deviation	0.64				
5%-value	6.25				

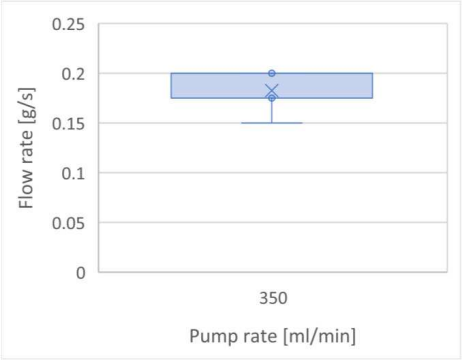

A.3 Adhesive Spread

Test							
Robot speed [mm/s]	Samples [-]	ID [-]	Spread [mm]	Robot speed [mm/s]	Samples [-]	ID [-]	Spread [mm]
10	5	S25-1	40	80	5	S75-1	15
		S25-2	38			S75-2	18
		S25-3	40			S75-3	24
		S25-4	40			S75-4	20
		S25-5	38			S75-5	20
		Mean	39.2			**Mean**	19.4
		Standard deviation	1.0			**Standard deviation**	2.9
		5%-value	37.6			**5%-value**	14.6
20	5	S25-1	24	100	5	S100-1	17
		S25-2	20			S100-2	18
		S25-3	32			S100-3	30
		S25-4	36			S100-4	22
		S25-5	40			S100-5	22
		Mean	30.4			**Mean**	21.8
		Standard deviation	7.4			**Standard deviation**	4.6
		5%-value	18.2			**5%-value**	14.3
30	5	S25-1	20	150	5	S150-1	20
		S25-2	24			S150-2	20
		S25-3	30			S150-3	19
		S25-4	25			S150-4	23
		S25-5	25			S150-5	20
		Mean	24.8			**Mean**	20.4
		Standard deviation	3.2			**Standard deviation**	1.4
		5%-value	19.6			**5%-value**	18.2
50	5	S50-1	20				
		S50-2	18				
		S50-3	24				
		S50-4	20				
		S50-5	20				
		Mean	20.4				
		Standard deviation	2.0				
		5%-value	17.2				

Constants			
Pump rate [ml/min]	Flow rate [g/s]	Required adhesive [m^2/kg]	Required adhesive [g/mm^2]
250	0.15	6.00	0.0001667

Fitted Function		
Constant [-]	Fitted result [-]	
A	61.322	
B	-0.245	
Speed	33.55	[mm/s]
Spread	25.93	[mm]
Speed*spread	870.00	[mm^2/s]
Flow rate/required	870	[mm^2/s]
Required speed	33.55	[mm/s]

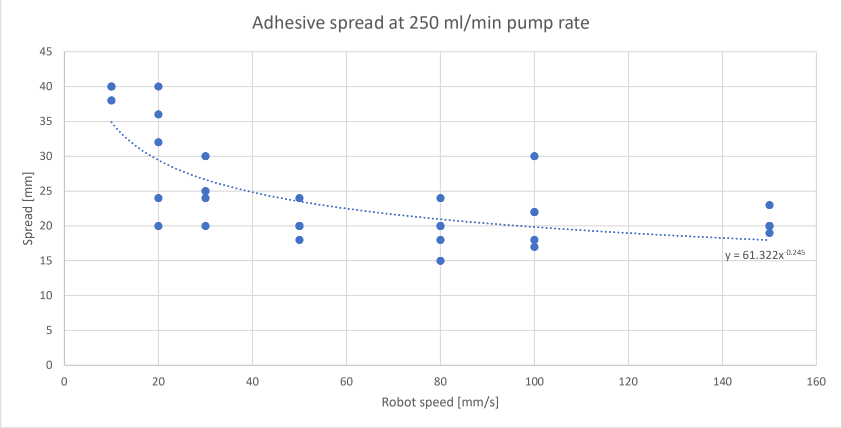

B Experimental Results Timber Elasticity

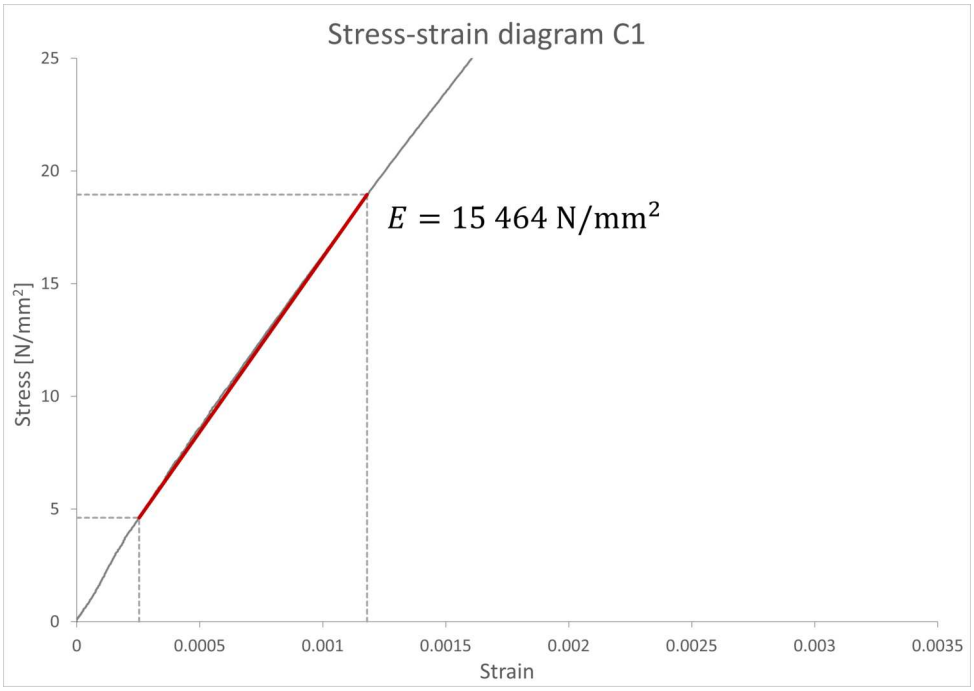

Figure B.1: Stress-strain results and elasticity of sample C1.

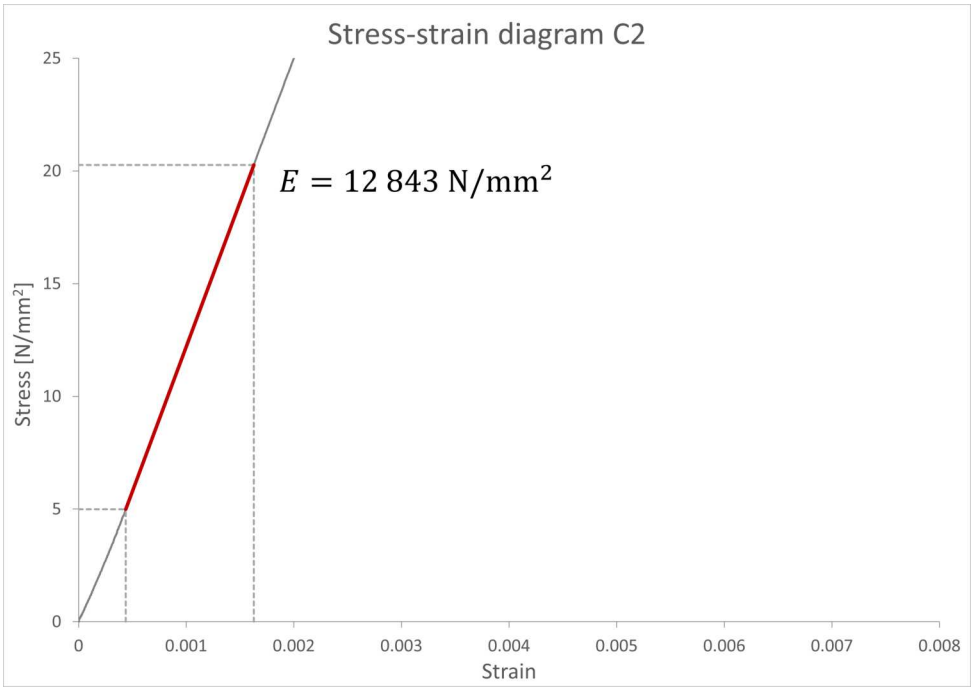

Figure B.2: Stress-strain results and elasticity of sample C2.

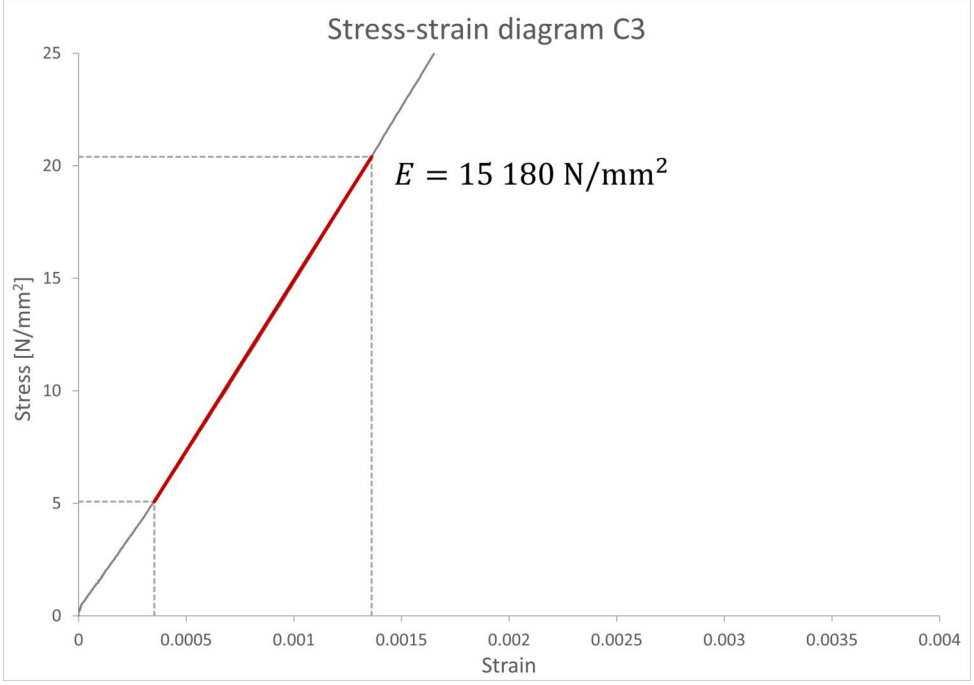

Figure B.3: Stress-strain results and elasticity of sample C3.

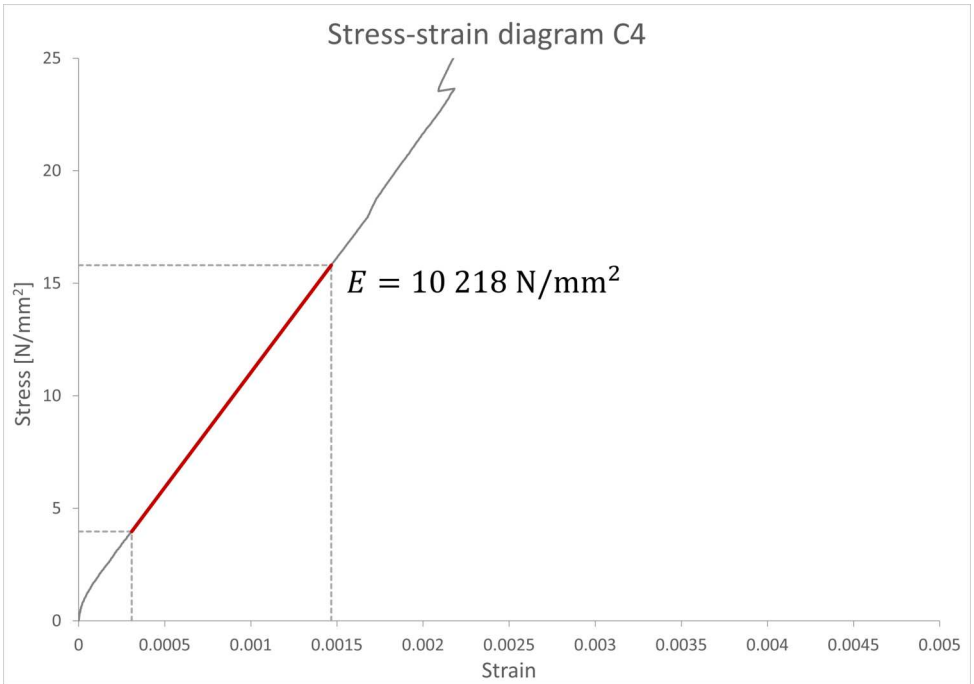

Figure B.4: Stress-strain results and elasticity of sample C4.

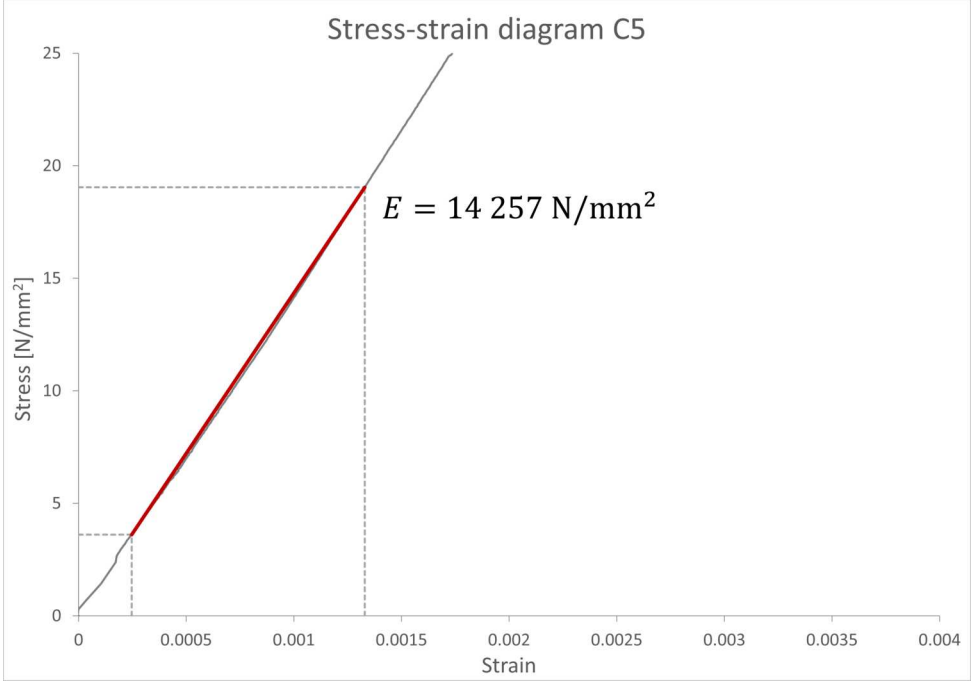

Figure B.5: Stress-strain results and elasticity of sample C5.

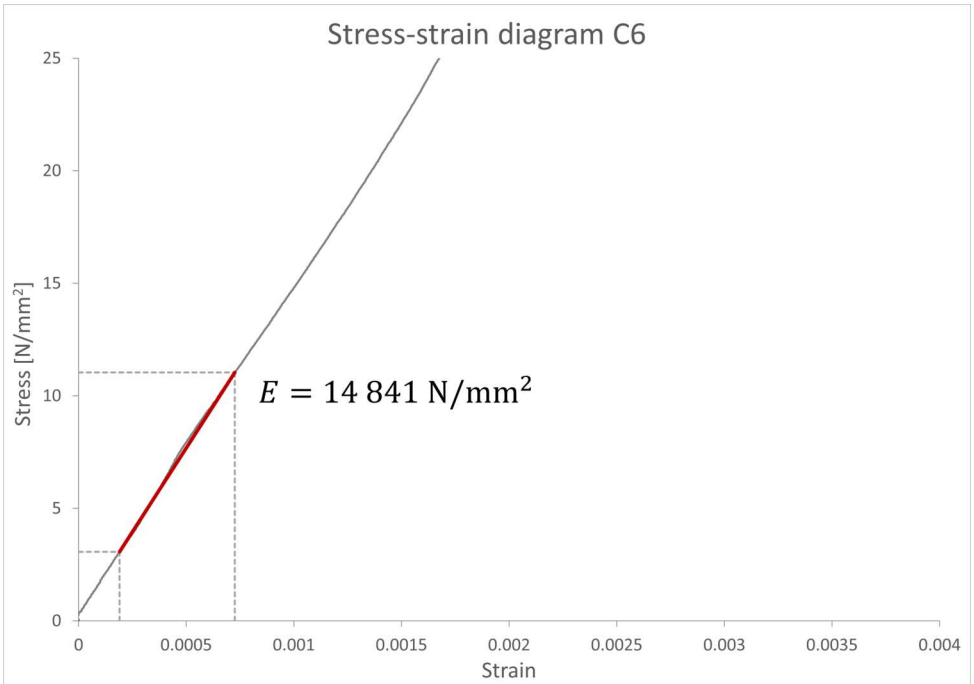

Figure B.6: Stress-strain results and elasticity of sample C6.

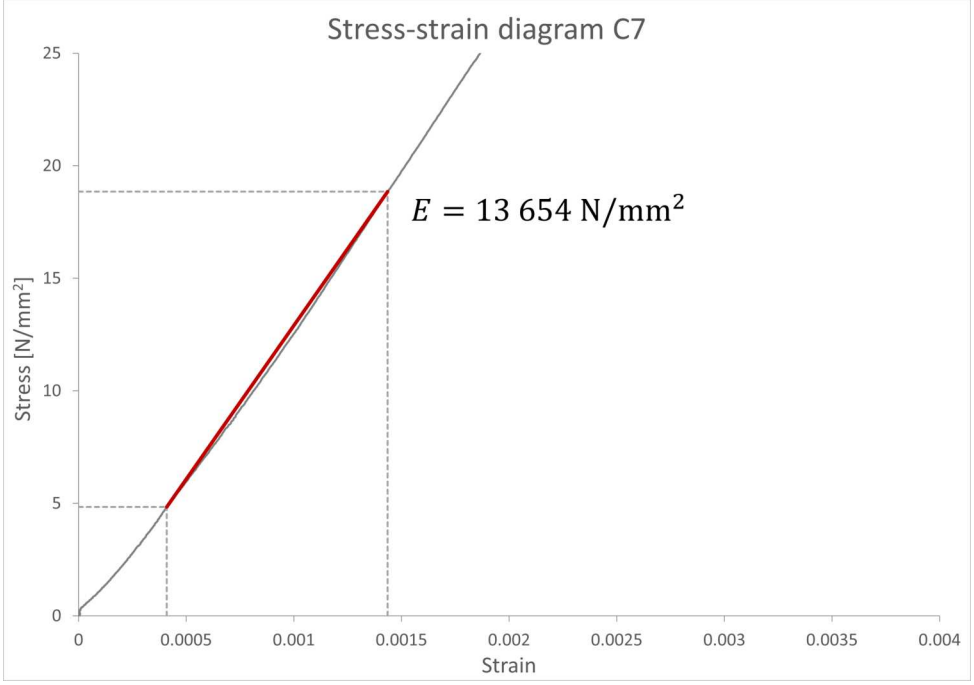

Figure B.7: Stress-strain results and elasticity of sample C7.

C Shear Resistance Python Code

```
__author__ = "T.H.W. Bindels"
__version__ = "2024.02.04"

# Packages and settings
import rhinoscriptsyntax as rs
import math as m
ghenv.Component.Message = "Joint Shear Resistance"


# Constants
alpha_f = m.pi/2        # Fastener inclination, perpendicular
M_yRk = M_yRk*1000      # Product specification, Nm to Nmm
perc_axial = 1          # 100% for screws (EN 1995-1-1 / 8.2.2 (2))

# Withdrawal capacity for screws (using outer thread/nominal diameter)
k_d = min(d_f_nom/8, 1)
F_axRk = n_f**0.9*f_axRk*d_f_nom*l_f_eff*k_d/(1.2*m.cos(alpha_f)**2+m.sin(
    alpha_f)**2)
F_vRk_ax = F_axRk/4

# Member embedment strengths (using inner thread/shank diameter)
f_1_h0k = 0.082*(1-0.01*d_f_inner)*rho_1_k
f_2_h0k = 0.082*(1-0.01*d_f_inner)*rho_2_k
k_90 = 1.35+0.015*d_f_inner
alpha_1 = m.radians(alpha_1)
alpha_2 = m.radians(alpha_2)
f_1_halphak = f_1_h0k/(k_90*m.sin(alpha_1)**2+m.cos(alpha_1)**2)
f_2_halphak = f_2_h0k/(k_90*m.sin(alpha_2)**2+m.cos(alpha_2)**2)
beta = f_2_halphak/f_1_halphak


# Double lap joints
if DLJ:
    ## FAILURE MODE I - UNEQUAL MEMBER THICKNESS
    # Governing timber member
    f_halphak = min(f_1_halphak*h_1, 0.5*f_2_halphak*h_2)

    # Shear strength mode I
    F_vRk_FI = f_halphak*d_f_inner


    ## FAILURE MODE II
    # Shear strength mode II
    F_vRk_FII_Johansen = 1.05*(f_1_halphak*h_1*d_f_inner/(2+beta))*(m.sqrt
   (2*beta*(1+beta)+(4*beta*(2+beta)*M_yRk)/(f_1_halphak*d_f_inner*h_1**2))
   -beta)
```

```
    if F_vRk_ax > (perc_axial*F_vRk_FII_Johansen):
        F_vRk_FII = F_vRk_FII_Johansen+perc_axial*F_vRk_FII_Johansen
    else:
        F_vRk_FII = F_vRk_FII_Johansen+F_vRk_ax


    ## FAILURE MODE III
    # Shear strength mode III
    F_vRk_FIII_Johansen = 1.15*m.sqrt((2*beta)/(1+beta))*m.sqrt(2*M_yRk*
    f_1_halphak*d_f_inner)
    if F_vRk_ax > (perc_axial*F_vRk_FIII_Johansen):
        F_vRk_FIII = F_vRk_FIII_Johansen+perc_axial*F_vRk_FIII_Johansen
    else:
        F_vRk_FIII = F_vRk_FIII_Johansen+F_vRk_ax


    ## GOVERNING FAILURE
    # Store all failure loads
    F_vRk_list = [F_vRk_FI, F_vRk_FII, F_vRk_FIII]
    failure_modes = [1, 2, 3]

    # Governing shear strength
    F_vRk = min([F_vRk_FI, F_vRk_FII, F_vRk_FIII])

    # Failure mode tag
    failure_mode_idx = F_vRk_list.index(F_vRk)
    failure_mode = failure_modes[failure_mode_idx]


# Single lap joints
else:
    ## FAILURE MODE I - UNEQUAL MEMBER THICKNESS
    # Governing timber member
    f_halphak = min(f_1_halphak*h_1, f_2_halphak*h_2)

    # Shear strength mode I_1
    F_vRk_FI_1 = f_halphak*d_f_inner


    ## FAILURE MODE I - EQUAL MEMBER THICKNESS
    # Shear strength mode I_2
    F_vRk_FI_2_Johansen = (f_1_halphak*h_1*d_f_inner)/(1+beta)*(m.sqrt(beta
    +2*beta**2*(1+h_2/h_1+(h_2/h_1)**2)+beta**3*(h_2/h_1)**2)-beta*(1+h_2/
    h_1))
    if F_vRk_ax > (perc_axial*F_vRk_FI_2_Johansen):
        F_vRk_FI_2 = F_vRk_FI_2_Johansen+perc_axial*F_vRk_FI_2_Johansen
    else:
        F_vRk_FI_2 = F_vRk_FI_2_Johansen+F_vRk_ax

    # Shear strength mode I
    F_vRk_FI = min(F_vRk_FI_1, F_vRk_FI_2)

```

```
93
94      ## FAILURE MODE II
95      # Shear strength mode II_1
96      F_vRk_FII_1_Johansen = 1.05*(f_1_halphak*h_1*d_f_inner/(2+beta))*(m.
        sqrt(2*beta*(1+beta)+(4*beta*(2+beta)*M_yRk)/(f_1_halphak*d_f_inner*h_1
        **2)) - beta)
97      if F_vRk_ax > (perc_axial*F_vRk_FII_1_Johansen):
98          F_vRk_FII_1 = F_vRk_FII_1_Johansen+perc_axial*F_vRk_FII_1_Johansen
99      else:
100         F_vRk_FII_1 = F_vRk_FII_1_Johansen+F_vRk_ax
101
102     # Shear strength mode II_2
103     F_vRk_FII_2_Johansen = 1.05*(f_1_halphak*h_2*d_f_inner/(1+2*beta))*(m.
        sqrt(2*beta**2*(1+beta)+(4*beta*(1+2*beta)*M_yRk)/(f_1_halphak*d_f_inner
        *h_2**2)) - beta)
104     if F_vRk_ax > (perc_axial*F_vRk_FII_2_Johansen):
105         F_vRk_FII_2 = F_vRk_FII_2_Johansen+perc_axial*F_vRk_FII_2_Johansen
106     else:
107         F_vRk_FII_2 = F_vRk_FII_2_Johansen+F_vRk_ax
108
109      # Shear strength mode II
110     F_vRk_FII = min(F_vRk_FII_1, F_vRk_FII_2)
111
112
113     ## FAILURE MODE III
114     # Shear strength mode III
115     F_vRk_FIII_Johansen = 1.15*m.sqrt((2*beta)/(1+beta))*m.sqrt(2*M_yRk*
        f_1_halphak*d_f_inner)
116     if F_vRk_ax > (perc_axial*F_vRk_FIII_Johansen):
117         F_vRk_FIII = F_vRk_FIII_Johansen+perc_axial*F_vRk_FIII_Johansen
118     else:
119         F_vRk_FIII = F_vRk_FIII_Johansen+F_vRk_ax
120
121
122     ## GOVERNING FAILURE
123     # Store all failure loads
124     F_vRk_list = [F_vRk_FI_1, F_vRk_FI_2, F_vRk_FII_1, F_vRk_FII_2,
        F_vRk_FIII]
125     failure_modes = [11, 12, 21, 22, 3]
126
127     # Governing shear strength
128     F_vRk = min(F_vRk_list)
129
130     # Failure mode tag
131     failure_mode_idx = F_vRk_list.index(F_vRk)
132     failure_mode = failure_modes[failure_mode_idx]
133
134
135 ## GROUP EFFECTS / EFFECTIVE FASTENERS
136 # Effective fasteners per row
137 n_eff_tmp = []
138 for i in range(0, len(n_row)):
```

```
139     if n_row[i] != 1:
140         n_eff_tmp_1 = n_row[i]
141         n_eff_tmp_2 = n_row[i]**0.9*(a1_row[i]/(13*d_f_nom))**(0.25)
142         n_eff_tmp.append(min(n_eff_tmp_1, n_eff_tmp_2))
143     else:
144         n_eff_tmp.append(n_row[i])
145 
146 # Shear resistance per row using governing shear strength
147 F_vRk_row = []
148 for i in range(0, len(n_row)):
149     F_tmp = n_eff_tmp[i]*F_vRk
150     F_vRk_row.append(F_tmp)
151 
152 # Shear resistance of fastener group
153 F_vRk_eff = sum(F_vRk_row)
154 if DLJ:
155     F_vRk_eff = 2*F_vRk_eff
156 F_vRk_eff_kN = F_vRk_eff/1000
```

D Analytical Adhesive Stress Analysis Summary

Analytical method	Material linearity				Adherends					Adhesive stresses			Solution	
	Adhesive		Adherend		Isotropic	Composite	Similar	Dissimilar		σ_x	σ_y	τ_{xy}	Closed-form	Numerical
	Linear	Nonlinear	Linear	Nonlinear				Thickness	Material					
Volkersen (1938)	X		X		X		X	X				X	X	
Goland and Reissner (1944)	X		X		X		X				X	X	X	
Wah (1973)	X		X		X	X	X	X				X	X	X
Hart-Smith (1973a, 1973b)	X	X	X		X		X				X	X	X	
Pirvics (1974)	X		X		X		X	X	X	X	X	X		X
Grimes and Greimann (1975)	X	X	X	X	X	X	X	X	X		X	X		X
Renton and Vinson (1975b)	X		X		X	X	X	X	X		X	X		
Srinivas (1975)	X		X		X	X	X	X	X		X	X	X	
Allman (1977)	X		X		X	X	X				X	X	X	

Figure D.1: Summary of both linear and nonlinear two-dimensional analytical models available in the literature (Campilho, 2017).

Analytical method	Material linearity				Adherends					Adhesive stresses			Solution	
	Adhesive		Adherend		Isotropic	Composite	Similar	Dissimilar		σ_x	σ_y	τ_{xy}	Closed-form	Numerical
	Linear	Nonlinear	Linear	Nonlinear				Thickness	Material					
Volkersen (1938)	X		X		X		X	X				X	X	
Goland and Reissner (1944)	X		X		X		X				X	X	X	
Wah (1973)	X		X		X	X	X	X				X	X	X
Hart-Smith (1973a, 1973b)	X	X	X		X		X				X	X	X	
Pirvics (1974)	X		X		X		X	X	X	X	X	X		X
Grimes and Greimann (1975)	X	X	X	X	X	X	X	X	X		X	X		X
Renton and Vinson (1975b)	X		X		X	X	X	X	X		X	X		
Srinivas (1975)	X		X		X	X	X	X	X		X	X	X	
Allman (1977)	X		X		X	X	X				X	X	X	

Figure D.2: Summary of both linear and nonlinear two-dimensional analytical models available in the literature (Campilho, 2017).

Analytical method	Material linearity				Adherends					Adhesive stresses			Solution	
	Adhesive		Adherend		Isotropic	Composite	Similar	Dissimilar		σ_x	σ_y	τ_{xy}	Closed-form	Numerical
	Linear	Nonlinear	Linear	Nonlinear				Thickness	Material					
Volkersen (1938)	X		X		X		X	X				X	X	
Goland and Reissner (1944)	X		X		X		X				X	X	X	
Wah (1973)	X		X		X	X	X	X				X	X	X
Hart-Smith (1973a, 1973b)	X	X	X		X		X				X	X	X	
Pirvics (1974)	X		X		X		X	X	X	X	X	X		X
Grimes and Greimann (1975)	X	X	X	X	X	X	X	X	X		X	X		X
Renton and Vinson (1975b)	X		X		X	X	X	X	X		X	X		
Srinivas (1975)	X		X		X	X	X	X	X		X	X	X	
Allman (1977)	X		X		X	X	X				X	X	X	

Figure D.3: Summary of both linear and nonlinear two-dimensional analytical models available in the literature (Campilho, 2017).

E Material Data Sheets

E.1 Rothoblaas KOS Fastener

KOS

CE
EN 14592

HEXAGONAL HEAD BOLT

- Cylindrical metal connector with CE marking according to EN 14592
- Carbon steel of strength grade 8.8 for all hexagonal head bolts (KOS)
- Hexagonal head bolt supplied with an incorporated nut (for the carbon steel version)
- Available also in A2 | AISI304 stainless steel for outdoor applications (service class 3)

KOS KOS A2

CODES AND DIMENSIONS

KOS – hexagonal head bolt with nut and CE marking

Steel class 8.8 - zinc plated
DIN 601 (ISO 4016*)

d [mm]	CODE	L [mm]	A_{max} [mm]	pcs
M12	KOS12100B	100	75	25
	KOS12120B	120	95	25
	KOS12140B	140	115	25
	KOS12160B	160	135	25
	KOS12180B	180	155	25
	KOS12200B	200	175	25
	KOS12220B	220	195	25
	KOS12240B	240	215	25
	KOS12260B	260	235	25
	KOS12280B	280	255	25
	KOS12300B	300	275	25
	KOS12320B	320	295	25
	KOS12340B	340	315	25
	KOS12360B	360	335	25
	KOS12380B	380	355	25
	KOS12400B	400	375	25
M16	KOS16140B	140	105	15
	KOS16160B	160	125	15
	KOS16180B	180	145	15
	KOS16200B	200	165	15
	KOS16220B	220	185	15
	KOS16240B	240	205	15
	KOS16260B	260	225	15
	KOS16280B	280	245	15
	KOS16300B	300	265	15
	KOS16320B	320	285	15
	KOS16340B	340	305	15
	KOS16360B	360	325	15
	KOS16380B	380	345	15
	KOS16400B	400	365	15
	KOS16420B	420	385	15
	KOS16440B	440	405	15
	KOS16460B	460	425	15
	KOS16500B	500	465	15

d [mm]	CODE	L [mm]	A_{max} [mm]	pcs
M20	KOS20120B	120	75	10
	KOS20140B	140	95	10
	KOS20160B	160	115	10
	KOS20180B	180	135	10
	KOS20200B	200	155	10
	KOS20220B	220	175	10
	KOS20240B	240	195	10
	KOS20260B	260	215	10
	KOS20280B	280	235	10
	KOS20300B	300	255	10
	KOS20320B	320	275	10
	KOS20340B	340	295	10
	KOS20360B	360	315	10
	KOS20380B	380	335	10
	KOS20400B	400	355	10
	KOS20420B	420	375	10
	KOS20440B	440	395	10
	KOS20460B	460	415	10

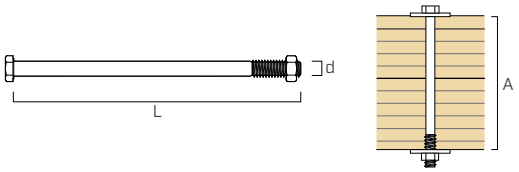

The maximum thickness A is evaluated considering a nut MUT934 and two ULS 440 washers.

* Standard ISO 4016 differs from standard DIN 601 in the M12 diameter for parameter SW.

KOS A2 | AISI304 - hexagonal head bolt

A2 | AISI304 stainless steel
DIN 931 (ISO 4014*)

d [mm]	CODE	L [mm]	pcs
M12	**AI60112100**	100	25
	AI60112120	120	25
	AI60112140	140	25
	AI60112160	160	10
	AI60112180	180	10
	AI60112200	200	10
	AI60112220	220	10
	AI60112240	240	10
	AI60112260	260	10
M16	**AI60116120**	120	25
	AI60116140	140	25
	AI60116150	150	25
	AI60116160	160	10
	AI60116180	180	10
	AI60116200	200	10
	AI60116220	220	10
	AI60116240	240	10
	AI60116260	260	10
	AI60116280	280	10
	AI60116300	300	10

d [mm]	CODE	L [mm]	pcs
M20	**AI60120160**	160	10
	AI60120180	180	10
	AI60120200	200	10
	AI60120220	220	10
	AI60120240	240	10
	AI60120260	260	10
	AI60120280	280	10
	AI60120300	300	5
	AI60120320	320	5
	AI60120340	340	5
	AI60120360	360	5
	AI60120380	380	5
	AI60120400	400	5

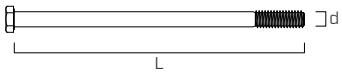

* Standard ISO 4014 differs from standard DIN 931 in the M12 diameter for parameter SW.

MATERIAL AND DURABILITY

KOS: strength grade 8.8 bright zinc plated carbon steel.
Use for service classes 1 and 2 (EN 1995-1-1).

KOS A2 | AISI304: A2 | AISI304 stainless steel.
To be used in service class 3 (EN 1995-1-1).

FIELD OF USE

- Timber-to-timber joints
- Timber-to-steel joints

EXTERNAL LOADS

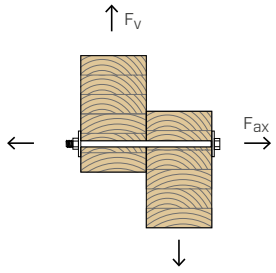

GEOMETRY AND MECHANICAL CHARACTERISTICS | KOS

Nominal diameter	d	[mm]		M12	M16	M20
Wrench	SW	[mm]		19	24	30
Head thickness	k	[mm]		7,5	10,0	12,5
Thread length	b	[mm]	L ≤ 125 mm	30	38	46
		[mm]	125 < L ≤ 200 mm	36	44	52
		[mm]	L > 200 mm	49	57	65

Design according to standard DIN 601 (ISO 4016) and DIN 931 (ISO 4014).

	steel		8,8	8,8	8,8
Material	$f_{u,k}$	[N/mm²]	800	800	800
	$f_{y,k}$	[N/mm²]	640	640	640
Characteristic yield moment	$M_{y,k}$	[Nmm]	153000	324000	579000

Mechanical parameters according to CE marking, in accordance with EN 14592.

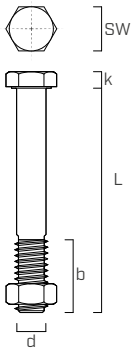

MINIMUM DISTANCES FOR CONNECTORS SUBJECTED TO SHEAR STRESS[1]

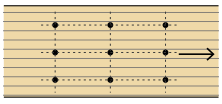

Load-to-grain angle α = 0°

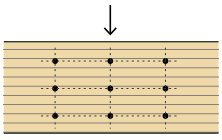

Load-to-grain angle α = 90°

		12	16	20	12	16	20
a_1	[mm]	60	80	100	48	64	80
a_2	[mm]	48	64	80	48	64	80
$a_{3,t}$	[mm]	84	112	140	84	112	140
$a_{3,c}$	[mm]	48	64	80	84	112	140
$a_{4,t}$	[mm]	36	48	60	48	64	80
$a_{4,c}$	[mm]	36	48	60	36	48	60

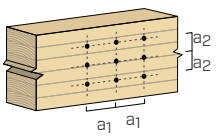

stressed end
-90° < α < 90°

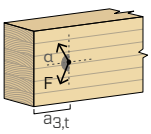

unloaded end
90° < α < 270°

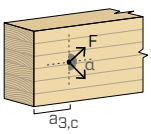

stressed edge
0° < α < 180°

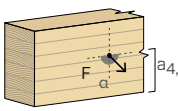

unload edge
180° < α < 360°

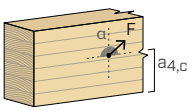

NOTES:

(1) The minimum distances are compliant with EN 1995-1-1.

STATIC VALUES | KOS

NODE WITH 3 WOODEN ELEMENTS

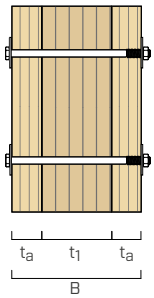

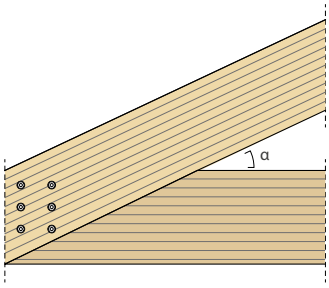

d	L	t_a	t_1	$R_{vk,0°}$	$R_{vk,30°}$	$R_{vk,45°}$	$R_{vk,60°}$	$R_{vk,90°}$
[mm]	[mm]	[mm]	[mm]	[kN]	[kN]	[kN]	[kN]	[kN]
	220	60	60	20,0	20,0	20,0	19,3	18,5
	240	60	80	22,5	21,2	20,2	19,3	18,5
	260	60	100	22,5	21,2	20,2	19,3	18,5
	280	60	120	22,5	21,2	20,2	19,3	18,5
12	300	80	100	26,0	24,3	22,9	21,7	20,7
	320	80	120	26,0	24,3	22,9	21,7	20,7
	340	80	140	26,0	24,3	22,9	21,7	20,7
	360	80	160	26,0	24,3	22,9	21,7	20,7
	≥ 380	-	-	26,8	26,1	25,4	24,4	23,2
	280	80	80	33,9	33,9	33,8	32,2	30,5
	300	80	100	38,1	35,7	33,8	32,2	30,5
	320	80	120	38,1	35,7	33,8	32,2	30,5
	340	80	140	38,1	35,7	33,8	32,2	30,5
	360	80	160	38,1	35,7	33,8	32,2	30,5
16	380	100	140	42,7	39,6	37,2	35,2	33,5
	400	100	160	42,7	39,6	37,2	35,2	33,5
	420	100	180	42,7	39,6	37,2	35,2	33,5
	440	100	200	42,7	39,6	37,2	35,2	33,5
	460	120	180	44,7	43,3	40,9	38,5	36,4
	500	120	220	44,7	43,3	40,9	38,5	36,4
	380	100	120	55,8	51,9	48,9	46,4	44,0
	400	100	140	55,8	51,9	48,9	46,4	44,0
20	420	100	160	55,8	51,9	48,9	46,4	44,0
	440	100	180	55,8	51,9	48,9	46,4	44,0
	460	120	160	61,2	56,4	52,7	49,7	47,2

GENERAL PRINCIPLES:

- Characteristic values according to EN 1995-1-1.
- The design values are obtained from the characteristic values as follows:

$$R_d = \frac{R_k \cdot k_{mod}}{\gamma_M}$$

  The coefficients γ_M and k_{mod} should be taken according to the current regulations used for the calculation.
- For the calculation process a timber density ρ_k = 385 kg/m^3 has been considered.
- Dimensioning and verification of the timber elements must be carried out separately.
- The calculation was made taking into account the hollow effect of the bolt with DIN 9021 washers.
- The angle of inclination indicated for R_{vk} is referred to the two external elements.

STATIC VALUES | KOS

NODE WITH 2 METAL BITS IN A WOODEN ELEMENT

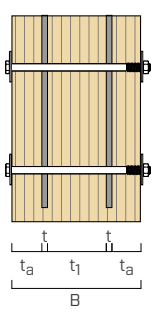

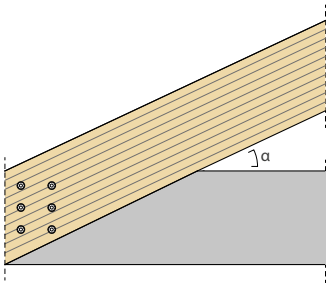

d	L	B	t_a	t_1	$R_{vk,0°}$	$R_{vk,30°}$	$R_{vk,45°}$	$R_{vk,60°}$	$R_{vk,90°}$
[mm]	[mm]	[mm]	[mm]	[mm]	[kN]	[kN]	[kN]	[kN]	[kN]
12	140	100	29	45	34,3	30,3	27,1	24,6	22,4
	160	120	39	45	39,1	36,0	32,4	29,3	26,8
	180	140	39	65	45,8	41,9	37,7	34,1	31,2
	200	160	39	85	50,9	47,8	43,0	38,9	35,5
	220	180	49	85	52,0	48,6	44,6	41,4	38,7
	240	200	49	105	52,0	48,9	46,4	44,3	42,6
	260	220	59	105	53,6	50,2	47,5	45,2	43,3
	280	240	59	125	53,6	50,2	47,5	45,2	43,3
16	140	100	29	35	39,5	34,4	30,5	27,4	24,8
	160	120	29	55	47,9	41,8	37,0	33,2	30,2
	180	140	39	55	56,4	49,2	43,6	39,1	35,5
	200	160	39	75	64,9	56,6	50,1	45,0	40,8
	220	180	39	95	73,4	64,0	56,7	50,9	46,2
	240	200	49	95	80,5	71,4	63,2	56,8	51,5
	260	220	59	95	81,7	73,7	67,5	62,5	56,8
	280	240	59	115	86,1	80,7	74,0	68,4	62,2
20	160	100	28	47	52,0	44,8	39,3	35,0	31,5
	180	120	29	65	62,1	53,4	46,9	41,8	37,7
	200	140	29	85	72,2	62,1	54,5	48,6	43,8
	220	160	39	85	82,3	70,8	62,1	55,4	49,9
	240	180	49	85	92,4	79,5	69,8	62,1	56,0
	260	200	49	105	102,5	88,2	77,4	68,9	62,1
	280	220	59	105	111,2	96,9	85,0	75,7	68,3
	300	240	59	125	121,3	105,6	92,6	82,5	74,4

CORRECTIVE COEFFICIENT k_F FOR DIFFERENT DENSITIES ρ_k

Strength class	C24	GL22h	C30	GL24h	C40 / GL32c	GL28h	D24	D30
ρ_k [kg/m^3]	350	370	380	385	400	425	485	530
k_F	0,91	0,96	0,99	1,00	1,02	1,04	1,17	1,23

For different densities ρ_k the wood-side design resistance is calculated as: $R'_{v,d} = R_{v,d} \cdot k_F$.

GENERAL PRINCIPLES:

- Characteristic values according to EN 1995-1-1.
- The design values are obtained from the characteristic values as follows:

$$R_d = \frac{R_k \cdot k_{mod}}{\gamma_M}$$

  The coefficients γ_M and k_{mod} should be taken according to the current regulations used for the calculation.
- The values provided are calculated using 5 mm thick plates, a 6 mm thick milled cut in the timber and a single KOS bolt.
- For the calculation process a timber density ρ_k = 385 kg/m^3 has been considered.
- Dimensioning and verification of the timber elements must be carried out separately.
- The calculation was made taking into account the hollow effect of the bolt with DIN 9021 washers.
- The angle of inclination indicated for R_{vk} is referred to the two external elements.

E.2 Rothoblaas VGS Fastener

VGS

UKTA-0836 22/6195 | AC233 ESR-4645 | ETA-11/0030

FULLY THREADED SCREW WITH COUNTERSUNK OR HEXAGONAL HEAD

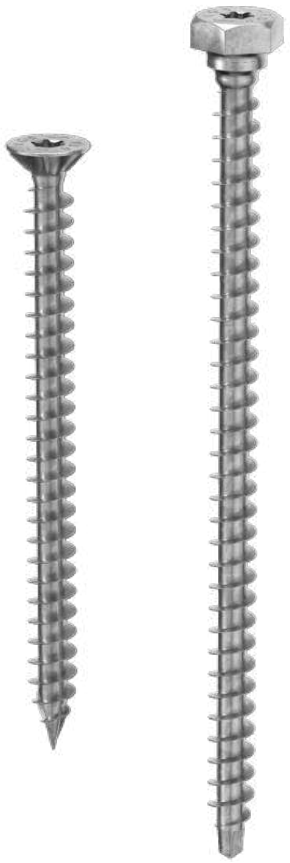

3 THORNS TIP

Thanks to the 3 THORNS tip, minimum installation distances are reduced. More screws can be used in less space and larger screws in smaller elements.
Costs and time for project implementation are reduced.

CERTIFICATION FOR TIMBER AND CONCRETE

Structural connector approved for timber applications according to ETA-11/0030 and for timber-concrete applications according to ETA-22/0806.

TENSILE STRENGTH

Deep thread and high strength steel for excellent tensile or sliding performance. Approved for structural applications subject to stresses in any direction vs the grain (0° ÷ 90°).
Can be used on steel plates in combination with the VGU and HUS washers.

COUNTERSUNK OR HEXAGONAL HEAD

Countersunk head up to L = 600 mm, ideal for use on plates or for concealed reinforcements. Hexagonal head L > 600 mm to facilitate gripping with screwdriver.

MY PROJECT SOFTWARE | MANUALS | BIT INCLUDED

DIAMETER [mm]	9 **9** — **15** 15
LENGTH [mm]	80 **80** — **2000** 2000
SERVICE CLASS	SC1 SC2
ATMOSPHERIC CORROSIVITY	C1 C2
WOOD CORROSIVITY	T1 T2
MATERIAL	Zn ELECTRO PLATED — electrogalvanized carbon steel

METAL-to-TIMBER recommended use:

NO IMPACT | TORQUE LIMITER | $M_{ins,rec}$

FIELDS OF USE

- timber based panels
- solid timber
- glulam (Glued Laminated Timber)
- CLT and LVL
- high density woods

TC FUSION

The ETA-22/0806 approval of the TC FUSION system allows the VGS screws to be used together with the reinforcements in the concrete so that the panel floor slabs and the bracing core can be bonded together with a small integration of the casting.

GEOMETRY AND MECHANICAL CHARACTERISTICS

VGS Ø9

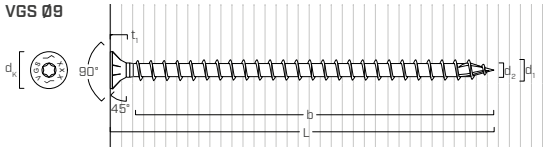

L ≤ 520 mm

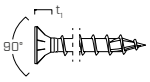

L > 520 mm

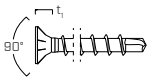

VGS Ø11

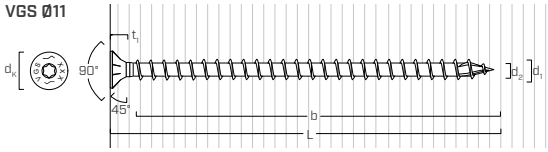

L ≤ 250 mm

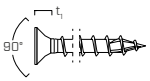

250 mm < L ≤ 600 mm

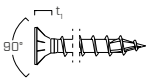

L > 600 mm

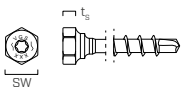

VGS Ø13

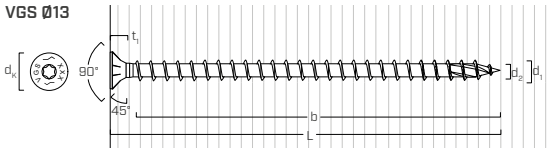

L ≤ 250 mm

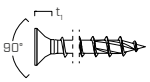

250 mm < L ≤ 600 mm

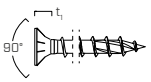

L > 600 mm

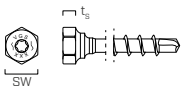

VGS Ø15

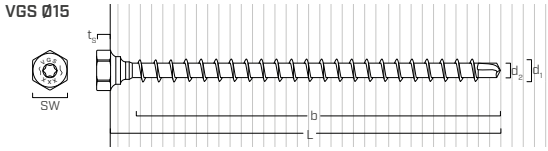

L > 600 mm

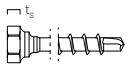

Nominal diameter	**d_1**	**[mm]**	**9**	**11**	**11**	**13**	**13**	**15**
Length	L	[mm]	-	≤ 600 mm	> 600 mm	≤ 600 mm	> 600 mm	-
Countersunk head diameter	d_K	[mm]	16,00	19,30	-	22,00	-	-
Countersunk head thickness	t_1	[mm]	6,50	8,20	-	9,40	-	-
Wrench size	SW	-	-	-	SW 17	-	SW 19	SW22
Hexagonal head thickness	t_s	[mm]	-	-	6,40	-	7,50	8,80
Thread diameter	d_2	[mm]	5,90	6,60	6,60	8,00	8,00	9,10
Pre-drilling hole diameter(1)	$d_{V,S}$	[mm]	5,0	6,0	6,0	8,0	8,0	9,00
Pre-drilling hole diameter(2)	$d_{V,H}$	[mm]	6,0	7,0	7,0	9,0	9,0	10,00
Characteristic tensile strength	$f_{tens,k}$	[kN]	25,4	38,0	38,0	53,0	53,0	65,0
Characteristic yield moment	$M_{y,k}$	[Nm]	27,2	45,9	45,9	70,9	70,9	95,0
Characteristic yield strength	$f_{y,k}$	[N/mm²]	1000	1000	1000	1000	1000	1000

(1) Pre-drilling valid for softwood.
(2) Pre-drilling valid for hardwood and beech LVL.
The mechanical parameters for VGS Ø15 are obtained analytically and validated by experimental tests.

			softwood *(softwood)*	**LVL softwood** *(LVL softwood)*	**pre-drilled beech LVL** *(beech LVL predrilled)*
Withdrawal resistance parameter	$f_{ax,k}$	[N/mm²]	11,7	15,0	29,0
Associated density	ρ_a	[kg/m³]	350	500	730
Calculation density	ρ_k	*[kg/m³]*	*≤ 440*	*410 ÷ 550*	*590 ÷ 750*

For applications with different materials please see ETA-11/0030.

TC FUSION SYSTEM FOR TIMBER-CONCRETE APPLICATION

Nominal diameter	**d_1**	**[mm]**	**9**	**11**	**13**	**15**
Tangential strength of adhesion in concrete C25/30	$f_{b,k}$	[N/mm²]	12,5	12,5	12,5	-

For applications with different materials please see ETA-22/0806

CODES AND DIMENSIONS

d_1 [mm]	CODE	L [mm]	b [mm]	pcs	
9 TX40	VGS9100	100	90	25	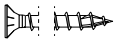
	VGS9120	120	110	25	
	VGS9140	140	130	25	
	VGS9160	160	150	25	
	VGS9180	180	170	25	
	VGS9200	200	190	25	
	VGS9220	220	210	25	
	VGS9240	240	230	25	
	VGS9260	260	250	25	
	VGS9280	280	270	25	
	VGS9300	300	290	25	
	VGS9320	320	310	25	
	VGS9340	340	330	25	
	VGS9360	360	350	25	
	VGS9380	380	370	25	
	VGS9400	400	390	25	
	VGS9440	440	430	25	
	VGS9480	480	470	25	
	VGS9520	520	510	25	
	VGS9560	560	550	25	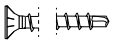
	VGS9600	600	590	25	
11 TX 50	VGS1180	80	70	25	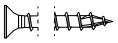
	VGS11100	100	90	25	
	VGS11125	125	115	25	
	VGS11150	150	140	25	
	VGS11175	175	165	25	
	VGS11200	200	190	25	
	VGS11225	225	215	25	
	VGS11250	250	240	25	
	VGS11275	275	265	25	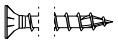
	VGS11300	300	290	25	
	VGS11325	325	315	25	
	VGS11350	350	340	25	
	VGS11375	375	365	25	
	VGS11400	400	390	25	
	VGS11425	425	415	25	
	VGS11450	450	440	25	
	VGS11475	475	465	25	
	VGS11500	500	490	25	
	VGS11525	525	515	25	
	VGS11550	550	540	25	
	VGS11575	575	565	25	
	VGS11600	600	590	25	
11 SW 17 TX 50	VGS11650	650	630	25	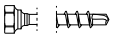
	VGS11700	700	680	25	
	VGS11750	750	680	25	
	VGS11800	800	780	25	
	VGS11850	850	830	25	
	VGS11900	900	880	25	
	VGS11950	950	930	25	
	VGS111000	1000	980	25	

d_1 [mm]	CODE	L [mm]	b [mm]	pcs	
13 TX 50	VGS1380	80	70	25	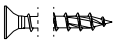
	VGS13100	100	90	25	
	VGS13150	150	140	25	
	VGS13200	200	190	25	
	VGS13250	250	240	25	
	VGS13300	300	280	25	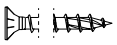
	VGS13350	350	330	25	
	VGS13400	400	380	25	
	VGS13450	450	430	25	
	VGS13500	500	480	25	
	VGS13550	550	530	25	
	VGS13600	600	580	25	
13 SW 19 TX 50	VGS13650	650	630	25	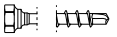
	VGS13700	700	680	25	
	VGS13750	750	730	25	
	VGS13800	800	780	25	
	VGS13850	850	830	25	
	VGS13900	900	880	25	
	VGS13950	950	930	25	
	VGS131000	1000	980	25	
	VGS131100	1100	1080	25	
	VGS131200	1200	1180	25	
	VGS131300	1300	1280	25	
	VGS131400	1400	1380	25	
	VGS131500	1500	1480	25	
15 SW 21 TX 50	VGS15600	600	580	25	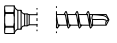
	VGS15700	700	680	25	
	VGS15800	800	780	25	
	VGS15900	900	880	25	
	VGS151000	1000	980	25	
	VGS151200	1200	1180	25	
	VGS151400	1400	1380	25	
	VGS151600	1600	1580	25	
	VGS151800	1800	1780	25	
	VGS152000	2000	1980	25	

RELATED PRODUCTS

VGU
45° WASHER FOR VGS

page 190

TORQUE LIMITER
TORQUE LIMITER

page 408

WASP
HOOK FOR TIMBER ELEMENTS TRANSPORT

page 413

MINIMUM DISTANCES FOR AXIAL STRESSES

screws inserted **WITH and WITHOUT pre-drilled hole**



d_1	[mm]		9	11
a_1	[mm]	**5·d**	45	55
a_2	[mm]	**5·d**	45	55
$a_{2,LIM}$	[mm]	**2,5·d**	23	28
$a_{1,CG}$	[mm]	**8·d**	72	88
$a_{2,CG}$	[mm]	**3·d**	27	33
a_{CROSS}	[mm]	**1,5·d**	14	17

d_1	[mm]		13
a_1	[mm]	**5·d**	65
a_2	[mm]	**5·d**	65
$a_{2,LIM}$	[mm]	**2,5·d**	33
$a_{1,CG}$	[mm]	**8·d**	104
$a_{2,CG}$	[mm]	**3·d**	39
a_{CROSS}	[mm]	**1,5·d**	20

d_1	[mm]		9	11	13	15
a_1	[mm]	**5·d**	45	55	65	75
a_2	[mm]	**5·d**	45	55	65	75
$a_{2,LIM}$	[mm]	**2,5·d**	23	28	33	38
$a_{1,CG}$	[mm]	**5·d**	45	55	65	150
$a_{2,CG}$	[mm]	**3·d**	27	33	39	60
a_{CROSS}	[mm]	**1,5·d**	14	17	20	23

SCREWS UNDER TENSION INSERTED WITH AN ANGLE α WITH RESPECT TO THE GRAIN

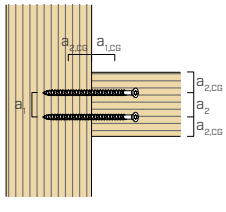

plan front

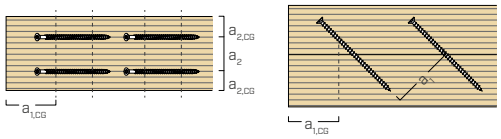

plan front

SCREWS INSERTED WITH α = 90° ANGLE WITH RESPECT TO THE GRAIN

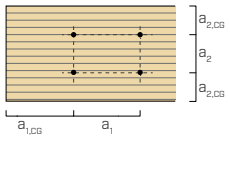

plan front

CROSS SCREWS INSERTED WITH AN ANGLE α WITH RESPECT TO THE GRAIN

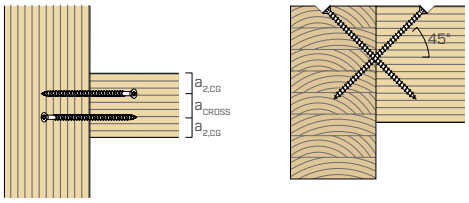

plan front

NOTES

- Minimum distances according to ETA-11/0030.
- The minimum distances are independent of the insertion angle of the connector and the angle of the force with respect to the grain.
- The axial distance a_2 can be reduced down to $a_{2,LIM}$ if for each connector a "joint surface" $a_1 \cdot a_2 = 25 \cdot d_1^2$ is maintained.
- For 3 THORNS tip, RBSN and self-drilling tip screws, the minimum distances in the table are derived from experimental tests; alternatively, adopt $a_{1,CG} = 10 \cdot d$ and $a_{2,CG} = 4 \cdot d$ in accordance with EN 1995:2014.

EFFECTIVE THREAD USED IN CALCULATION

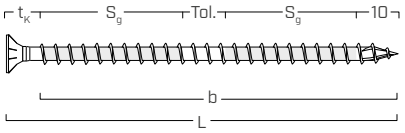

b = $S_{g,tot} = L - t_K$ represents the entire length of the threaded part

$S_g = (L - t_K - 10\ mm - Tol.)/2$ represents the partial length of the threaded part net of a laying tolerance (Tol.) of 10 mm

t_K = 10 mm (countersunk head)
t_K = 20 mm (hexagonal head)

MINIMUM DISTANCES FOR SHEAR LOADS

screws inserted **WITHOUT pre-drilled hole** — $\rho_k \leq 420$ kg/m^3

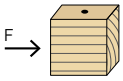

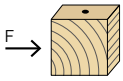

d_1	[mm]		9	11	13	15
a_1	[mm]	**10·d**	90	110	130	150
a_2	[mm]	**5·d**	45	55	65	75
$a_{3,t}$	[mm]	**15·d**	135	165	195	225
$a_{3,c}$	[mm]	**10·d**	90	110	130	150
$a_{4,t}$	[mm]	**5·d**	45	55	65	75
$a_{4,c}$	[mm]	**5·d**	45	55	65	75

d_1	[mm]		9	11	13	15
a_1	[mm]	**5·d**	45	55	65	75
a_2	[mm]	**5·d**	45	55	65	75
$a_{3,t}$	[mm]	**10·d**	90	110	130	150
$a_{3,c}$	[mm]	**10·d**	90	110	130	150
$a_{4,t}$	[mm]	**10·d**	90	110	130	150
$a_{4,c}$	[mm]	**5·d**	45	55	65	75

screws inserted **WITH pre-drilled hole**

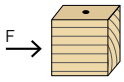

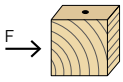

d_1	[mm]		9	11	13	15
a_1	[mm]	**5·d**	45	55	65	75
a_2	[mm]	**3·d**	27	33	39	45
$a_{3,t}$	[mm]	**12·d**	108	132	156	180
$a_{3,c}$	[mm]	**7·d**	63	77	91	105
$a_{4,t}$	[mm]	**3·d**	27	33	39	45
$a_{4,c}$	[mm]	**3·d**	27	33	39	45

d_1	[mm]		9	11	13	15
a_1	[mm]	**4·d**	36	44	52	60
a_2	[mm]	**4·d**	36	44	52	60
$a_{3,t}$	[mm]	**7·d**	63	77	91	105
$a_{3,c}$	[mm]	**7·d**	63	77	91	105
$a_{4,t}$	[mm]	**7·d**	63	77	91	105
$a_{4,c}$	[mm]	**3·d**	27	33	39	45

α = load-to-grain angle
d = d_1 = nominal screw diameter

stressed end
$-90° < \alpha < 90°$

unloaded end
$90° < \alpha < 270°$

stressed edge
$0° < \alpha < 180°$

unload edge
$180° < \alpha < 360°$

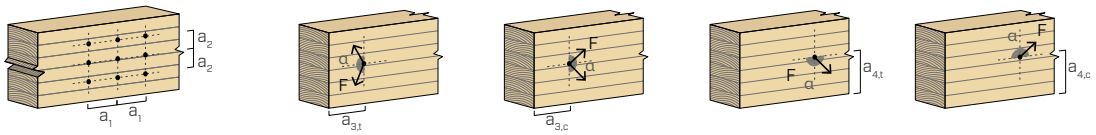

NOTES

- Minimum distances are in accordance with EN 1995:2014 as per ETA-11/0030 considering a timber characteristic density of $\rho_k \leq 420$ kg/m^3.
- The minimum spacing for all steel-to-timber connections (a_1, a_2) can be multiplied by a coefficient of 0,7.
- The minimum spacing for all panel-to-timber connections (a_1, a_2) can be multiplied by a coefficient of 0,85.
- The spacing a_1 in the table for screws with 3 THORNS tip inserted without pre-drilling hole in timber elements with density $\rho_k \leq 420$ kg/m^3 and load-to-grain angle α=0° was assumed to be 10·d based on experimental tests; alternatively, adopt 12·d in accordance with EN 1995:2014.

EFFECTIVE NUMBER FOR SHEAR LOADS

The load-bearing capacity of a connection made with several screws, all of the same type and size, may be lower than the sum of the load-bearing capacities of the individual connection system. For a row of n screws arranged parallel to the direction of the grain at a distance a_1, the characteristic effective load-bearing capacity is equal to:

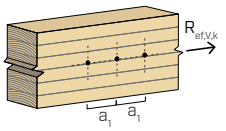

$$R_{ef,V,k} = n_{ef} \cdot R_{V,k}$$

The n_{ef} value is given in the table below as a function of n and a_1.

		a_1(*)										
		4·d	**5·d**	**6·d**	**7·d**	**8·d**	**9·d**	**10·d**	**11·d**	**12·d**	**13·d**	**≥ 14·d**
n	**2**	1,41	1,48	1,55	1,62	1,68	1,74	1,80	1,85	1,90	1,95	2,00
	3	1,73	1,86	2,01	2,16	2,28	2,41	2,54	2,65	2,76	2,88	3,00
	4	2,00	2,19	2,41	2,64	2,83	3,03	3,25	3,42	3,61	3,80	4,00
	5	2,24	2,49	2,77	3,09	3,34	3,62	3,93	4,17	4,43	4,71	5,00

(*)For intermediate a_1 values a linear interpolation is possible.

STRUCTURAL VALUES | TIMBER

CHARACTERISTIC VALUES
EN 1995:2014

TENSION / COMPRESSION

geometry		total thread withdrawal				partial thread withdrawal				steel tension	instability
		ε=90°		ε=0°		ε=90°		ε=0°			ε=90°
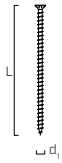		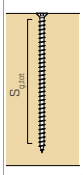		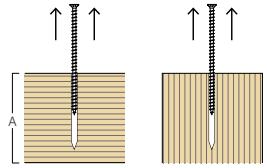		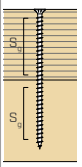		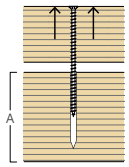		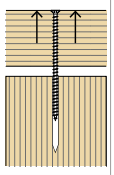	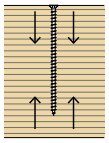
d_1	L	$S_{g,tot}$	A_{min}	$R_{ax,90,k}$	$R_{ax,0,k}$	S_g	A_{min}	$R_{ax,90,k}$	$R_{ax,0,k}$	$R_{tens,k}$	$R_{ki,90,k}$
[mm]	[mm]	[mm]	[mm]	[kN]	[kN]	[mm]	[mm]	[kN]	[kN]	[kN]	[kN]
9	100	90	110	10,23	3,07	35	55	3,98	1,19	25,40	17,25
	120	110	130	12,50	3,75	45	65	5,11	1,53		
	140	130	150	14,77	4,43	55	75	6,25	1,88		
	160	150	170	17,05	5,11	65	85	7,39	2,22		
	180	170	190	19,32	5,80	75	95	8,52	2,56		
	200	190	210	21,59	6,48	85	105	9,66	2,90		
	220	210	230	23,87	7,16	95	115	10,80	3,24		
	240	230	250	26,14	7,84	105	125	11,93	3,58		
	260	250	270	28,41	8,52	115	135	13,07	3,92		
	280	270	290	30,68	9,21	125	145	14,21	4,26		
	300	290	310	32,96	9,89	135	155	15,34	4,60		
	320	310	330	35,23	10,57	145	165	16,48	4,94		
	340	330	350	37,50	11,25	155	175	17,61	5,28		
	360	350	370	39,78	11,93	165	185	18,75	5,63		
	380	370	390	42,05	12,61	175	195	19,89	5,97		
	400	390	410	44,32	13,30	185	205	21,02	6,31		
	440	430	450	48,87	14,66	205	225	23,30	6,99		
	480	470	490	53,41	16,02	225	245	25,57	7,67		
	520	510	530	57,96	17,39	245	265	27,84	8,35		
	560	550	570	62,50	18,75	265	285	30,12	9,03		
	600	590	610	67,05	20,11	285	305	32,39	9,72		
11	80	70	90	9,72	2,92	25	45	3,47	1,04	38,00	21,93
	100	90	110	12,50	3,75	35	55	4,86	1,46		
	125	115	135	15,97	4,79	48	68	6,60	1,98		
	150	140	160	19,45	5,83	60	80	8,33	2,50		
	175	165	185	22,92	6,88	73	93	10,07	3,02		
	200	190	210	26,39	7,92	85	105	11,81	3,54		
	225	215	235	29,86	8,96	98	118	13,54	4,06		
	250	240	260	33,34	10,00	110	130	15,28	4,58		
	275	265	285	36,81	11,04	123	143	17,01	5,10		
	300	290	310	40,28	12,08	135	155	18,75	5,63		
	325	315	335	43,75	13,13	148	168	20,49	6,15		
	350	340	360	47,22	14,17	160	180	22,22	6,67		
	375	365	385	50,70	15,21	173	193	23,96	7,19		
	400	390	410	54,17	16,25	185	205	25,70	7,71		
	425	415	435	57,64	17,29	198	218	27,43	8,23		
	450	440	460	61,11	18,33	210	230	29,17	8,75		
	475	465	485	64,59	19,38	223	243	30,90	9,27		
	500	490	510	68,06	20,42	235	255	32,64	9,79		
	525	515	535	71,53	21,46	248	268	34,38	10,31		
	550	540	560	75,00	22,50	260	280	36,11	10,83		
	575	565	585	78,48	23,54	273	293	37,85	11,35		
	600	590	610	81,95	24,58	285	305	39,59	11,88		
	650	630	660	87,51	26,25	305	325	42,36	12,71		
	700	680	710	94,45	28,33	330	350	45,84	13,75		
	750	680	760	94,45	28,33	330	350	45,84	13,75		
	800	780	810	108,34	32,50	380	400	52,78	15,83		
	850	830	860	115,28	34,59	405	425	56,25	16,88		
	900	880	910	122,23	36,67	430	450	59,73	17,92		
	950	930	960	129,17	38,75	455	475	63,20	18,96		
	1000	980	1010	136,12	40,84	480	500	66,67	20,00		

STRUCTURAL VALUES | TIMBER

CHARACTERISTIC VALUES
EN 1995:2014

TENSION / COMPRESSION

geometry		total thread withdrawal ε=90°			total thread withdrawal ε=0°	partial thread withdrawal ε=90°			partial thread withdrawal ε=0°	steel tension	instability ε=90°
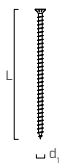		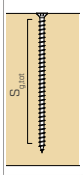	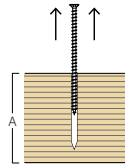		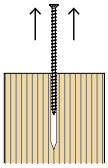	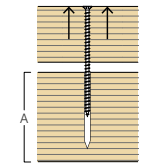			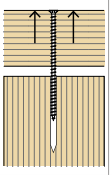		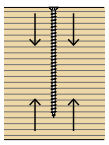
d_1	L	$S_{g,tot}$	A_{min}	$R_{ax,90,k}$	$R_{ax,0,k}$	S_g	A_{min}	$R_{ax,90,k}$	$R_{ax,0,k}$	$R_{tens,k}$	$R_{ki,90,k}$
[mm]	[mm]	[mm]	[mm]	[kN]	[kN]	[mm]	[mm]	[kN]	[kN]	[kN]	[kN]
13	80	70	90	11,49	3,45	25	45	4,10	1,23	53,00	32,69
	100	90	110	14,77	4,43	35	55	5,75	1,72		
	150	140	160	22,98	6,89	60	80	9,85	2,95		
	200	190	210	31,19	9,36	85	105	13,95	4,19		
	250	240	260	39,40	11,82	110	130	18,06	5,42		
	300	280	310	45,96	13,79	130	150	21,34	6,40		
	350	330	360	54,17	16,25	155	175	25,44	7,63		
	400	380	410	62,38	18,71	180	200	29,55	8,86		
	450	430	460	70,58	21,18	205	225	33,65	10,10		
	500	480	510	78,79	23,64	230	250	37,75	11,33		
	550	530	560	87,00	26,10	255	275	41,86	12,56		
	600	580	610	95,21	28,56	280	300	45,96	13,79		
	650	630	660	103,42	31,02	305	325	50,07	15,02		
	700	680	710	111,62	33,49	330	350	54,17	16,25		
	750	730	760	119,83	35,95	355	375	58,27	17,48		
	800	780	810	128,04	38,41	380	400	62,38	18,71		
	850	830	860	136,25	40,87	405	425	66,48	19,94		
	900	880	910	144,45	43,34	430	450	70,58	21,18		
	950	930	960	152,66	45,80	455	475	74,69	22,41		
	1000	980	1010	160,87	48,26	480	500	78,79	23,64		
	1100	1080	1110	177,28	53,18	530	550	87,00	26,10		
	1200	1180	1210	193,70	58,11	580	600	95,21	28,56		
	1300	1280	1310	210,11	63,03	630	650	103,42	31,02		
	1400	1380	1410	226,53	67,96	680	700	111,62	33,49		
	1500	1480	1510	242,94	72,88	730	750	119,83	35,95		
15	600	580	610	109,85	32,96	280	300	53,03	15,91	65,00	42,86
	700	680	710	128,80	38,64	330	350	62,50	18,75		
	800	780	810	147,74	44,32	380	400	71,97	21,59		
	900	880	910	166,68	50,00	430	450	81,44	24,43		
	1000	980	1010	185,62	55,69	480	500	90,91	27,27		
	1200	1180	1210	223,50	67,05	580	600	109,85	32,96		
	1400	1380	1410	261,38	78,41	680	700	128,80	38,64		
	1600	1580	1610	299,26	89,78	780	800	147,74	44,32		
	1800	1780	1810	337,14	101,14	880	900	166,68	50,00		
	2000	1980	2010	375,02	112,51	980	1000	185,62	55,69		

ε = screw-to-grain angle

NOTES and **GENERAL PRINCIPLES** on page 176.

STRUCTURAL VALUES | TIMBER

CHARACTERISTIC VALUES
EN 1995:2014

		SLIDING									SHEAR			
geometry		timber-to-timber				steel-to-timber				steel tension			timber-to-timber ε=90°	timber-to-timber ε=0°
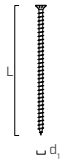		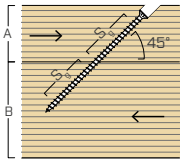				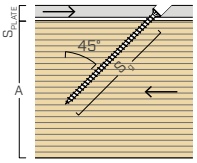				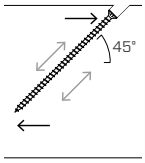	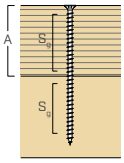		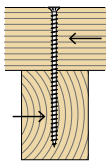	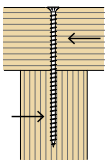
d_1 [mm]	L [mm]	S_g [mm]	A [mm]	B_{min} [mm]	$R_{V,k}$ [kN]	S_{PLATE} [mm]	S_g [mm]	A_{min} [mm]	$R_{V,k}$ [kN]	$R_{tens,45,k}$ [kN]	S_g [mm]	A [mm]	$R_{V,90,k}$ [mm]	$R_{V,0,k}$ [kN]
9	100	35	40	55	2,81	15	85	80	6,83	17,96	35	50	4,04	2,07
	120	45	45	60	3,62		105	95	8,44		45	60	4,53	2,30
	140	55	55	70	4,42		125	110	10,04		55	70	4,81	2,55
	160	65	60	75	5,22		145	125	11,65		65	80	5,10	2,81
	180	75	70	85	6,03		165	135	13,26		75	90	5,38	3,08
	200	85	75	90	6,83		185	150	14,87		85	100	5,67	3,18
	220	95	85	100	7,63		205	165	16,47		95	110	5,95	3,27
	240	105	90	105	8,44		225	180	18,08		105	120	6,23	3,35
	260	115	95	110	9,24		245	195	19,69		115	130	6,50	3,44
	280	125	105	120	10,04		265	205	21,29		125	140	6,50	3,52
	300	135	110	125	10,85		285	220	22,90		135	150	6,50	3,61
	320	145	120	135	11,65		305	235	24,51		145	160	6,50	3,69
	340	155	125	140	12,46		325	250	26,12		155	170	6,50	3,78
	360	165	130	145	13,26		345	265	27,72		165	180	6,50	3,86
	380	175	140	155	14,06		365	280	29,33		175	190	6,50	3,95
	400	185	145	160	14,87		385	290	30,94		185	200	6,50	4,03
	440	205	160	175	16,47		425	320	34,15		205	220	6,50	4,21
	480	225	175	190	18,08		465	350	37,37		225	240	6,50	4,38
	520	245	190	205	19,69		505	375	40,58		245	260	6,50	4,55
	560	265	205	220	21,29		545	405	43,79		265	280	6,50	4,72
	600	285	215	230	22,90		585	435	47,01		285	300	6,50	4,89
11	80	25	35	50	2,46	18	60	60	5,89	26,87	25	40	3,67	2,16
	100	35	40	55	3,44		80	75	7,86		35	50	4,72	2,69
	125	48	50	65	4,67		105	95	10,31		48	63	6,03	2,99
	150	60	60	75	5,89		130	110	12,77		60	75	6,61	3,33
	175	73	65	80	7,12		155	130	15,22		73	88	7,05	3,71
	200	85	75	90	8,35		180	145	17,68		85	100	7,48	4,10
	225	98	85	100	9,58		205	165	20,13		98	113	7,92	4,44
	250	110	95	110	10,80		230	185	22,59		110	125	8,35	4,57
	275	123	100	115	12,03		255	200	25,04		123	138	8,79	4,70
	300	135	110	125	13,26		280	220	27,50		135	150	9,06	4,83
	325	148	120	135	14,49		305	235	29,96		148	163	9,06	4,96
	350	160	130	145	15,71		330	255	32,41		160	175	9,06	5,09
	375	173	140	155	16,94		355	270	34,87		173	188	9,06	5,22
	400	185	145	160	18,17		380	290	37,32		185	200	9,06	5,35
	425	198	155	170	19,40		405	305	39,78		198	213	9,06	5,48
	450	210	165	180	20,63		430	325	42,23		210	225	9,06	5,61
	475	223	175	190	21,85		455	340	44,69		223	238	9,06	5,74
	500	235	180	195	23,08		480	360	47,14		235	250	9,06	5,87
	525	248	190	205	24,31		505	375	49,60		248	263	9,06	6,00
	550	260	200	215	25,54		530	395	52,05		260	275	9,06	6,13
	575	273	210	225	26,76		555	410	54,51		273	288	9,06	6,26
	600	285	215	230	27,99		580	430	56,96		285	300	9,06	6,39
	650	305	230	245	29,96		-	-	-		305	320	9,06	6,60
	700	330	250	265	32,41		-	-	-		330	345	9,06	6,85
	750	330	250	265	32,41		-	-	-		330	345	9,06	6,85
	800	380	285	300	37,32		-	-	-		380	395	9,06	6,85
	850	405	300	315	39,78		-	-	-		405	420	9,06	6,85
	900	430	320	335	42,23		-	-	-		430	445	9,06	6,85
	950	455	335	350	44,69		-	-	-		455	470	9,06	6,85
	1000	480	355	370	47,14		-	-	-		480	495	9,06	6,85

STRUCTURAL VALUES | TIMBER

CHARACTERISTIC VALUES
EN 1995:2014

		SLIDING									SHEAR			
geometry		timber-to-timber				steel-to-timber				steel tension			timber-to-timber ε=90°	timber-to-timber ε=0°
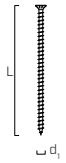		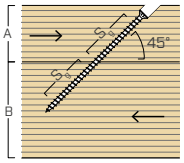				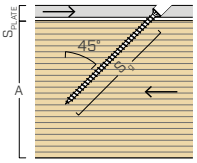				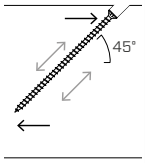	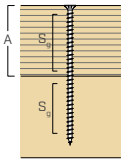		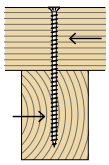	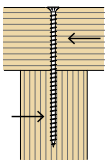
d_1	L	S_g	A	B_{min}	$R_{V,k}$	S_{PLATE}	S_g	A_{min}	$R_{V,k}$	$R_{tens,45,k}$	S_g	A	$R_{V,90,k}$	$R_{V,0,k}$
[mm]	[mm]	[mm]	[mm]	[mm]	[kN]	[mm]	[mm]	[mm]	[kN]	[kN]	[mm]	[mm]	[mm]	[kN]
13	80	25	35	50	2,90	20	60	60	6,96	37,48	25	40	4,18	2,44
	100	35	40	55	4,06		80	75	9,29		35	50	5,37	3,10
	150	60	60	75	6,96		130	110	15,09		60	75	8,37	4,06
	200	85	75	90	9,87		180	145	20,89		85	100	9,46	4,88
	250	110	95	110	12,77		230	185	26,70		110	125	10,49	5,77
	300	130	110	125	15,09		280	220	32,50		130	145	11,31	6,11
	350	155	125	140	17,99		330	255	38,30		155	170	11,94	6,42
	400	180	145	160	20,89		380	290	44,11		180	195	11,94	6,73
	450	205	160	175	23,79		430	325	49,91		205	220	11,94	7,04
	500	230	180	195	26,70		480	360	55,71		230	245	11,94	7,35
	550	255	195	210	29,60		530	395	61,52		255	270	11,94	7,65
	600	280	215	230	32,50		580	430	67,32		280	295	11,94	7,96
	650	305	230	245	35,40		-	-	-		305	320	11,94	8,27
	700	330	250	265	38,30		-	-	-		330	345	11,94	8,58
	750	355	265	280	41,21		-	-	-		355	370	11,94	8,88
	800	380	285	300	44,11		-	-	-		380	395	11,94	9,03
	850	405	300	315	47,01		-	-	-		405	420	11,94	9,03
	900	430	320	335	49,91		-	-	-		430	445	11,94	9,03
	950	455	335	350	52,81		-	-	-		455	470	11,94	9,03
	1000	480	355	370	55,71		-	-	-		480	495	11,94	9,03
	1100	530	390	405	61,52		-	-	-		530	545	11,94	9,03
	1200	580	425	440	67,32		-	-	-		580	595	11,94	9,03
	1300	630	460	475	73,13		-	-	-		630	645	11,94	9,03
	1400	680	495	510	78,93		-	-	-		680	695	11,94	9,03
	1500	730	530	545	84,73		-	-	-		730	745	11,94	9,03
15	600	280	215	230	37,50	-	-	-	-	45,96	280	295	14,53	9,47
	700	330	250	265	44,20		-	-	-		330	345	14,53	10,18
	800	380	285	300	50,89		-	-	-		380	395	14,53	10,89
	900	430	320	335	57,59		-	-	-		430	445	14,53	10,99
	1000	480	355	370	64,29		-	-	-		480	495	14,53	10,99
	1200	580	425	440	77,68		-	-	-		580	595	14,53	10,99
	1400	680	495	510	91,07		-	-	-		680	695	14,53	10,99
	1600	780	565	580	104,47		-	-	-		780	795	14,53	10,99
	1800	880	640	655	117,86		-	-	-		880	895	14,53	10,99
	2000	980	710	725	131,25		-	-	-		980	995	14,53	10,99

ε = screw-to-grain angle

NOTES and GENERAL PRINCIPLES on page 176.

STRUCTURAL VALUES | FURTHER APPLICATIONS

SHEAR CONNECTION WITH CROSSED CONNECTORS

VGS Ø9 - 11 mm

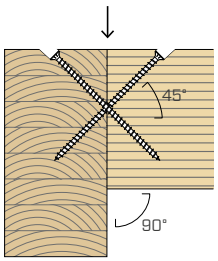

STRUCTURAL VALUES on page 130.

SLIDING CONNECTION WITH VGU WASHER

VGS Ø9 - 11 - 13 mm

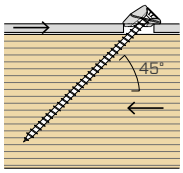

STRUCTURAL VALUES on page 192.

CONNECTIONS WITH CLT ELEMENTS

VGS Ø9 - 11 mm

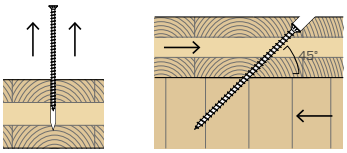

STRUCTURAL VALUES on page 134.

CONNECTIONS WITH LVL ELEMENTS

VGS Ø9 - 11 mm

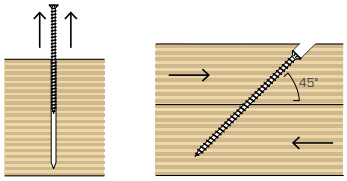

STRUCTURAL VALUES on page 138.

EFFECTIVE NUMBER FOR AXIAL STRESSES

The load-bearing capacity of a connection made with several screws, all of the same type and size, may be lower than the sum of the load-bearing capacities of the individual connection system.

For a connection with inclined screws, the characteristic effective sliding load-bearing capacity for a row of n screws is equal to:

$$R_{ef,V,k} = n_{ef,ax} \cdot R_{V,k}$$

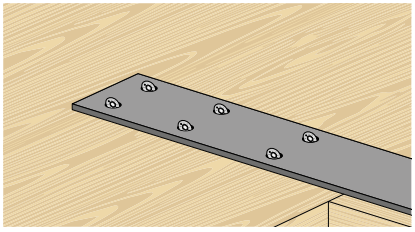

The n_{ef} value is given in the table below as a function of n (number of screws in a row).

n	2	3	4	5	6	7	8	9	10
$n_{ef,ax}$	1,87	2,70	3,60	4,50	5,40	6,30	7,20	8,10	9,00

STRUCTURAL VALUES | TC FUSION

CHARACTERISTIC VALUES
EN 1995:2014

TENSILE CONNECTION
CLT - CONCRETE

geometry	CLT	concrete

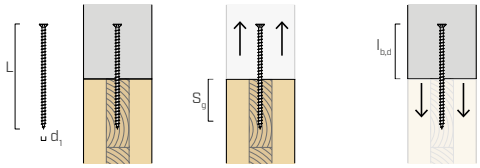

d_1 [mm]	L [mm]	S_g [mm]	$R_{ax,0,k}$ [kN]	$l_{b,d}$ [mm]	$R_{ax,C,k}$ [kN]
9	200	85	6,32	100	35,34
	220	105	7,65	100	
	240	125	8,95	100	
	260	145	10,22	100	
	280	165	11,49	100	
	300	185	12,73	100	
	320	205	13,96	100	
	340	225	15,18	100	
	360	245	16,39	100	
	380	265	17,59	100	
	400	285	18,78	100	
	440	325	21,14	100	
	480	365	23,47	100	
	520	405	25,40	100	
	560	445	25,40	100	
	600	485	25,40	100	
11	225	110	9,36	100	43,20
	250	135	11,26	100	
	275	160	13,12	100	
	300	185	14,95	100	
	325	210	16,75	100	
	350	235	18,54	100	
	375	260	20,31	100	
	400	285	22,05	100	
	425	310	23,79	100	
	450	335	25,51	100	
	475	360	27,22	100	
	500	385	28,91	100	
	525	410	30,59	100	
	550	435	32,27	100	
	575	460	33,93	100	
	600	485	35,59	100	
	650	535	38,00	100	
	700	585	38,00	100	
	750	635	38,00	100	
	800	685	38,00	100	
	850	735	38,00	100	
	900	785	38,00	100	
	950	835	38,00	100	
	1000	885	38,00	100	

TENSILE CONNECTION
CLT - CONCRETE

geometry	CLT	concrete

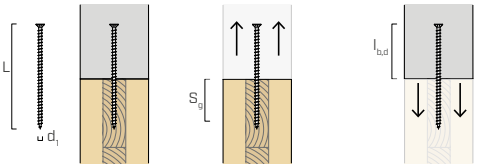

d_1 [mm]	L [mm]	S_g [mm]	$R_{ax,0,k}$ [kN]	$l_{b,d}$ [mm]	$R_{ax,C,k}$ [kN]
13	300	165	15,41	120	61,26
	350	215	19,56	120	
	400	265	23,61	120	
	450	315	27,58	120	
	500	365	31,50	120	
	550	415	35,35	120	
	600	465	39,16	120	
	650	515	42,93	120	
	700	565	46,67	120	
	750	615	50,37	120	
	800	665	53,00	120	
	850	715	53,00	120	
	900	765	53,00	120	
	950	815	53,00	120	
	1000	865	53,00	120	
	1100	965	53,00	120	
	1200	1065	53,00	120	
	1300	1165	53,00	120	
	1400	1265	53,00	120	
	1500	1365	53,00	120	

NOTES and **GENERAL PRINCIPLES** on page 176.

TC FUSION

TIMBER-TO-CONCRETE
JOINT SYSTEM

The innovation of VGS, VGZ and RTR all-thread connectors for timber-concrete applications.

Find it out on page 270.

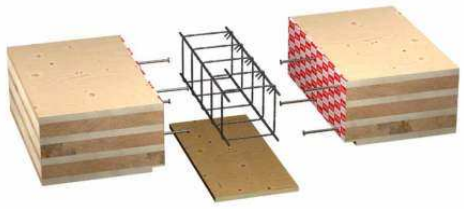

STRUCTURAL VALUES

GENERAL PRINCIPLES

- Characteristic values comply with the EN 1995:2014 standard in accordance with ETA-11/0030.
- The tensile design strength of the connector is the lower between the timber-side design strength ($R_{ax,d}$) and the steel-side design strength ($R_{tens,d}$).

$$R_{ax,d} = min \begin{cases} \frac{R_{ax,k} \cdot k_{mod}}{\gamma_M} \\ \frac{R_{tens,k}}{\gamma_{M2}} \end{cases}$$

- The compression design strength of the connector is the lower between the timber-side design strength ($R_{ax,d}$) and the instability design strength ($R_{ki,d}$).

$$R_{ax,d} = min \begin{cases} \frac{R_{ax,k} \cdot k_{mod}}{\gamma_M} \\ \frac{R_{ki,k}}{\gamma_{M1}} \end{cases}$$

- The design sliding strength of the joint is either the timber-side design strength ($R_{V,d}$) and the design strength on the steel side projected ($R_{tens,45,d}$), whichever is lower:

$$R_{V,d} = min \begin{cases} \frac{R_{V,k} \cdot k_{mod}}{\gamma_M} \\ \frac{R_{tens,45,k}}{\gamma_{M2}} \end{cases}$$

- The design shear strength of the connector is obtained from the characteristic value as follows:

$$R_{V,d} = \frac{R_{V,k} \cdot k_{mod}}{\gamma_M}$$

- The coefficients γ_M and k_{mod} should be taken according to the current regulations used for the calculation.
- For the mechanical resistance values and the geometry of the screws, reference was made to ETA-11/0030.
- Dimensioning and verification of the timber elements must be carried out separately.
- The screws must be positioned in accordance with the minimum distances.
- The characteristic thread withdrawal strengths were evaluated considering a penetration length of $S_{g,tot}$ or S_g, as shown in the table.
  For intermediate values of S_g it is possible to linearly interpolate.
- The shear srength and sliding values were evaluated considering the centre of gravity of the connector placed in correspondence with the shear plane.
- The characteristic shear resistances are calculated for screws inserted without pre-drilling hole. In the case of screws inserted with pre-drilling hole, greater resistance values can be obtained.
- The values in the table are evaluated considering mechanical strength parameters of the Ø15 VGS screws obtained analytically and validated by experimental tests.
- For different calculation configurations, the MyProject software is available (www.rothoblaas.com).

NOTES | TIMBER

- The characteristic thread withdrawal resistances were evaluated considering both an ε angle of 90° ($R_{ax,90,k}$) and of 0° ($R_{ax,0,k}$) between the grains of the timber element and the connector.
- The characteristic sliding strengths were evaluated by considering an angle ε of 45° between the grains of the timber element and the connector.
- The plate thickness (S_{PLATE}) are understood to be the minimum values to allow the countersunk head of the screw to be accommodated.
- The characteristic timber-to-timber shear strengths were evaluated considering both an ε angle of 90° ($R_{V,90,k}$) and 0° ($R_{V,0,k}$) between the grains of the second element and the connector.
- For the calculation process a timber characteristic density ρ_k = 385 kg/m^3 has been considered.
  For different ρ_k values, the strength values in the table (withdrawal, compression, sliding and shear) can be converted via the k_{dens} coefficient.

$$R'_{ax,k} = k_{dens,ax} \cdot R_{ax,k}$$
$$R'_{ki,k} = k_{dens,ki} \cdot R_{ki,k}$$
$$R'_{V,k} = k_{dens,ax} \cdot R_{V,k}$$
$$R'_{V,90,k} = k_{dens,V} \cdot R_{V,90,k}$$
$$R'_{V,0,k} = k_{dens,V} \cdot R_{V,0,k}$$

ρ_k [kg/m^3]	350	380	**385**	405	425	430	440
C-GL	*C24*	*C30*	*GL24h*	*GL26h*	*GL28h*	*GL30h*	*GL32h*
$k_{dens,ax}$	0,92	0,98	1,00	1,04	1,08	1,09	1,11
$k_{dens,ki}$	0,97	0,99	1,00	1,00	1,01	1,02	1,02
$k_{dens,v}$	0,90	0,98	1,00	1,02	1,05	1,05	1,07

Strength values thus determined may differ, for higher safety standards, from those resulting from an exact calculation.

NOTES | TC FUSION

- Characteristic values according to ETA-22/0806.
- The axial thread withdrawal resistance in the narrow face is valid for minimum CLT thickness $t_{CLT,min} = 10 \cdot d_1$ and minimum screw pull-through depth $t_{pen} = 10 \cdot d_1$.
- Connectors with shorter lengths than those in the table do not comply with the minimum penetration depth requirements and are not reported.
- A concrete grade of C25/30 was considered in the calculation. For applications with different materials please see ETA-22/0806.
- The tensile design strength of the connector is the lower between the timber-side design strength ($R_{ax,d}$) and the concrete-side design strength ($R_{ax,C,d}$).

$$R_{ax,d} = min \begin{cases} \frac{R_{ax,0,k} \cdot k_{mod}}{\gamma_M} \\ \frac{R_{ax,C,k}}{\gamma_{M,concrete}} \end{cases}$$

- The concrete element must have adequate reinforcement bars.
- The connectors must be arranged at a maximum distance of 300 mm.

RELATED PRODUCTS

JIG VGU
page 409

LEWIS
page 414

CATCH
page 408

TORQUE LIMITER
page 408

B 13 B
page 405

INSTALLATION SUGGESTIONS

MANUALS

LONG SCREWS

Thanks to CATCH, even longer screws can be screwed on quickly and safely without the risk of the bit slipping. Can be combined with TORQUE LIMITER.

VGS + VGU

The JIG VGU template makes it easy to prepare a 45° angle pre-drill, thus facilitating subsequent tightening of the VGS screws inside the washer. A pre-drill length of at least 20 mm is recommended.

To ensure control of the applied torque, the correct TORQUE LIMITER model must be used depending on the chosen connector.

VGS +WASPL

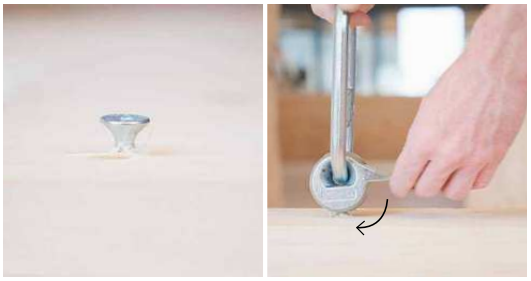

Insert the screw so that the head protrudes 15 mm and engage the WASPL hook.

After lifting, the WASPL hook releases quickly and easily ready for use again.

IMPORTANCE OF THE PILOT HOLE

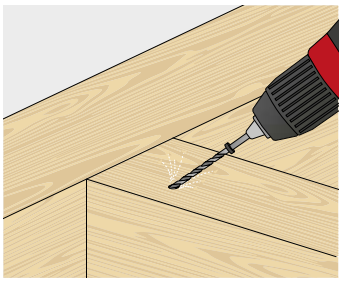

pilot hole

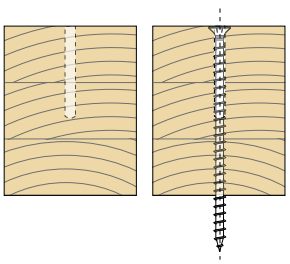

insertion with pilot hole

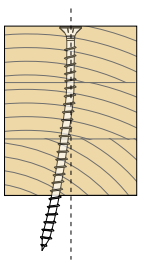

insertion without pilot hole

Deviation of the screw from the direction of screwing often occurs during installation.
This phenomenon is linked to the very conformation of the wood material, which is inhomogeneous and non-uniform, e.g. due to the localised presence of knots or physical properties dependent on grain direction. The operator's skill also plays an important role.

The use of pilot holes facilitates the insertion of screws, particularly long ones, allowing a very precise insertion direction.

INSTALLATION INSTRUCTIONS

MANUALS

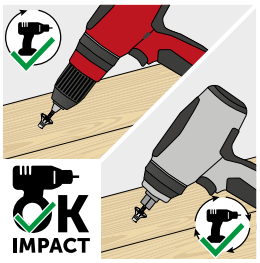

In the case of installation of screws used in timber-to-timber (softwood) structural connections, a pulse screw gun/screwdriver can also be used.

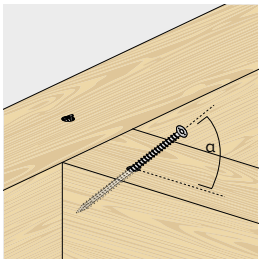

Respect the insertion angle with the help of a pilot hole and/or installation template.

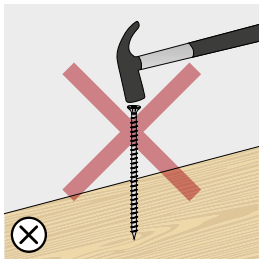

Do not hammer the screw tips into the timber.

The screw cannot be reused.

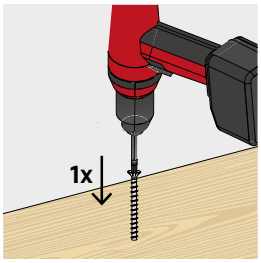

In general, it is recommended to install the connector in a single operation, without stopping and restarting which could create additional stress in the screw.

STEEL-TO-TIMBER APPLICATION

The use of pulse screw guns/impact wrenches is not permitted.

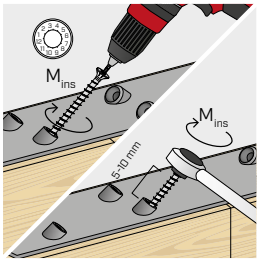

Ensure correct tightening. We recommend the use of torque-controlled screwdrivers, e.g. with TORQUE LIMITER. Alternatively, tighten with a torque wrench.

VGS	d_1 [mm]	$M_{ins,rec}$ [Nm]
Ø9	9	20
Ø11 L < 400 mm	11	30
Ø11 L ≥ 400 mm	11	40
Ø13	13	50

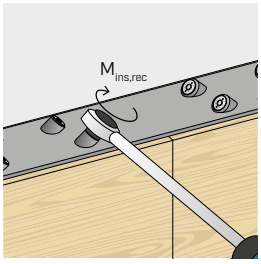

After installation, the fasteners can be inspected using a torque wrench.

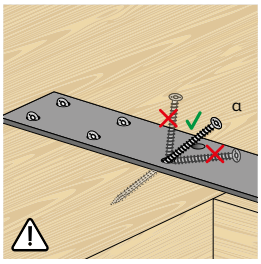

Avoid bending.

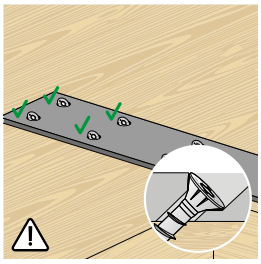

The installation of multiple screws must be performed to guarantee that loads are distributed evenly to all fasteners.

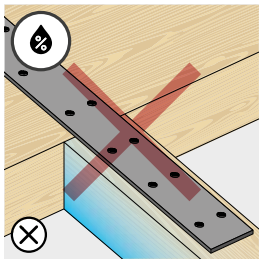

Shrinkage or swelling of timber elements due to changes in moisture content must be avoided.

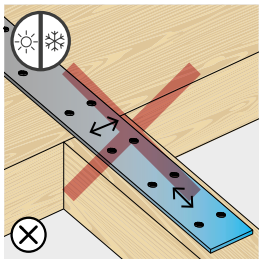

Avoid dimensional changes in the metal, e.g. due to large temperature fluctuations.

SHAPED PLATE

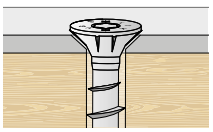

Countersunk hole.

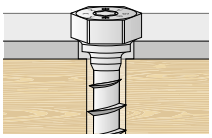

Cylindrical hole.

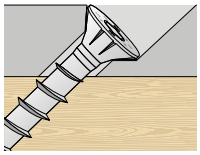

Inclined countersunk hole.

WASHERS

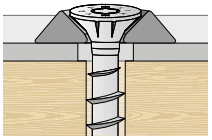

Cylindrical hole with countersunk washer HUS.

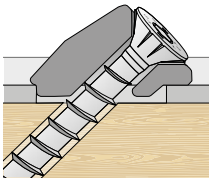

Slotted hole with VGU washer.

APPLICATION EXAMPLES: REINFORCEMENT

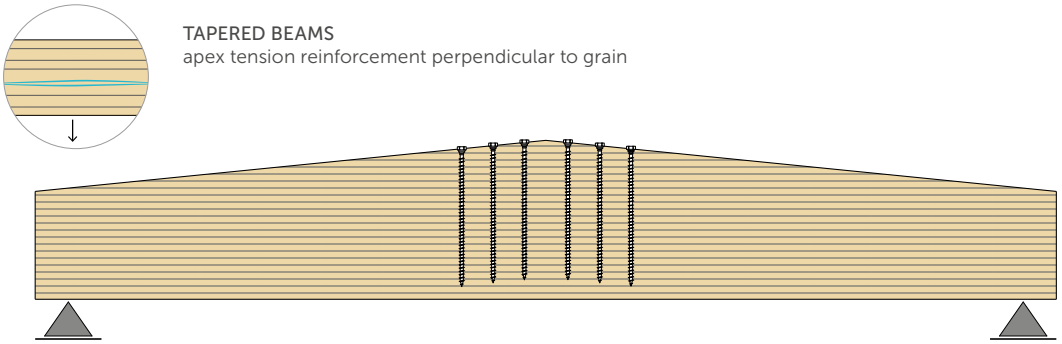

TAPERED BEAMS
apex tension reinforcement perpendicular to grain

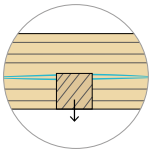

HANGING LOAD
tension reinforcement perpendicular to grain

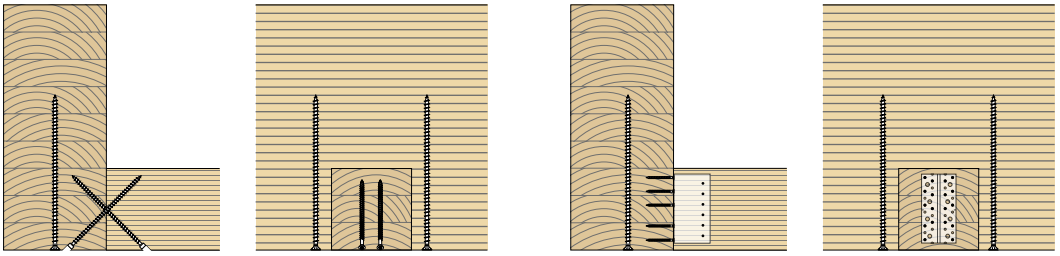

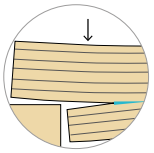

NOTCH
tension reinforcement
perpendicular to grain

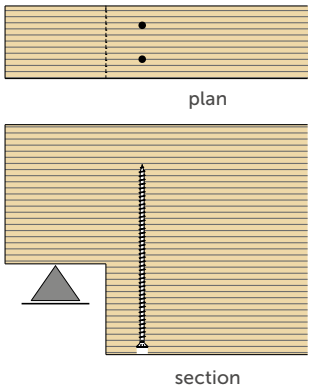

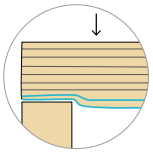

SUPPORT
compression reinforcement
perpendicular to grain

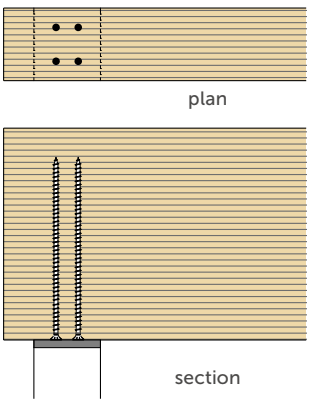

E.3 Griffon D3

6305082 - GRIFFON HOUTLIJM VB20® FLACON 750 G NL/FR/DE

PVAC HOUTLIJM VB20 (D3)

WATERBESTENDIGE PVAC HOUTLIJM

PRODUCTOMSCHRIJVING

Waterbestendige, witte houtlijm op basis van PVAC.

TOEPASSINGSGEBIED

Voor het waterbestendig (D3) verlijmen en lamineren van vrijwel alle zachte, harde en exotische houtsoorten. Toepasbaar voor goed passende, niet-dragende houtconstructies d.m.v. diverse houtverbindingen, zoals vingerlassen, zwaluwstaarten, pen-gat verbindingen, drevels en veren. Geschikt voor binnen- en buitentoepassingen (buitenruimten niet blootgesteld aan weersinvloeden), zoals kozijnen, deuren en meubels in bijvoorbeeld woonkamers, kantoren, keukens en badkamers. Voor vlakverlijming van hout, zacht- en hardboard, spaanplaat, multiplex, MDF, papier, karton en board. Ook voor het lamineren van fineer en hard plastic plaat (HPL; Formica, Duropal, Resopal) op houten ondergronden. D3: Binnenruimten, waar regelmatig gedurende een korte periode langslopend water, condensvorming en/of een zware belasting ten gevolge van een verhoogde relatieve luchtvochtigheid optreedt. Buitenruimten niet blootgesteld aan weersinvloeden.

EIGENSCHAPPEN

· Voor gebruik binnen en buiten
· Watervast (EN 204 D3)
· Transparant na droging
· Oplosmiddelvrij
· Overschilderbaar

KEUREN & NORMERINGEN

Certificaten	
KOMO®	KOMO: Lijmen voor niet-dragende toepassingen. Certificaat 32394 op basis van BRL 2339 (EN 204: D3 klasse).

Normeringen	
EN 204 D3	EN 204: D3

VOORBEREIDING

Verwerkingsomstandigheden: De temperatuur van omgeving, de lijm en de te verlijmen materialen mag niet lager zijn dan +5°C. Relatieve luchtvochtigheid van maximaal 65%. Houtvochtigheidsgehalte tussen de 8% en 12%.
Eisen oppervlakken: De te lijmen oppervlakken moeten schoon, droog en stofvrij zijn. Zorg voor een goed passende verbinding.
Voorbehandeling oppervlakken: Vette houtsoorten vooraf ontvetten.
Gereedschap: Fijngetande lijmkam (1 mm), kwast of roller, klem of pers.

VERWERKING

Verbruik: 5-7 m²/kg, eenzijdig opgebracht, afhankelijk van de aard van de materialen.
Gebruiksaanwijzing:
De lijm dun en gelijkmatig op één of beide delen aanbrengen m.b.v. fijngetande lijmkam (1 mm), kwast of roller. Lijm enkele minuten laten intrekken. Verbinding binnen 8 minuten monteren en klemmen of persen.
Vlekken/resten: Natte lijmresten direct verwijderen met water. Opgedroogde lijmresten zijn alleen mechanisch te verwijderen.
Aandachtspunten: Let op voor aantasting van metalen (b.v. onderdelen van pompen/machines). Gebruik zuurresistente componenten bij machinale verwerking.

PVAC HOUTLIJM VB20 (D3)

WATERBESTENDIGE PVAC HOUTLIJM

TECHNISCHE SPECIFICATIES

Basisgrondstof:	Polyvinylacetaatdispersie
Kleur:	Wit
Kleur na uitharden/ drogen:	Transparant
Dichtheid ca.:	1.1 g/cm³
Verdunnen:	Alleen verdunnen met water.
Vullend vermogen:	Niet
Minimale temperatuurbestendigheid:	-20 °C
Maximale temperatuurbestendigheid:	60 °C
Vochtbestendigheid:	Goed
Open tijd ca.:	8 minuten
Overschilderbaarheid:	Goed
pH-waarde ca.:	3
Persdruk:	5-10 kg/cm²
Vastestofgehalte ca.:	50 %
Perstijd:	15 minuten (meer in geval van spanning)
Viscositeit:	Vloeibaar
Viscositeit ca.:	13000 mPa·s
Waterbestendigheid:	Goed
Witpunt:	3 °C

OPSLAGCONDITIES

Minimaal 36 maanden.
Aangebroken verpakking beperkt houdbaar.
Opslaan in goed gesloten verpakking op een droge plaats bij een temperatuur tussen +10°C en +20°C.

F Equipment Technical Information

F.1 Qdos 30 Peristaltic Pump

Qdos 30

Qdos-doseerpomp

Kenmerken en voordelen

- Lagere chemicaliën kosten dankzij nauwkeurige dosering
- Eenvoudige drop-in installatie maakt randapparatuur overbodig
- Minder onderhoud omdat een enkel component zonder gereedschap kan worden vervangen
- De cost of ownership is lager dan die van een membraanpomp
- Opbrengsten van 0.1 tot 500 ml/min bij tot 7 bar
- Geen tegendrukkleppen, pulsatiedemper, ontgassingskleppen, voetkleppen, filters of vlotterschakelaars

Prestaties Qdos 30

	qdos		qdos remote uitvoering	
	Snelheid (tpm)	**Opbrengst ml/min***	**Snelheid (tpm)**	**Opbrengst ml/min***
qdos 30	0,025 - 125	0,1-500 (0,001-7,93)	0,078-125	0,3-500 (0,005-7,93)

*nauwkeurigheid ±1%, herhaalbaarheid ±0,5%

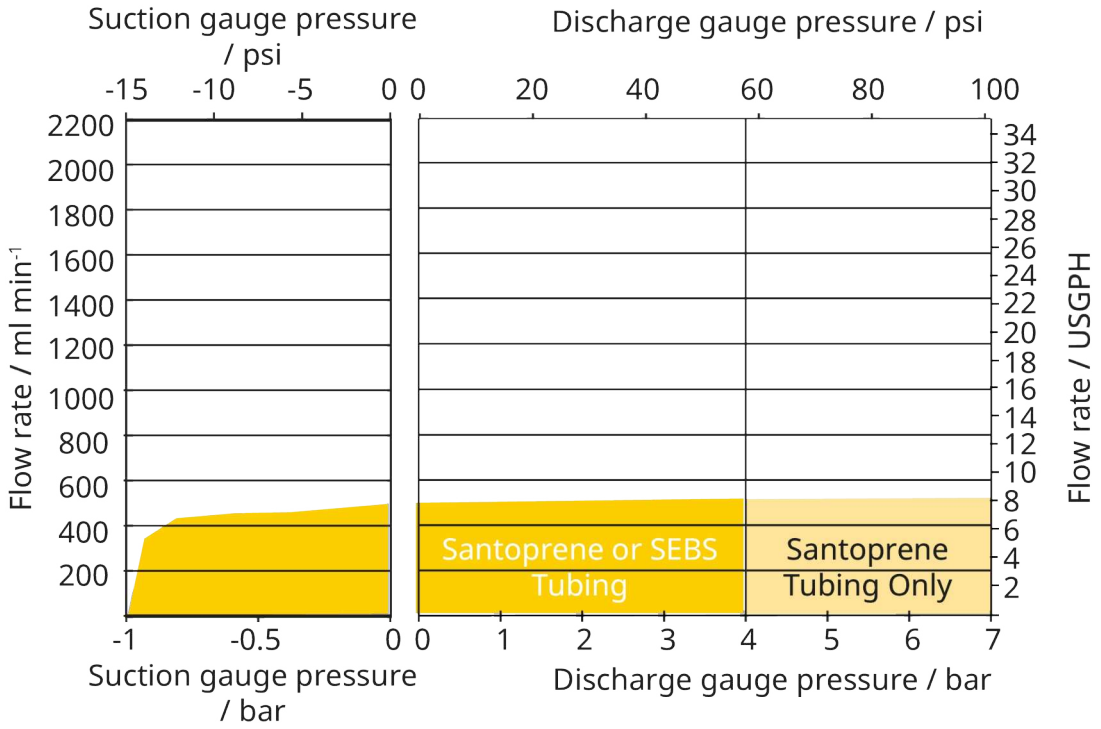

Technische specificaties

	Qdos 30
Max. opbrengst	500 ml/min
Min. opbrengst	0.1 ml/min
Max. opbrengst	7.93 USGPH
Min. opbrengst	0.001 USGPH
Maximale werkdruk	7 bar
Maximale werkdruk	100 psi
Max. bedrijfssnelheid	125 tpm
Omgevingstemperatuurbereik	5 tot 45 °C
Omgevingstemperatuurbereik	41 tot 113 °F
Gewicht	5.05 kg
Gewicht	11.1 lbs
Besturingstypen	Handmatig, Op afstand / Remote, Profibus®, Universal, Universal+
Standaarden	CE, cETLus, CSA, C-Tick, IRAM S-markering, NSF 61
IP-klasse	IP66, NEMA 4X
Vochtigheid	80 % tot 31 °C, 88 °F, lineair dalend tot 50 % bij 40 °C, 104 °F
Geluid	< 70 dB(A) op 1 m
Max. hoogte	2000
Voeding	100-240 VAC 50-60 Hz 190 VA, 12-24 VDC

Min. opbrengst is afhankelijk van het model, flow-unit en regelmethode.
Sommige varianten van de pompkopslangen beperken de maximale druk tot 4 bar.

Constructie materialen

	Qdos 30
Lagers	Roestvrij staal, Staal
Aandrijfas	Roestvrij staal 440C
Behuizing aandrijving	20 % glasgevulde PPE/ PS
Coating van behuizing van aandrijving	20 % glasgevulde PPE/ PS
Vloeistofkoppelingen	Polypropyleen, PVDF
Toetsenbord/HMI	Polyester
Smeermiddel	Op basis van PFPE
Pompkopbehuizing	40 % glasgevulde PPE/ PS
Pompkoprotor	Glasgevuld nylon
Slangen	Santoprene, SEBS

De vermelde informatie heeft betrekking op het volledige assortiment.
Voor gedetailleerde specificaties van individuele modellen/componenten kunt u de gebruikershandleiding raadplegen of contact opnemen met de vertegenwoordiger van WMFTS.

Qdos 30 Afmetingen

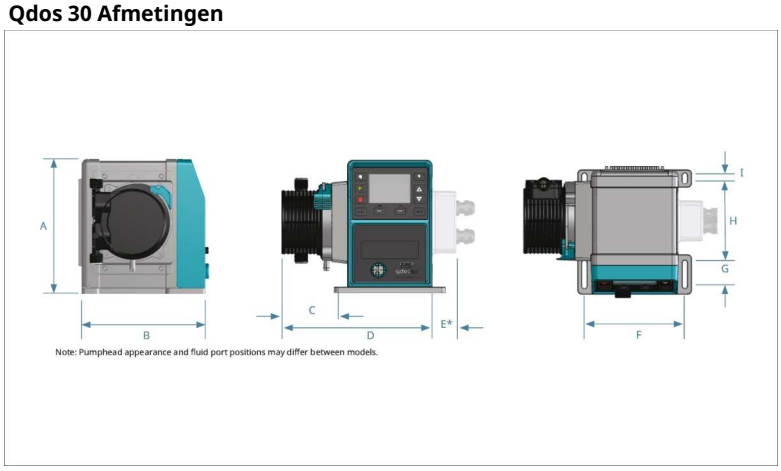

Model	A	B	C	D	E	F	G	H	I
qdos 30	234 mm (9,2")	214 mm (8,4")	71,5mm (2,8")	233mm (9,2")	43 mm (1,7")	173 mm (6,8")	40 mm (1,6")	140 mm (5,5")	10 mm (0,4")
* Optionele relaismodule									

Bedieningsopties

Operationele modus	Handmatig	Op afstand / Remote	PROFIBUS	Universal	Universal+
Handmatig	✓		✓	✓	✓
PROFIBUS - bussnelheid 9,6 -1.500 kb/s			✓		
Contact				✓	✓
4-20 mA		✓		✓	✓
Storingsmelding	✓	✓	✓	✓	✓

Kenmerken	Handmatig	Op afstand / Remote	PROFIBUS	Universal	Universal+
Numerieke weergave van opbrengst	✓		✓	✓	✓
Numerieke snelheidsweergave	✓		✓	✓	✓
Vloeistofmeter	✓		✓	✓	✓
Max (prime)	✓		✓	✓	✓
Automatisch herstarten (nadat voeding is hersteld)	✓	✓	✓	✓	✓
Vloeistofterugwinning	✓		✓	✓	✓
Lekdetectie	✓	✓	✓	✓	✓
3,5" (88,9mm) TFT-kleurenscherm	✓		✓	✓	✓
LED Pompstatus iconen		✓			

Regelmethodes	Handmatig	Op afstand / Remote	PROFIBUS	Universal	Universal+
Opties ingang/uitgang		L	L	L of R	L of R
Mogelijkheid van handmatige besturing	✓		✓	✓	✓
4-20 mA ingang		✓		✓	✓
4-20 mA ingang tweepuntskalibratie					✓
4-20 mA uitgang		✓			✓
Contactingang (puls/batch)				L of R	L of R
Bereik voor handmatige toerentalaanpassing	3.333:1 (Qdos 20) 5.000:1 (Qdos 30) 10.000:1 (Qdos 60) 20.000:1 (Qdos 120)		3.333:1 (Qdos 20) 5.000:1 (Qdos 30) 10.000:1 (Qdos 60) 20.000:1 (Qdos 120)	3.333:1 (Qdos 20) 5.000:1 (Qdos 30) 10.000:1 (Qdos 60) 20.000:1 (Qdos 120)	3.333:1 (Qdos 20) 5.000:1 (Qdos 30) 10.000:1 (Qdos 60) 20.000:1 (Qdos 120)
Minimale stapsgewijze verhoging van het motortoerental (Afhankelijk van de bedrijfsmodus en de gekozen flow-unit)	0,006	0,078	0,100	0,003	0,003
Resolutie van 4-20 mA		1.600:1		1.600:1	1.600:1
Profibus-snelheidsresolutie			550:1 (Qdos 20) 1.250:1 (Qdos 30) 1.250:1 Qdos 60 1.400:1 (Qdos 120)		
Ingang bedrijfsstop		✓		✓	✓
Uitgang bedrijfsstatus		✓		✓	L
Alarmsignaal		✓		✓	L
Vier configureerbare relaisuitgangen					R
Vloeistofterugwinning op afstand		✓		✓	✓

PROFIBUS	Handmatig	Op afstand / Remote	PROFIBUS	Universal	Universal+
Snelheidsinstellingspunt			✓		
Snelheid terugkoppeling			✓		
Opbrengstkalibratie-functie			✓		
Bedrijfsuren			✓		
Toerenteller			✓		
Lekdetectie			✓		
Alarm bij laag vloeistofniveau			✓		
Diagnostische terugkoppeling			✓		

Beveiliging	Handmatig	Op afstand / Remote	PROFIBUS	Universal	Universal+
Toetsenbord-vergrendeling	✓		✓	✓	✓
PIN-vergrendeling om instellingen te beschermen	✓		✓	✓	✓

*Besturingsopties – Universal en Universal+ modellen		
Variant	**Standaardpomp (L)**	**Relaismodule (R)**
Ingang	5-24 VDC	5-24 VDC 110 VAC
Uitgang	Open collector	Nominaal vermogen 110V AC, 4A 30V DC, 4A

Productcodes

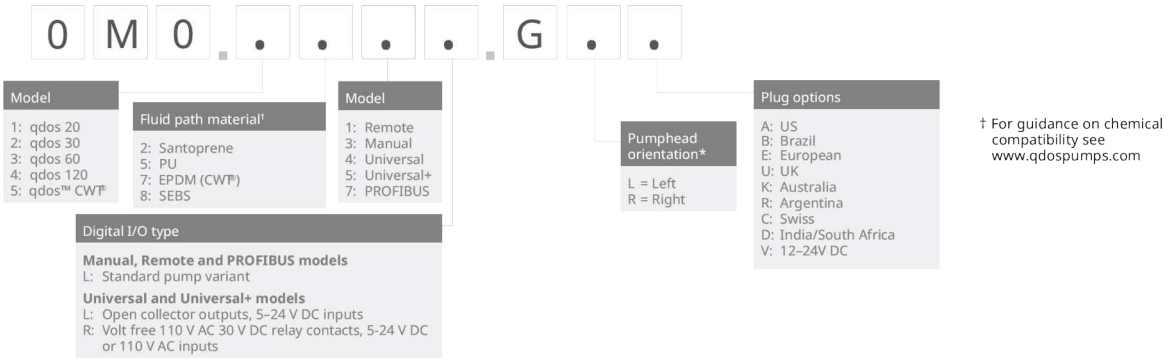

† For guidance on chemical compatibility see www.qdospumps.com

* The pumphead side location is required when ordering. The left/right perspective assumes the user is looking at the front of the pump. The pump in the dimensions diagram is considered a pumphead located to the left.

Productcodes

Omschrijving	Artikelcode
ReNu 30 pompkop Santoprene / PFPE 7 bar (100 psi)	0M3.2200.PFP
ReNu 30 pompkop SEBS / PFPE 4 bar (60 psi)	0M3.2800.PFP

wmfts.com/global

21 September 2023

F.2 Nozzle Technical Drawing

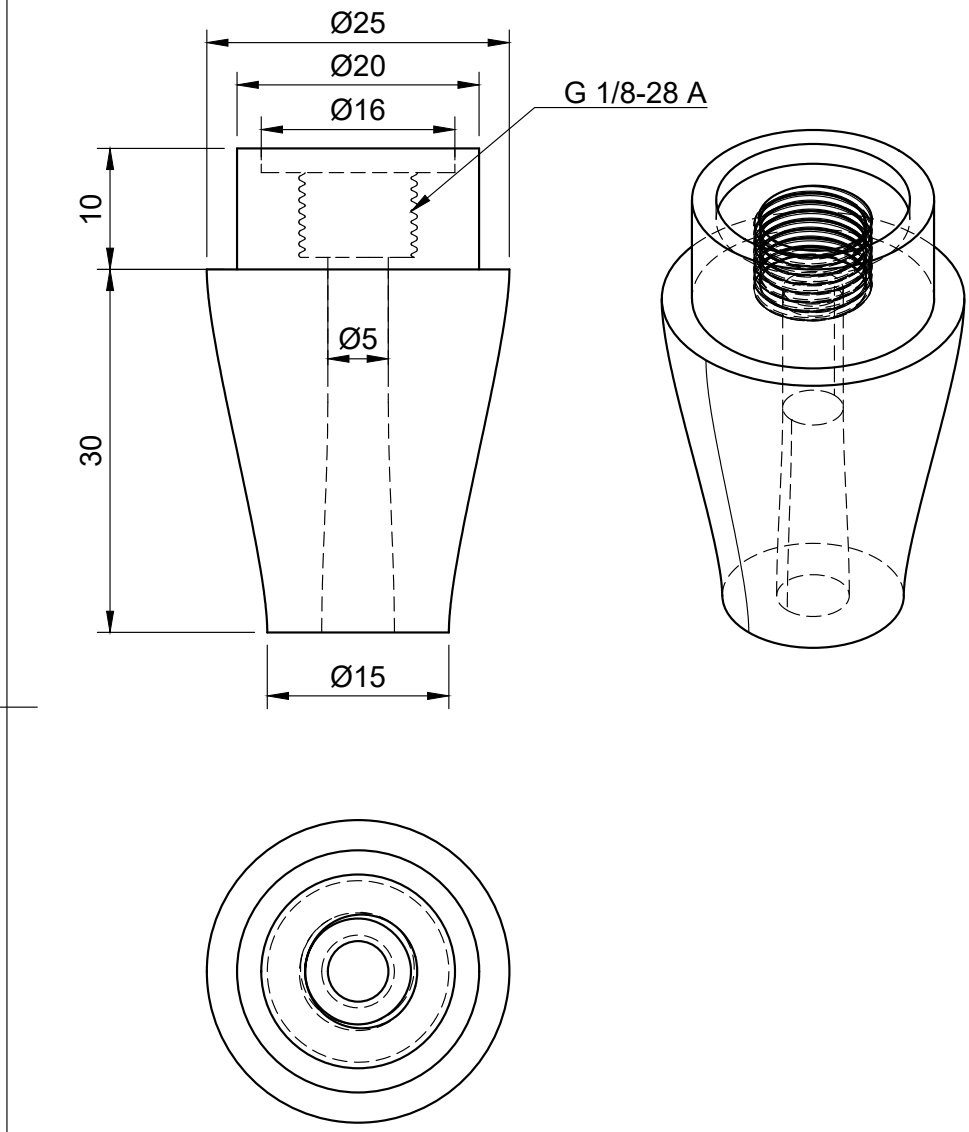

Dept.	Technical reference	Created by Thom Bindels 02/03/2024	Approved by	
		Document type	Document status	
		Title Dispensing nozzle	DWG No.	
			Rev. / Date of issue	Sheet 1/1

Eindhoven
University of
Technology

PO Box 513
5600 MB Eindhoven
The Netherlands

www.tue.nl